FLUID FLOW THROUGH VEGETATION

CLINT Y. H. WONG
University of Oxford

A thesis submitted for the degree of
Doctor of Philosophy
September 2020

PREFACE

This thesis comprises research that was undertaken at the Mathematical Institute, University of Oxford between July 2017 and September 2020, under the supervision of Prof. Jon Chapman, Dr Aggelos Dimakopoulos and Dr Philippe Trinh. The research involves collaborations with HR Wallingford and the US Army Engineer Research and Development Center, and was funded by our collaborators and also the EPSRC Centre for Doctoral Training in Industrially Focused Mathematical Modelling.

No part of my thesis has been accepted or is currently being submitted for any degree, diploma, certificate or other qualification, apart from the degree of Doctor of Philosophy at the University of Oxford. I also confirm that the thesis I am submitting is wholly my own work.

An article that is based on the content of Chapter 6 of this thesis has been published in the *Journal of Fluid Mechanics*, co-authored by S. J. Chapman and P. H. Trinh.

Oxford, September 2020

ACKNOWLEDGEMENTS

First and foremost, I am deeply indebted to my academic supervisors, Jon Chapman and Phil Trinh, for their unparalleled insight, knowledge, humour, and trust. I really appreciate how well we have managed to work together over the past three-and-a-half years, even though we are based in different cities, have hectic schedules, and also have to cope with a global pandemic. They have never failed to inspire me and I hope that they will continue to do so.

I have also very much enjoyed the collaboration with HR Wallingford and the US Army Engineer Research and Development Center (ERDC), thanks to Aggelos Dimakopoulos, my industrial supervisor. His expertise in CFD and also his trust in me from the very start of this project is much appreciated. Chris Kees and Tristan de Lataillade from ERDC have also been extremely helpful with their technical support on low-level coding and running numerical simulations in *Proteus*.

I have to thank James Jackaman for supplying the numerical code for solving the Korteweg-de Vries equation (Jackaman and Pryer, 2019)—this code has been modified for analysing vegetative flows in Chapter 4. I also have to thank Federico Danieli, for introducing me to Jack, and also for the fruitful discussions on eigenvalues and pseudospectra.

I must thank Dominic Vella for introducing me to the crucial elements of research before I even started my master's degree, and encouraging me to pose purposeful scientific questions ever since. In addition to my two examiners, Ian Hewitt and Paul Milewski, Yuki Asano, Peter Howell, Kristian Kiradjiev and Attila Kovács have all given me valuable comments and suggestions about my work. I must also extend my special thanks to Jessica Williams for her incredible support during multiple stages of my degree (on top of being the best officemate and friend).

I gratefully acknowledge St Anne's College, Oxford, for their multiple research and travelling grants.

On a personal note, many thanks to Raquel González Fariña, Scott Marquis and other housemates at Wharf House for being a cheerful lot. Thanks should also go to Judy Chu for her hospitality while I was at an ERDC workshop at UC Berkeley. I am also very grateful to Domen Prešern, Cynthia Cheloff, Nikol Lambeva, Gianmarco Luppi et al. from the university wine team for the pair of 1975 Romanée-Conti and Bollinger R.D., dinner at Ch. Lafite Rothschild, and filming a documentary with HBO on the four-thousand wines that we have assessed.

Finally, I have to thank Nadia Tai for keeping me vaguely sane, and my parents, Gary and Carrie, for their love and support.

ABSTRACT

This thesis is concerned with the mechanical aspects of fluid-vegetation interaction in coastal flows and their resultant instabilities. Specifically, we consider the evolution of periodic waves as they propagate through vegetated domains, and the emergence of *monami* – the progressive, synchronous oscillation of submerged vegetation under sufficiently strong flows. We divide our analysis between rigid and flexible vegetative canopies. These new predictions and physical insights will be applicable in the analysis of a diverse range of industrial and environmental applications involving fluid-vegetation interactions.

In the case of rigid vegetation, using the method of multiple scales, we derive the evolution of small-amplitude waves propagating over a varying substrate fully covered with vegetation. In particular, we give time-averaged predictions for both the amplitude and the wavelength of the waves as functions of the distance of propagation. We then extend this analysis to include the situations of (i) combined current-wave flows and (ii) shallow-water waves through vegetation. For the case of combined current-wave flows, we demonstrate the manner in which the surface waves vary as a function of the current, and also how the current remains unaffected by the evolving wave. For shallow-water waves, we explore how cnoidal waves, nonlinear periodic solutions of the Korteweg-de Vries equation, evolve on horizontal substrates. For all of the flows considered above on rigid vegetation, their evolutions are only drag-dependent and hence independent of added mass and virtual buoyancy.

In the case of flexible vegetation, we propose a model where the plants are described by elastic cantilever beams. Our first analysis concerns the propagation of small-amplitude waves. Compared to the case of rigid vegetation, the fluid will load and deform each vegetative structure. This deformation, in turn, must affect the flow. Although the flow and the beam dynamics have to be determined simultaneously, we show that when the wavelength is sufficiently small, such quantities are asymptotically decoupled – this allows us to first determine the local beam dynamics before evaluating the momentum loss in the macroscopic flow. In contrast to rigid vegetation, we find that added mass and virtual buoyancy play a role.

Finally, we focus on understanding the mechanisms and critical conditions for triggering monami. We treat the current as unidirectional and solve for the steady configurations of the flow and the deflected canopy. Our stability analysis predicts that monami is induced by shear along the top of the canopy. Meanwhile, monami can be suppressed if the canopy is sufficiently sparse or if there is sufficient inertia in the system.

CONTENTS

1 INTRODUCTION

> Water is the driving force in nature.
>
> *Leonardo da Vinci*

The study of fluid-structure interactions with vegetation has a wide range of industrial and environmental applications, including flood control, environmental conservation, and energy production (Morris et al., 2018). However, there are many challenges in modelling such flows, particularly due to the multi-scale nature of the problem, as well as the fact that the vegetation and flow can be coupled. This thesis is dedicated to the development of compact mathematical models that describe flows through vegetated regions and their resultant instabilities.

1.1 MOTIVATION

Climate change is increasing the frequency and severity of hydrological disasters (Webster et al., 2005). While there is a great deal of work into infrastructure design and its effect on flow management, there is also an emerging interest in utilising aquatic vegetation to dampen waves and mitigate floods—such methods are particularly attractive as the vegetation forms part of the natural habitat helping to sustain our ecosystems.

Aquatic vegetation is abundant in nature: to provide some context, approximately 10% of seabeds at depths 0–40 m are covered by seagrass, with the specie, *Posidonia oceanica*, alone covers 25% of the seabeds in the Mediterranean Sea (Borum et al., 2004). Furthermore, compared to artificial measures, aquatic vegetation can be equally effective, while possessing the promising abilities of adapting to the local environment, growing, and also self-repairing after destructive events – a review is given by Morris et al. (2018). The same review has also mentioned about how plants are used as coastal defence, either on their own or complimented with other artificial infrastructures to maximise benefits. In light of this, however, flows through vegetation are extremely challenging to model. We begin by highlighting the aspects involved in modelling the vegetation:

(i) Plants naturally have complex geometries, with different components that have length scales and material properties that differ in multiple orders of magnitude *e.g.* the leaves and branches of a mangrove. To reduce complexity, many researchers model such

structures with simpler geometries such as cylinders and blades (Nepf, 2012).

(ii) Distinct from terrestrial flows, aquatic vegetation can have heights that are comparable in magnitude to the water depth to photosynthesise (Nepf, 2012; Marion et al., 2014). As a result, although the total volume fraction of vegetation can be low compared to its surrounding fluid, a significant proportion of the domain is obstructed by the *canopy*—a vegetative layer or a community of vegetation. Free-surface effects can also be important.

(iii) Above all, in contrast to mangroves, which has permanent wood, certain families of aquatic vegetation, such as seagrass, are narrow, flexible and streamlined – an example is given in the margin. Such properties allow them to passively reconfigure and consequently reducing the flow-induced load and increase survivability at exposed sites (Vogel, 1994). At sheltered sites, other photosynthetic organisms such as macroalgae (seaweed) can be wide and ruffled to increase photosynthesis and reduce shielding (Koehl et al., 2008).

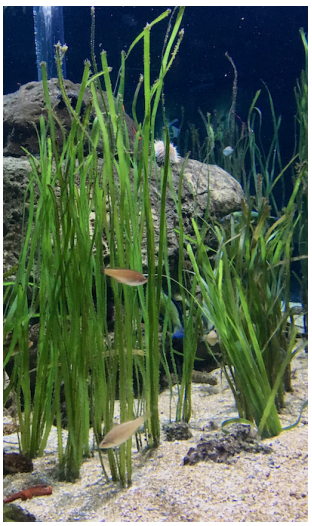

A seagrass meadow. Image is taken at The Oceanographic, Spain.

Thus far, we have only outlined the complexities involved in modelling vegetation—we recall that the other part of the challenge is to account for the different types of coastal flows, which contributes additional length scales and physical effects. Together with all these factors, we quote from Mendez and Losada (2004) that:

> *The variability of wave damping is very large and trying to define a generalized behaviour of the 'plant-induced dissipation' is absolutely impossible.*

Consequently, the efficiency of aquatic vegetation in protecting coastal regions, and the physical mechanisms involved are yet to be fully understood (Marion et al., 2014). However, substantial research has also been done in modelling flows through vegetation. In the upcoming sections, we will outline the different sub-problems involved and the purpose of this work.

1.2 PROBLEM DESCRIPTION AND SCOPE

Suppose we have an incident wave that is propagating through some vegetation in a coastal region. In Figure 1.1, we provide a schematic diagram that illustrates the types of waves that may arise, categorised by water depth (in relation to wavelength) shown on the horizontal, and amplitude (in relation to water depth) shown on the vertical. We first discuss the regimes which are beyond the scope of this thesis, before discussing the regimes of interest (annotated in green) in further detail. We will separately address the problem of current-dominated flows.

In the vicinity of the shore, deep-water waves do not exist unless the wave frequency is high. This regime is thus more relevant to infinitesimal capillary-gravity waves rather than surface gravity waves. Furthermore,

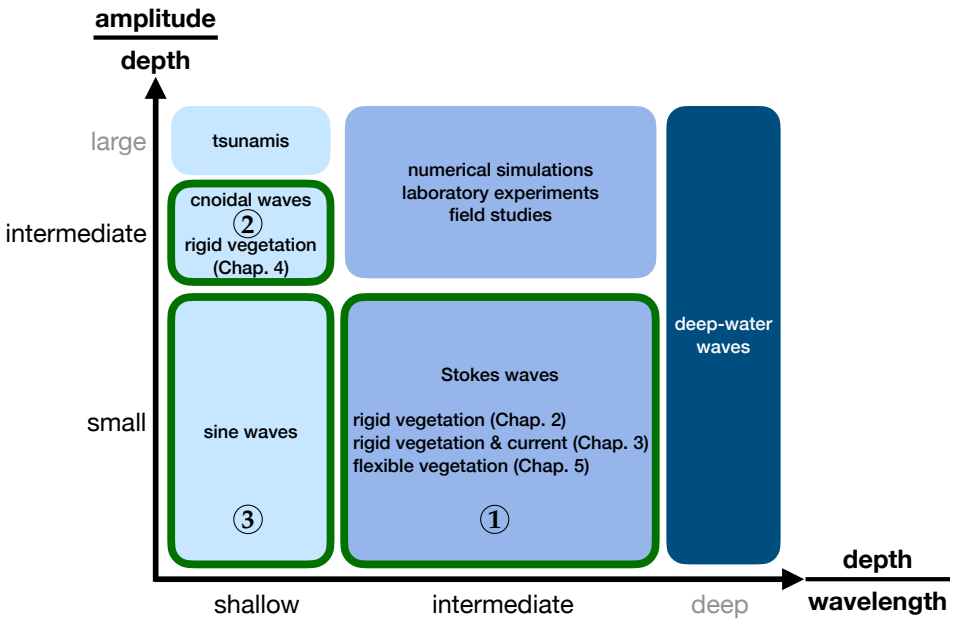

Figure 1.1: Schematic diagram that outlines the different regimes involved in waves through vegetation in a coastal region. The regimes which are considered in this work are annotated in green.

submerged structures, including the substrate and any vegetation that is present, typically contribute negligible effects to the dynamics of deep-water waves. Therefore, deep-water waves are not considered in this work. Meanwhile, we also ignore tsunamis in the large-amplitude shallow-water regime (top-left of Figure 1.1) by focusing our analysis on periodic waves.

For waves at intermediate depth (centre column of Figure 1.1), unless the wave amplitude is small, they cannot be explained mathematically with classic Stokes' linear theory, which is derived from asymptotic expansions in the amplitude-to-depth ratio (or expansions in the amplitude-to-wavelength ratio, assuming that the depth is comparable to the wavelength) (Mei, 1992). In such cases, we have to result to numerical simulations, laboratory experiments or field observations (see *e.g.* Figure 1.2). However, they can come at high costs and can often only explain small parts of the parameter space.

Fortunately, many coastal waves with (relatively) small amplitudes can still be explained by Stokes' theory and similarly, cnoidal theory for shallow-water waves, at least in the absence of vegetation (Hamm et al., 1993). Such theories are what researchers have been utilising as well for theoretical work on flows through vegetation. We now discuss the individual regimes of interest, what questions are yet to be answered, and how we will address some of these questions. We emphasise that will provide a more detailed review of the various existing theories in each individual chapter.

1.2.1 *Small-amplitude waves*

We begin by considering the small-amplitude waves of intermediate-depth propagating through vegetation [shown ① in Figure 1.1]. Firstly, in the absence of vegetation, the classic phenomenon of *shoaling* – waves increasing in amplitude (while decreasing in wavelength) as they approach the shore

Figure 1.2: An operating 12 × 20 m wave flume with waves generated by multiple paddles (in red) and absorbed by the wave absorber (in dark-blue at the bottom-left of each image). Unidirectional waves are generated by paddles which are moving in phase; cross waves are generated by imposing constant phase shifts between consecutive paddles. Images are taken at the Hydrodynamics laboratory, Imperial College London.

– is well understood, provided that the topography is varying on a much longer length scale than the wavelength itself (Keller, 1958). On the other hand, predictions of amplitude decay for waves through rigid vegetation along a simple horizontal substrate was first derived by Dalrymple et al. (1984) based on an energy balance argument. This has since been the default prediction, with different ad-hoc variations are used for more complex flows *e.g.* the drag coefficient can be fitted to account for plant flexibility.

However, the more realistic combined problem has only been studied in the shallow-water limit (Mendez and Losada, 2004) (bottom-left of the schematic in Figure 1.1). A reasonable but fundamental question has been neglected: *How do waves evolve differently for the combined problem if the wave velocity is also depth-dependent? More importantly, can we predict the wave evolution using a rigorous framework?*

A rigorous but generalisable framework is beneficial for addressing other types of flows that arise. A natural extension of this problem is to understand how a combined current-wave flow evolves in the presence of rigid vegetation. With the coupling between the current and the wave, we may ask: *How does the current affect the wave and vice versa? Under what regimes do they decouple?* Some of these questions have been answered in the literature for the fluid-only scenarios (Peregrine, 1976) but not in the context of vegetative flows.

Another natural extension of the pure-wave problem through vegetation is to consider scenarios in which the vegetation is flexible. The study of flexible aquatic vegetation has gained a lot of interest, driven by both the complex dynamics and also the applications in coastal management with seagrass [see the review by Nepf (2012)]. The problem of waves acting on a single plant is relatively well understood, thanks to the research from various researchers on modelling plants as elastic cantilever beams – we highlight the work by Luhar and Nepf (2016) and Leclercq and de Langre

(2018). In terms of wave evolution, however, *can we extend the plant dynamics from a single plant to a canopy? How will the resulting predictions differ from rigid-canopy predictions?* The recent work by Luhar et al. (2017) and Lei and Nepf (2019) have approached the plant-to-canopy upscaling based on how a flexible plant is compared in load to a rigid plant and utilised the predictions from Dalrymple et al. (1984) for rigid canopies. *Are there more subtleties to account for?*

1.2.2 *Intermediate-amplitude waves*

Thus far, we have only discussed small-amplitude waves (bottom row of Figure 1.1), which can be explained mathematically with Stokes' theory. For larger waves, they are significantly more difficult to analyse mathematically due to nonlinear effects such as advection, which can no longer be ignored. With the additional complexity from the presence of vegetation, there is naturally less analytical work in this subfield.

However, as we had mentioned when we first discussed shoaling, waves have relatively larger amplitudes in the vicinity of the shore or more generally shallower domains, in relation to the wavelength. Due to the small aspect ratio between depth and wavelength, the number of flow variables can be reduced in this limit. Thus, researchers have studied periodic shallow-water waves, at least in the absence of vegetation, with cnoidal theory [shown ② in Figure 1.1] – a class of periodic solutions which satisfy the celebrated Korteweg-de Vries equation (Korteweg and de Vries, 1895). We note that the small-amplitude limit of cnoidal waves is consistent with the shallow-water limit of Stokes waves [shown ③ in Figure 1.1]. However, we are not aware of theoretical work which applies cnoidal theory to predict wave evolution through vegetation. *Can we improve our predictions in this shallow-water limit compared to Stokes' theory?*

1.2.3 *Instabilities of flows through vegetation*

Moving away from waves, another interesting phenomenon that has gained attention is *monami*—the progressive synchronous oscillation of submerged vegetation under strong flows (Nepf, 2012). We illustrate this with its analogue for terrestrial plants, *honami*, in Figure 1.3, which is easily observable in daily life (de Langre, 2008). In addition to mathematical interest and visual aesthetics, an understanding of monami can give insights on transport in such aquatic systems (Nepf, 2012).

Under a sufficiently strong current (or gust of wind for terrestrial flows), it is known that vortices roll up along the top of the canopy and monami (or honami) is the visible mechanical response of such vortices (Nepf, 2012). The emergence of monami is first explained by Raupach et al. (1996) as a shear-induced phenomenon analogous to a Kelvin-Helmholtz instability. Since, many researchers have tried to understand other physical factors

Figure 1.3: Snapshots of a *honami*, the synchronous waving of terrestrial plants, at two instances. In this example, a honami is observed travelling from left to right along all three canopies. In particular, for the reeds, the approximate positions where plants nearby experience minimum (▲) and maximum (▼) deflection are marked. Grid lines and coloured curves act as visual guides to highlight that at each of the four annotated positions, plants near ▼ are further suppressed in comparison to neighbouring plants (at ▲) and also the same plants a different instance (at ▲). Images are taken along the Thames Path, United Kingdom.

involved via linear stability analysis on some modelled steady flows [see Singh et al. (2016) and references therein]. However, there is a lack of understanding of the role of flexibility and other effects such as inertia and the presence of a free surface (in contrast to terrestrial flows), which can be crucial. *Can such physical effects alter the known shearing mechanism for triggering monami? Can such effects encourage or suppress monami?*

1.3 Objectives and structure of the thesis

In the previous section, we highlighted many open questions on the mechanical aspects and evolution of flows in the presence of vegetation. This thesis is dedicated to address some of these issues. We shall systematically construct continuum mechanical models and develop rigorous frameworks for analysing both wave evolution and flow instabilities. We primarily divide our analysis between rigid (Chapters 2–4) and flexible vegetation (Chapters 5–6).

Chapter 2: Small-amplitude waves through rigid vegetation

In Chapter 2 we first explore how small-amplitude waves evolve in the presence of rigid vegetation. Since we are interested in the macroscopic flow, we derive how drag and inertial contributions from individual plants can be homogenised in space to give a bulk momentum sink in the fluid momentum equations. By considering the limit in which the wavelength-to-domain ratio is small, we use the method of multiple scales to formally derive new predictions on wave evolution, which simultaneously accounts for vegetation, substrate variations, and depth-dependence. In particular, we predict how the amplitude and the wavelength vary with the distance of propagation.

Chapter 3: Combined current-wave flows through rigid vegetation

We then extend our multiple-scales analysis from pure (small-amplitude) waves to combined current-wave flows in Chapter 3. By investigating how a steady current and a small-amplitude wave interact with each other, we highlight how certain physical effects which have been neglected in previous work could be or should be accounted for. Such physical effects include variations of the mean free surface and the substrate.

Chapter 4: Shallow-water waves through rigid vegetation

To cover another common regime on waves through rigid vegetation, we bypassed the small-amplitude approximation in Chapter 4 by considering periodic shallow-water waves. In particular, we again apply the method of multiple scales to give new theoretical predictions on how cnoidal waves evolve in the presence of vegetation. We highlight how such waves evolve differently from small-amplitude waves and also in what regimes do the two wave theories formally coincide.

Chapter 5: Small-amplitude waves through flexible vegetation

After analysing flows through rigid vegetation, we turn, in Chapter 5 to explores how waves evolve differently through flexible vegetation. We focus our analysis on small-amplitude waves. This involves extending our modelling framework from the previous chapters to account for plant flexibility. By modelling individual plants as elastic cantilever beams, we first understand how a single beam deflects in the presence of a wave. We then apply the method of multiple scales to formally derive how such beam dynamics can be extended to the canopy scale and ultimately predict how waves evolve. We advanced from previous predictions by accounting for subtle but crucial aspects involved in the plant-to-canopy upscaling.

Chapter 6: Instabilities of flows through flexible vegetation

Finally, in Chapter 6, we explore temporal evolutions of a flow by understanding how a monami, the synchronous waving of submerged flexible vegetation, emerges from instabilities. We first consider steady configurations of the system under a unidirectional flow. We then consider infinitesimal perturbations to the steady configurations and predict mechanisms and critical conditions for instabilities. A significant advancement compared to previous analyses is that our work addresses the role of flexibility by concerning the coupling between flow perturbations and canopy deformations. Furthermore, we simultaneously account for inertia and free-surface effects.

2 SMALL-AMPLITUDE WAVES THROUGH RIGID VEGETATION

> Great things are done by a series of small things brought together.
>
> *Vincent van Gogh*

SYNOPSIS

In this chapter, we develop a multiple-scales methodology for the evolution of linear waves through rigid vegetation over a slowly varying substrate. In particular, this describes the phenomena of shoaling, where the amplitude of the wave increases as it approaches the coastline. We introduce the modelling framework for subsequent chapters and discuss the homogenisation of the vegetative canopy. Our analytical predictions agree with previous estimates that have studied shoaling and rigid vegetation separately. The predictions also demonstrate good agreement with experimental data for the constant-depth problem and numerical predictions for the varying-depth problem.

2.1 INTRODUCTION

In coastal flows, free-surface waves approaching the shore will typically grow in amplitude until they eventually break. The mathematical theory behind this phenomenon, known as *shoaling*, was first developed by George Green in 1838 for shallow-water waves with wavelengths exceeding the mean water depth by a factor of twenty (Lamb, 1932). Since this seminal work, mathematical theories have been developed for shoaling flows in a broader range of scenarios. For example, Stoker (1947) extended Green's theory to the case of two-dimensional linear waves over plane sloping beaches. See the review by Meyer (1979) for a general summary of the main works in shoaling flows.

Our focus in this chapter is motivated by work by Keller (1958), who studied more general three-dimensional flows over slowly varying substrate profiles using linear wave theory and ray theory. By considering the asymptotic limit where the water depth and the wavelength are both much smaller than the horizontal scale of the substrate contour, a WKB

(or Liouville-Green) approximation explained how the wave amplitude, frequency and the phase would modulate as the wave propagates.

In the case of oscillatory vegetative flows, the theory is much less developed. In general, researchers have mainly focused on experimental and field studies [see *e.g.* Bradley and Houser (2009); Anderson and Smith (2014); Möller et al. (2014); Lei and Nepf (2019)] and also computational fluid dynamics [see Zeller et al. (2015) for a detailed review and also work by Lowe et al. (2005); Suzuki et al. (2012); Mattis et al. (2019)]. As it pertains to analytical approaches, the bulk of the research has been devoted to the development of energy balance arguments.

For example, Dalrymple et al. (1984) and Kobayashi et al. (1993) both predicted how sinusoidal waves evolve through rigid vegetation over horizontal substrates using energy balance arguments. The predictions were extended by Mendez and Losada (2004) to random waves and also shallow-water waves over sloping beaches—such predictions have been widely used in the engineering community [see *e.g.* Luhar et al. (2017) and the references therein]. However, the current predictions consider drag as the only source of momentum loss and neglects other forces that are simultaneously acting on the vegetation.

In this chapter, we extend previous predictions by made by Keller (1958), Dalrymple et al. (1984) and Mendez and Losada (2004) by giving a formal derivation on wave decay through vegetation over a general slowly varying substrate—the more realistic joint problem, where all the forces which act on the vegetation are considered. We first present the general governing equations of the fluid and the modelling framework of the vegetation in 3D. We then homogenise the contributions of individual plants and reduce the problem to 2D. By exploiting the slowly varying nature of waves along the domain, we apply a generalised multiple-scales analysis developed by Kuzmak (1959) to deriving an evolution equation for the wave amplitude. We solve the equation in various simplified cases to demonstrate extensions from and agreement with previous predictions. Finally, we validate our asymptotic predictions with full two-phase numerical simulations and experimental data from previous studies.

2.2 HOMOGENISATION FOR INVISCID FLOWS WITH VEGETATION

Even for simplified formulations, it is impractical to monitor the positions and effects of individual plants in the flow. Here, we shall develop a simpler averaged model in which the canopy is an effective medium that contributes a bulk volumetric sink term. Although this has been done by others in specific settings [see *e.g.* Nepf (2012) and references therein], our derivation uses more systematic arguments based on volume averaging and has the potential to be generalised to more complicated scenarios.

We consider a three-dimensional inviscid fluid with velocity $\mathbf{u}(\mathbf{x}) =$

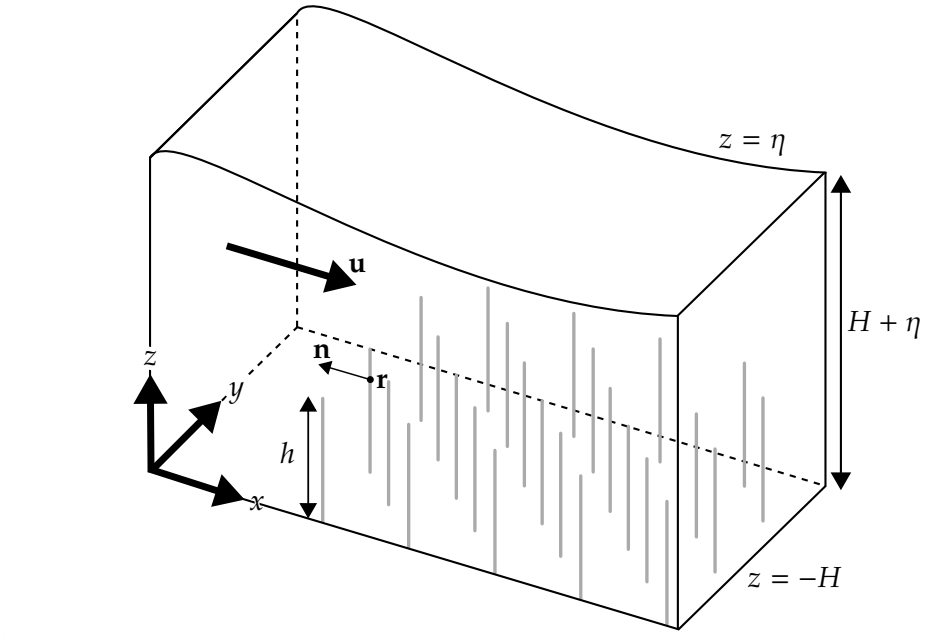

Figure 2.1: Schematic diagram of waves with fluid velocity $\mathbf{u}$ propagating through a rigid canopy over a varying substrate with $z = -H$. The free-surface elevation is parametrised with $z = \eta$ and the submerged grey obstacles represent individual plants with height h. For a plant with position $\mathbf{r}$, we let $\mathbf{n}$ to be the local upstream normal from $\mathbf{r}$.

(u, v, w) and dynamic pressure $p(\mathbf{x})$ that flows over a canopy region of finite depth. We assume that a fully-submerged vegetative canopy covers the entire substrate. For the canopy, the individual plants are assumed to be identical, and we model each as a rigid upright beam with diameter b and length h. The precise geometry of the plant cross-sections will be included in the later modelling framework. A schematic of the setup is given in Figure 2.1.

From the inviscid Navier-Stokes equations, the fluid satisfies

$$\nabla \cdot \mathbf{u} = 0, \tag{2.1}$$

$$\rho \left(\frac{\partial \mathbf{u}}{\partial t} + \mathbf{u} \cdot \nabla \mathbf{u} \right) = -\nabla p - \mathbf{F}, \tag{2.2}$$

where the density ρ is taken to be constant. The additional sink term, $\mathbf{F}$, in the momentum equation (2.2) incorporates the contribution of the N plants. Let us assume that the collective sink term can be written as

$$\mathbf{F}(\mathbf{x}, t) \equiv \sum_{k=1}^{N} \mathbf{F}^k(\mathbf{x}, t), \tag{2.3}$$

with each term, $\mathbf{F}^k$, accounting for the momentum loss due to the load on the k^{th} plant. Our task is to homogenise the momentum loss of individual plants and consider a continuum (averaged) approximation of $\mathbf{F}$.

In considering the force balance on a rigid and static object that is submerged in a fluid, we have to account for drag $\mathbf{F}_D^k$, added mass $\mathbf{F}_A^k$, and virtual buoyancy $\mathbf{F}_V^k$ (Newman, 1977; Batchelor, 2000), and thus,

$$\mathbf{F}^k = \mathbf{F}_D^k \text{ (drag)} + \mathbf{F}_A^k \text{ (added mass)} + \mathbf{F}_V^k \text{ (virtual buoyancy)}. \tag{2.4}$$

Physically, the added mass, $\mathbf{F}_A^k$, accounts for an additional local pressure gradient induced to accelerate the fluid which surrounds the object in a

time-dependent flow (Gosselin, 2019). Similarly, the virtual buoyancy, $\mathbf{F}_V^k$, also known as the Froude-Krylov force (Luhar and Nepf, 2016), accounts for a pressure gradient that is proportional to the mass of the fluid the object has displaced (Dean and Dalrymple, 1991).

Following previous analyses on submerged beams by Luhar and Nepf (2016) and Leclercq and de Langre (2018), the component forces at a given $(\mathbf{x}, t)$ due to a beam at position $\mathbf{x} = \mathbf{r}^k$ are as follows:

$$\mathbf{F}_D^k = \frac{1}{2}\rho b C_D \int_0^h \delta(\mathbf{x} - \mathbf{r}^k)\mathbf{u}\cdot\mathbf{n}^k \left|\mathbf{u}\cdot\mathbf{n}^k\right|\mathbf{n}^k \,\mathrm{d}s, \tag{2.5a}$$

$$\mathbf{F}_A^k = \rho\mathcal{A}C_M \int_0^h \delta(\mathbf{x} - \mathbf{r}^k)\frac{\partial\mathbf{u}}{\partial t}\cdot\mathbf{n}^k\mathbf{n}^k \,\mathrm{d}s, \tag{2.5b}$$

$$\mathbf{F}_V^k = \rho\mathcal{A} \int_0^h \delta(\mathbf{x} - \mathbf{r}^k)\frac{\partial\mathbf{u}}{\partial t} \,\mathrm{d}s. \tag{2.5c}$$

For the integrals, at a given arc length $s = z + H$ measured from the root, δ denotes the Dirac delta function and $\mathbf{n}^k$ is the upstream normal of the k^{th} beam's centreline in the xz-plane (see Figure 2.1). We will generalise the expressions above when we consider flexible vegetation in Chapter 5.

In defining the parameters C_D, $\mathcal{A}$, and C_M in the expressions above, we consider a cross-section of unit length taken perpendicular to the axis of the beam, *e.g.* a circular cross-section for cylindrical beams. Then we write C_D for its drag coefficient in cross-flow, $\mathcal{A}$ for its cross-section, and C_M for its added mass coefficient.

We now explain how the force expression (2.3) can be averaged for the case of vegetative plants. Consider a fixed point $\mathbf{x} = (x, y, z)$. We define $\bar{\mathbf{F}}_R$ as the local average of the collective sink over a disk of radius R, namely

$$\bar{\mathbf{F}}_R(\mathbf{x}, t) = \frac{1}{\pi R^2} \iint_{C_R(x,y;z)} \mathbf{F}(\mathbf{x}', t)\,\mathrm{d}x'\mathrm{d}y', \tag{2.6}$$

where $C_R(x, y; z)$ is the two-dimensional disk of radius R centred at the point $\mathbf{x}$ *i.e.*

$$C_R(x, y; z) = \{(x', y', z) : (x - x')^2 + (y - y')^2 \le R\}. \tag{2.7}$$

By the definition of $\mathbf{F}$ in (2.3),

$$\bar{\mathbf{F}}_R(\mathbf{x}, t) = \frac{1}{\pi R^2} \iint_{C_R(x,y;z)} \left[\sum_{k=1}^{N} \int_0^h \mathbf{Q}^k \delta(\mathbf{x}' - \mathbf{r}^k)\,\mathrm{d}s\right] \mathrm{d}x'\mathrm{d}y', \tag{2.8}$$

where

$$\mathbf{Q}^k = \frac{1}{2}\rho b C_D \mathbf{u}\cdot\mathbf{n}^k \left|\mathbf{u}\cdot\mathbf{n}^k\right|\mathbf{n}^k + \rho\mathcal{A}C_M\left(\frac{\partial\mathbf{u}}{\partial t}\cdot\mathbf{n}^k\right)\mathbf{n}^k + \rho\mathcal{A}\frac{\partial\mathbf{u}}{\partial t}. \tag{2.9}$$

Now, by definition,

$$\delta(\mathbf{x}' - \mathbf{r}^k) = \delta(x' - r_1^k)\delta(y' - r_2^k)\delta(z - r_3^k). \tag{2.10}$$

Therefore,

$$\bar{\mathbf{F}}_R(\mathbf{x}, t) = \frac{1}{\pi R^2} \sum_{k=1}^{N} \mathbf{Q}^k(\mathbf{r}^k, t) \mathbb{1}_R^k(\mathbf{x}, t) \tag{2.11}$$

where $\mathbb{1}_R^k$ is an indicator function with $\mathbb{1}_R^k(\mathbf{x}, t) = 1$ if the k^{th} plant passes through C_R; otherwise it is zero.

We now consider the limit in which $R \to 0$ (with the neighbouring plant separation also tending to zero so that there are still many plants crossing C_R). Since we have assumed that the plants are identical in the canopy, we approximate $\mathbf{u}$ to be uniform in C_R and similarly for the configuration and motion of the plants. With reference to the local averaging argument presented by Chapman (1995), we deduce the continuum approximation of $\mathbf{F}$ as

$$\bar{\mathbf{F}} = \lim_{R \to 0} \bar{\mathbf{F}}_R = \bar{N} \mathrm{H}(h - H - z) \mathbf{Q}(\mathbf{x}, t) \tag{2.12}$$

where $\bar{N}(x, y)$ is the number of plants planted per unit area (along the substrate) and H is the Heaviside step function. For the remainder of this work, we will replace $\mathbf{F}$ with $\bar{\mathbf{F}}$ in the Euler's equations (2.1)–(2.2).

2.3 REDUCTION TO TWO-DIMENSIONAL FLOWS

In the previous section, we have derived an averaged formulation for the momentum contribution from a collection of identical plants. Crucially, the expression (2.12) for $\bar{\mathbf{F}}$ depends on three macroscopic quantities: a local plant density $\bar{N}$, a Heaviside step function H linked to canopy position, and the local momentum loss. Notice that in the case of three-dimensional flow where the geometry and initial conditions are independent of y, then solutions are expected to be two-dimensional (in xz); we may then verify that the momentum contributions (2.12) are also independent of y. This is the configuration that we shall consider for the remainder of this thesis.

Consider inviscid flow in a domain of finite depth bounded below by a variable bottom substrate, $z = -H$, and above by a free surface, $z = \eta$. The bottom and the canopy height are assumed to be independent of y, and we assume that the initial condition consists of a monochromatic incident wave with amplitude, A_0, and frequency, ω_0, propagating in the positive x-direction. The flow is assumed to be two-dimensional, and hence y-independent with transverse velocity, $v = 0$. Thus, fluid is contained in

$$-H(x) \leq z \leq \eta(x). \tag{2.13}$$

A schematic of the setup is given in Figure 2.2. Notice that since all the plants are assumed to be rigid and upright, then the outward normal in the expression for the momentum sink (2.12) simplifies to $\mathbf{n} \equiv -\hat{\mathbf{e}}_x$.

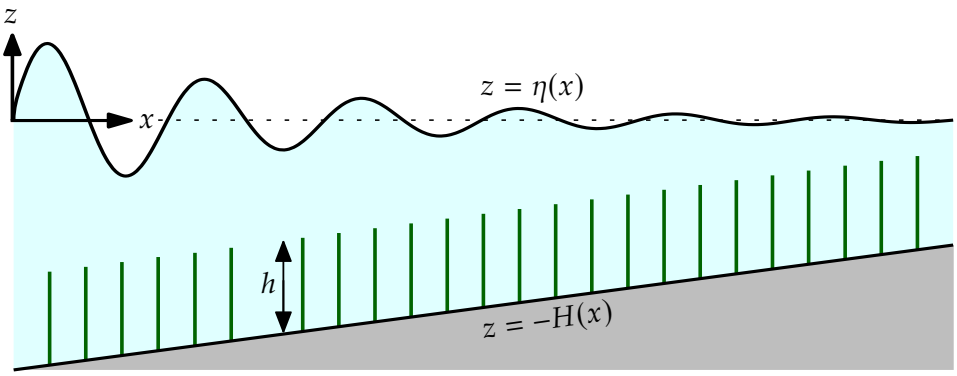

Figure 2.2: Schematic diagram of waves propagating through a rigid canopy over a varying substrate with $z = -H(x)$. The waves propagate along the x-direction, with the free surface being parametrised with $z = \eta(x)$. The green obstacles represent individual plants with height h.

The Navier-Stokes equations (2.1)–(2.2) are now given by

$$\nabla \cdot \mathbf{u} = 0, \tag{2.14a}$$

$$\rho\left(\frac{\partial \mathbf{u}}{\partial t} + \mathbf{u} \cdot \nabla \mathbf{u}\right) = -\nabla p - \bar{N}\mathrm{H}(h - H - z)\mathbf{F}, \tag{2.14b}$$

with the homogenised momentum sinks $\mathbf{F} = \mathbf{F}_D + \mathbf{F}_A + \mathbf{F}_V$ being

$$\mathbf{F}_D = \frac{1}{2}\rho b C_D u\,|u|\,\hat{\mathbf{e}}_x, \tag{2.14c}$$

$$\mathbf{F}_A = \rho \mathcal{A} C_M \frac{\partial u}{\partial t}\hat{\mathbf{e}}_x, \tag{2.14d}$$

$$\mathbf{F}_V = \rho \mathcal{A} \frac{\partial \mathbf{u}}{\partial t}, \tag{2.14e}$$

reduced from (2.5). With the formal reductions in place, we are now ready to nondimensionalise our governing equations and boundary conditions.

2.4 NONDIMENSIONALISATION

For a given incident wave with amplitude A_0 and wavelength ω_0, we nondimensionalise the variables in our problem with the following scales:

$$[\mathbf{x}] = L, \quad [A] = [\eta] = A_0, \quad [t] = \omega_0^{-1}, \quad [\mathbf{u}] = A_0\omega_0, \quad [p] = \rho g A_0, \tag{2.15}$$

where g is the acceleration due to gravity and L is the scale of the horizontal domain. Recall that the pressure p is defined as the dynamic pressure, and hence includes contributions of gravitational forces. We have also chosen to nondimensionalise lengths with the horizontal domain parameter, L, rather than the depth or wavelength; this is for convenience of the forthcoming multiple-scales analysis in §2.5.

As an aside, in this work, we have chosen to scale the wave velocity with the quantity, $A_0\omega_0$. In some of the previous works, such as by Luhar and Nepf (2016) and Leclercq and de Langre (2018), authors have chosen instead to designate a velocity scale of $\tilde{A}_0\omega_0$, where $\tilde{A}_0$ is the length-scale of wave excursion *i.e.* the horizontal displacement of the water particle

over half a time period. However, these two choices of nondimensionalisation are comparable for various coastal waves (Mei et al., 2014) and experimental setups [see *e.g.* Wu et al. (2012)]. We will consider more appropriate scales when we specifically analyse nonlinear shallow-water waves in Chapter 4.

2.4.1 *Dimensionless governing equations*

The dimensionless governing equations (2.1)–(2.2) for $\mathbf{u} = \mathbf{u}(x, z, t) = (u, w)$, are now

$$\nabla \cdot \mathbf{u} = 0, \tag{2.16a}$$

$$\frac{\partial \mathbf{u}}{\partial t} + \gamma \mathbf{u} \cdot \nabla \mathbf{u} = -\alpha \nabla p - \lambda \mathrm{H}(h - H - z)\mathbf{F}, \tag{2.16b}$$

with the momentum sink term now being

$$\mathbf{F}(x, z, t) = \begin{pmatrix} F_{\parallel} \\ F_{\perp} \end{pmatrix} = \begin{pmatrix} u|u|/2 + (M_1 + M_2)u_t \\ M_2 w_t \end{pmatrix}. \tag{2.16c}$$

The dimensionless boundary conditions are

$$\boxed{\text{Free-slip}} \quad u\frac{\mathrm{d}H}{\mathrm{d}x} + w = 0, \qquad \text{at } z = -H(x), \tag{2.16d}$$

$$\boxed{\text{Kinematic}} \quad w - \frac{\partial \eta}{\partial t} - \gamma u \frac{\partial \eta}{\partial x} = 0, \qquad \text{at } z = \gamma\eta, \tag{2.16e}$$

$$\boxed{\text{Dynamic}} \quad p = \eta, \qquad \text{at } z = \gamma\eta. \tag{2.16f}$$

The dimensionless parameters α, γ, λ, M_1, and M_2 are defined in Table 2.1. For each beam, the parameters M_1 and M_2 characterise the respective effects of added mass and beam inertia (or virtual buoyancy) relative to drag. When $M_1 \gg M_2$, we note that M_1 can also be interpreted as the reciprocal of the problem-specific Keulegan-Carpenter number (Keulegan and Carpenter, 1958; Leclercq and de Langre, 2018). Although there are conventions in the literature which consider $M_1 + M_2$ as a single dimensionless parameter [see *e.g.* Lowe et al. (2005)], we have kept M_1 and M_2 as separate parameters for the analyses in Chapters 5 and 6 on flexible beams.

Finally, we note that to incorporate the presence of the plants into the fluid momentum equations via a momentum sink, we require that both the dimensionless added mass and the volume fraction of the solid at any point in space to be much smaller than unity *i.e.* $\lambda M_{1,2} \ll 1$.

Foreseeing the calculations ahead, we rewrite our governing equations (2.16a)–(2.16b) into a single equation with $\nabla^2 p$, by evaluating p_{xx} and p_{zz} with (2.16b) respectively, and imposing the incompressibility condition (2.16a). We also rewrite the boundary conditions in terms of p using the momentum equations. Together, we get

$$\nabla^2 p + \frac{\lambda}{\alpha}\nabla \cdot [\mathrm{H}(h - H - z)\mathbf{F}] + \frac{\gamma}{\alpha}\nabla \cdot \begin{pmatrix} u u_x + w u_z \\ u w_x + w w_z \end{pmatrix} = 0, \tag{2.17a}$$

	SYMBOL	EXPRESSION
Wavelength	α	$\dfrac{g}{\omega_0^2 L}$
Amplitude	γ	$\dfrac{A_0}{L}$
Canopy density	λ	$C_D \bar{N} b A_0$
Added mass	M_1	$\dfrac{C_M \mathcal{A}}{\rho b C_D A_0}$
Beam inertia (or virtual buoyancy)	M_2	$\dfrac{\mathcal{A}}{b C_D A_0}$

Table 2.1: A summary of the dimensionless parameters in the governing equations of flow through a homogenised rigid canopy (2.16). For cylindrical beams, $C_M \approx (\pi b^2/4)/\mathcal{A} = 1$ (Brennen, 1982). For cantilever blades with thin rectangular cross sections, $C_M \approx (\pi b^2/4)/\mathcal{A} \gg 1$ and hence $M_1 \gg M_2$ (Leclercq and de Langre, 2018). Finally, we note that we can model obstacles with spatial variations along the stem by incorporating non-uniform drag and added mass coefficients.

with the boundary conditions

$$p_x \frac{\mathrm{d}H}{\mathrm{d}x} + p_z + \frac{\lambda}{\alpha}\left(F_\parallel \frac{\mathrm{d}H}{\mathrm{d}x} + F_\perp\right) + \frac{\gamma}{\alpha}\left[(uu_x + wu_z)\frac{\mathrm{d}H}{\mathrm{d}x} + (uw_x + ww_z)\right] = 0, \quad \text{at } z = -H(x), \tag{2.17b}$$

$$p_{tt} + \alpha p_z + \gamma\left[(uw_x + ww_z) + u_t p_x + u p_{xt}\right] = 0, \quad \text{at } z = \gamma\eta, \tag{2.17c}$$

$$p = \eta, \quad \text{at } z = \gamma\eta. \tag{2.17d}$$

Notice that when the wave amplitude is sufficiently small $\gamma/\alpha \ll 1$ and the canopy is sufficiently sparse $\lambda \ll 1$, the governing equation (2.17a) reduces to the classic Laplace's equation for p that governs surface-gravity waves.

2.5 MULTIPLE-SCALES ANALYSIS OF WAVE MODULATION

In many coastal settings, consecutive waves have similar profiles when they are away from the shore: each wave experiences small change over one time period. This occurs when both the effects of the canopy and the varying substrate (on the waves) are small over the scale of a wavelength. However, the cumulative effects can be significant when we compare waves along the entire domain, which is typically much longer than a wavelength.

In our modelling framework, the ratio between the two length scales is quantified by $\alpha \ll 1$. The sparsity of the canopy and the slowly varying substrate correspond to having $\lambda \ll 1$ and $\mathrm{d}H/\mathrm{d}x \ll 1$ respectively. Besides, we also stated at the end of §2.4 that if the wave amplitude is sufficiently small, in the sense that $\gamma/\alpha \ll 1$, the waves are approximately linear. In certain distinguished regimes, we can analytically exploit these small parameters to evaluate the wave evolution on the domain scale using weakly nonlinear wave theory—an important objective in applications in coastal management. Therefore, it is natural for us to solve this problem (2.17)

with the method of multiple scales, with $\alpha \ll 1$ being the small asymptotic parameter.

We summarise the mathematical concepts and procedures as follows:

1. Introduce the fast periodic wave scale and the slow domain scale;
2. Solve for the wave dynamics on the wave scale;
3. Evaluate the small variations of the wave in each time period due to the substrate and the vegetation;
4. Formally predict the cumulative effect of the wave variations on the domain scale.

The multiple-scales analysis in this section will extend previous theories on shoaling flows by Keller (1958), and vegetative flows by Dalrymple et al. (1984) and Mendez and Losada (2004) to elucidate the combined effects of the vegetation (measured with λ) and substrate variation (measured with $\mathrm{d}H/\mathrm{d}x$). For a given incident wave with amplitude A, the objective is to derive an ordinary differential equation in the form

$$\frac{\mathrm{d}A}{\mathrm{d}x} = f(x, A, \lambda, H) \tag{2.18}$$

describing the quasi-static wave envelope after being locally-averaged in time and space. This is given by (2.40) later in this section. We will now present the formal analysis in deriving (2.40).

2.5.1 *Theoretical formulation*

Mathematically, we formulate this multiple-scales problem by keeping x as the slow or domain variable, and let

$$\bar{x} = \frac{\Phi(x)}{\alpha} \tag{2.19}$$

be the fast or wave variable, where Φ is a function that is solved as part of the problem (as in WKB approximations). We then impose that $\bar{x}$ and x are independent of each other and consider solutions where the wave variables in (2.17) are functions of $(\bar{x}, x, z, t)$ and periodic in $\bar{x}$ with period 2π.

Compared to the classic problem of shoaling, we have a nonlinear drag term in (2.17a) due to the presence of vegetation. Therefore, we cannot perform a classic WKB approximation, where p takes a certain solution form (Chapman and Farrell, 2017). On the other hand, we cannot impose $\bar{x}$ being a constant rescale of x and consider simple harmonic solutions due to the effects of wavelength-modulation from variations of the substrate topography. To preserve both the nonlinearity and wavelength modulation in the problem, we solve the problem with the method by Kuzmak (1959)—a generalised multiple-scales analysis that is also known in other literature as *principles of adiabatic invariants* (Landau and Lifshitz, 1976) [see also Ablowitz (2011)]. Such formal derivations being applied on vegetative flows are to our knowledge, new. Crucially, the same powerful machinery

can be applied to waves through flexible vegetation—we will go through this in Chapter 5.

With $\bar{x}$ and x defined, we map the x-derivatives in the problem (2.17) accordingly so that

$$\frac{\partial}{\partial x} \mapsto \frac{\partial}{\partial x} + \frac{\Phi'}{\alpha}\frac{\partial}{\partial \bar{x}}, \tag{2.20a}$$

$$\frac{\partial^2}{\partial x^2} \mapsto \frac{\partial^2}{\partial x^2} + \frac{2\Phi'}{\alpha}\frac{\partial^2}{\partial x \partial \bar{x}} + \frac{\Phi''}{\alpha}\frac{\partial}{\partial \bar{x}} + \frac{(\Phi')^2}{\alpha^2}\frac{\partial^2}{\partial \bar{x}^2}, \tag{2.20b}$$

where primes ($'$) denote $\mathrm{d}/\mathrm{d}x$. To solve for the local wave dynamics, we rescale $z = \alpha\bar{z}$ and its associated derivatives, so that $h = \alpha\bar{h}$ and $H(x) = \alpha\bar{H}(x)$. We emphasise that we consider the substrate to vary sufficiently slowly such that H is formally independent of $\bar{x}$. We then consider an asymptotic expansion in α for our wave variables in the form

$$f = \sum_{n=0}^{\infty} \alpha^n f_n. \tag{2.21}$$

Finally, in the multiple-scales expansion, we consider the distinguished limit in which

$$\lambda = \alpha\bar{\lambda} \quad \text{and} \quad \gamma = \alpha^2\bar{\gamma}, \tag{2.22}$$

where $\bar{\lambda}$ and $\bar{\gamma}$ are $O(1)$ (see Table 2.1). The number of bars denote the order of the original parameter (or variable) in powers of α.

2.5.2 *Solving the leading-order problem*

For the $O(1)$ problem, p_0 satisfies

$$\bar{\nabla}^2 p_0 \coloneqq (\Phi')^2 p_{0\bar{x}\bar{x}} + p_{0\bar{z}\bar{z}} = 0, \tag{2.23a}$$

with

$$\boxed{\text{Free-slip}} \quad p_{0\bar{z}} = 0, \qquad \text{at } \bar{z} = -\bar{H}(x), \tag{2.23b}$$

$$\boxed{\text{Kinematic}} \quad p_{0\bar{z}} = -p_{0tt}, \qquad \text{at } \bar{z} = 0, \tag{2.23c}$$

$$\boxed{\text{Dynamic}} \quad p_0 = \eta_0, \qquad \text{at } \bar{z} = 0. \tag{2.23d}$$

Note that since Φ' and $\bar{H}$ are independent of $\bar{x}$, the leading-order problem is linear with constant coefficients. Hence, the solutions of p_0 are sums of exponentials in space and 2π-periodic in time by choice of the nondimensionalisation (2.15). Since we are considering a monochromatic incident wave, the solutions only consist of the fundamental Fourier mode of the form

$$p_0 = C(x)\cosh\left[k(x)[\bar{z} + \bar{H}(x)]\right] \mathrm{e}^{\mathrm{i}[k(x)/\Phi'(x)]\bar{x}} e^{-\mathrm{i}t}, \tag{2.24}$$

real part understood (of which we also only consider the forward propagating wave), for some functions $C(x)$ and $k(x)$. Imposing periodicity on p_0 in

$\bar{x}$ with period 2π, the mapping between $\alpha\bar{x}$ and x, Φ, in (2.19) satisfies the eikonal equation

$$\Phi'(x) = \frac{\mathrm{d}\Phi}{\mathrm{d}x} = k(x). \tag{2.25}$$

Foreseeing the calculations ahead, without loss of generality, it is convenient to impose the initial phase of the wave so that $p_0 = C(x)\cosh[k(\bar{z} + \bar{H})]\cos(\bar{x} - t)$. Finally, since the free surface has a dimensionless amplitude $|\eta_0| = A$, which is yet to be determined, we have that

$$C(x) = \frac{A}{\cosh k\bar{H}}. \tag{2.26}$$

Note that similar to $k(x)$, $A = A(x)$ is a function of the slow domain variable, so that the wave is locally periodic in $\bar{x}$ and t but varies along the domain.

In summary, with $u_{0t} = -kp_{0\bar{x}}$ and $w_{0t} = -p_{0\bar{z}}$ from (2.16), we obtain the classic sinusoidal solution for waves in the local domain. The solution has the form

$$\eta_0 = A(x)\cos(\bar{x} - t), \tag{2.27a}$$

$$u_0 = A(x)\frac{\cosh[k(\bar{z} + \bar{H})]}{\sinh k\bar{H}}\cos(\bar{x} - t), \tag{2.27b}$$

$$w_0 = A(x)\frac{\sinh[k(\bar{z} + \bar{H})]}{\sinh k\bar{H}}\sin(\bar{x} - t), \tag{2.27c}$$

$$p_0 = A(x)\frac{\cosh[k(\bar{z} + \bar{H})]}{\cosh k\bar{H}}\cos(\bar{x} - t), \tag{2.27d}$$

with k being the dimensionless wavenumber which satisfies the dispersion relation

$$k(x)\tanh[k(x)\bar{H}(x)] = 1. \tag{2.28}$$

The objective now is to evaluate $A(x)$. In particular, A is determined by the momentum loss due to the canopy and the wavelength modulation. Since both effects only become significant over the domain scale, we have to consider the higher-order problem.

2.5.3 *Formulating the first-order problem*

The first-order problem involves contributions from the Heaviside step function and its derivatives. To maintain clarity in the formulation, we abbreviate $\mathrm{H}(\bar{h} - \bar{H} - \bar{z})$ with H, and the Dirac delta function $\delta(\bar{h} - \bar{H} - \bar{z})$ with δ.

For the $O(\alpha)$ problem, p_1 satisfies

$$\bar{\nabla}^2 p_1 + \frac{\mathrm{d}k}{\mathrm{d}x}p_{0\bar{x}} + 2kp_{0\bar{x}x} + \bar{\lambda}(kF_{\parallel 0\bar{x}} + F_{\perp 0\bar{z}})\mathrm{H} + \bar{\gamma}\Gamma = \bar{\lambda}F_{\perp 0}\delta \tag{2.29a}$$

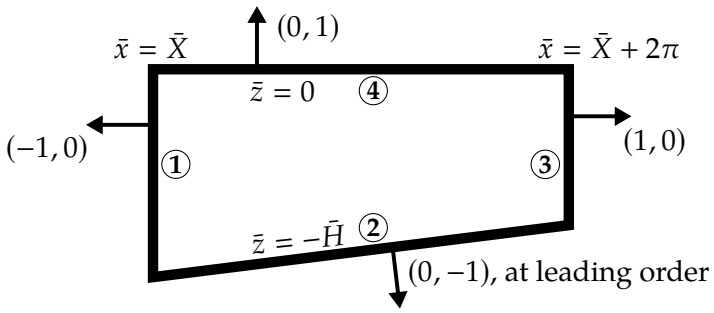

Figure 2.3: Schematic diagram for the periodic cell $\bar{\Omega} = [\bar{X}, \bar{X} + 2\pi] \times [-\bar{H}, 0]$ in the multiple-scales analysis.

with the boundary conditions

$$k\frac{\mathrm{d}\bar{H}}{\mathrm{d}x}p_{0\bar{x}} + p_{1\bar{z}} + \bar{\lambda}F_{\perp 0} + \bar{\bar{\gamma}}\left[ku_0w_{0\bar{x}} + w_0w_{0\bar{z}}\right] = 0, \qquad \text{at } \bar{z} = -\bar{H}, \tag{2.29b}$$

$$p_{1\bar{z}} + p_{1tt} + \bar{\bar{\gamma}}\tilde{\Gamma} = 0, \qquad \text{at } \bar{z} = 0, \tag{2.29c}$$

$$p_1 + \bar{\bar{\gamma}}p_0p_{0\bar{z}} = \eta_1, \qquad \text{at } \bar{z} = 0, \tag{2.29d}$$

and the functions Γ and $\tilde{\Gamma}$ being

$$\Gamma = w_{0\bar{z}}^2 + w_0w_{0\bar{z}\bar{z}} + k^2(u_{0\bar{x}}^2 + u_0u_{0\bar{x}\bar{x}}) + k(w_{0\bar{x}}u_{0\bar{z}} + w_0u_{0\bar{z}\bar{x}} + w_{0\bar{z}}u_{0\bar{x}} + w_0u_{0\bar{x}\bar{z}}), \tag{2.29e}$$

$$\tilde{\Gamma} = p_0p_{0\bar{z}\bar{z}} + p_0p_{0tt\bar{z}} + w_0w_{0\bar{z}} + k(u_0w_{0\bar{x}} + u_{0t}p_{0\bar{x}} + u_0p_{0\bar{x}t}). \tag{2.29f}$$

The aim of deriving the higher-order problem is so that we can express p_1 and its derivatives in terms of the leading-order solution (2.27). We will later find that this is crucial in deriving $A(x)$.

Since $(p_0, \mathbf{u}_0)$ satisfies the homogeneous version of the equation for $(p_1, \mathbf{u}_1)$ given by (2.29a), by the Fredholm Alternative, there is a solution at first-order if and only if a certain solvability condition is satisfied.

2.5.4 *Deriving the solvability condition*

For an arbitrary 2D domain, $\bar{\Omega}$, we can deduce from the Divergence theorem that for a given function p_0^*, p_1 satisfies the identity

$$\int_{\bar{\Omega}} \begin{pmatrix} p_1 \\ -p_0^* \end{pmatrix} \cdot \begin{pmatrix} \bar{\nabla}^2 p_0^* \\ \bar{\nabla}^2 p_1 \end{pmatrix} \mathrm{d}V = \int_{\partial\bar{\Omega}} \left[p_1 \begin{pmatrix} k^2 p_{0\bar{x}}^* \\ p_{0\bar{z}}^* \end{pmatrix} - p_0^* \begin{pmatrix} k^2 p_{1\bar{x}} \\ p_{1\bar{z}} \end{pmatrix} \right] \cdot \mathrm{d}\mathbf{n}_{\bar{\Omega}}, \tag{2.30}$$

with $\mathbf{n}_{\bar{\Omega}}$ being the unit outward normal of the domain $\bar{\Omega}$. The subtlety here is to choose appropriate properties for p_0^* and $\bar{\Omega}$ so that we can rewrite p_1 and reduce the identity down to an equation for $A(x)$ only.

Suppose we take $\bar{\Omega} = [\bar{X}, \bar{X}+2\pi]\times[-\bar{H}, 0]$, for a given $\bar{X}$, as illustrated in Figure 2.3. Since $\bar{H}$ is a constant on the wave scale, $\bar{\Omega}$ is a rectangular domain at leading order with outward normal $\mathbf{n}_\Omega = (0, -1)$ along the substrate. Furthermore, we have chosen $\bar{\Omega}$ so that p_0 is periodic in $\bar{x}$ in this cell.

Suppose we then take p_0^* to be an adjoint solution of the leading-order problem, namely

$$p_0^* = A(x)\frac{\cosh[k(\bar{z} + \bar{H})]}{\cosh k\bar{H}}\sin(\bar{x} - t). \tag{2.31}$$

By definition, p_0^* is also 2π-periodic in $\bar{x}$ and t.

Finally, by the construction of $\bar{x}$, we also impose that p_1 and its derivatives to be 2π-periodic in $\bar{x}$. Different from a standard WKB approximation, we do not assume that p_1 or higher-order terms take a certain solution form in additional to being 2π-periodic in $\bar{x}$ and t.

With the properties of p_1, p_0^* and $\bar{\Omega}$ imposed, we can now simplify the identity (2.30). For its left-hand side, it can be rewritten via (2.23a) and (2.29a) as

$$\begin{aligned}&\int_{\bar{\Omega}} -p_0^*(k^2 p_{1\bar{x}\bar{x}} + p_{1\bar{z}\bar{z}})\,\mathrm{d}V \\ &= \int_{\bar{\Omega}} p_0^* \left[\frac{\mathrm{d}k}{\mathrm{d}x} p_{0\bar{x}} + 2k p_{0\bar{x}x} + \bar{\lambda}(kF_{\parallel 0\bar{x}} + F_{\perp 0\bar{z}})\mathrm{H} - \bar{\lambda}F_{\perp 0}\delta + \bar{\bar{\gamma}}\Gamma\right] \mathrm{d}V, \end{aligned} \tag{2.32}$$

which is now an integral that we can evaluate explicitly with our leading-order solution. We note that the $\bar{\bar{\gamma}}$-dependent term in the integral is a linear combination of triple products of sinusoidal functions. Hence, they have zero contributions when we integrate them over $\bar{x} \in [\bar{X}, \bar{X} + 2\pi]$ in $\bar{\Omega}$.

On the other hand, $\partial\bar{\Omega}$ on the right-hand side of (2.30) can be split into four edges, ①–④, as labelled in Figure 2.3, so that

$$\mathrm{RHS} = \int_{①+②+③+④} \left[p_1 \begin{pmatrix} k^2 p_{0\bar{x}}^* \\ p_{0\bar{z}}^* \end{pmatrix} - p_0^* \begin{pmatrix} k^2 p_{1\bar{x}} \\ p_{1\bar{z}} \end{pmatrix}\right] \cdot \mathrm{d}\mathbf{n}_{\bar{\Omega}}. \tag{2.33}$$

We now analyse the four integrals separately:

(i) Contributions from ① and ③: they cancel out each other by the periodicity of p_0^* and p_1.

(ii) Contribution from ②: we first deduce that $p_{0\bar{z}}^* = 0$ at $\bar{z} = -\bar{H}$ from the leading-order free-slip condition (2.23b). For the higher-order free-slip condition (2.29b), we again note that we get zero contribution from any $\bar{\bar{\gamma}}$-dependent terms [as in (2.32)]. Hence, with $w_0 = 0$ at $\bar{z} = -\bar{H}$ (2.27), this integral simplifies to

$$-\int_{\bar{x}=\bar{X}}^{\bar{X}+2\pi} k\frac{\mathrm{d}\bar{H}}{\mathrm{d}x} p_0^* p_{0\bar{x}}|_{\bar{z}=-\bar{H}}\,\mathrm{d}\bar{x}. \tag{2.34}$$

(iii) Contribution from ④: recall that from the leading-order dispersion relation (2.28), $p_{0\bar{z}}^* = p_0^*$ at $\bar{z} = 0$. From the higher-order kinematic condition (2.29c), we can also rewrite $p_{1\bar{z}}$ in terms of p_0^* and deduce that we will ultimately get zero contributions from the $\bar{\bar{\gamma}}$-dependent terms. Suppose we further integrate this integral in time over one period, we have then

$$-\int_{t=0}^{2\pi}\int_{\bar{x}=\bar{X}}^{\bar{X}+2\pi} p_1 p_0^* + p_0^* p_{1tt}\Big|_{\bar{z}=0} \mathrm{d}\bar{x}\mathrm{d}t \tag{2.35}$$

If we integrate $p_0^* p_{1tt}$ in t by parts and impose periodicity on p_1 and p_{1t} in time, we get

$$-\int_{t=0}^{2\pi}\int_{\bar{x}=\bar{X}}^{\bar{X}+2\pi} p_1(p_0^*+p_{0tt}^*)\Big|_{\bar{z}=0}\,\mathrm{d}\bar{x}\mathrm{d}t=0, \tag{2.36}$$

by the expression of p_0^* (2.31). Hence, this integral along ④ is also zero, but over one time period.

In summary, by equating (2.32) and (2.33), the identity (2.30) reduces down to solving

$$\int_{t=0}^{2\pi}\int_{\bar{\Omega}} p_0^*\left[\frac{\mathrm{d}k}{\mathrm{d}x}p_{0\bar{x}}+2kp_{0\bar{x}x}+\bar{\lambda}(kF_{\|0\bar{x}}+F_{\perp 0\bar{z}})\mathrm{H}-\bar{\lambda}F_{\perp 0}\delta\right]\mathrm{d}V\mathrm{d}t$$
$$=-\int_{t=0}^{2\pi}\int_{\bar{x}=\bar{X}}^{\bar{X}+2\pi} k\frac{\mathrm{d}\bar{H}}{\mathrm{d}x}p_0^* p_{0\bar{x}}|_{\bar{z}=-\bar{H}}\,\mathrm{d}\bar{x}\mathrm{d}t \tag{2.37}$$

over one time period at every given x. In terms of Fredholm theory, since this identity is independent of p_1, we have deduced a solvability condition for the system of equations for p_1 (2.29). We can collect and evaluate integrals above which are independent of $\mathbf{F}_0=(F_{\|0},F_{\perp 0})$ in (2.16c) to deduce that

$$\frac{\pi^2 A}{\bar{\lambda}k\cosh^2 k\bar{H}}\left[2A(\bar{H}-1)\frac{\mathrm{d}(k\bar{H})}{\mathrm{d}x}-(2k\bar{H}+\sinh 2k\bar{H})\frac{\mathrm{d}A}{\mathrm{d}x}\right]=\mathcal{D} \tag{2.38}$$

with the $\mathbf{F}_0$-contribution, $\mathcal{D}$, being only drag-dependent, with

$$\mathcal{D}=\frac{1}{2}\int_{t=0}^{2\pi}\int_{\bar{z}=-\bar{H}}^{-\bar{H}+\bar{h}}\int_{\bar{x}=\bar{X}}^{\bar{X}+2\pi} p_{0\bar{x}}^* u_0\,|u_0|\,\mathrm{d}\bar{x}\mathrm{d}\bar{z}\mathrm{d}t. \tag{2.39}$$

We will generalise the expression for $\mathcal{D}$ in the subsequent chapters for other settings. For this problem, evaluating $\mathcal{D}$ explicitly yields an ordinary differential equation for $A(x)$ with

$$\frac{\mathrm{d}A}{\mathrm{d}x}=\frac{18\pi\left(\bar{H}-1\right)\left(k\bar{H}\right)'A-8\bar{\lambda}k^2\operatorname{sech}k\bar{H}\left[3\sinh k\bar{h}+\sinh^3 k\bar{h}\right]A^2}{9\pi\left[2k\bar{H}+\sinh 2k\bar{H}\right]} \tag{2.40}$$

with primes ($'$) again denoting $\mathrm{d}/\mathrm{d}x$ and $A(0)=1$ from the initial normalisation. We note that this result is independent of M_1 and M_2—the $\bar{\bar{\gamma}}$-dependent terms, contributions of added mass and virtual buoyancy, average out to zero over a time period. Mathematically, this is because such contributions to $\mathbf{F}_0$ (2.16c) are linear in $\mathbf{u}_0$ and hence, time-reversible.

The equations (2.25), (2.28) and (2.40) now form a simple system of ordinary differential equations with which we can predict the evolution of the amplitude and wavelength, for any given small-amplitude wave (2.27).

2.6 Analytical results: comparison with limiting cases

Now that we have derived the analytical prediction for the evolution of the wave amplitude (2.40), we would like to compare this with predictions from previous studies that are mentioned in §2.1 in simpler scenarios.

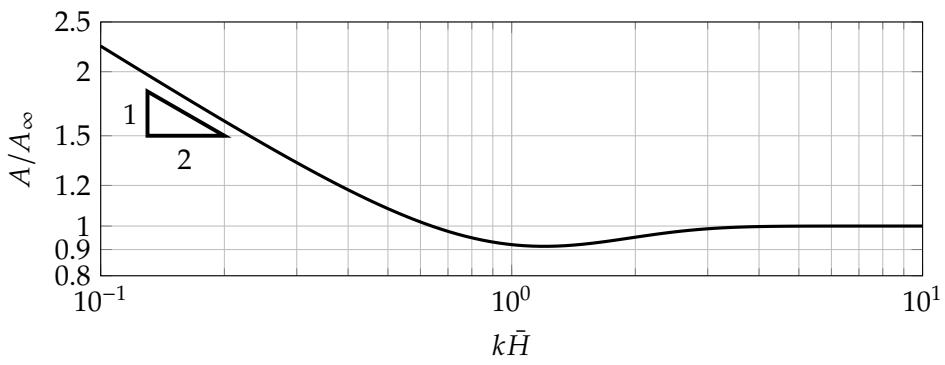

Figure 2.4: Plot of amplitude versus $k\bar{H}$ in the absence of vegetation (2.48), with A being normalised by A_∞, the amplitude in the deep-water limit $k\bar{H} \to \infty$. In the shallow-water regime $k\bar{H} \ll 1$, we recover Green's law $A \propto \bar{H}^{-1/4}$ (2.52) using the dispersion relation (2.28). The quantity on the vertical axis is also known as the *shoaling coefficient* (Dean and Dalrymple, 1991).

2.6.1 *Case 1: Slowly varying bed with no vegetation ($\bar{\lambda} = 0$)*

When the canopy is absent, (2.40) simplifies to

$$\frac{\mathrm{d}A}{\mathrm{d}x} = \frac{2\left(\bar{H}-1\right)A}{2k\bar{H}+\sinh 2k\bar{H}}\frac{\mathrm{d}(k\bar{H})}{\mathrm{d}x}. \tag{2.41}$$

Suppose we define

$$\tilde{A} = \frac{A}{\cosh k\bar{H}}, \tag{2.42}$$

then by the dispersion relation (2.28), we can deduce from (2.41) that $\tilde{A}$ satisfies

$$\frac{\mathrm{d}\tilde{A}}{\mathrm{d}x} = -\frac{2\tilde{A}\cosh^2 k\bar{H}}{\left[2k\bar{H}+\sinh 2k\bar{H}\right]}\frac{\mathrm{d}(k\bar{H})}{\mathrm{d}x}. \tag{2.43}$$

This differential equation can be integrated directly to get

$$\tilde{A} = c_0\left[2k\bar{H}+\sinh\left(2k\bar{H}\right)\right]^{-1/2} \tag{2.44}$$

for some constant c_0. Finally, since the same dispersion relation gives $\sinh 2k\bar{H} + 2k\bar{H} = 2k(\sinh^2 k\bar{H} + \bar{H})$, we recover the classic shoaling prediction by Keller (1958, equation (30)) using a WKB approximation with

$$\tilde{A}^2 k\left(\sinh^2 k\bar{H}+\bar{H}\right) = \text{constant}. \tag{2.45}$$

In terms of A, we get the explicit solution

$$A = \left[\frac{\left[k\sinh^2 k\bar{H}+k\bar{H}\right]^{1/2}}{\cosh k\bar{H}}\right]_{x=0}\frac{\cosh k\bar{H}}{\left[k\sinh^2 k\bar{H}+k\bar{H}\right]^{1/2}}. \tag{2.46}$$

By using the dispersion relation to replace k with $\coth k\bar{H}$ (2.28) in the expression above, we plot in Figure 2.4 the ratio between A and its value in the deep-water limit $k\bar{H} \to \infty$, for different values of $k\bar{H}$. In particular, since $\bar{H}$ varies monotonically with $k\bar{H}$ (due to the same dispersion relation), this plot indicates how the (normalised) amplitude evolves with depth.

We observe from Figure 2.4 that the amplitude remains constant in deep-water. In the transitional regime, with decreasing depth, we note that the amplitude can actually decay before it eventually grows (*i.e.* shoaling) in the shallow-water regime. We will elaborate on the shallow-water regime in §2.6.3.

2.6.2 *Case 2: Flow over a horizontal substrate* ($\mathrm{d}H/\mathrm{d}x = 0$)

When the mean water depth is constant, the wavenumber k is also constant by the dispersion relation (2.28). In this case, we get

$$\frac{\mathrm{d}A}{\mathrm{d}x} = -\underbrace{\frac{8\bar{\lambda}}{9\pi}\frac{k^2}{\cosh k\bar{H}}\frac{3\sinh k\bar{h} + \sinh^3 k\bar{h}}{2k\bar{H} + \sinh 2k\bar{H}}}_{\Lambda} A^2. \tag{2.47}$$

Since Λ is a constant decay factor, we get the explicit solution

$$A = \frac{1}{1 + \Lambda x}. \tag{2.48}$$

If we further replace this equation with dimensional variables, we can demonstrate that (2.48) agrees with Dalrymple et al. (1984, equation (50)). While previous linear-wave theories have either assumed or approximated that the momentum loss in the system is solely due to drag (Dalrymple et al., 1984; Kobayashi et al., 1993; Mendez and Losada, 2004), we have justified that (2.48) holds for arbitrary values of M_1 and M_2.

Finally, we note that when $\Lambda x \ll 1$ *i.e.* for sparse canopies or short distances, we can approximate A as an exponential decay in x with

$$A(x) = \mathrm{e}^{-\Lambda x}. \tag{2.49}$$

Although many experimental studies have described wave attenuation with exponential decays, it has been pointed out in both Mendez and Losada (2004) and also the review by Bradley and Houser (2009) that this is not always applicable, due to the large variation in how much vegetation can attenuate waves.

2.6.3 *Case 3: Shallow-water approximation* ($k\bar{H} \ll 1$)

When $k\bar{H} \ll 1$, the dispersion relation (2.28) reduces to $k^2 = \alpha/H$. Applying this approximation to (2.40), we get at leading order in $k\bar{H}$,

$$\frac{\mathrm{d}A}{\mathrm{d}x} = -\frac{2\lambda}{3\pi}\frac{h}{H^2}A^2 - \frac{1}{2}\frac{1}{H}\frac{\mathrm{d}H}{\mathrm{d}x}A. \tag{2.50}$$

Multiplying both sides by $AH^{1/2}$ gives

$$\frac{\mathrm{d}\left(A^2H^{1/2}\right)}{\mathrm{d}x} = -\frac{4\lambda}{3\pi}\frac{h}{H^{3/2}}A^3, \tag{2.51}$$

and we recover the shallow-water approximation by Mendez and Losada (2004, equation (12)). In particular, when the vegetation is absent ($\lambda = 0$), we recover Green's law for shallow-water waves with (Lamb, 1932)

$$A \propto H^{-1/4}. \tag{2.52}$$

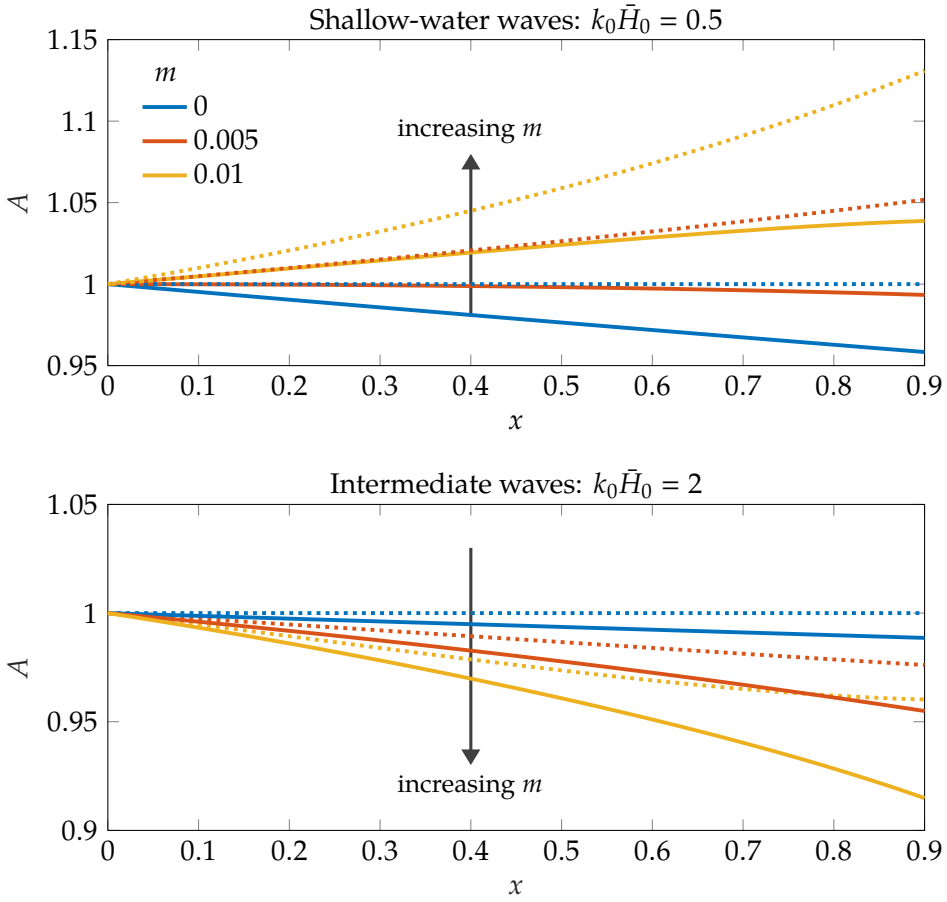

Figure 2.5: Evolution of the wave amplitude over a vegetated plane-sloping substrate $z = -H(x) = -H_0 + mx$ with initial depth H_0 and constant gradient m. The wave has an initial wavenumber $k(x = 0) = k_0$ satisfying the dispersion relation (2.28). The subfigures correspond to the amplitude of shallow-water incident waves ($k_0\bar{H}_0 = 0.5$) and intermediate waves ($k_0\bar{H}_0 = 2$) respectively. Colours indicate different values of m, with solids lines indicating the full problem and dotted lines indicating the classic shoaling problem with no vegetation [see (2.48) and Figure 2.4]. In this figure, we consider an initial depth of $H_0 = 0.02$, with canopy density $\lambda = 0.01$ and submergence ratio $h/H_0 = 0.5$.

We now give some illustrative examples of the wave evolution in space. In Figure 2.5, we consider the simplest case where we have a plane-sloping substrate with gradient m, so that the water depth reduces with the distance of propagation. We introduce a shallow-water incident wave and an intermediate wave respectively and plot $A(x)$ for different values of m. We first observe that in the shallow-water limit in Figure 2.5, waves would shoal if vegetation is absent (see Case 1 in §2.6.1). When we introduce vegetation back in the problem, there is an interesting competition between shoaling and attenuation by vegetation. An analogous plot was done in Mendez and Losada (2004, Fig. 1) using the approximation (2.51).

On the other hand, for the intermediate wave, we observe a less intuitive behaviour that the waves decay more rapidly with steeper substrates – there are two physical reasons behind this. Firstly, when the canopy is absent, we can derive from (2.41) that waves may not grow, but instead decay in this regime solely due to the slope—this is illustrated in Figure 2.4. Secondly, as the wave propagates, the vertical domain contracts and more of the domain is covered by vegetation, which leads to more momentum loss.

As an aside, for deep-water waves, we will observe negligible change in the amplitude unless $h \approx H$. Mathematically, since most of the wave energy is localised near the free surface (2.27), the wave is insensitive to both the

substrate and the deeply-submerged canopy.

The purpose of the example above is to highlight that the presence of a slowly varying substrate and vegetation can have opposite effects between shallow-water and intermediate waves. More importantly, we will later find in the rest of this work that there exist waves in both regimes in real-life applications and flume experiments.

2.7 SUMMARY ON THE MULTIPLE-SCALES ANALYSIS

Although it appears that our rigorous momentum analysis gives the same result as previous predictions using simpler energy arguments in certain regimes, there are many advantages in using our mathematical framework.

Firstly, we have generalised the predictions to waves with arbitrary wavenumbers, added masses, and virtual buoyancies, for any given slowly varying substrates. More importantly, the physics can be less obvious in more sophisticated settings, and it requires very careful considerations then to get the correct energy balance. In our framework, however, we have a systematic and formal deduction of $A(x)$ from the governing equations: any physics are naturally incorporated. Finally, our framework quantifies under what conditions will our predictions remain valid. For example, by following the derivation in this chapter, we can verify that we yield the same equation for $A(x)$ (2.40) when we allow h to vary over the slow scale *i.e.* $h = h(x)$ since additional contributions will only be relevant at higher orders in α. Similarly, we can have $\lambda = \lambda(x)$. In more sophisticated real-life scenarios, we can imagine that it might be relevant to allow h and λ to slowly vary along the coast *e.g.* due to different growth rates or plant species.

2.8 NUMERICAL SIMULATIONS: IMPLEMENTATION

Now that we have given an analytical prediction for wave decay, we want to analyse its accuracy in a more realistic scenario. Here, we want to solve the full two-phase dynamical problem numerically. However, this problem is computationally costly due to its multi-scale nature. In particular, we need to monitor the wave amplitude, which is typically much smaller than the wavelength, along a domain that is much longer than the wavelength. Formally, we need to accurately resolve for small changes in amplitude in every period, such that the amplitude, which is $O(\alpha^2)$, is accurate over an $O(1)$ domain.

To reduce the computational cost while we verify the asymptotic predictions in §2.5, we compromise by solving the 2D incompressible Navier-Stokes equations for both air and water, modified to include a homogenised momentum sink term as presented in (2.12) to account for the presence of the vegetation.

PHASE	DENSITY (kg/m^3)	KINEMATIC VISCOSITY (m^2/s)
air	1.205	1.5×10^{-5}
water	9.982×10^2	1.004×10^{-6}

Table 2.2: Parameters used for *Proteus* simulations.

We solve this problem with *Proteus*, an open-source computational and simulation toolkit that solves partial differential equations using finite element methods over unstructured meshes. The toolkit is developed by the US Army Engineer Research and Development Center and HR Wallingford for solving large scale coastal and hydraulics problems. The implementations have been benchmarked with experimental work—a full list of publications can be found in `https://proteustoolkit.org/`.

The *Proteus* toolkit has various physical and numerical modules, which can be called from a Python interface. For our particular problem, which by and large is a classic dynamic two-phase flow problem that has an additional momentum sink, we solve it with the inbuilt `RANS2P` module. We solve for the evolution of the free surface with a continuous conservative level-set method (Kees et al., 2011).

2.8.1 *Governing equations and the level-set method*

We briefly outline the level-set method that is used in *Proteus* and the adaptations we have made for solving our problem. Suppose we use the subscripts a and w to denote quantities for air and water respectively, we define a level set function ϕ, such that it satisfies the evolution equation

$$\frac{\partial \phi}{\partial t} + \mathbf{u} \cdot \nabla \phi = 0 \tag{2.53}$$

from its initial configuration, with $V_a = \{\mathbf{x} | \phi(\mathbf{x}, t) > 0\}$ being the air domain, $V_w = \{\mathbf{x} | \phi(\mathbf{x}, t) < 0\}$ being the water domain, and the free surface being defined by the zero level set of ϕ. The velocity above satisfies the Navier-Stokes equations,

$$\nabla \cdot \mathbf{u} = 0, \tag{2.54}$$

$$\rho \left(\frac{\partial \mathbf{u}}{\partial t} + \mathbf{u} \cdot \nabla \mathbf{u} \right) = -\nabla p + \mu \nabla^2 \mathbf{u} - \bar{\mathbf{F}}, \tag{2.55}$$

with the density ρ and dynamic viscosity μ being interpolated between the two phases such that

$$\rho = \rho_a S(\phi) + \rho_w [1 - S(\phi)], \tag{2.56}$$

$$\mu = \mu_a S(\phi) + \mu_w [1 - S(\phi)]. \tag{2.57}$$

The values for $\rho_{a,w}$ and $\mu_{a,w}$ are given in Table 2.2. In the expressions above, S is a Heaviside step function that is parametrised by ϕ using the half maximum convention, with

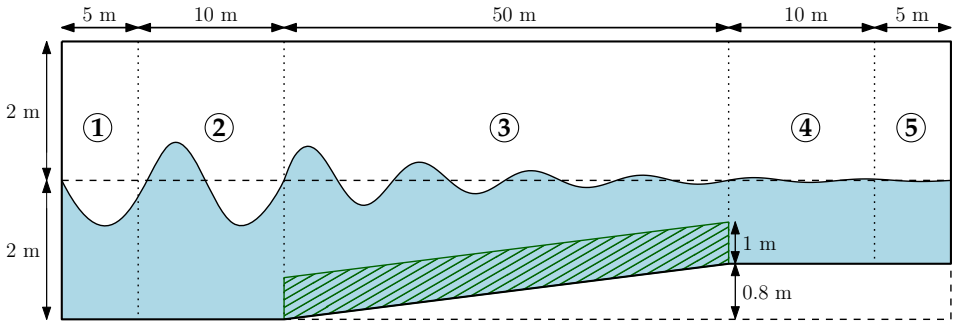

Figure 2.6: Schematic diagram on the dimensions of the numerical wave flume, with the canopy denoted in green. The flume consists of five zones: generation zone, pre-canopy zone, canopy zone, post-canopy zone, and absorption zone.

$$S(\phi) = \begin{cases} 1, & \text{if } \phi > 0, \\ 0.5, & \text{if } \phi = 0, \\ 0, & \text{if } \phi < 0. \end{cases} \tag{2.58}$$

Finally, to incorporate the momentum sink $\bar{\mathbf{F}}$ in the *Proteus* framework, we consider the simplified case where $M_{1,2} = 0$ in (2.12). The main reason for this is that the linear theory has predicted that added mass and virtual buoyancy would have zero contributions over a time period (see §2.5). Furthermore, we can avoid coding the governing equations explicitly and is hence easier for *Proteus* users to reproduce this setup.

We set up the canopy as a *porous zone* of unit porosity. This allows us to include a Darcy-Forchheimer type momentum sink in the Navier-Stokes equations. We then recode this sink as $\bar{\mathbf{F}}$ (2.12) with $M_{1,2} = 0$ in the source code of the `RANS2P` module. Once the source code has been modified, the canopy density can be specified from the user interface.

For a more detailed description on the numerical implementations in solving for $\mathbf{u}$ and ϕ, including weak formulations, automated time-stepping and numerical stabilisations, see Bentley et al. (2017).

2.8.2 *Configuration of the wave flume*

We consider a setup as illustrated in Figure 2.6. We give the dimensional parameters due to the nature of *Proteus*. The dimensions of the flume are chosen to represent a realistic scenario.

With reference to the setup in Dimakopoulos et al. (2019) on numerical wave flumes with fast random waves, our flume is divided into five zones, labelled as ①–⑤ in Figure 2.6:

1. Generation zone: A region in which the wave is generated. The details on how the wave is generated are outlined in the next section;
2. Pre-canopy zone: An obstacle-free horizontal domain between the generation zone and the canopy zone;
3. Canopy zone: the only region in which there is a canopy and any variation in depth. We prescribe the substrate to be a plane slope;
4. Post-canopy zone: An obstacle-free horizontal domain between the canopy zone and the absorption zone;

5. Absorption zone: a virtual sponge which absorbs the momentum to mitigate reflections which propagate back into the main flume.

We are mainly interested in how the wave evolves through the canopy zone [labelled as ③ in Figure 2.6]. The pre-canopy zone helps to mitigate the feedback from the canopy and the slope on wave generation. Similarly, the post-canopy zone mitigates reflections from the absorption zone.

To not save the full configuration at every time step, we set up virtual gauges which log the location of the free surface at fixed intervals along the canopy zone. Formally, since it is a two-phase problem, the definition of the free surface here corresponds to positions at which the volume fraction of water is 0.5, after interpolating vertically along z.

We initially start with the two phases being steady under hydrostatic pressure. We then generate the water wave in the generation zone and allow the system to evolve the until transients have decayed and we have a periodic solution—this is measured by the periodicity of the wave signal at the start of the absorption zone. Finally, once the system is periodic, we take a simple average of the amplitude at ten subsequent periods at each gauge to get a time-averaged profile for $A(x)$ in the canopy zone.

A typical simulation would have the domain discretised into triangular elements with a maximum diameter of 150–200 units per wavelength, with the latter being calculated from the dispersion relation (2.28) *a priori*. For a time period of $T = 2\pi/\omega_0 = 1.5$ s, the finite element mesh would have over 1.7×10^6 elements. The computational time for a simulation up to $t = 100$ s is typically 48–96 hours using 96 cores. The CPUs are 2$^{\text{nd}}$ generation Intel Xeon Scalable Processors (Cascade Lake) with a sustained all-core Turbo CPU frequency of 3.6 GHz. We note that a long simulation time ($t = 100$ s) is required to allow the incident waves to propagate to the end of the flume and the system to fully develop into a time-harmonic state. The same applies to physical experiments with wave flumes.

2.8.3 *Theory on wave generation*

We generate the incident wave with a prescribed amplitude and time period using the `WaveTools` module in the generation zone. The module has the option to either impose a linear wave [the dimensional version of (2.27)] or a Fenton wave (Fenton, 1988) as an incident wave. By ignoring the contributions from air and assuming that the water flow is both inviscid and irrotational, a Fenton wave has its stream function ψ in the form

$$\psi = \sum_{n=1}^{N} B_n \frac{\sinh\left[nk(z+H)\right]}{\cosh kH} \cos\left[n(kx - \omega t)\right] \tag{2.59}$$

for some N and coefficients B_n (in addition to wavenumber k and angular frequency ω). This truncated Fourier series ansatz is constructed such that each mode satisfies both the governing equation $\nabla^2\psi = 0$ and the no

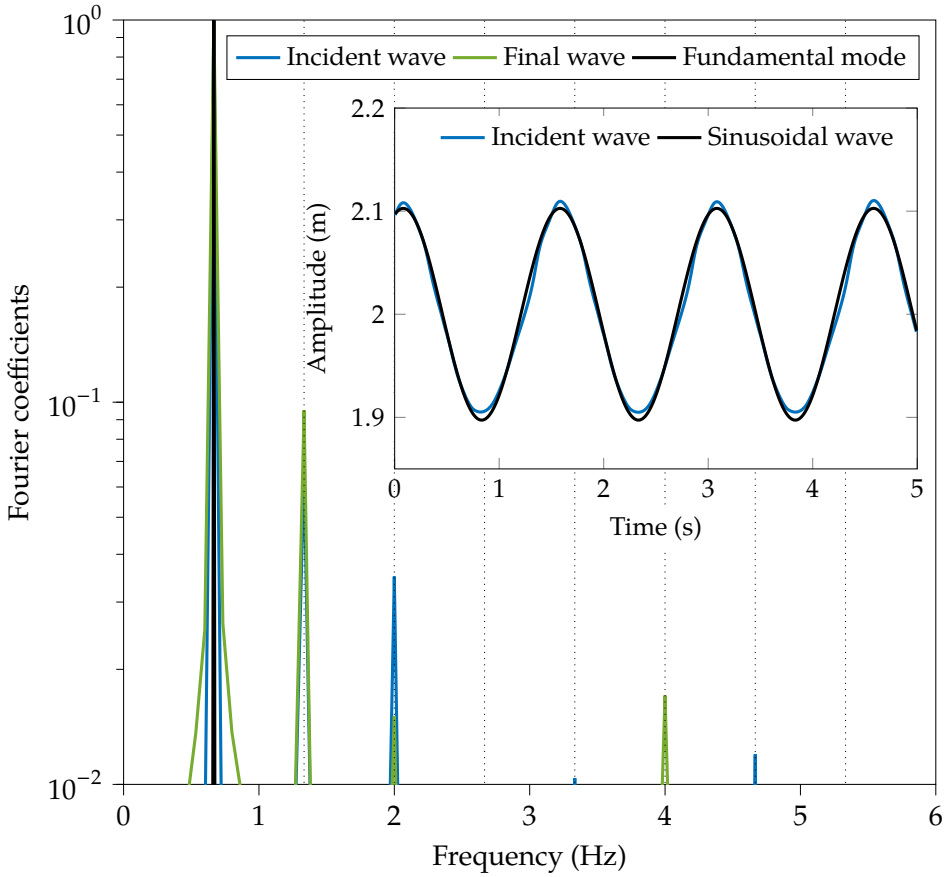

Figure 2.7: Fourier transforms of the incident wave and the final wave. Shown is the case where $A_0 = 0.1$ m, $T = 2\pi/\omega_0 = 1.5$ s and dimensionless canopy density $\lambda = 0.1$. The frequency spectra shown have been normalised by their respective Fourier coefficient at the fundamental frequency. The vertical dotted lines indicate the harmonics. The black solid line indicates the same function that is extracted from both waves (up to normalisation) to approximate the fundamental mode. The inset illustrates the physical difference between the incident wave, which generated the frequency spectrum in the main figure, and its corresponding sinusoidal fit.

penetration condition along the substrate. The coefficients are then solved numerically to satisfy the full free-surface conditions while also giving the resulting wave the prescribed amplitude.

The advantage of this spectral approach compared to higher-order Stokes' theory or cnoidal theory (for shallow-water waves in Chapter 4) is that the coefficients B_n in (2.59) would converge exponentially. Meanwhile, the mentioned classic theories evaluate waves using asymptotic expansions which are based on the wavenumber. Hence, such series may suffer from slow convergence when the water is sufficiently shallow or deep.

In our implementation, we found it more numerically stable to impose a Fenton wave as an incident wave rather than a sinusoidal wave (2.27). Although we are comparing with analytical predictions from linear wave theory in §2.5, forcing a linear incident wave would nonlinearly transform along the flume due to the nonlinear governing equations. Hence, we impose a Fenton wave that has the same fundamental time period and extract its (linear) fundamental mode for comparison with analytical predictions.

By imposing a Fenton wave that has a sufficiently small amplitude compared to the depth, the higher-order harmonics in the truncated series for ψ (2.59) have negligible contributions and the Fenton wave is still well-approximated by the fundamental mode. To illustrate this, we provide an example of the Fourier transform of both a typical incident wave and its cor-

responding final wave (after passing through a canopy) in Figure 2.7. The incident wave is measured at the end of the generation zone, and the final wave is measured at the start of the absorption zone in Figure 2.6. When we analyse the spectra of both waves (and waves at various points along the canopy zone), the Fourier coefficients of other frequencies are always ten times smaller than the coefficient of the fundamental frequency. The inset in Figure 2.7 also illustrates the proximity between the Fenton wave and its sinusoidal fit when they share the same wave height and time period.

Finally, to compare the amplitude between our numerical simulations and analytical predictions in §2.5, we extract the fundamental mode from the wave signal at each gauge. We do so by approximating the δ-function in the (discrete) frequency domain as the original signal with all the frequencies but the fundamental frequency set to zero (see the black line in Figure 2.7). We then transform the signal back into the temporal domain and evaluate its amplitude.

As an aside, we would also like to compare our analytics against the full numerical profiles for completeness. However, unlike sinusoidal waves, there is an ambiguity on the definition of the amplitude in such cases. In this work, we measure A as half of the difference between the maximum and minimum elevation at every time period to remove any steady profiles that have developed.

We present our results in the next section.

2.9 NUMERICAL SIMULATIONS: RESULTS

In Figure 2.8, we present a series of plots on the evolution of the amplitude due to the sloped substrate and increasing canopy density in the canopy zone. We have chosen an incident wave that has its wavelength comparable to the water depth—this is so that when the canopy is absent ($\lambda = 0$), the amplitude gradually decays as kH reduces from 3.6 to 1.8 along the domain (see Figure 2.4). This regime is mainly chosen to provide some different insights to what has already been established with shallow-water approximations from previous work *e.g.* (Mendez and Losada, 2004). In addition, we can also simulate such cases on a finer mesh. Shallow-water waves have a relatively longer wavelength. To be in the correct asymptotic regime ($\alpha \ll 1$), we would then require a longer domain. However, the maximum element size cannot be compromised since we require sufficient resolution for the wave amplitude.

In each subplot in Figure 2.8, we first note that the full numerical wave (in blue) has a higher amplitude than its own fundamental mode (in green) by construction. However, we emphasise that provided that the amplitude is sufficiently small compared to the depth, the fundamental mode is a good approximation of the full-wave along the canopy zone. This is evident in all five cases here by the proximity of the two amplitudes: its accuracy has

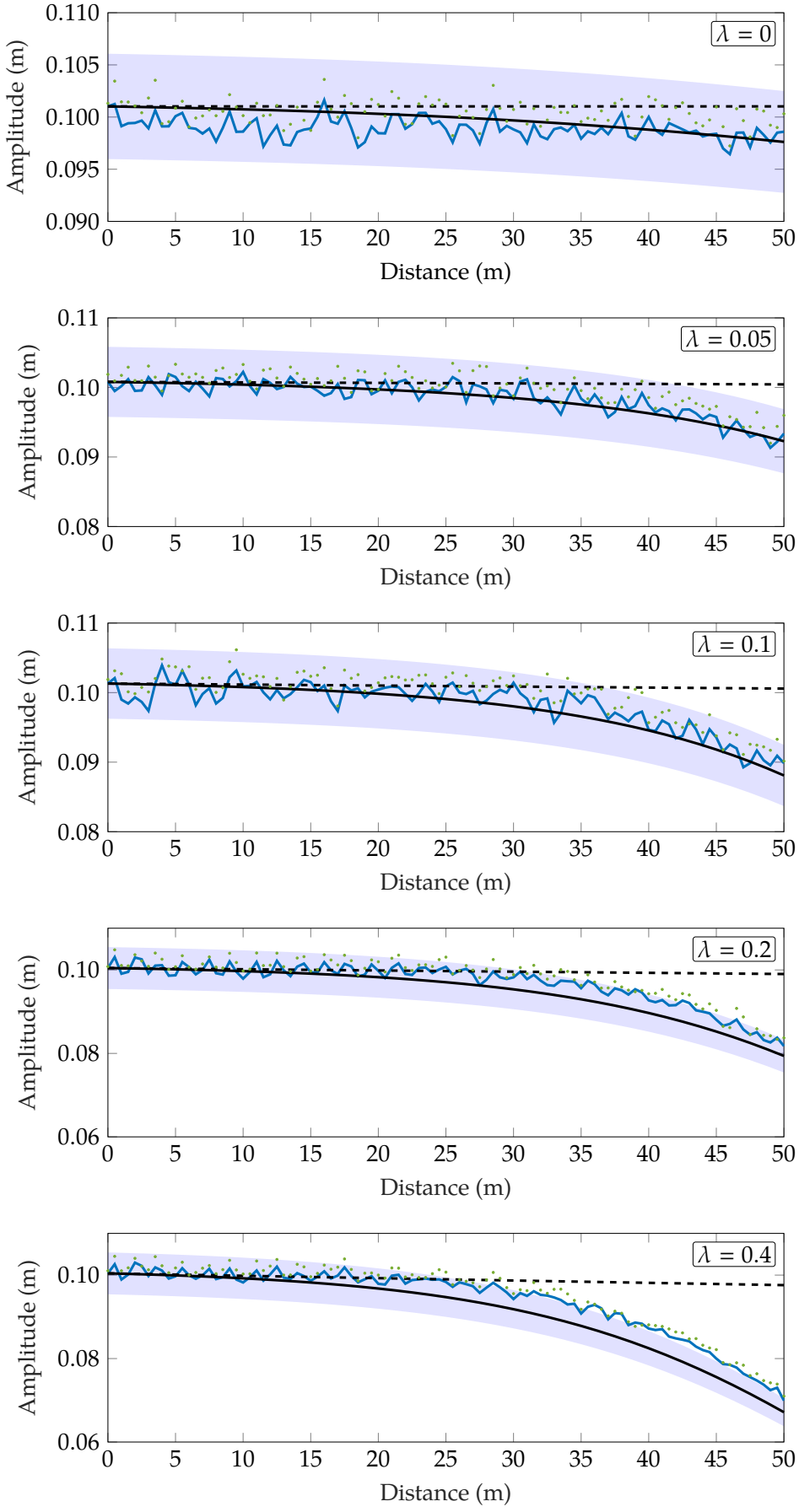

Figure 2.8: Series of plots of the period-averaged amplitude along the canopy zone in Figure 2.6 for canopies with increasing densities, λ. Note that the scales of the vertical axes are different in each subplot. The green data points denote the amplitude of the numerical wave at each virtual gauge. The fundamental modes that are extracted at each gauge using the procedure in §2.8.3 are connected by blue lines. For each setup, the corresponding analytical predictions for the amplitude (2.40) are plotted in black solid lines, together with 5% error bands being shaded in as visual guides. The black dashed lines represent the predictions for the constant-depth problem with $H = 2$ m. All of the analytical curves are scaled so that the amplitudes match the amplitude of the fundamental mode at the start of the canopy zone (see Figure 2.6).

been previously quantified in §2.8.3.

We observe that increasing canopy density increases the amplitude decay. In all five cases, our analytical predictions capture this reasonably well quantitatively. We have also compared each plot against the corresponding predictions for constant depth to highlight that the effects of substrate and canopy do not simply sum. For example, the theory predicts that $A(50) = 0.067$ m when $\lambda = 0.4$ but only $A(50) = 0.098$ m when $\lambda = 0$, despite the fact that when $\lambda = 0.4$ with flat bottom, $A(50) = 0.098$ m. More importantly, the depth reduction in this case substantially increases amplitude decay. The main physical reason for this is that the fluid velocity is faster near the free surface [see (2.27)]. With depth reduction, more momentum is lost when the vertical domain is increasingly covered by vegetation. We have also illustrated this effect via an example in §2.6.3. Additional numerical simulations regarding this effect are given in Appendix B.

2.9.1 Large vegetation density

For canopies with $\lambda = 0.2$ and 0.4, the predictions become less accurate as waves propagate along the canopy zone. Mathematically, we derived the rate of change of the amplitude in space (2.40) based on asymptotic expansions with the multiple-scales parameter, $\alpha \ll 1$. Hence, deviations are expected when the canopy is sufficiently dense that the leading-order wave approximation (2.27) is no longer asymptotically accurate. Meanwhile, we also note that we underestimate the momentum loss, despite that the model (2.1)–(2.2) is inviscid and hence does not account for viscous dissipation. We anticipate that the reduced momentum loss is due to the nonlinear nature of the full problem—the higher harmonics interact with the fundamental mode (which allows energy conversion between modes – this is illustrated by the distinct Fourier decomposition between the incident wave and the final wave in Figure 2.7) and mitigate the overall drag after every time period. Such effects accumulate and eventually become apparent once the waves reach the end of the canopy zone.

On the other hand, the high-density plots that are mentioned above also suggest that our predictions can be useful by their proximity to the numerical profile. In particular, although our derivation is based on the canopy being sufficiently sparse, the literature review by Nepf (2012) stated that for aquatic vegetation, the dimensionless geometric canopy density

$$\frac{\sqrt{3}}{2}\frac{h}{C_D A_0}\lambda = \frac{\sqrt{3}}{2} b\bar{N}h = 0.1 \tag{2.60}$$

is the threshold at which sparse canopies transition to dense canopies. Since $h/A_0 = 10$ for all of the cases considered here, the canopies are considered to be dense in real life. In general, by how we have nondimensionalised our problem, this statement has to be revised based on the scale of the amplitude.

2.9.2 *Discussion on using an infinite-canopy approximation*

We recall from our derivations in §2.5 that we have considered an infinite canopy along the domain so that the domain is asymptotically periodic on the local wave scale. This is distinct to the typical finite-canopy setup in both the numerical wave flume considered in this work (see Figure 2.6) and other real experiments. We emphasise that our prediction (2.40) is asymptotically correct since we are considering the limit in which the canopy density scales with α – the ratio between the wavelength and the domain scale. Hence, any finite-canopy correction will only correspond to asymptotically small horizontal adjustments in the prediction curves at the order of a wavelength.

2.9.3 *Discussion on the fluctuations of the wave amplitude*

Finally, we attempt to explain the fluctuations of the numerical amplitude at each gauge in Figure 2.8. In addition to wave reflections from the absorption zone, the fluctuations are due to the resolution of the amplitude *i.e.* numerical errors from the discretisation. In all the simulations, the maximum element size is below 0.02, which is the scale of the noise. Furthermore, we have to interpolate along the elements in z to obtain the location of the free surface. We expect this fluctuation to reduce with higher resolution. However, the computational cost would increase exponentially. For example, suppose we are to reduce the maximum element size by half to 0.01, the mesh would approximately quadruple in the number of elements in 2D. This would further lead to smaller time steps for numerical stability. The computational cost that is associated with problems that have such slowly varying nature highlights the power and also the need for simple and accurate asymptotic approximations.

2.10 PREDICTING WAVE ATTENUATION IN LABORATORIES

Now that we have verified the asymptotic predictions of the continuum model, we would now like to compare how well it predicts decay in a physical wave flume with individual vegetation. We compare our predictions against the experimental data from multiple studies on flow over a mimic canopy of rigid cylinders (Augustin et al., 2009; Wu et al., 2012; Ozeren et al., 2014). Although similar comparisons have been made before, we would now like to see how it works without any fitting parameters. This particular validation is also new.

2.10.1 *Variation of the drag coefficient*

Thus far, we have assumed that the drag coefficient, C_D is constant and focused on introducing the multiple-scales analysis. In a complete model, it has been established from direct force measurements that for oscillatory

flows, C_D for a single obstacle is a function of the dimensionless Keulegan-Carpenter number K_C with (Keulegan and Carpenter, 1958)

$$C_D = C_D\left(K_C = \frac{UT}{b}\right), \tag{2.61}$$

where U is the maximum velocity, $T = 2\pi/\omega_0$ is the time period of the wave and b is the streamwise diameter of the obstacle. This parameter K_C quantifies the ratio between the travelling distance of a fluid particle in relation to the obstacle width. We can typically consider C_D to be a constant in the limit $K_C \to \infty$, where the flow is unidirectional for the majority of the period (on the scale of the obstacle).

According to the review by Chen et al. (2018), the conventional approach to validating the decay relation (2.48) is to fit it against the experimental data by fitting the value for C_D. However, since we are interested in predicting wave attenuation, we want to understand its predictive accuracy. In particular, based on our homogenised canopy model, we want to impose the drag coefficient as the one which corresponds to individual stems. Hence, instead of fitting C_D, we use the experimental relation between C_D and K_C (2.61) by Keulegan and Carpenter (1958) on cylinders.

We also note in a complete model, the velocity scale U in K_C (2.61) would also vary in both the water depth and the distance of propagation as the wave evolves. For simplicity, we use the common modelling assumption of treating C_D constant within the domain once C_D is fixed by the initial value of K_C [see *e.g.* Luhar and Nepf (2016), Leclercq and de Langre (2018) and references therein].

2.10.2 *Results*

The studies by Augustin et al. (2009); Wu et al. (2012); Ozeren et al. (2014) consist of regular waves propagating through a uniform finite canopy in a horizontal flume. The amplitudes are measured by individual wave gauges along the canopy. The raw data and the individual plots of wave decay are given in the Appendix A.

For the theoretical predictions, we recall from §2.6.2 that on a horizontal substrate, the amplitude along the canopy satisfies

$$A = \frac{1}{1 + \Lambda x} \tag{2.62}$$

where the constant decay factor $\Lambda \propto C_D$ for individual experiments is given by (2.47). We present the comparison in Figure 2.9.

The experimental data reasonably collapses onto the theory curve, which is shown as a single black solid line in Figure 2.9. The theory curve gives an R^2-value of 0.78. Although not shown here, the equivalent prediction using a standard choice of $C_D = 1.2$ (for cylinders in uniform flow) only gives R^2-value of 0.62 (see Appendix A). We can compare the difference between the choice of C_D in the inset.

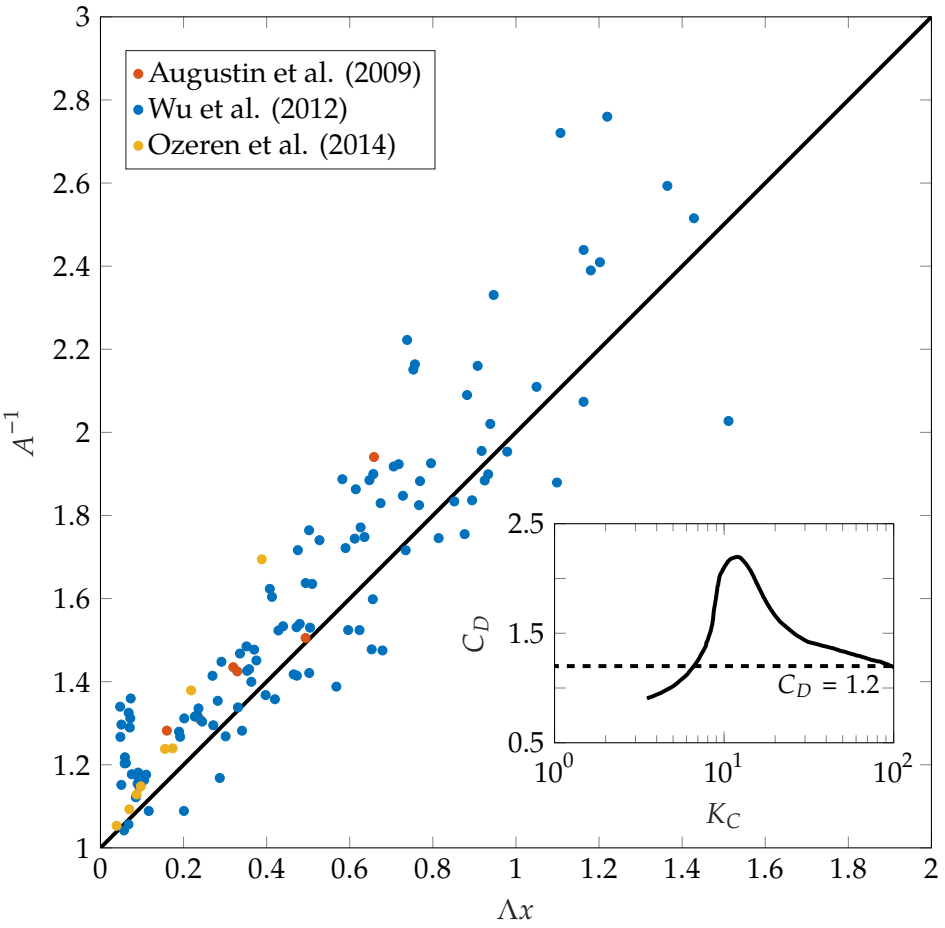

Figure 2.9: Experimentally determined dimensionless decay for waves propagating through a rigid canopy. The black solid line indicates the theoretical prediction $A = (1 + \Lambda x)^{-1}$ (2.48) and dots indicate the measurements for individual experiments. We compared 28 of the 29 sets of experiments available – the details of individual experiments are given in Appendix A. The inset plots the experimentally determined relation between the drag coefficient C_D and the Keulegan-Carpenter number K_C (2.61) for a single cylinder under uniform oscillatory flows (Keulegan and Carpenter, 1958). Since wave velocities are depth-dependent, following the definition by Chen et al. (2018), the velocity scale in K_C (2.61) is chosen to be the maximum velocity at the half water depth.

We note that there is a cluster of points at $\Lambda x \approx 0.1$ that is under-predicted *i.e.* the amplitude A is over-predicted by the theory (2.48). We anticipate that this is due to wave reflection due to the canopy front, which we do not account for in our infinite-canopy model. The scatter also increases for larger values of Λx. This can be explained by the weak-decay approximation we had in our multiple-scales analysis. Again, we assumed that the canopy is sufficiently sparse [the rigorous definition is given by (2.22)].

2.11 SUMMARY AND DISCUSSION

This chapter began with the aim of predicting wave attenuation due to the presence of vegetation, motivated by applications in coastal management. We first considered the reduced problem where the vegetation is rigid, so that we could have a good physical understanding of the pure fluid problem.

We first posed the problem in a general 3D framework and modelled the vegetation as rigid beams that are rooted along a known varying substrate. The momentum loss in the water wave due to vegetation is accounted for via a sink in the fluid momentum equations, which consisted of drag, added mass and virtual buoyancy effects. Since we are mainly interested in the

macroscopic flow and its associated momentum loss, we homogenised the contributions of individual plants so that we could consider a bulk drag term (2.12). We then reduced the problem to 2D and presented the dimensionless governing equations and the key parameters, summarised in Table 2.1.

By exploiting the typical scenario in which waves are only slowly evolving in space, we separated the large domain scale from the small wave scale and formulated a general multiple-scales problem in §2.5, with the small parameter being the ratio between the two scales. By considering monochromatic waves with small amplitudes propagating over slowly varying substrates with sparse canopies, we formally decoupled the local flow from both the substrate and vegetation. This allowed us to recover the classic sinusoidal approximation for the wave from linear wave theory, with the property where both the amplitude and the wavenumber vary over the macro scale. Finally, we derived ordinary differential equations for the evolution of the wavelength (2.25) and the amplitude (2.40) along the domain.

By solving for the amplitude explicitly in various simplified cases in §2.6, we demonstrated how we have generalised the results from previous work by Keller (1958), Dalrymple et al. (1984), and Mendez and Losada (2004). We then validated the asymptotic predictions with numerical simulations of a more realistic two-phase problem using *Proteus*, which accounted for nonlinear effects and viscosity. We demonstrated that there is good agreement between the two in Figure 2.8 and the capabilities of our predictions on analysing dense-canopy flows. Finally, we also validated our prediction with experimental data from Augustin et al. (2009); Wu et al. (2012); Ozeren et al. (2014) in Figure 2.9, by allowing the drag coefficient to vary with the Keulegan-Carpenter number.

The systematic and rigorous framework of multiple-scales analysis allowed us to give new predictions. We have also highlighted in §2.7 how our predictions could be readily extended to non-uniform canopies by following the same derivation. However, there are additional physics that have to be accounted for when we consider more complex flows, such as nonlinear waves and combined current-wave flows. Above all, we are interested in generalising the multiple-scales framework so that we can analyse flexible vegetation—another main focus of this study. Mathematically, there are subtleties which make such extended problems rich. In particular, the vegetation will deform and interact with the flow to become a coupled problem. We will explore such extensions in the subsequent chapters.

3 COMBINED CURRENT-WAVE FLOWS THROUGH RIGID VEGETATION

We must take the current when
it serves, or lose our ventures.

William Shakespeare

SYNOPSIS

In this chapter, we consider the problem of combined current-wave flows through rigid vegetation. By focusing on the regime in which the current, which we consider being steady, and the fluid velocity in the wave are comparable in magnitude, we perform a multiple-scales analysis to analyse how the combined flow varies along the domain. In particular, we find that the coupling is only one-way—the amplitude decays differently from the pure wave problem, but the steady current remains fixed in space. The current is maintained by the elevation of the mean free surface.

3.1 INTRODUCTION

In the previous chapter, we considered the fundamental problem of a pure sinusoidal wave propagating through rigid vegetation. In certain coastal regions and tidal situations, waves can also be superimposed with a current, which is a special case of a polychromatic wave.

The polychromatic problem of waves propagating through vegetation is complex for two reasons: (i) the wavelengths evolve along the domain; (ii) the harmonics interact with each other. Suppose we only have a monochromatic wave. According to our multiple-scales analysis in Chapter 2, we can quantify the slow evolution of the wavelength along the domain via its dispersion relation (2.28). For polychromatic waves, however, we no longer have a simple dispersion relation that governs the spatial periodicity. Hence, we no longer have a well-defined mapping between the microscale and the macroscale coordinates.

A particularly relevant regime to consider, however, is to understand what happens when a steady current is superimposed with a wave. From the perspective of the multiple-scales analysis, since the additional current

will not alter the original dispersion relation, we can solve for the flow using similar techniques as in Chapter 2. Nevertheless, the current and the wave can still interact with each other along the domain, which makes this problem rich.

Suppose we continue from the 2D modelling framework in Chapter 2 and consider the wave to be propagating along the same direction as the current. Depending on the velocity scale of the current relative to the wave, different physical effects dominate. This has resulted in different subfields of research. Suppose U_c is the velocity scale of the current and U_w is the velocity scale of the fluid flow in the wave, we have three cases to consider:

1. $U_c \ll U_w$: Since we can gain most of our insights from the pure wave problem in terms of wave attenuation and ultimately coastal protection, we do not pursue further.
2. $U_c \gg U_w$: Mathematically, the wave can be treated as a perturbation of the current and can experience *Doppler shift*. Suppose a linear wave that propagates along a horizontal domain (with no vegetation) has angular frequency ω and wavenumber k in still water. Using the same coordinate system as in the previous chapter, when this wave propagates with a current of velocity $\mathbf{u}_c = u_c \hat{\mathbf{e}}_x$, the new observed frequency ω_c satisfies the dimensional dispersion relation

$$(\omega_c - k u_c)^2 \approx \omega^2 = gk \tanh kH \tag{3.1}$$

for a given water depth H (Peregrine, 1976). Mathematically, this shift is a direct result of the kinematic condition of the wave at the free surface. If $z = \eta$ is the free surface and $\mathbf{u} = (u, w)$ is the flow velocity in 2D, the dimensional condition reads

$$w = \frac{\partial \eta}{\partial t} + \mathbf{u} \cdot \nabla \eta \quad \text{at } z = \eta. \tag{3.2}$$

When the flow velocity is significant, η is advected by $\mathbf{u} = u_c \hat{\mathbf{e}}_x$ at leading order if we consider a formal asymptotic expansion in $U_w/U_c \ll 1$. In Chapter 2, the waves were approximated to experience no drift since such effects were asymptotically small.

Since the main focus of this work concerns hydrodynamic momentum loss due to vegetation, the velocity of the flow would naturally scale with U_c rather than U_w. As a result, vegetative drag would scale with U_c^2. Analogous to the wave-dominant regime we considered in point 1, in this current-dominant regime, the wave is no longer important in terms of quantifying momentum loss. Furthermore, it is known that currents could cause flow instabilities due to the canopy—this is addressed in Chapter 6. There is an extensive amount of literature which addresses wave evolution under strong currents [see *e.g.* Turpin et al. (1983) and Kirby (1984)] but not for vegetated flows.

3. $U_c \sim U_w$: The regime in which the wave and the current are comparable in magnitude has gained recent interest in the field. There are experimental studies by Hu et al. (2014) on rigid cylinders and Losada et al. (2016) on current with and against the direction of wave propagation. In terms of the theoretical predictions they have made on wave attenuation, Hu et al. (2014) considered the simplified problem of shallow-water linear waves. The predictions by Losada et al. (2016) on canopies in horizontal flumes also assumed that the contribution of the current in the drag expression could be neglected in the dense-canopy regime. Hence, both estimates warrant further generalisation. Furthermore, the evolution of the current and the free surface along the domain are not addressed mathematically in either study.

In this chapter, we consider the problem of the combined current-wave flows through rigid vegetation where the velocity of the two are comparable in magnitude. The modelling framework of the flow is directly adapted from the pure wave problem in Chapter 2. Hence, for ease of reference, we inherit the notations and variables unless otherwise stated. We solve for profiles of both the current and the wave simultaneously by evaluating how they interact with each other.

3.2 HORIZONTAL SUBSTRATE WITH NO VEGETATION

We begin by considering the simple problem of how a current is superimposed with a monochromatic wave in a horizontal substrate with no vegetation. By closely following the derivation in Baddour and Song (1990) on two-dimensional inviscid flows, we can deduce that the flow field $\mathbf{u}$ in the xz–domain can be expressed as the simple sum

$$\mathbf{u} = \begin{pmatrix} u_c \\ 0 \end{pmatrix} + \mathbf{u}_w \tag{3.3}$$

where u_c is any constant horizontal current and $\mathbf{u}_w$ is the dimensional velocity profile of the linear wave (2.27).

In this simple problem, the mean free-surface elevation is unchanged, and the waveform is also unchanged from the pure wave problem (2.27)—any interactions between the current and the wave are formally higher-order effects when the current has the same velocity scale as the wave (Peregrine, 1976). However, the wave can experience Doppler shift (3.1) as mentioned in §3.1 if the current is much faster than the wave. We also note that the dynamic pressure is also unchanged from the pure wave case since there is no resistance which slows down the additional current—this will change when we introduce vegetation to the problem.

3.3 PURE STEADY CURRENT OVER RIGID VEGETATION

When we introduce the vegetation and allow the substrate to slowly vary, the current cannot be imposed since it varies along the domain. Hence, the current has to be solved as part of the problem. For intuition, we first neglect the wave and solve the steady-current problem—this corresponds to the solution of the combined current-wave problem in the limit of vanishing wave amplitude. In particular, we solve the dimensional problem so that the results would both apply to more general settings and help us to verify our derivations in the combined problem in the subsequent sections.

We first return to our set of dimensional governing equations with the homogenised momentum sink (2.14). We solve for the flow field $\mathbf{u}$, dynamic pressure p, and the free-surface elevation η by adapting a classic derivation of shallow-water equations. For convenience, we use primes ($'$) to denote $\mathrm{d}/\mathrm{d}x$.

By integrating the incompressibility condition (2.14a) with respect to z and applying the Leibniz rule on η and the substrate at $z = -H(x)$, we get

$$\int_{-H}^{\eta} u_x \,\mathrm{d}z + u(z=\eta)\eta' + u(z=-H)H' = \frac{\partial}{\partial x}\int_{-H}^{\eta} u \,\mathrm{d}z = 0. \tag{3.4}$$

By letting $\bar{u}$ to be the height-averaged horizontal velocity with

$$\bar{u} = \frac{1}{H+\eta}\int_{-H}^{\eta} u \,\mathrm{d}z, \tag{3.5}$$

we deduce that

$$(H+\eta)\bar{u} = Q \tag{3.6}$$

where Q is some fixed downstream flux along x. If we also consider the flow to be irrotational, then

$$u_z - w_x = 0. \tag{3.7}$$

Assuming that $|w| \ll |u|$ in shallow-water flows, a standard simplification for domains with a small aspect ratio (between the depth and the length of the fluid domain), we deduce that $u_z \approx 0$. Hence, $u \approx u(x)$ and $u \approx \bar{u}$, and we can neglect any contributions from w.

From the z-momentum equation in (2.14b), we can deduce from the same approximation that the static pressure is approximately hydrostatic with the dynamic pressure satisfying $p' \approx \rho g \eta'$. By substituting this streamwise pressure gradient into the height-averaged x-momentum equation in (2.14b), we deduce that

$$uu' = -g\eta' - \frac{1}{2}bC_D\bar{N}u|u|\frac{h}{H+\eta}. \tag{3.8}$$

In summary, we yield a set of steady shallow-water equations

$$\big(H+\eta\big)\,u = Q, \tag{3.9}$$

$$uu' + g\eta' + \frac{1}{2}bC_D\bar{N}u|u|\frac{h}{H+\eta} = 0. \tag{3.10}$$

The top equation physically represents mass conservation. We can also interpret the bottom equation as the momentum balance along the domain between nonlinear advection, pressure gradient, and vegetative drag. Suppose we rewrite the equations into a single equation for u, we have

$$\left(u - \frac{gQ}{u^2}\right) u' - gH' + \frac{1}{2} b C_D \bar{N} u|u| \left(\frac{uh}{Q}\right) = 0. \tag{3.11}$$

From this equation, we can deduce that when vegetation is absent and the substrate is flat, the current is constant; the free-surface elevation η is also constant, which can be set to zero.

We can also rewrite the shallow-water equations (3.9)–(3.10) in terms of H and η only, so that

$$g\eta' + \frac{1}{2} b C_D \bar{N} \frac{Qh}{(H+\eta)^2} \left|\frac{Q}{H+\eta}\right| = \frac{Q^2}{(H+\eta)^3} \left(H+\eta\right)'. \tag{3.12}$$

Thus far, we have derived the steady shallow-water equations in a general setting. We would now like to understand how the equations differ in the domain that we have considered in Chapter 2 for the pure wave problem.

3.3.1 *Nondimensionalisation and relations to the pure wave problem*

Suppose we nondimensionalise shallow-water equation (3.12) with the scales

$$[\eta] = [H] = \frac{g}{\omega_0^2} \quad \text{and} \quad [Q] = [\mathbf{u}][H] = A_0 \omega_0 \frac{g}{\omega_0^2}. \tag{3.13}$$

By inheriting the same dimensionless parameters Table 2.1 from the pure wave problem in Chapter 2, and also the bar notation ($\bar{\cdot}$) from considering the same distinguished limits (2.22), we get the dimensionless equation

$$\eta' + \alpha \underbrace{\bar{\bar{\gamma}} \frac{\bar{\lambda}}{2} \frac{Q\bar{h}}{(\bar{H}+\eta)^2} \left|\frac{Q}{\bar{H}+\eta}\right|}_{O(1)} = \alpha^2 \underbrace{\bar{\bar{\gamma}} \frac{Q^2}{(\bar{H}+\eta)^3} \left(\bar{H}+\eta\right)'}_{O(1)}. \tag{3.14}$$

In particular, we recall that the small parameter α describes the ratio between the wavelength and the domain scale. If we consider an expansion for the flow variables in powers of $\alpha \ll 1$, then $\eta_0' = 0$ at leading order. Hence, $\eta_0 \equiv 0$, by choosing the origin such that $\eta_0(0) = 0$. This results in the mass conservation equation

$$\bar{H} u_0 = Q_0. \tag{3.15}$$

A more appropriate nondimensionalisation for η in the shallow-water equation (3.12) is to take $[\eta]$ to be the amplitude scale A_0. If we apply the same expansion in α under the new scaling, we will deduce the same equation for mass conservation (3.15). For the momentum equation (3.12), however,

we have the balance between the pressure gradient and the vegetative drag on the left-hand side, giving

$$\eta_0' = -\frac{\bar{\lambda}}{2}\frac{Q_0\bar{h}}{\bar{H}^2}\left|\frac{Q_0}{\bar{H}}\right|. \tag{3.16}$$

Physically, the two different nondimensionalisations in η indicate that:

(i) When we consider a flux that is comparable to the pure wave scenario, the free surface has negligible displacement compared to the wavelength (which is assumed to be comparable to the water depth) along the entire domain.

(ii) For any positive downstream flux $Q_0 > 0$ in (3.16), the free-surface elevation would decrease downstream monotonically. This gradient maintains a pressure gradient in the flow which balances the vegetative drag. This physical phenomenon is observed experimentally in *e.g.* Tanino and Nepf (2008).

(iii) When we consider the combined wave-current problem, we expect to recover the set of shallow-water equations (3.15)–(3.16) in the limit of vanishing wave amplitude.

3.3.2 *Generating pressure gradient with sloped substrates*

As an aside, we can deduce from (3.12) that if the flux is sufficiently large or the canopy is sufficiently dense, the variation of η can be significant downstream. For a substantial number of experimental work on currents through vegetation, flumes with a flat substrate are tilted so that the pressure gradient along the canopy is driven by gravity rather than surface elevation [see *e.g.* Dunn et al. (1996), Okamoto and Nezu (2009) and Boothroyd et al. (2017)]. The tilting angle of the flume can be adjusted so that water depth would be uniform along the stream. Hence, mathematical analysis can be nicely confined to unidirectional flows with $\mathbf{u} = u(z)\hat{\mathbf{e}}_x$, where x and z denote directions parallel and perpendicular to the tilted flume (Nepf, 2012) respectively. This is further discussed in Chapter 6 when we analyse the instabilities of such flows.

With the insights that we have gained from the steady current problem, we are ready to analyse the combined current-wave problem.

3.4 THE COMBINED CURRENT-WAVE PROBLEM

Suppose we apply the same multiple-scales analysis as in §2.5 in $\alpha \ll 1$ but for the combined current-wave problem. By recalling that x denotes the distance along the macroscopic domain and $(\bar{x}, \bar{z})$ denotes the local coordinates on the wave scale, the leading-order flow in α has the solution

form:

$$\eta_0 = \eta_c(x) + A(x)\cos(\bar{x} - t), \tag{3.17a}$$

$$u_0 = u_c(x) + A(x)\frac{\cosh[k(\bar{z} + \bar{H})]}{\sinh k\bar{H}}\cos(\bar{x} - t), \tag{3.17b}$$

$$w_0 = A(x)\frac{\sinh[k(\bar{z} + \bar{H})]}{\sinh k\bar{H}}\sin(\bar{x} - t), \tag{3.17c}$$

$$p_0 = p_c(x) + A(x)\frac{\cosh[k(\bar{z} + \bar{H})]}{\cosh k\bar{H}}\cos(\bar{x} - t), \tag{3.17d}$$

with the dispersion relation $k(x)\tanh[k(x)\bar{H}(x)] = 1$ (2.28). The additional variables η_c, u_c and p_c define the presence of a current; their expressions would tend to solutions of the steady shallow-water equations (3.15)–(3.16) in the limit $A(x) \to 0$.

We are permitted to consider solutions of the form given in (3.17) since we are seeking for a steady stream and $p_c(x)$ is a constant on the microscale, which would always satisfy the leading-order microscale problem (2.23). We also note that we can treat the vertical current to be zero since the flow always satisfies the leading order free-slip condition $w_0 = 0$ (2.16d) along the substrate.

The main objective here is to derive a system of differential equations in the macroscale variable x for η_c, u_c, and p_c, in addition to A.

3.4.1 *Differential equation for the wave amplitude $A(x)$*

To solve for $A(x)$, we can follow an identical derivation to the one in §2.5 apart from replacing the original pure wave solution (2.27) with the combined flow above (3.17) as the base flow. We derive a solvability condition by applying the same integral identity (2.30) and considering the adjoint solution p_0^* given by (2.31).

With the new base flow, we can verify that all the additional contributions in (2.30) due to the current average to zero over a time period of the wave, apart from a having a new drag contribution in (2.37). In particular, we can derive an equation for the amplitude $A(x)$ in the form of (2.38), namely

$$\frac{\pi^2 A}{\bar{\lambda}k\cosh^2 k\bar{H}}\left[2A(\bar{H} - 1)\frac{\mathrm{d}\left(k\bar{H}\right)}{\mathrm{d}x} - (2k\bar{H} + \sinh 2k\bar{H})\frac{\mathrm{d}A}{\mathrm{d}x}\right] = \mathcal{D} \tag{3.18}$$

with the drag contribution $\mathcal{D}$ expressed in terms of the streamwise velocity of the combined current-wave flow (3.17b) so that

$$\mathcal{D} = \frac{1}{2}\int_{t=0}^{2\pi}\int_{\bar{z}=-\bar{H}}^{-\bar{H}+\bar{h}}\int_{\bar{x}=\bar{X}}^{\bar{X}+2\pi} p_{0\bar{x}}^* u_0\,|u_0|\;\mathrm{d}\bar{x}\mathrm{d}\bar{z}\mathrm{d}t. \tag{3.19}$$

Similar to the pure wave problem, the amplitude decay along the domain is independent of inertial effects *i.e.* M_1 and M_2. In order to solve for $A(x)$ however in this combined problem (3.18), we need to first determine the steady current u_c in u_0 (3.17b).

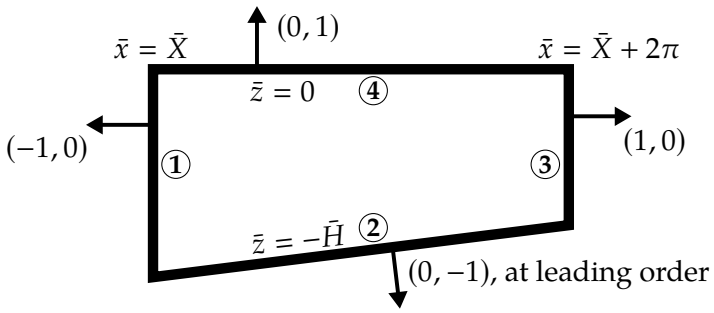

Figure 3.1: Schematic diagram for the periodic cell $\bar{\Omega} = [\bar{X}, \bar{X} + 2\pi] \times [-\bar{H}, 0]$ in the multiple-scales analysis. Notice that the definitions of $\bar{\Omega}$ between this figure and Figure 2.3 are identical—the figures are duplicated for the ease of reference.

3.4.2 *Differential equations for the current variables: u_c, p_c, and η_c*

To solve for the current, distinct from the derivation in §2.5, we do not combine the governing equations and determining the flow field by solving for the pressure field alone. From the original Navier-Stokes equations (2.14), we have on the microscale

$$ku_{1\bar{x}} + u_{0x} + w_{1\bar{z}} = 0, \tag{3.20a}$$

$$u_{1t} + \bar{\gamma}(ku_0u_{0\bar{x}} + w_0u_{0\bar{z}}) = -kp_{1\bar{x}} - p_{0x} - \bar{\lambda}\mathrm{H}(\bar{h} - \bar{H} - \bar{z})F_{\|0}, \tag{3.20b}$$

$$w_{1t} + \bar{\gamma}(ku_0w_{0\bar{x}} + w_0w_{0\bar{z}}) = -p_{1\bar{z}} - \bar{\lambda}\mathrm{H}(\bar{h} - \bar{H} - \bar{z})F_{\perp 0}, \tag{3.20c}$$

with $\mathbf{F} = (F_{\|}, F_{\perp})$ given in (2.16c) and the boundary conditions

$$\boxed{\text{Free-slip}} \quad u_0\bar{H}' + w_1 = 0, \qquad \text{at } \bar{z} = -\bar{H}(x), \tag{3.20d}$$

$$\boxed{\text{Kinematic}} \quad w_1 + \bar{\gamma}\eta_0 w_{0\bar{z}} = \bar{\gamma}ku_0\eta_{0\bar{x}}, \qquad \text{at } \bar{z} = 0, \tag{3.20e}$$

$$\boxed{\text{Dynamic}} \quad p_0 = \eta_0, \qquad \text{at } \bar{z} = 0, \tag{3.20f}$$

$$p_1 + \bar{\gamma}p_{0\bar{z}}\eta_0 = \eta_1, \qquad \text{at } \bar{z} = 0. \tag{3.20g}$$

From the Divergence theorem, we can deduce the identity

$$\int_{\bar{\Omega}} ku_{1\bar{x}} + w_{1\bar{z}}\,\mathrm{d}V = \int_{\bar{\Omega}} \nabla \cdot \begin{pmatrix} ku_1 \\ w_1 \end{pmatrix} \mathrm{d}V = \int_{\partial\bar{\Omega}} \begin{pmatrix} ku_1 \\ w_1 \end{pmatrix} \cdot \mathrm{d}\mathbf{n}_{\bar{\Omega}}, \tag{3.21}$$

with $\mathbf{n}_{\bar{\Omega}}$ being the unit outward normal of the domain $\bar{\Omega}$. By imposing $\bar{\Omega}$ to be the domain defined in Figure 3.1, we can evaluate or simplify the integrals in this identity (3.21) by partitioning $\partial\bar{\Omega}$ into sub-contours labelled in the figure:

(i) Contributions from ① and ③ to the surface integral: they cancel out each other by the periodicity of u_1 in $\bar{\Omega}$.

(ii) Contribution from ④ to the surface integral: by rewriting the integrand via the kinematic condition (3.20e), we can explicitly show that this integral is zero.

(iii) Contribution from ② to the surface integral: we can rewrite the integrand via the free-slip condition (3.20d).

(iv) Volume integral: we can rewrite the integrand $ku_{1\bar{x}} + w_{1\bar{z}}$ in terms of u_{0x} via the incompressibility condition (3.20a).

By evaluating the integrals in the identity above (3.21) explicitly, we derive an equation for mass conservation

$$\bar{H}u_c = Q \tag{3.22}$$

for some constant mean flux Q. In particular, since the wave contributes zero mean flux along the domain, Q is the also flux where $x = 0$ is defined.

Finally, to determine p_c and η_c, we first note that at $\bar{z} = 0$, we have the leading order dynamic condition $p_0 = \eta_0$ (2.23d). Integrating this over time gives $p_c = \eta_c$. Therefore, we only require to solve for p_c to get the full current-wave solution.

We evaluate p_c by integrating the x-momentum equation (3.20b) in $\bar{\Omega}$ and also over a time period of the wave so that

$$\frac{\mathrm{d}p_c}{\mathrm{d}x} = \frac{\mathrm{d}\eta_c}{\mathrm{d}x} = -\frac{\bar{\lambda}}{4\pi\bar{H}} \int_{t=0}^{2\pi} \int_{\bar{z}=-\bar{H}}^{0} \int_{\bar{x}=\bar{X}}^{\bar{X}+2\pi} \mathrm{H}(\bar{h}-\bar{H}-\bar{z}) u_0 |u_0| \, \mathrm{d}\bar{x}\mathrm{d}\bar{z}\mathrm{d}t, \tag{3.23}$$

with u_0 given by (3.17b). As an aside, we found that it is complicated to present the analytical form of the double integral above in (3.23). In particular, since u_0 (3.17b) is the sum of a current and a wave which is $\bar{z}$-dependent, contributions of $|u_0|$ will result in multiple conditional expressions for the double integral.

In summary, we derived a system of equations for the wave amplitude A (3.18)–(3.19), the current velocity u_c (3.22), the current pressure p_c (3.23), and the current-induced free-surface displacement η_c (3.23). We will now compare them against the corresponding expressions in (i) the pure current problem in §3.3, and (ii) the pure wave problem in Chapter 2.

3.4.3 *Reductions to the current-only & wave-only problems*

In the limit when the wave amplitude $A \to 0$, the equations for u_c and η_c (3.22)–(3.23) reduces to the corresponding equations (3.15)–(3.16) for the pure current problem. For $A > 0$ however, to maintain the same current, both the pressure gradient and the free-surface elevation have to be increased in order to balance the momentum loss due to the combined current-wave flow.

On the other hand, in the limit when the mean flux $Q \to 0$, we would get $u_c = 0$, which results in (3.23) reducing to $\mathrm{d}p_c/\mathrm{d}x = \mathrm{d}\eta_c/\mathrm{d}x = 0$. By choosing the definitions of p and z so that $p_c = 0$ and $\eta_c = 0$, we recover the pure wave solution we derived in Chapter 2 with $A(x)$ satisfying the differential equation (2.40).

3.5 CONTRIBUTIONS FROM THE CURRENT IN WAVE DECAY

With the differential equation (3.18) that we have derived for the amplitude decay, it is natural for us to understand how this is affected by the presence

of a current. In this section, we discuss how wave decay is affected by the magnitude and the direction of the current.

Firstly, we have to return to the integral expression for $\mathcal{D}$ in (3.18) *i.e.* (3.19). We note that if the current in the integrand has switched signs, we can show that this is algebraically equivalent to a phase shift by π in the original integrand. Therefore, by integrating the integrand in (3.19) over a period, $\mathcal{D}$ is symmetric between positive and negative currents. However, we are aware that this symmetry in drag can break in reality due to higher-order current-wave interactions such as Doppler shift [see *e.g.* Losada et al. (2016)].

If we assume that the drag coefficient is always constant, we can also show that the wave amplitude would always experience a stronger local decay with a faster current (positive or negative, by symmetry). However, the drag coefficient is known to vary with the flow velocity [in the drag formula (2.14c)]. Hence, waves can experience stronger or weaker local decay compared to the pure wave case in Chapter 2 depending on the velocity ratio between the current and the fluid in the wave – this is experimentally shown by Hu et al. (2014) for positive currents over a domain with constant depth.

In general, the drag coefficient should be predetermined experimentally for different velocity ratios, in addition to the Keulegan-Carpenter number (2.61). However, as commented by the aforementioned authors in this section, there is yet to be standard experimental work or a literature survey on such combined current-wave flows.

3.6 SUMMARY AND DISCUSSION

In this chapter, we extended the multiple-scales analysis on small-amplitude waves in Chapter 2 to combined-wave current flows through rigid vegetation. In particular, we considered an interesting regime where the current is comparable in magnitude to the fluid velocity in the wave. The new analysis in §3.4 indicates that the wave decay, given by (3.18)–(3.19), is coupled to the current (3.22) due to the canopy drag but not vice versa. To further clarify, the velocity profile of the steady current does not asymptotically deviate from the pure current problem (3.15) due to the presence of the wave. However, the pressure gradient (3.23) and the location of the free surface (3.23) interact with the wave via the canopy drag to maintain this current.

We generalised the previous predictions by Hu et al. (2014) by allowing the fluid velocity in the wave to vary in depth. Compared to the predictions by Losada et al. (2016), although we have neglected Doppler shift (3.1), we have justified that this is asymptotically correct when the current is comparable in magnitude to the fluid velocity in the wave. In such cases, the mean free-surface profile would also scale with the wave amplitude. Furthermore, we have generalised their predictions by accounting for the

contribution of the current in drag (3.19) and elevation of the mean free surface along the domain. Finally, analogous to the pure wave predictions in Chapter 2 on the wave amplitude, we can formally establish that the predictions for the flow variables A, u_c, p_c, and η_c hold when both the canopy density and the canopy height vary in the slow scale x.

4 SHALLOW-WATER WAVES THROUGH RIGID VEGETATION

Seriousness is the only refuge of the shallow.

Oscar wilde

SYNOPSIS

In this chapter, we analyse how nonlinear shallow-water waves decay due to rigid vegetation. In particular, we consider how cnoidal waves – periodic solutions of the classic Korteweg-de Vries (KdV) equation – slowly modulate in wave height and waveform as they propagate in space. Our multiple-scales analysis predicts that cnoidal waves experience stronger decay than sinusoidal waves of the same height. The predictions also show good agreement with both numerical simulations and analytical predictions in various sub-limits.

4.1 INTRODUCTION

For a given situation involving wave propagation, if the associated water waves are small in height, then we can analyse them using standard linear (Stokes') wave theory. However, in the situation of coastal flows, there is a myriad of scenarios where it is crucial to study large-amplitude waves, and these require other mathematical tools. For instance, in the case of bores and tsunamis, such phenomena belong to a class of waves where the mean water depth is significantly smaller than the wavelength—these are commonly referred to as *shallow-water* waves.

For shallow-water waves, we can exploit the fact that the fluid velocity is predominantly streamwise. Therefore, other variables of the problem, including the dynamic pressure and the free surface can be expressed in terms of the streamwise velocity, u. The governing equations can be formally reduced to a single nonlinear partial differential equation in u. In addition, we will show in this chapter that for simple configurations, the small-amplitude wave limit of the resultant shallow-water formulation yields sinusoidal waves that are consistent with the (linear) shallow-water approximation considered in Chapter 2. The key, however, is to select

the right balance between the height and the wavelength – both as functions of water depth – and this yields an important family of shallow-water waves—*cnoidal waves*. The investigation of such waves was pioneered by Korteweg and de Vries (1895) and the corresponding governing equation is known as the Korteweg-de Vries (KdV) equation. A detailed survey on its historical development is given by Miles (1981).

Although the KdV equation or cnoidal wave theory, in general, is nonlinear, it forms a rich field of study. Mathematically, the classic KdV equation with appropriate boundary conditions has integrable properties which make it exactly solvable in certain situations (Ablowitz, 2011). Physically, this equation and its variations also arise in problems in optics, plasma physics, and quantum field theory (Wazwaz, 2010). For coastal flows in particular, apart from the Stokes' theory considered in Chapter 2, cnoidal wave theory is widely used to provide analytical insight for water-wave behaviour in the nearshore zone [see review by Hamm et al. (1993)]. The theory is considered to be valid when the depth-to-wavelength ratio is less than about 1/7 (Dingemans, 1997) or 1/5 (Isobe, 1985).

We can primarily divide the field of nonlinear shallow-water waves into the analysis of periodic waves and solitary waves (waves with an infinite period). There are a large number of studies on solitary waves, particularly motivated by specific properties (*e.g.* the preservation of shape in time for the case of solitons) and their wide applicability in modelling *tsunami* [see review by Ablowitz (2011)]. There are few, if any, works on the subject of solitary wave propagation through vegetation. In the absence of vegetation, researchers have studied solitary waves in configurations with sloped substrates (Kaup and Newell, 1978) and capillary effects (Benilov et al., 1993), and we refer the reader to the reviews of Miles (1980) and Johnson (1997). For the case of vegetative flows, the primary source of research has been towards experimental and numerical studies [see Mei et al. 2011; Tang et al. 2013; Maza et al. 2015, 2016]. In this work, we are primarily interested in the less-studied general theory of periodic waves.

Similar to the case of solitary waves, the analysis of periodic shallow-water waves through vegetation has been predominantly numerical or experimental. Here we refer readers to the detailed review by Tang et al. (2017) where the authors note the importance of understanding the precise relationships between (i) wave decay and wave period; and (ii) wave decay and vegetation. Although the recent work by Chang and Liu (2019) has given insight into how higher harmonics are generated as weakly-nonlinear waves decay, there is yet to be a comprehensive theory for quantifying nonlinear wave decay in vegetative flows. The main purpose of this chapter is to use our modelling framework in Chapter 2 to systematically analyse how cnoidal waves evolve in the presence of rigid vegetation.

The structure of this chapter is as follows. Firstly, we will select the appropriate scales and nondimensionalise the governing equations of Chap-

ter 2 for application to shallow-water flow. We then consider a particular balance between the wave height and the wavelength which allows us to derive a modified KdV equation for the free-surface elevation. Then in the absence of the canopy, we discuss how nonlinear cnoidal waves arise as solutions to the classic KdV problem, and we then demonstrate how these waves are reduced to sinusoidal and solitary waves in different limits. Finally, by considering waves which are slowly-modulating due to the presence of vegetation, we perform a multiple-scales analysis on the modified KdV equation to quantify how cnoidal waves decay.

4.2 NONDIMENSIONALISATION

The purpose of this section is to nondimensionalise the 2D fluid momentum equations (2.14) in the shallow-water regime and highlight the different balances involved.

Suppose λ_0 is the dimensional wavelength of the incident wave and H_0 is the dimensional water depth at $x = 0$, we nondimensionalise the fluid variables with the scalings:

$$[x] = \lambda_0,\ [z] = H_0,\ [t] = \frac{\lambda_0}{\sqrt{gH_0}},\ [u] = \sqrt{gH_0},\ [w] = \frac{H_0\sqrt{gH_0}}{\lambda_0}, \qquad [p] = \rho g H_0,\ [\eta] = A_0. \tag{4.1}$$

The main difference here compared to the general depth problem in Chapter 2 [see (2.15)] is that we analyse the dynamics on the wave scale from the start – the timescale is chosen such that it coincides with the time period of small-amplitude waves in the shallow-water limit (2.28). This choice gives us a velocity scale for the streamwise velocity $[u]$. Finally, $[w]$ is chosen via the incompressibility condition.

In summary, we have from (2.14), the dimensionless problem:

$$u_x + w_z = 0, \tag{4.2a}$$

$$u_t + uu_x + wu_z = -p_x - \lambda\left[\frac{1}{2}u|u| + (M_1 + M_2)u_t\right]\mathrm{H}(h - 1 - z), \tag{4.2b}$$

$$\delta^2(w_t + uw_x + ww_z) = -p_z - \delta^2\lambda M_2 w_t, \tag{4.2c}$$

with the boundary conditions

$$\boxed{\text{Free-slip}} \quad w = 0, \qquad \text{at } z = -1, \tag{4.2d}$$

$$\boxed{\text{Kinematic}} \quad w = \epsilon(\eta_t + u\eta_x), \qquad \text{at } z = \epsilon\eta, \tag{4.2e}$$

$$\boxed{\text{Dynamic}} \quad p = \epsilon\eta, \qquad \text{at } z = \epsilon\eta. \tag{4.2f}$$

The key dimensionless parameters for this problem are summarised in Table 4.1. The motivation here is to explore the different balances between ϵ and δ. In particular, the ratio between ϵ and δ^2 is commonly referred to

	Symbol	Expression
Shallow-water aspect ratio	δ	$\dfrac{H_0}{\lambda_0}$
Wave height	ϵ	$\dfrac{A_0}{H_0}$
Ursell number	Ur	$\dfrac{1}{4\pi}\dfrac{\epsilon}{\delta^2} = \dfrac{A_0\lambda_0^2}{4\pi^2 H_0^3}$
Canopy density	λ	$C_D\bar{N}b\lambda_0$
Added mass	M_1	$\dfrac{C_M m}{\rho b C_D \lambda_0}$
Beam inertia (or virtual buoyancy)	M_2	$\dfrac{m}{\rho b C_D \lambda_0}$

Table 4.1: A summary of the dimensionless parameters in the governing equations of flow through a homogenised canopy (4.2). We note that both the canopy density parameter and the inertia parameters λ, M_1 and M_2 in this chapter are scaled with the wavelength rather than the height (see Table 2.1). This is more natural choice for waves with $\delta \ll 1$, when the typical horizontal and vertical excursion of fluid particles in space are not comparable – a more detailed discussion is given in §2.4.

as the *Ursell number* with (Mei, 1992)

$$\mathrm{Ur} = \frac{1}{4\pi^2}\frac{\epsilon}{\delta^2} = \frac{A_0\lambda_0^2}{4\pi^2 H_0^3}. \tag{4.3}$$

The Ursell number quantifies the nonlinearity of the wave. Depending on its magnitude, the governing equations (4.2) should be approximated differently (asymptotically) to incorporate the relevant physical effects.

4.3 Deriving a KdV-type equation for vegetated flow

In the absence of the canopy, it is known that by considering the distinguished limit $\epsilon = \delta^2 \ll 1$ by fixing $[\eta] = A_0 = \delta^2 H_0$ *i.e.* shallow-water waves with a sufficiently small height, the waves have analytical forms satisfying the celebrated Korteweg-de Vries equation—a nonlinear partial differential equation which can be solved exactly (Miles, 1981). In this work, we derive the corresponding governing equation with the presence of a canopy. Once we have the equation, we will also discuss the other two limits of $\epsilon \ll \delta^2$ and $\delta^2 \ll \epsilon$.

The procedures are as follows:

1. We first expand u, w, p and η in powers of ϵ up to $O(\epsilon^2)$.
2. Suppose we also consider a wave that is propagating along the positive x-direction at unit speed. Foreseeing the calculations ahead, if we are to monitor the long-time evolution of the wave, it is natural for us to switch to the travelling frame (ξ, z, τ) (Ockendon and Tayler, 1983), where

$$\xi = x - t \quad \text{and} \quad \tau = \epsilon t. \tag{4.4}$$

For the governing equations (4.2), we can map the derivatives from

the laboratory frame (x, z, t) to the travelling frame (ξ, z, τ) via

$$\frac{\partial}{\partial x} \to \frac{\partial}{\partial \xi} \quad \text{and} \quad \frac{\partial}{\partial t} \to -\frac{\partial}{\partial \xi} + \epsilon \frac{\partial}{\partial \tau}. \tag{4.5}$$

3. We consider the distinguished limit in which the canopy density and the inertia coefficient are

$$\lambda = O(1), \tag{4.6a}$$
$$M = M_1 + M_2 = O(\epsilon) \text{ with } M = \epsilon \bar{M}. \tag{4.6b}$$

We note that $M \sim b/\lambda_0 \ll H_0/\lambda_0 = \delta$ (see Table 4.1). By considering the regime in which $M = O(\epsilon)$, we are considering plants with diameters that are at most comparable to the wave height.

4. By expressing u, w and p in terms of η, we derive a governing equation for η in the limit $\epsilon \to 0$.

Suppose we follow the procedures above, we would find that the leading-order expressions for the fluid variables are trivial *i.e.* $u_0 = w_0 = p_0 = 0$, apart from η_0, which is yet to be determined. For the $O(\epsilon)$ problem, we can use the linearised momentum equations to deduce that

$$u_1 = \eta_0, \tag{4.7a}$$
$$p_1 = \eta_0, \tag{4.7b}$$
$$w_1 = -(z+1)\eta_{0\xi}. \tag{4.7c}$$

For the $O(\epsilon^2)$ problem, we have to incorporate the contributions from the canopy so that

$$u_{2\xi} + w_{2z} = 0, \tag{4.8a}$$
$$u_{2\xi} - u_{1\tau} - u_1 u_{1\xi} - w_1 u_{1z} = p_{2\xi} + \lambda \left(\frac{u_1 |u_1|}{2} - \bar{M} u_{1\xi} \right) \mathrm{H}(h - 1 - z), \tag{4.8b}$$
$$w_{1\xi} = p_{2z}, \tag{4.8c}$$

with

$$\boxed{\text{Free-slip}} \quad w_2 = 0, \qquad \text{at } z = -1, \tag{4.8d}$$
$$\boxed{\text{Kinematic}} \quad w_2 + \eta_0 w_{1z} = -\eta_{1\xi} + \eta_{0\tau} + u_1 \eta_{0\xi}, \qquad \text{at } z = 0, \tag{4.8e}$$
$$\boxed{\text{Dynamic}} \quad p_2 + \eta_0 p_{1z} = \eta_1, \qquad \text{at } z = 0. \tag{4.8f}$$

By substituting the expression for $u_{2\xi}$ in (4.8b) into the incompressibility condition (4.8a), we get

$$u_{1\tau} + u_1 u_{1\xi} + w_1 u_{1z} + p_{2\xi} + \lambda \left(\frac{u_1 |u_1|}{2} - \bar{M} u_{1\xi} \right) \mathrm{H}(h - 1 - z) + w_{2z} = 0. \tag{4.9}$$

The aim here is to express all the terms in the equation above in terms of η_0 and η_1. We can:

(i) Express the velocities, u_1 and w_1, in terms of η_0 via (4.7).

(ii) Express w_2 in terms of η_0 at $z = 0$ via the kinematic condition (4.8e), so that

$$w_2 = 2\eta_0\eta_{0\xi} - \eta_{1\xi} + \eta_{0\tau}. \tag{4.10}$$

(iii) For p_2, we deduce from (4.8c) and the dynamic boundary condition (4.8f) that

$$p_2 = \eta_1 - \left(\frac{z^2}{2} + z\right)\eta_{0\xi\xi}. \tag{4.11}$$

Finally, by integrating the incompressibility condition (4.9) along the depth between $z \in [-1, 0]$ and applying the boundary conditions for w_2, the η_1-dependent terms in (4.9) cancel and we arrive at the modified KdV equation

$$\eta_{0\tau} + \frac{3}{2}\eta_0\eta_{0\xi} + \frac{1}{6}\eta_{0\xi\xi\xi} + \frac{h\lambda}{2}\left(\frac{1}{2}\eta_0|\eta_0| - \bar{M}\eta_{0\xi}\right) = 0. \tag{4.12}$$

From now on, we drop the '0' subscripts and consider

$$\eta_\tau + \frac{3}{2}\eta\eta_\xi + \frac{1}{6}\eta_{\xi\xi\xi} + \frac{h\lambda}{2}\left(\frac{1}{2}\eta|\eta| - \bar{M}\eta_\xi\right) = 0. \tag{4.13}$$

This equation is modified in the sense that we have a $h\lambda$-dependent momentum sink – this term describes the effect of drag and inertia in addition to nonlinear advection ($\eta\eta_\xi$) and dispersion ($\eta_{\xi\xi\xi}$).

We can rewrite the derivatives in the modified KdV equation (4.13) in terms of the laboratory frame (x, z, t) by mapping

$$\frac{\partial}{\partial\xi} \to \frac{\partial}{\partial x} \quad \text{and} \quad \frac{\partial}{\partial\tau} \to \frac{1}{\epsilon}\frac{\partial}{\partial x} + \frac{1}{\epsilon}\frac{\partial}{\partial t}, \tag{4.14}$$

and get

$$\eta_x + \eta_t + \epsilon\left[\frac{3}{2}\eta\eta_x + \frac{1}{6}\eta_{xxx} + \frac{h\lambda}{2}\left(\frac{1}{2}\eta|\eta| - \bar{M}\eta_x\right)\right] = 0 \tag{4.15}$$

Although we have reduced the physical problem of waves propagating through vegetation into a single partial differential equation in η, we will demonstrate in the subsequent sections that this problem is still very rich.

4.4 SOLUTIONS OF THE CLASSIC KDV EQUATION

In the absence of the canopy ($\lambda = 0$), we recover the celebrated KdV equation

$$\eta_\tau + \frac{3}{2}\eta\eta_\xi + \frac{1}{6}\eta_{\xi\xi\xi} = 0. \tag{4.16}$$

By considering travelling wave solutions of the form $\eta = f(\zeta = \xi - V\tau)$, for some wave speed V in the (ξ, τ)–frame, η satisfies

$$-V\frac{\mathrm{d}\eta}{\mathrm{d}\zeta} + \frac{3}{2}\eta\frac{\mathrm{d}\eta}{\mathrm{d}\zeta} + \frac{1}{6}\frac{\mathrm{d}^3\eta}{\mathrm{d}\zeta^3} = 0. \tag{4.17}$$

By solving this ordinary differential equation, we can yield exactly periodic cnoidal waves or solitary waves (with infinite wave period and wavelength). A detailed derivation is given in Dingemans (1997).

4.4.1 *Cnoidal waves*

If we solve for periodic solutions satisfying (4.17), we would get

$$\eta(\zeta) = A\left(B + \operatorname{cn}^2\left[\sqrt{\frac{3A}{4m}}(x - ct)\middle|m\right]\right) \tag{4.18}$$

where A is the dimensionless wave height. Note that such waves are asymmetric about the mean free surface, so we no longer consider the notion of an amplitude. We also have the trough elevation

$$B = B(m) = \frac{1}{m}\left[1 - m - \frac{E(m)}{K(m)}\right]. \tag{4.19}$$

In the expression above, m is the elliptic parameter of the Jacobi elliptic function, cn, and K and E are the complete elliptic integrals of the first and second kind respectively. In particular, we note that cn is even and periodic with period $4K(m)$. Therefore, η is $2K(m)$-periodic with wavelength

$$\Lambda = 4K(m)\sqrt{\frac{m}{3A}}. \tag{4.20}$$

Finally, we can also write the wave speed c in (4.18) in terms of A and m with

$$c = 1 + \frac{\epsilon A}{m}\left[1 - \frac{m}{2} - \frac{3}{2}\frac{E(m)}{K(m)}\right]. \tag{4.21}$$

Examples of cnoidal waves are given in Figure 4.1. To avoid ambiguity in the different conventions on elliptic functions, here we state that all of the elliptic functions in this work are parametrised by the elliptic parameter m, rather than the elliptic modulus (Abramowitz and Stegun, 1948). In the small-amplitude limit where we take $\epsilon, m \to 0$, cnoidal waves would reduce to sinusoidal waves. We will demonstrate this in the next section.

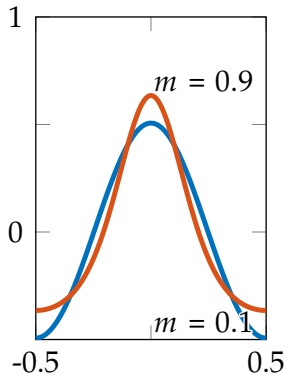

Figure 4.1: Examples of cnoidal waves with unit wave height over one wavelength – the horizontal domain has been normalised to unity. Cnoidal waves have narrow crests and wide troughs: this asymmetry is quantified by the elliptic parameter m. We note that this is distinct from the elliptic modulus k, with $m = k^2$.

4.4.2 *Small-amplitude shallow-water waves*

We derived the modified KdV equation (4.15) in §4.3 by considering the limit where $\epsilon = \delta^2 \ll 1$ (see Table 4.1). If we linearise the equation (4.15) in $\eta \ll 1$, which corresponds to taking the small-Ursell number limit $\epsilon \ll \delta^2 \ll 1$, we would get at leading order

$$\eta_x + \eta_t + \frac{\epsilon}{6}\eta_{xxx} = 0. \tag{4.22}$$

By considering solutions in the form of sinusoidal waves $\eta = A\cos(kx - \omega t)/2$, the dimensionless wave velocity satisfies

$$\frac{\omega}{k} = 1 - \frac{\epsilon}{6}k^2. \tag{4.23}$$

Hence, the corresponding dimensional wave velocity for such dispersive sinusoidal waves are $\sqrt{gH_0}(1 - k^2H_0^2/6)$—this is consistent with the classic dispersion relation (2.28) of Stokes waves in the $kH_0 \ll 1$ limit up to $O((kH_0)^2)$ (Ockendon and Tayler, 1983).

4.4.3 *Solitary waves*

We note that solitary waves are special cases of cnoidal waves by taking the limit $m \to 1$, where $K(m) \to \infty$ and $E(m) \to 1$ in (4.18)–(4.21) (Svendsen and Hansen, 1978). In this limit, we get a one-parameter family of solitary waves in A with

$$\eta(\zeta) = A\,\mathrm{sech}^2\left(\sqrt{\frac{3A}{4}}\zeta\right) = A\,\mathrm{sech}^2\left[\sqrt{\frac{3A}{4}}\left[x - \left(1 + \frac{\epsilon A}{2}\right)t\right]\right]. \tag{4.24}$$

An example of a solitary wave is given in Figure 4.2. The same result can be obtained by solving for (nontrivial) solutions of (4.17) where η and its derivatives in ζ tend to zero as $\zeta \to \pm\infty$. Physically, this corresponds to solving for solitary waves with the water being still at the far-field. Such waves have been studied extensively due to their simple analytical form and also their unique properties when they collide with one another [see Ablowitz (2011) and references therein].

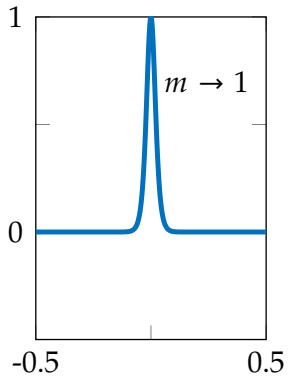

Figure 4.2: An example of a solitary wave with unit wave height: the free surface is undisturbed at the far-field. The horizontal domain here has been rescaled to coincide with the $m \to 1$ limit for cnoidal waves in Figure 4.1.

4.4.4 *Large-amplitude shallow-water waves*

As an aside, we briefly discuss why we have considered waves with the balance $\epsilon = \delta^2$, in addition to the shallow-water simplification ($\delta \ll 1$).

Suppose we have expanded the variables of the original governing equations (4.2) in powers of δ in the limit $\delta, \epsilon \ll 1$, but with $\delta^2 \ll \epsilon$ *i.e.* in the large-Ursell number limit. In the absence of the canopy, we would then derive a standard set of shallow-water equations instead of the KdV equation (4.16). In this regime, solutions would be *simple waves* of the form

$$u_0 = F\left[\bar{x} - \left(\frac{3}{2}u_0 - c\right)t\right] \tag{4.25}$$

for any arbitrary F and constant c, with the Riemann invariant $u_0 + 2\sqrt{\eta_0 - 1} = 2c$ being constant everywhere. The issue here is that for any non-constant F, u_0 is known to become multi-valued in finite time (Ockendon and Tayler, 1983). Since we do not consider breaking waves in this work, we confine our analysis to waves with small and intermediate heights.

4.5 A REVIEW ON SOLVING MODIFIED KDV EQUATIONS

In this section, beyond the context of vegetative flows, we discuss which, and more importantly, how various modified KdV equations have been solved by researchers—a detailed review is given by El and Hoefer (2016).

Nonlinear wave modulation theory, or the *Whitham's method*, is first introduced by Whitham (1965a,b), which involve averaging either conservation laws or the Lagrangians of the governing equations. Meanwhile, the nonlinear multiple-scales analysis approach (Kuzmak, 1959) was considered by

Luke (1966), in the context of obtaining asymptotic solutions for modified wave equations. This approach has been extended by Myint and Grimshaw (1995) to solve modified KdV equations which involve linear, viscous, and boundary-layer damping respectively.

Other methods include (i) considering an energy balance on how solitary waves Miles (1983a) and cnoidal waves (Miles, 1983b) vary due to drag and depth-variation [which is analogous to the derivations in Dalrymple et al. (1984) and Mendez and Losada (2004) for linear waves]; and (ii) *inverse scattering transforms* for particular integrable systems.

In terms of incorporating quadratic drag, El et al. (2007) considered substrate roughness in their KdV model, which is mathematically equivalent to neglecting inertia ($\bar{M} = 0$) in (4.15), and setting the effective vegetation density $\epsilon h \lambda$ to be a spatially-dependent roughness parameter [see *e.g.* Whitham (1974) on how roughness is modelled with Chezy's law]. However, the authors utilised the (version of) Whitham's method, which involves both Riemann invariants and so-called finite-gap integration theory. In this work, we solve for asymptotic solutions of (4.15) with inertia using a more direct and generalisable multiple-scales framework, which involves the same machinery as in the previous chapters.

4.6 MODIFIED KDV EQUATION AND LINEAR-WAVE DECAY

For waves with sufficiently small height so that they can be asymptotically approximated as sinusoidal waves, the modified KdV equation (4.13) should predict the same height decay as (2.50) in the shallow-water limit. As a check, we formally consider a multiple-scale analysis on the modified KdV equation (4.15) in the limit where $\epsilon \ll \epsilon h \lambda \ll 1$. A schematic on the limits taken is shown in Figure 4.3.

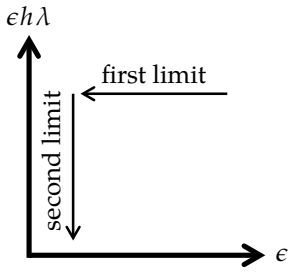

Figure 4.3: Schematic on the limits taken for the analysis on waves in §4.6.

Firstly, as in §4.4.2, we can simplify (4.15) in this limit and get

$$\eta_x + \eta_t + \epsilon \frac{h\lambda}{2} \left(\frac{1}{2} \eta |\eta| - \bar{M} \eta_x \right) = 0. \tag{4.26}$$

Suppose we then consider a multiple-scales expansion in space on $\eta = \eta(x, \chi, t)$ in powers of $\epsilon h \lambda \ll 1$ with x being the fast scale and $\chi = \epsilon h \lambda x$ being the slow domain scale. By rewriting the derivatives in x in (4.26) in terms of (x, χ) [see (2.20) for the precise mapping] and expanding η in powers of $\epsilon h \lambda$, η_0 satisfies the linear equation

$$\eta_{0x} + \eta_{0t} = 0. \tag{4.27}$$

By considering the momentum equations (4.7) and choosing the initial phase, we can deduce that for monochromatic waves,

$$\eta_0 = \frac{A(\chi)}{2} \cos \left[\frac{2\pi}{T} (x - t) \right], \tag{4.28}$$

where T is a given time period, and $A(\chi)$ is the dimensionless wave height that is yet to be determined. Note that we have again defined A as the wave height rather than the amplitude for the ease of comparison with cnoidal waves in the upcoming sections. This is due to the asymmetry of cnoidal waves about the mean water level. We will use this convention for the remainder of this chapter.

Analogous to the multiple-scales analysis in §2.5, we solve for A by considering the $O(\epsilon h\lambda)$ problem, where η_1 satisfies

$$\eta_{1x} + \eta_{1t} + \eta_{0\chi} + \frac{1}{2}\left(\frac{1}{2}\eta_0|\eta_0| - \bar{M}\eta_{0x}\right) = 0. \tag{4.29}$$

Suppose we consider time-harmonic solutions for η, so that η and its derivatives are periodic in time with period T. By multiplying the equation above by η_0 and integrate both sides of the equation in $x \in [0, T]$ and $t \in [0, T]$, we can show from integration by parts that the η_1-dependent contributions cancel each other out via (4.27). This simplifies to an equation for η_0 namely,

$$\int_{t=0}^{T}\int_{x=0}^{T} \eta_0\eta_{0\chi}\,\mathrm{d}x\mathrm{d}t = -\frac{1}{4}\int_{t=0}^{T}\int_{x=0}^{T} \eta_0^2|\eta_0|\,\mathrm{d}x\mathrm{d}t \tag{4.30}$$

which can be reduced to the differential equation

$$\frac{\mathrm{d}A}{\mathrm{d}\chi} = \frac{1}{\epsilon h\lambda}\frac{\mathrm{d}A}{\mathrm{d}x} = -\frac{1}{3\pi}A^2. \tag{4.31}$$

Up to scaling, we can verify that this decay rate is consistent with our predictions in Chapter 2 for linear waves in the shallow-water limit (2.50). Furthermore, this can be integrated to give

$$A = \left[1 + \frac{\epsilon h\lambda}{3\pi}x\right]^{-1}. \tag{4.32}$$

4.7 TIME-HARMONIC WAVES THROUGH VEGETATION

After considering the small-amplitude limit, we would like to generalise the multiple-scales analysis in the previous section for the height decay of cnoidal waves. Recall that in the laboratory frame, $\eta = \eta(x, t)$ satisfies

$$\eta_x + \eta_t + \epsilon\left[\frac{3}{2}\eta\eta_x + \frac{1}{6}\eta_{xxx} + \frac{h\lambda}{2}\left(\frac{1}{2}\eta|\eta| - \bar{M}\eta_x\right)\right] = 0. \tag{4.33}$$

As in the multiple-scales analysis in §4.6, we first let $\tilde{\epsilon} = \epsilon h\lambda \ll 1$ be the small parameter and

$$\chi = \tilde{\epsilon}x \tag{4.34}$$

to be the slow domain variable. By rewriting the modified KdV equation in terms of χ and t, we get

$$\eta_t + \tilde{\epsilon}\eta_\chi + \epsilon\left(\frac{3\tilde{\epsilon}}{2}\eta\eta_\chi + \frac{\tilde{\epsilon}^3}{6}\eta_{\chi\chi\chi}\right) + \frac{\tilde{\epsilon}}{2}\left(\frac{1}{2}\eta|\eta| - \tilde{\epsilon}\bar{M}\eta_\chi\right) = 0. \tag{4.35}$$

Due to the frequency modulation in this problem, we introduce a new fast wave variable,

$$\bar{\chi} = \frac{\Phi(\chi)}{\tilde{\epsilon}} \tag{4.36}$$

for some function Φ that will be chosen such that η is spatially-periodic in $\bar{\chi}$ with constant period T. The expression for T will be specified later. We consider a multiple-scales expansion in space on $\eta = \eta(\bar{\chi}, \chi, t)$.

By rewriting the derivatives in χ in (4.35) in terms of $(\bar{\chi}, \chi)$ and expanding η in powers of $\tilde{\epsilon}$, η_0 satisfies a rescaled KdV equation

$$\eta_{0t} + \Phi'\eta_{0\bar{\chi}} + \epsilon\left[\frac{3}{2}\Phi'\eta_0\eta_{0\bar{\chi}} + \frac{1}{6}(\Phi')^3\eta_{0\bar{\chi}\bar{\chi}\bar{\chi}}\right] = 0. \tag{4.37}$$

Here, we used primes ($'$) to denote $\mathrm{d}/\mathrm{d}\chi$. If we scale this problem in terms of the original KdV equation (4.15) and take

$$\Phi'(\chi) = \frac{1}{c} = \left(1 + \frac{\epsilon A}{m}\left[1 - \frac{m}{2} - \frac{3}{2}\frac{E(m)}{K(m)}\right]\right)^{-1} \tag{4.38}$$

with the wave speed c given by (4.21), we have the leading-order solution form [see (4.18)]

$$\eta_0 = A\left(B + \mathrm{cn}^2\left[\frac{2K(m)}{T}(\bar{\chi} - t)\middle| m\right]\right) \tag{4.39}$$

for a cnoidal wave with trough elevation B given by (4.19) and time period T given by

$$T = 4K(m)\sqrt{\frac{m}{3A}}\left(1 + \frac{\epsilon A}{m}\left[1 - \frac{m}{2} - \frac{3E(m)}{2K(m)}\right]\right)^{-1}. \tag{4.40}$$

For a given value of ϵ, this cnoidal wave is determined by two parameters, A and m. We allow these two parameters to vary with the slow variable χ so that $A = A(\chi)$ and $m = m(\chi)$.

By considering time-harmonic solutions, we fix the time period. Hence, T is also the initial time period. Suppose $A(\chi = 0) = A_0$ and $m(\chi = 0) = m_0$, then

$$T = 4K(m_0)\sqrt{\frac{m_0}{3A_0}}\left(1 + \frac{\epsilon A_0}{m_0}\left[1 - \frac{m_0}{2} - \frac{3E(m_0)}{2K(m_0)}\right]\right)^{-1}. \tag{4.41}$$

Together with (4.40), we deduced a relationship between $m(\chi)$ and $A(\chi)$. We note that A_0 here is distinct from the dimensional scaling of η (4.1), with the latter being fixed by considering the balance $\epsilon = \delta^2$. By considering the higher-order contributions, we can use the relations (4.40)–(4.41) to determine A.

For the $O(\tilde{\epsilon})$ problem, η_1 satisfies

$$\begin{aligned}\eta_{1t} + \Phi'\eta_{1\bar{\chi}} + \eta_{0\chi} + \frac{\epsilon}{6}\left[(\Phi')^3\eta_{1\bar{\chi}\bar{\chi}\bar{\chi}} + 3\left((\Phi')^2\eta_{0\bar{\chi}\bar{\chi}\chi} + \Phi'\Phi''\eta_{0\bar{\chi}\bar{\chi}}\right)\right] \\ + \frac{3\epsilon}{2}\left[\eta_0\eta_{0\chi} + \Phi'\left(\eta_0\eta_1\right)_{\bar{\chi}}\right] = -\frac{1}{4}\eta_0|\eta_0| + \frac{\bar{M}}{2}\Phi'\eta_{0\bar{\chi}}.\end{aligned} \tag{4.42}$$

For ease of reference:

x is the original distance of propagation

χ is the slow variable

$\bar{\chi}$ is the fast variable

We can multiply both sides of this equation by η_0 and integrate in $\bar{\chi}$ and t over $[0, T]$. By imposing the periodicity of η_0 and η_1, we can show with integration by parts that the η_1-dependent terms cancel each other out via the leading order KdV equation for η_0 (4.37). We also have no contributions from the $\bar{M}$-dependent inertia term over one period. Therefore, we have the integral equation

$$\int_{t=0}^{T}\int_{\bar{\chi}=0}^{T}\left\{\eta_0\eta_{0\chi}+\frac{3\epsilon}{2}\eta_0^2\eta_{0\chi}+\frac{\epsilon}{2}\left[(\Phi')^2\eta_0\eta_{0\bar{\chi}\bar{\chi}\chi}+\Phi'\Phi''\eta_0\eta_{0\bar{\chi}\bar{\chi}}\right]\right\}\,\mathrm{d}\bar{\chi}\mathrm{d}t = -\frac{1}{4}\int_{t=0}^{T}\int_{\bar{\chi}=0}^{T}\eta_0^2|\eta_0|\,\mathrm{d}\bar{\chi}\mathrm{d}t. \tag{4.43}$$

The multiple-scales predictions are valid when the wavelength (4.20) is much smaller than the decay scale $(\epsilon h\lambda)^{-1}$ in space.

The solvability condition (4.43) can be used to obtain values of the wave height A as follows. First, we substitute η_0 in (4.40) into the solvability condition and note that the four integrals on the left-hand-side involve $\mathrm{d}A/\mathrm{d}\chi$. We also express m in terms of A via (4.40), where

$$\frac{\mathrm{d}m}{\mathrm{d}\chi}=\frac{\mathrm{d}m}{\mathrm{d}A}\frac{\mathrm{d}A}{\mathrm{d}\chi}. \tag{4.44}$$

Finally we obtain an autonomous differential equation for A given by the general form

$$\frac{\mathrm{d}A}{\mathrm{d}\chi}=f(A,\epsilon,T(\epsilon,A_0,m_0)), \tag{4.45}$$

for some function f. For a given wave with a known wavelength and frequency, which fixes ϵ and T, we sample $\mathrm{d}A/\mathrm{d}\chi$ for different values of A (*e.g.* using *Mathematica*). Once numerical values of (4.45) are tabulated, we then solve for $A(\chi) = A(\epsilon h\lambda x)$ using a finite-difference differential equations solver.

4.7.1 *Small-amplitude approximation*

Note that the above multiple-scales procedure is dependent upon the parameter $\tilde{\epsilon} = \epsilon h\lambda \to 0$. Before we present our predictions from solving (4.43), we take the additional small-amplitude approximation of $\epsilon \to 0$. Neglecting the integrals in (4.43) that are $O(\epsilon)$, we have a reduced integral equation

$$\int_{t=0}^{T}\int_{\bar{\chi}=0}^{T}\eta_0\eta_{0\chi}\,\mathrm{d}\bar{\chi}\mathrm{d}t = -\frac{1}{4}\int_{t=0}^{T}\int_{\bar{\chi}=0}^{T}\eta_0^2|\eta_0|\,\mathrm{d}\bar{\chi}\mathrm{d}t. \tag{4.46}$$

This is the analogue of the integral equation (4.30) for small-amplitude waves (which was derived by first taking the linear KdV limit with $\epsilon \to 0$ and subsequently $\epsilon h\lambda \to 0$). A schematic on the limits taken in the present analysis is given in Figure 4.4.

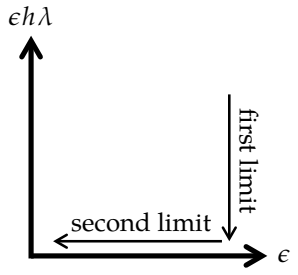

Figure 4.4: Schematic on the limits taken for the analysis on waves in §4.7.1.

For additional verification, we may further take the limit that the elliptic parameter, $m \to 0$. Taylor expanding the functions B (4.19) and cn in η_0 (4.39) in powers of m give (Abramowitz and Stegun, 1948)

$$B(m) = -\frac{1}{2} + O(m), \tag{4.47a}$$

$$\mathrm{cn}^2[\chi|m] = \frac{1}{2} + \frac{1}{2}\cos\left[\frac{\pi}{K(m)}\chi\right] + O(m). \tag{4.47b}$$

Together, they give

$$\eta_0 = \frac{A}{2}\cos\left[\frac{2\pi}{T}(\bar{\chi} - t)\right] + O(m). \tag{4.48}$$

Finally, by substituting this expression into the reduced integral equation (4.46), we recover the same solvability condition $\mathrm{d}A/\mathrm{d}\chi = -A^2/(3\pi)$ (4.31).

4.7.2 *Numerical predictions on the wave height*

In this section, we shall describe the wave height A as given by our differential equation (4.45), and discuss its decaying properties, particularly in relation to two key processes:

(i) increasing wave nonlinearity (or dimensional wave height) by increasing ϵ; and

(ii) increasing time period T by increasing the initial ellipticity m_0. Notice that the limit of $m_0 \to 1$ corresponds to the limit of a localised solitary wave.

Results with changing ϵ are presented in the grouping of Figure 4.5a while results with changing m_0 are presented in the grouping of Figure 4.5b. A key observation related to the primary subfigure of both groups is that the numerical results deviate from the single theoretical curve for small-amplitude waves (shown as a black dashed line).

For a given point in the rescaled domain, $\epsilon h \lambda x$, increasing the wave nonlinearity ϵ increases the wave decay; this is compared to the minimum wave decay associated with linear waves in (4.31). We may observe this trend via the inset of Figure 4.5a where we see curves with larger ϵ corresponding to larger $|\mathrm{d}A/\mathrm{d}x|$. In particular, we note that in the limit $A \to 0$,

$$\frac{\mathrm{d}A}{\mathrm{d}x} \propto -A^2, \tag{4.49}$$

where the constant of proportionality depends on ϵ and can be read off by the y-intercepts of the figure inset. A similar trend is observed for all of m_0 seen in Figure 4.5b. To mathematically explain these observations, we return to our solvability condition (4.43).

For $\epsilon,\ A \ll 1$, our numerical results suggest that the main contributions to the solvability condition (4.43) arise from the $\eta_0\eta_{0\chi}$ and $\eta_0\eta_{0\bar{\chi}\bar{\chi}\chi}$ terms. We note that the advective term, $\eta_0^2\eta_{0\chi}$, is asymptotically small (in comparison

(*a*) varying ϵ

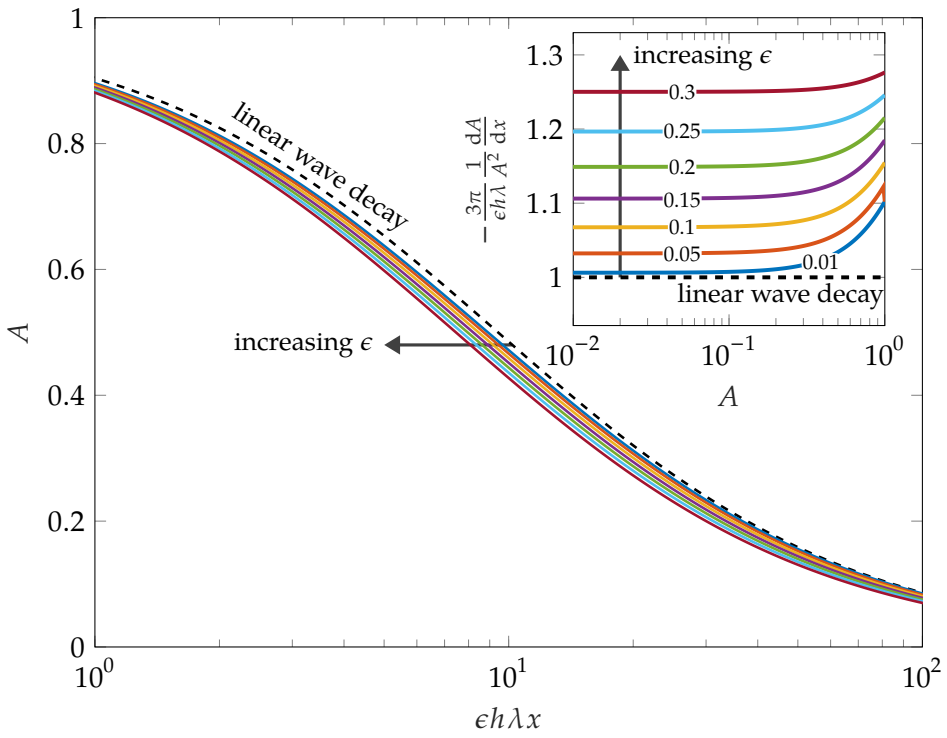

(*b*) varying m_0

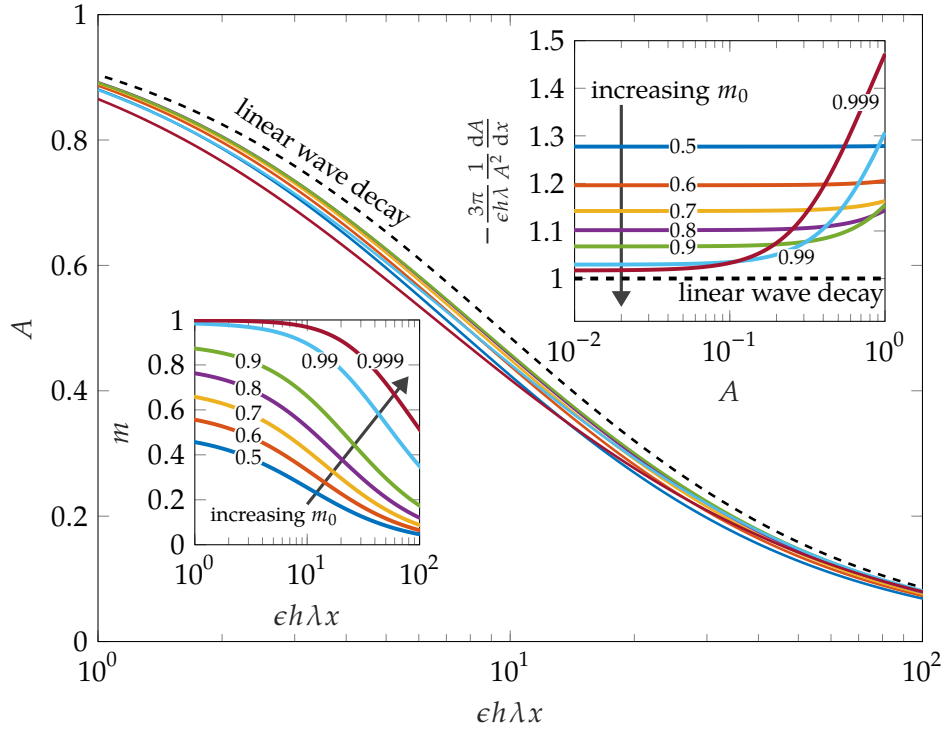

Figure 4.5: Time-averaged wave height of time-harmonic cnoidal waves vs. scaled distance of propagation, obtained by solving (4.43) with initial height $A_0 = 1$. The dashed lines indicate the small-amplitude prediction $A = [1 + \epsilon h\lambda x/(3\pi)]^{-1}$ (4.32). The top-right inset of each subfigure plots specific ratios expected to tend to unity for linear decay via (4.31). (*a*) The effect of increasing the nonlinearity ϵ (varying colours) for waves with initial ellipticity $m_0 = 0.9$. (*b*) The effect of increasing the initial ellipticity $m = m_0$ (varying colours) for waves with $\epsilon = 0.1$. The bottom-left inset plots the corresponding evolution of m along the domain. Below this caption, we also have the initial waveform for each prediction curve over one wavelength where the horizontal domain has been normalised to unity.

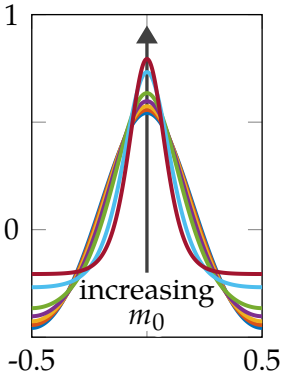

with $\eta_0\eta_{0\chi}$) when $A \ll 1$. Similarly, since $\Phi' = 1 + O(\epsilon A)$ from (4.38), we see that the dispersive term, $\eta_0\eta_{0\tilde{\chi}\tilde{\chi}}$, is $O(\epsilon^2)$. Notice as well that as $A \to 0$, the corresponding elliptic parameter $m \to 0$ by the relation (4.40) – this is verified via the inset in the lower-left of Figure 4.5b.

We have also shown from (4.48) that for $m \ll 1$, the wave is approximately sinusoidal with $\eta_0 \sim A\cos[2\pi(\bar{\chi}-t)/T]/2$. Suppose we substitute this into the solvability condition (4.43), since $\eta_{0\bar{\chi}\bar{\chi}} \sim -(2\pi/T)^2\eta_0$, the solvability condition would reduce to

$$\left[1-\frac{\epsilon}{2}\left(\frac{2\pi}{T}\right)^2\right]\int_{t=0}^{T}\int_{\bar{\chi}=0}^{T}\eta_0\eta_{0\chi}\,\mathrm{d}\bar{\chi}\mathrm{d}t \sim -\frac{1}{4}\int_{t=0}^{T}\int_{\bar{\chi}=0}^{T}\eta_0^2|\eta_0|\,\mathrm{d}\bar{\chi}\mathrm{d}t. \quad (4.50)$$

Using the linear-wave approximation (4.31) we thus deduce that

$$-\frac{3\pi}{A^2}\frac{\mathrm{d}A}{\mathrm{d}\chi} = -\frac{3\pi}{A^2}\frac{1}{\epsilon h\lambda}\frac{\mathrm{d}A}{\mathrm{d}x} \sim 1+\frac{\epsilon}{2}\left(\frac{2\pi}{T}\right)^2, \quad (4.51)$$

and this provides the y-intercept values in the inset of Figure 4.5a. In particular, if we normalise the decay rates $\mathrm{d}A/\mathrm{d}x$ in Figure 4.5 with the approximation above relation, we would get a very good collapse, compared with the small-amplitude normalisation (4.31) in the current insets.

Finally, let us consider the limit of $m_0 \to 1$. Based on the inset at the top-right of Figure 4.5b, we conclude that larger values of m_0 are associated with larger values of $|\mathrm{d}A/\mathrm{d}x|$ [this dependence is difficult to see by visual inspection of the graph of $A(x)$ but is highlighted in the upper-right inset]. However, examining the lower-left inset of Figure 4.5b, we note that as $m_0 \to 1$, we also have $m \to 1$ at fixed points in the domain. Thus the limit of $m_0 \to 1$ is associated with the rapid decay of wave height, but for a wave that largely preserves its form.

We find that the qualitative behaviours derived above are in good agreement with both numerical simulations and experimental results by Huang et al. (2011) and Maza et al. (2015); however, in order compare quantitatively, it is more convenient to study temporal decay rates in t, rather than spatial decay in the domain, x. In the next section, we shall perform the analogous temporal multiple-scales analysis; we later return to justify how spatial and temporal analyses are compatible in the limit of solitary waves.

4.8 SPATIALLY-PERIODIC WAVES THROUGH VEGETATION

In theory, we can compare our time-harmonic multiple-scales predictions (4.43) against full numerical simulations. However, this requires a wave flume where a cnoidal wave is specified at the source, and an outlet condition is specified at the far boundary of the flume. The resultant simulations must then be analysed via the extracted wave heights, as functions of the distance of propagation, after all transients have decayed (see the wave flume setup in §2.8 for large-scale simulations).

Another approach in verifying the general multiple-scales framework is to consider spatially-periodic solutions. By deriving the corresponding multiple-scales predictions for such waves where now the wave height is

given by $A = A(t)$, we can compare with solutions of the modified KdV equation (4.13) in a periodic domain. Furthermore, this allows us to predict the decay of solitary waves in time.

In this section, we adapt the multiple-scales analysis in §4.7 and derive the wave height of spatially-periodic waves. We then present the method for solving the modified KdV equation numerically and verify our predictions.

4.8.1 *Multiple-scales predictions for spatially-periodic waves*

This analysis asymptotically predicts how cnoidal waves decay over a long timescale rather than over the macroscopic domain. For this, we consider a multiple-scales analysis in time. Since the derivation closely follows the one in §4.7 for time-harmonic waves, we will only outline the key assumptions and procedures.

With $\tilde{\epsilon} = \epsilon h\lambda \ll 1$ being the small parameter, we let $\mathcal{T} = \tilde{\epsilon}t$ be the slow-time variable and $\bar{\mathcal{T}} = \Phi(\mathcal{T})/\tilde{\epsilon}$ to be the fast-time variable. The function Φ will be chosen such that η is periodic in $\bar{\mathcal{T}}$ with constant period Λ. The expression for Λ will be specified later.

Considering $\eta = \eta(x, \bar{\mathcal{T}}, \mathcal{T})$, we find from (4.13) that η satisfies

$$\Phi'\eta_{\bar{\mathcal{T}}} + \tilde{\epsilon}\eta_{\mathcal{T}} + \eta_x + \epsilon\left[\frac{3}{2}\eta\eta_x + \frac{1}{6}\eta_{xxx} + \frac{h\lambda}{2}\left(\frac{1}{2}\eta|\eta| - \bar{M}\eta_x\right)\right] = 0. \tag{4.52}$$

We write η above as a series expansion in powers of $\tilde{\epsilon}$ and consequently, the leading-order η_0 satisfies a scaled KdV equation. This yields

$$\eta_0 = A\left(B + \mathrm{cn}^2\left[\frac{2K(m)}{\Lambda}(x - \bar{\mathcal{T}})\middle| m\right]\right), \tag{4.53}$$

where A, B, and m are all functions of $\mathcal{T}$. The above corresponds to a cnoidal wave with trough elevation, B, and wavelength, Λ, given by (4.19) and (4.20). We have chosen $\Phi' = c$ with c given by (4.21). Furthermore, since η_0 is assumed to be spatially periodic, Λ is also the time period *i.e.* $\Lambda = T$ and we assume that it is constant.

Continuing the multiple-scales procedure, we multiply the governing equation for η_1 by η_0 and integrate over time, $\bar{\mathcal{T}}$, and space, x, over one period of both. This yields the solvability condition

$$\int_{\bar{\mathcal{T}}=0}^{T}\int_{x=0}^{T}\eta_0\eta_{0\mathcal{T}}\,\mathrm{d}x\mathrm{d}\bar{\mathcal{T}} = -\frac{1}{4}\int_{\bar{\mathcal{T}}=0}^{T}\int_{x=0}^{T}\eta_0^2|\eta_0|\,\mathrm{d}x\mathrm{d}\bar{\mathcal{T}}. \tag{4.54}$$

Notice that different from the solvability condition for time-harmonic solutions in (4.43), the above prediction is independent of ϵ. As in §4.7, we can impose (4.54) in the following way: the analytical forms of η_0 are substituted into the expression, including all the necessary constants. The dependence on the unknown A and its derivative is manually extracted, and this allows us to sample $\mathrm{d}A/\mathrm{d}\mathcal{T}$ as a function of A, for given ϵ and $T(A_0, m_0)$. This is done via *Mathematica*. Once the derivative relation is tabulated, we then solve for $A(\mathcal{T}) = A(\epsilon h\lambda t)$.

For ease of reference:

- t is time
- $\mathcal{T}$ is the slow variable
- $\bar{\mathcal{T}}$ is the fast variable

4.8.2 *Limiting cases: sinusoidal waves and solitary waves*

For small-amplitude waves, we recall from §4.7.1 that the $m \to 0$ approximation of η_0 gives sinusoidal waves (4.48). Notice that if this is substituted into (4.54), then we obtain

$$A_{\text{lin}} \sim \left[1 + \frac{\epsilon h \lambda}{3\pi} t\right]^{-1}. \tag{4.55}$$

The above approximation indeed matches the amplitude expression (4.32) in §4.4.2 with x replaced by t, which was derived by first taking the $\epsilon \to 0$ limit and then subsequently applying the multiple-scales limit [see Figure 4.3]. Notice that although (4.32) is derived by assuming that slow decay in space, the same prediction applies for slow temporal decay since space x and time t are interchangeable for linear waves.

In the opposite limit in which $m \to 1$, we can evaluate (4.54) analytically for solitary waves with η_0 given by (4.24), which results in

$$A_{\text{sol}} \sim \left[1 + \frac{4\epsilon h \lambda}{15} t\right]^{-1}. \tag{4.56}$$

Formally, notice that the above multiple-scales approximation for the wave height has assumed that the time period, T, of a cnoidal wave (4.20) is fixed and $O(1)$. In particular, we must assume that it is much less than the decay timescale $(\epsilon h \lambda)^{-1}$. As $m \to 1$ however, we obtain from (4.20)

$$T = 4\sqrt{\frac{m}{3A}}\left[\log 4 - \frac{1}{2}\log(1-m) + O(1-m)\right] \to \infty. \tag{4.57}$$

Hence, the prediction (4.56) is beyond the considered regime and multiple-scales framework. Indeed, we will later demonstrate that (4.56) still provides a reasonable approximation to the numerical simulations.

Finally, comparing the decay rates $\mathrm{d}A/\mathrm{d}t$ between the two opposite limits, we notice that in both cases

$$\frac{\mathrm{d}A}{\mathrm{d}t} \propto -A^2 \tag{4.58}$$

but the decay rate for solitary waves (4.56) is $4\pi/5$-times larger than that of sinusoidal waves (4.55).

With the asymptotic insights (4.55)–(4.56) that we have derived above, we are now ready to numerically investigate the full problem and determine how (spatially-periodic) cnoidal waves decay for intermediate values of m.

4.8.3 *Numerical strategy*

In the absence of vegetation – since it is a classic problem – there are various established strategies in solving the KdV equation (4.16); this includes the

application of Fourier transforms [see Taha and Ablowitz (1984) and references therein] or spectral decompositions (Montanelli and Nakatsukasa, 2018). In general, the chosen numerical scheme can often suffer from numerical instabilities or artificial diffusion.

In this work, we solve the modified KdV equation by adapting a discontinuous Galerkin scheme developed by Jackaman and Pryer (2019). We have modified their finite-element scheme such that it solves the reformulated problem

$$W = \eta + \frac{3}{4}\eta^2 + \frac{1}{6}\eta_{xx} + \frac{h\lambda}{2}\bar{M}\eta_x, \tag{4.59a}$$

$$\eta_t + W_x + \frac{h\lambda}{4}\eta|\eta| = 0. \tag{4.59b}$$

Due to the choice of W, this scheme has desirable conservative and stability properties for the homogeneous KdV equation [see Jackaman and Pryer (2019) for further details]. Thus, we can accurately capture both the height of the wave crest and the location of the crest. We implement this numerical scheme in `Firedrake`—a Python-based finite-element library [see Balay et al. (1997); Dalcin et al. (2011); Rathgeber et al. (2016); Balay et al. (2019) for further details and source code].

We initialise the problem by considering a cnoidal wave (4.18), with unit wave height $A = A_0 = 1$, an elliptic parameter m_0 and ϵ. Since the wavelength, $\Lambda = \Lambda_0$, is considered fixed to its initial value, calculated via (4.20). The solution is assumed to be spatially-periodic, we solve on a periodic domain, $x \in [0, \Lambda_0]$. Once numerical values of $\eta(x, t)$ are obtained, we shall define the wave height, $A(t)$, by the maximal crest-to-trough distance in $[0, \Lambda_0]$. We observe the evolution of this wave height, which will be the main measure of comparison in the next section. The outputs for various test cases are benchmarked against a split-step algorithm using discrete Fourier transforms. Further details on the implementations of the split-step algorithm are given in Appendix C.

4.8.4 *Numerical predictions*

In Figure 4.6, we demonstrate good agreement between numerical predictions and asymptotic approximations for $\epsilon h\lambda \ll 1$ (4.54) for a range of initial ellipticity values, $m = m_0$, for spatially-periodic waves. The deviations of the approximations at large-time can be explained by the increasing time period (4.20) as $m \to 1$ [see the discussion in §4.8.2]. The multiple-scales predictions are only valid when the time period is much smaller than the decay timescale $(\epsilon h\lambda)^{-1}$.

In the inset of Figure 4.6, we also provide a comparison of the predicted wave heights versus the small-amplitude approximation, and this serves to highlight the improvements afforded by the multiple-scales procedure. By normalising the predicted heights with A_{lin} from (4.32), the inset also

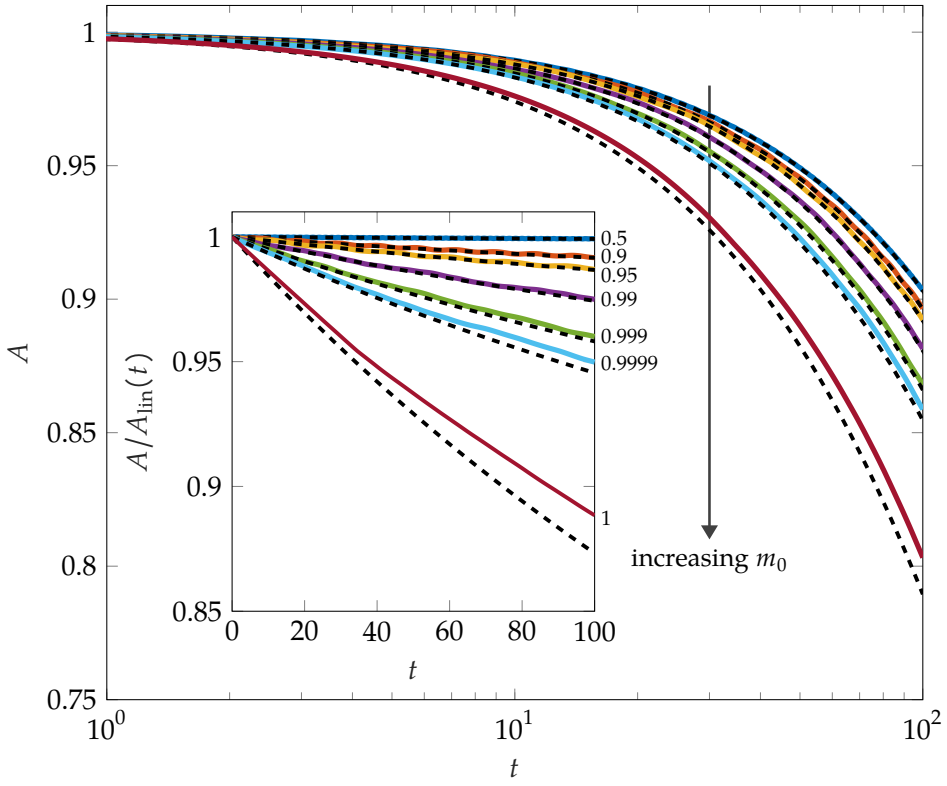

Figure 4.6: Wave height as a function of time for spatially-perioidic cnoidal waves. Solid lines indicate numerical predictions from solving the modified KdV equation (4.13) explicitly in a periodic domain [see §4.8.3]. Colours indicate different initial ellipticity $m = m_0$ – their values are labelled beside the inset. The black dashed lines indicate the corresponding asymptotic predictions (4.54) for $\epsilon h\lambda \ll 1$. The inset plots the ratio between the predicted wave heights in the main figure and the small-amplitude approximation A_{lin} (4.32). The parameter values in this figure corresponds to $\epsilon = 0.1$, $h\lambda = 0.1$, $\bar{M} = 0$ and $A_0 = 1$. For the numerical simulations, we time-stepped with $\Delta t = 10^{-4}$ while discretising the spatial domain into 2×10^3 points, apart from the $m \to 1$ case where $\Delta x = 10^{-3}$.

demonstrates that A_{lin} is a good approximation for A when $m \lessapprox 0.5$ and t is sufficiently small.

In summary, although the analysis for time-harmonic waves in §4.7 is more relevant for coastal flows, we have verified that the general multiple-scales framework is also valid for spatially-periodic waves.

4.9 SUMMARY AND DISCUSSION

In this chapter, we analysed the decay of nonlinear shallow-water waves through rigid vegetation. Here, the key distinguished asymptotic limit is one in which wave height to water depth is small, but still comparable to the shallow-water aspect ratio, *i.e.*

$$\frac{\text{wave height}}{\text{water depth}} \sim \left[\frac{\text{water depth}}{\text{wavelength}}\right]^2.$$

This allows us to derive a modified KdV equation (4.13) for the free-surface elevation. The equation is modified in the sense that there is an additional homogenised sink which accounts for the momentum loss due to the presence of a canopy. In particular, when the canopy is absent, solutions to the classic problem are in the form of cnoidal waves (4.18).

In §§4.7–4.8, we considered the problem of cnoidal waves propagating through sparse canopies. By performing multiple-scale analyses on time-harmonic and spatially-periodic waves respectively, we used the respective solvability conditions, (4.43) and (4.54), to show that cnoidal waves have a

stronger decay in height A than small-amplitude waves from the previous chapters. By establishing the relationship between A and the elliptic parameter m of cnoidal waves, we also predicted how waveforms are modulated from having narrow crests and wide troughs to being more sinusoidal. For spatially-periodic waves, the predictions also showed good agreement with numerical solutions of the full problem where the modified KdV equation is solved explicitly.

This marks the end of the first part of this work on the analysis for waves through rigid vegetation. We first considered how pure linear waves decay in Chapter 2 before extending the analysis to combined current-wave flows and nonlinear shallow-water waves in Chapters 3 and 4. In each case, we gave fast predictions on how each flow decays along the domain. In the next two chapters, we shall explore how coastal flows interact with flexible vegetation. The work in Chapter 5 extends the model and predictions in Chapter 2 by analysing how pure linear waves interact with flexible vegetation. Whilst, Chapter 6 considers a different problem in which a steady current triggers instabilities in the flow, causing the canopy to oscillate.

5 SMALL-AMPLITUDE WAVES THROUGH FLEXIBLE VEGETATION

Be flexible, but stick to your principles.

Eleanor Roosevelt

SYNOPSIS

In this chapter, we predict how small-amplitude coastal waves decay through flexible vegetation over a slowly-varying substrate. We extend the model from Chapter 2 to flexible vegetation. By modelling the canopy as a collection of homogeneous elastic beams, the theory couples the beam equations for the canopy to the fluid momentum equations. In this scenario, the vegetation interacts with the flow. We apply a multiple-scales analysis to derive both the wave evolution and the response of the vegetation. In contrast to the rigid case, however, this involves solving for the local plant dynamics in every temporal period. We find good agreement between our model, which quantifies the momentum loss, and experimental data. In terms of the multiple-scales analysis, we find that inertia affects the wave evolution, in addition to flexibility.

5.1 INTRODUCTION

The preceding chapters have focused on flows through rigid vegetation. Although this is a common modelling simplification, this analysis is more applicable to stiffer aquatic plants such as mangroves. For more flexible plants such as seagrass, there are numerous modelling challenges in capturing both the macro- and micro-scale properties of the system which relates feedback mechanisms between flow and vegetation. In particular contrast to rigid vegetation, the fluid will load and deform each vegetative structure. This deformation, in turn, must affect the flow. Thus, in a complete dynamic model, it appears the fluid flow must be solved simultaneously with the configuration of each plant. These multiple challenges require much greater sophistication in analytical, experimental, and computational studies.

A great deal of attention has been focused on generalising the standard loading models for static, rigid obstacles, considered in Chapter 2, to the case of deformable obstacles [see the reviews by de Langre (2008) and Gosselin (2019)]. For cylinders and strips, which are common geometric simplifications of plants, researchers have developed models [see *e.g.* Luhar and Nepf (2011)] and performed extensive laboratory measurements. These studies often seek to characterise the load as a function of *e.g.* the angle of attack of the flow, the aspect ratio of the obstacle, and the velocity of the obstacle (Sumer and Fredsøe, 2006). Due to the size and dimensions of the parameter space, a theory of fluid-plant loading remains to be an active field of research.

Meanwhile, there has been significant work in predicting wave attenuation through flexible vegetation, but the majority of theoretical analysis has been confined to the case of a rigid canopy. To account for plant flexibility and dynamics, one technique has been to fit the drag coefficient in the decay law (2.48) to experimental data [see the review by Lei and Nepf (2019) for previous studies]. Luhar and Nepf (2011) introduced the concept of an *effective length* for flexible plants in steady flows, which quantifies the experimentally determined load on a single plant as a function of flexibility. Although the generalisation of the effective length from steady individual plants to unsteady canopies has received less attention, this was recently done by Luhar et al. (2017) and Lei and Nepf (2019) to give wave-height predictions based on scaling law approximations.

In this chapter, we shall use the governing formulation developed in Chapter 2 where the fluid is coupled to the canopy via the homogenised momentum sink. This will be combined with a variety of fluid load models for flexible vegetation that have been proposed in the literature for the description of drag, added mass, and virtual buoyancy. We then apply a multiple-scales analysis which formally establishes a decoupling of hydrodynamics from plant dynamics at leading order. This allows us to approximate the leading-order plant dynamics as a standalone problem. Finally, these results are compared with experimental data and are used to predict wave decay along the domain.

5.2 THEORETICAL FORMULATION

We consider the same setup as in Chapter 2, with the rigid vegetation being replaced by flexible vegetation. In addition, we shall assume, as before, that after homogenising the effects of individual plants, solutions are only two-dimensional; thus, the plants deform in the same plane as the travelling wave. The setup is illustrated with the schematic in Figure 5.1.

Analogous to the rigid-canopy problem, the hydrodynamics are gov-

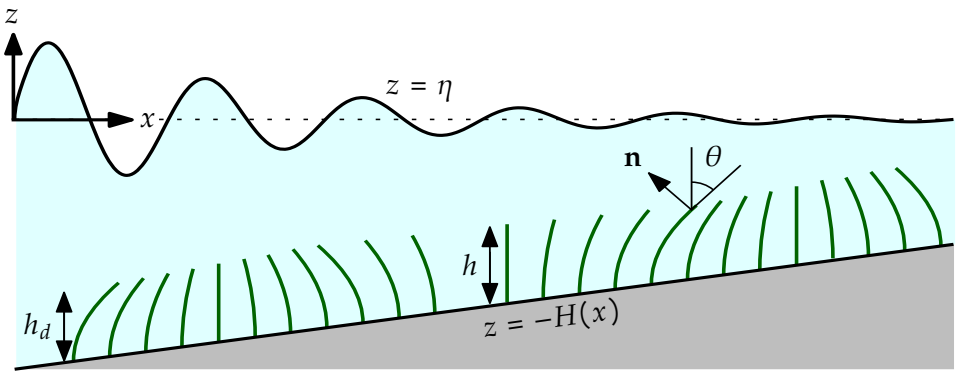

Figure 5.1: Schematic diagram of waves propagating through a flexible canopy over a varying substrate with $z = -H(x)$. The waves propagate along the x-direction, with the free surface being parametrised with $z = \eta$ and the green obstacles representing individual plants. Each plant configuration is parametrised by the arc length s and local angle of deflection θ. The two quantities, h and h_d, denote the length and the deflected height of a plant respectively.

erned by the equations

$$\nabla \cdot \mathbf{u} = 0, \tag{5.1}$$

$$\rho\left(\frac{\partial \mathbf{u}}{\partial t} + \mathbf{u} \cdot \nabla \mathbf{u}\right) = -\nabla p - \bar{\mathbf{F}}, \tag{5.2}$$

with the additional homogenised sink term, $\bar{\mathbf{F}}$, being a generalised form of (2.12) which accounts for the presence of a flexible canopy. We will give the precise form of $\bar{\mathbf{F}}$ once we have described the canopy configuration.

5.2.1 *Parametrisation of the vegetation*

Each individual plant is modelled as a linearly elastic beam with one end clamped vertically to the substrate, and the other end left free. Hence, they are upright when they are load-free (see Figure 5.1). We parametrise the centreline of each plant by $\mathbf{x} = (x, z) = \mathbf{r}$, where now $\mathbf{r} = \mathbf{r}(s, \tau; X)$ where s is the arc length, τ is time for fixed s, and $x = X$ is the position of the root on the substrate where $s = 0$. We use τ rather than t to emphasise the implicit change of variables from $(\mathbf{x}, t)$ to $(s, \tau; X)$; this is a Lagrangian description of the canopy. We shall return to this later in §6.4.1 when we discuss the relationship between Eulerian and Lagrangian frames. In the asymptotic regimes of our concern, we will later find that $\tau = t$.

With this definition, we have $\partial \mathbf{r}/\partial \tau$ and $\partial^2 \mathbf{r}/\partial \tau^2$ being the local plant velocity and acceleration respectively.

Finally, suppose we also let θ be the local angle of deflection in the xz–plane at a given s, as measured from the upward vertical; then the local upstream normal would be $\mathbf{n} = (-\cos\theta, \sin\theta)$ (see Figure 5.1).

5.2.2 *Equations for the vegetation*

Now that we have parametrised our vegetation, we require some governing equations which describe the coupling between the hydrodynamics and the deformation of the plants.

Since we model individual plants as elastic beams, then for each given beam and associated position vector, $\mathbf{r}$, we let $\mathbf{T} = (T_{\parallel}, T_{\perp})$ be the internal stress and $\mathbf{M}$ be the moment on the respective cross-section. Then by considering the momentum balance on this cross-section which has an infinitesimal thickness, $\mathbf{T}$ satisfies (Landau and Lifshitz, 1960)

$$\frac{\partial \mathbf{T}}{\partial s} + \mathbf{q} = m\frac{\partial^2 \mathbf{r}}{\partial \tau^2}, \tag{5.3}$$

where $\mathbf{q}$ is the external force per unit length on the beam. We also consider the angular momentum balance on this cross-section. Noting that $\partial \mathbf{r}/\partial s = (\sin\theta, \cos\theta)$ is the local tangent vector of the plant, we assume the standard constitutive relation between $\mathbf{M}$ and $\mathbf{r}$ holds and is given by (Landau and Lifshitz, 1960)

$$\mathbf{M} = EI\frac{\partial \mathbf{r}}{\partial s} \times \frac{\partial^2 \mathbf{r}}{\partial s^2}. \tag{5.4}$$

Consequently, θ satisfies (McMillen and Goriely, 2003)

$$\frac{\partial}{\partial s}\left(EI\frac{\partial \theta}{\partial s}\right) + T_{\parallel}\cos\theta - T_{\perp}\sin\theta = \rho I\frac{\partial^2 \theta}{\partial \tau^2}. \tag{5.5}$$

In the above equation, E is the Young's modulus, and I is the moment of inertia of the cross-section about the y–axis. In this work, since we will focus on the typical scenario where the velocity of the fluid is much smaller than the speed of sound in a beam $\sqrt{E/\rho}$, we can neglect the inertial term on the right-hand side of (5.5). Physically, this gives us a balance between bending and loading.

Note in addition that the EI-dependent bending term in (5.5) is expressed in a form such that the beam equations (5.3)–(5.5) can model beams with a non-uniform cross-section $b = b(s)$. However, in this work, we consider b constant.

Finally, we must determine the total external load on the plant, $\mathbf{q}$, in (5.3). We are aware that the momentum loss in the fluid must balance the load on the plant. Hence, with reference to the component forces in the fluid due to the presence of a single rigid beam (2.5a)–(2.5c), the corresponding load on a neutrally-buoyant flexible beam is given by

$$\mathbf{q} = \mathbf{q}_D + \mathbf{q}_A + \mathbf{q}_V. \tag{5.6}$$

Neglecting buoyancy effects is a common simplification since many aquatic plants are close to neutrally buoyant (Leclercq and de Langre, 2018) and they often play a negligible role compared to flexibility in oscillatory flows (Luhar and Nepf, 2016). For flexible plants, we shall use expressions for the individual drag $\mathbf{q}_D$, added mass $\mathbf{q}_A$, and virtual buoyancy $\mathbf{q}_V$ that have been developed by Luhar and Nepf (2016) and Leclercq and de Langre (2018). In particular, these loads are considered to be functions of s and τ, and given

by

$$\mathbf{q}_D = \frac{1}{2}\rho b C_D \int_\Omega \delta(\mathbf{x}-\mathbf{r}) \left(\mathbf{u} - \frac{\partial \mathbf{r}}{\partial \tau}\right) \cdot \mathbf{n} \left| \left(\mathbf{u} - \frac{\partial \mathbf{r}}{\partial \tau}\right) \cdot \mathbf{n} \right| \mathbf{n} \, \mathrm{d}\mathbf{x}, \tag{5.7a}$$

$$\mathbf{q}_A = C_M m \int_\Omega \delta(\mathbf{x}-\mathbf{r}) \left[\left(\frac{\partial \mathbf{u}}{\partial t} - \frac{\partial^2 \mathbf{r}}{\partial \tau^2} \right) \cdot \mathbf{n} \right] \mathbf{n} \, \mathrm{d}\mathbf{x}, \tag{5.7b}$$

$$\mathbf{q}_V = m \int_\Omega \delta(\mathbf{x}-\mathbf{r}) \frac{\partial \mathbf{u}}{\partial t} \, \mathrm{d}\mathbf{x}, \tag{5.7c}$$

where Ω is the fluid domain. Note that the expressions for $\mathbf{q}_D$ and $\mathbf{q}_A$ have been generalised from the rigid case so that the fluid velocities and accelerations in the original expressions (2.5a)–(2.5b) are replaced with their respective relative quantities. We also reiterate that since the plant is deflected, the local upstream normal $\mathbf{n} = (-\cos\theta, \sin\theta)$ (see Figure 5.1) is a function of the local angle of deflection θ. We will validate this loading model later in §5.5 by comparing it with experimental data from other studies.

The drag law in (5.7a) can be interpreted as follows: for each beam cross-section with unit thickness, $\mathbf{q}_D$ is the force a tilted cylinder of the same length would experience (Sumer and Fredsøe, 2006). It has been argued, both experimentally and numerically, that this drag law is accurate until the beam approaches a configuration parallel to the flow (Ramberg, 1983; Vakil and Green, 2009; Zhao et al., 2009). In the case of rigid and vertical beams, (5.7a) reduces to the formulation used in Singh et al. (2016). We refer readers to Zhou et al. (2010) for a more extensive review of drag on tilted cylinders. Finally, we also highlight that our drag law has also been used to compute blade drag in previous studies [*e.g.* by Luhar and Nepf (2016) and Leclercq and de Langre (2018) for unsteady flows].

We are now ready to formulate the homogenised sink term, $\bar{\mathbf{F}}$ in the fluid momentum equation (5.2) for flexible vegetation.

5.2.3 *Homogenised sink term*

With the loading on a single plant being defined in (5.7), the corresponding momentum loss in the fluid is $\mathbf{F} = \mathbf{F}_D + \mathbf{F}_A + \mathbf{F}_V$, with

$$\mathbf{F}_D = \frac{1}{2}\rho b C_D \int_0^h \delta(\mathbf{x}-\mathbf{r}) \left(\mathbf{u} - \frac{\partial \mathbf{r}}{\partial \tau}\right) \cdot \mathbf{n} \left| \left(\mathbf{u} - \frac{\partial \mathbf{r}}{\partial \tau}\right) \cdot \mathbf{n} \right| \mathbf{n} \, \mathrm{d}s, \tag{5.8a}$$

$$\mathbf{F}_A = C_M m \int_0^h \delta(\mathbf{x}-\mathbf{r}) \left[\left(\frac{\partial \mathbf{u}}{\partial t} - \frac{\partial^2 \mathbf{r}}{\partial \tau^2} \right) \cdot \mathbf{n} \right] \mathbf{n} \, \mathrm{d}s, \tag{5.8b}$$

$$\mathbf{F}_V = m \int_0^h \delta(\mathbf{x}-\mathbf{r}) \frac{\partial \mathbf{u}}{\partial t} \, \mathrm{d}s. \tag{5.8c}$$

This is the generalisation of the rigid-plant formulation (2.5). We can now apply the same local averaging argument on a collection of neighbouring plants in §2.2 to derive the expression for the homogenised sink, $\bar{\mathbf{F}}$, in (5.2).

Before proceeding, note that the averaging argument of this section is three-dimensional by nature (and accounts for the flow in the y-direction that will be eventually averaged). Thus we consider a fixed point $\mathbf{x} = (x, y, z)$ and define $\bar{\mathbf{F}}_R$ as the local average of N individual sinks (along the domain) over a local disk of radius R, or

$$\bar{\mathbf{F}}_R = \frac{1}{\pi R^2} \iint_{C_R(x,y;z)} \left[\sum_{k=1}^{N} \int_0^h \mathbf{F}^k \delta(\mathbf{x}' - \mathbf{r}^k) \, \mathrm{d}s \right] \mathrm{d}x' \mathrm{d}y', \tag{5.9}$$

where $C_R(x, y; z) = \{(x', y', z) : (x - x')^2 + (y - y')^2 \leq R\}$ is the two-dimensional disk of radius R centred at the point $\mathbf{x}$. If we first convert the s-integrals in (5.9) to z-integrals via the transformation

$$\frac{\mathrm{d}s}{\mathrm{d}z} = \sec\theta \tag{5.10}$$

and take the limit $R \to 0$, this results in the homogenised sink term for flexible vegetation in (5.2) at $\mathbf{x}$, given by

$$\overline{\mathbf{F}} = \bar{N} \sec\theta \, \mathrm{H}(h_d - H - z) \left(\bar{\mathbf{F}}_D + \bar{\mathbf{F}}_A + \bar{\mathbf{F}}_V \right). \tag{5.11}$$

In the above expression, recall that $\bar{N}$ is the number of plants planted per unit area, as in Chapter 2, and H is the Heaviside step function (distinguished from the height, H).

The corresponding homogenised forms for the various momentum losses due to drag $\bar{\mathbf{F}}_D$, added mass $\bar{\mathbf{F}}_A$, and virtual buoyancy $\bar{\mathbf{F}}_V$ are

$$\bar{\mathbf{F}}_D = \frac{1}{2} \rho b C_D \left(\mathbf{u} - \frac{\partial \mathbf{r}}{\partial \tau} \right) \cdot \mathbf{n} \left| \left(\mathbf{u} - \frac{\partial \mathbf{r}}{\partial \tau} \right) \cdot \mathbf{n} \right| \mathbf{n}, \tag{5.12a}$$

$$\bar{\mathbf{F}}_A = C_M m \left[\left(\frac{\partial \mathbf{u}}{\partial t} - \frac{\partial^2 \mathbf{r}}{\partial \tau^2} \right) \cdot \mathbf{n} \right] \mathbf{n}, \tag{5.12b}$$

$$\bar{\mathbf{F}}_V = m \frac{\partial \mathbf{u}}{\partial t}. \tag{5.12c}$$

We now highlight the main differences between (5.11) and the rigid-canopy momentum sink (2.12). Firstly, within the argument of the Heaviside function, we have introduced h_d, the deflected canopy height (see the schematic diagram Figure 5.1) in place of h in (2.12). Hence, fluid momentum will only be lost within the canopy.

More importantly in contrast to the rigid case, h_d is not known *a priori* since

$$h_d = \int_0^h \cos\theta \, \mathrm{d}s. \tag{5.13}$$

Secondly, the plant variables in (5.11), θ and $\mathbf{T}$, now correspond to the configuration of a representative plant rooted at x along the substrate. The dependence of $\overline{\mathbf{F}}$ on $\sec\theta$ (in addition to the component forces) accounts for the change in perpendicular distance between neighbouring plants when they tilt; in particular, if the plants do tilt, then the effective density of the canopy increases for the continuum model.

The formulation of the flexible canopy problem is now complete.

5.2.4 *Nondimensionalisation*

Note that the origin of the base coordinate system is such that a given undeflected plant corresponds to the position vector $\mathbf{r} = (X, -H + s)$ for a given X. It is thus convenient to introduce a displacement vector, $\tilde{\mathbf{r}}$, relative to this position via

$$\mathbf{r} = \begin{pmatrix} X \\ -H + s \end{pmatrix} + \tilde{\mathbf{r}}, \qquad \text{where } \tilde{\mathbf{r}} = \begin{pmatrix} \tilde{x} \\ \tilde{z} \end{pmatrix}. \tag{5.14}$$

Further, note from our analysis in Chapter 2 that it is sensible to scale the dimensional arc length, s, by L for the subsequent multiple-scales analysis. However, since every plant will only deform on the scale at which a local fluid particle would travel, we prefer to scale the plant displacement vector, $\tilde{\mathbf{r}}$ by a specified wave-amplitude scale A_0.

Together with the scales from the rigid-canopy problem (2.15), we thus nondimensionalise our governing equations with the scales,

$$[s] = L, \quad [\tau] = \omega_0^{-1}, \quad [\tilde{\mathbf{r}}] = A_0, \quad [\mathbf{q}] = \rho b C_D A_0^2 \omega_0^2, \quad [\mathbf{T}] = L[\mathbf{q}]. \tag{5.15}$$

We now present the dimensionless governing equations.

5.2.5 *Dimensionless governing equations*

With the above choice of scales, the dimensionless governing equations for the flexible-canopy problem are

$$\nabla \cdot \mathbf{u} = 0, \tag{5.16a}$$

$$\frac{\partial \mathbf{u}}{\partial t} + \gamma \mathbf{u} \cdot \nabla \mathbf{u} = -\alpha \nabla p - \lambda \sec\theta \mathrm{H}(h_d - H - z)\mathbf{F}, \tag{5.16b}$$

$$\frac{\partial \mathbf{T}}{\partial s} + \mathbf{F} = M_2 \frac{\partial^2 \tilde{\mathbf{r}}}{\partial \tau^2}, \tag{5.16c}$$

$$\frac{\partial^2 \theta}{\partial s^2} = \frac{C_Y}{\alpha^3}(-T_\parallel \cos\theta + T_\perp \sin\theta), \tag{5.16d}$$

with

$$\begin{aligned} \mathbf{F} = \frac{1}{2}\begin{pmatrix} u - \tilde{x}_\tau \\ w - \tilde{z}_\tau \end{pmatrix} \cdot \begin{pmatrix} -\cos\theta \\ \sin\theta \end{pmatrix} \left| \begin{pmatrix} u - \tilde{x}_\tau \\ w - \tilde{z}_\tau \end{pmatrix} \cdot \begin{pmatrix} -\cos\theta \\ \sin\theta \end{pmatrix} \right| \begin{pmatrix} -\cos\theta \\ \sin\theta \end{pmatrix} \\ + M_1 \left[\begin{pmatrix} u_t - \tilde{x}_{\tau\tau} \\ w_t - \tilde{z}_{\tau\tau} \end{pmatrix} \cdot \begin{pmatrix} -\cos\theta \\ \sin\theta \end{pmatrix} \right] \begin{pmatrix} -\cos\theta \\ \sin\theta \end{pmatrix} + M_2 \begin{pmatrix} u_t \\ w_t \end{pmatrix}. \end{aligned} \tag{5.16e}$$

The boundary conditions are

$$\boxed{\text{Free-slip}} \quad u\frac{\mathrm{d}H}{\mathrm{d}x} + w = 0, \qquad \text{at } z = -H(x), \tag{5.16f}$$

$$\boxed{\text{Kinematic}} \quad w - \frac{\partial \eta}{\partial t} - \gamma u \frac{\partial \eta}{\partial x} = 0, \qquad \text{at } z = \gamma\eta, \tag{5.16g}$$

$$\boxed{\text{Dynamic}} \quad p = \eta, \qquad \text{at } z = \gamma\eta. \tag{5.16h}$$

$$\boxed{\text{Plant}} \quad \theta(s = 0) = 0, \mathbf{T}(s = h) = \mathbf{0}, \left.\frac{\partial \theta}{\partial s}\right|_{s=h} = 0. \tag{5.16i}$$

We recall from Table 2.1 in Chapter 2 that:

- α is the ratio between the wavelength and the domain scale
- γ is the ratio between the amplitude and the domain scale
- λ is the canopy density
- M_1 and M_2 are parameters for inertia

Finally, we have the constraint

$$\int_0^h \cos\theta \, \mathrm{d}s = h_d. \tag{5.16j}$$

In addition to the dimensionless parameters we have defined in Table 2.1, we define the Cauchy number (de Langre, 2008)

$$C_Y = \frac{\rho b C_D A_0^2 \omega_0^2 (g/\omega_0^2)^3}{EI} \tag{5.17}$$

which describes a representative balance between bending and loading due to the wave. We will revisit the additional scaling factor α^{-3} in (5.16d) in the multiple-scales analysis in §5.3. In a complete model, the drag coefficient, C_D, would vary as the wave evolves—this was discussed in detail in §2.10.1 for rigid canopies. For simplicity, we continue to assume that C_D is constant [once C_D is fixed by the initial value of the Keulegan-Carpenter number K_C in (2.61)].

Before we begin our multiple-scales analysis, we rewrite the fluid equations in terms of p. Suppose we write $\mathbf{F} = (F_\parallel, F_\perp)$ in (5.16e), then

$$\nabla^2 p + \frac{\lambda}{\alpha}\nabla\cdot[\sec\theta \mathrm{H}(h_d - H - z)\mathbf{F}] + \frac{\gamma}{\alpha}\nabla\cdot\begin{pmatrix} uu_x + wu_z \\ uw_x + ww_z \end{pmatrix} = 0 \tag{5.18}$$

with the same boundary conditions as in the rigid-problem (2.17) [with $\mathbf{F}$ updated to (5.16e)]. However, we emphasise that this equation for pressure is now coupled to the beam equations (5.16c)–(5.16d).

Although the system of equations, either in its original form (5.16) or written in terms of pressure (5.18), appears to be complicated, we will later justify that under certain regimes, the dynamics between the wave and the canopy are asymptotically decoupled. Therefore, we can independently solve for the flow and the canopy dynamics.

5.3 MULTIPLE-SCALES ANALYSIS OF WAVE MODULATION

Analogous to the analysis in Chapter 2, provided that the domain (which includes both the topography and the flexible vegetation) has small contributions to the local wave dynamics, we can separate the wave scale from the domain scale and derive the evolution of the wave amplitude and wavelength. The key mathematical concept here is that on the wave scale, we will discover that the flow and the canopy dynamics asymptotically decouple. Hence, we can apply the following steps:

1. Evaluate the leading-order waveform analytically, as in the rigid-canopy problem, leaving an as-yet-unknown amplitude function.
2. Evaluate the canopy dynamics over one time period using the waveform in Step 1.

3. Evaluate the amplitude and wavelength over each time period; these are shown to vary as functions of the substrate and the flexible vegetation.
4. Predict the cumulative modulation on the wave along the domain.

We will provide the multiple-scales analysis below.

5.3.1 *Theoretical formulation*

We closely follow the procedures in §2.5.1 and consider x as the slow variable, while defining the fast variable as

$$\bar{x} = \frac{\Phi(x)}{\alpha} \tag{5.19}$$

with the wavelength-to-domain parameter, $\alpha \ll 1$. We will solve for $\Phi(x)$ as part of the problem so that the wave variables are 2π-periodic in $\bar{x}$.

To solve for the local wave dynamics, we first rescale $z = \alpha\bar{z}$ and its associated derivatives, while rescaling $h = \alpha\bar{h}$ and $H(x) = \alpha\bar{H}(x)$. In addition, for the flexible-canopy problem, we also rescale $s = \alpha\bar{s}$ and $\mathbf{T} = \alpha\bar{\mathbf{T}}$.

We then consider an asymptotic expansion in α for our variables, *e.g.* of the form

$$f = \sum_{n=0}^{\infty} \alpha^n f_n. \tag{5.20}$$

Finally, in the multiple-scales expansion, we consider the same distinguished limit as in Chapter 2 by taking $\lambda = O(\alpha)$ and $\gamma = O(\alpha^2)$ in (2.22).

As an aside, if we were to focus our analysis on canopy dynamics, it would be more natural for us to scale the spatial variables ($\bar{x}$, $\bar{z}$ and $\bar{s}$) with the plant length h in the nondimensionalisation. We could then solve the dimensionless plant problem in (5.16) over a fixed spatial domain [see *e.g.* Leclercq and de Langre (2018)]. In this work, however, we have chosen to scale all of the spatial variables in the fast scale with $g/\omega_0^2 = \alpha L$ (see our choice of dimensionalisation in Table 2.1) since it is more convenient for the multiple-scales analysis.

For ease of reference:

x is the slow variable

$\bar{x}$ is the fast variable

$\tilde{x}$ is the horizontal beam displacement (5.14)

5.3.2 *Leading-order problem for the flow and coordinate transformations*

For the leading-order problem, the dynamic pressure, p_0, of the fluid, obtained via (5.18) is Laplace's equation, which is compared with (2.23a). Hence, the flow is decoupled from the canopy dynamics, as in the rigid-problem in Chapter 2. By only considering the fundamental Fourier mode of a monochromatic incident wave, we obtain the sinusoidal base solutions

for the flow,

$$\eta_0 = A(x)\cos(\bar{x} - t), \tag{5.21a}$$

$$u_0 = A(x)\frac{\cosh[k(\bar{z} + \bar{H})]}{\sinh k\bar{H}}\cos(\bar{x} - t), \tag{5.21b}$$

$$w_0 = A(x)\frac{\sinh[k(\bar{z} + \bar{H})]}{\sinh k\bar{H}}\sin(\bar{x} - t), \tag{5.21c}$$

$$p_0 = A(x)\frac{\cosh[k(\bar{z} + \bar{H})]}{\cosh k\bar{H}}\cos(\bar{x} - t) \tag{5.21d}$$

with k satisfying the dispersion relation $k\tanh k\bar{H} = 1$ (2.28). The multiple-scales mapping function Φ and the wavenumber k are related via the eikonal equation $\mathrm{d}\Phi/\mathrm{d}x = k$ (2.25).

In solving the dynamics of a homogenised plant that is rooted at $x = X$, we have the choice of either Eulerian coordinates (x, z, t) or Lagrangian coordinates $(s, \tau; X)$. Since the governing equations are specified in Eulerian coordinates, it is more convenient to also solve for the plant dynamics in (x, z, t). Hence, in addition to the plant variables, θ and $\mathbf{T}$, expressed in powers of α, we also expand the Lagrangian independent variables, s and τ, in the governing equations (5.16). Consequently, on the wave scale, the leading-order beam equations are

$$\frac{\partial\bar{\mathbf{T}}_0}{\partial\bar{s}_0} + \mathbf{F}_0 = M_2\frac{\partial^2\tilde{\mathbf{r}}_0}{\partial\tau_0^2}, \tag{5.22a}$$

$$\frac{\partial^2\theta_0}{\partial\bar{s}_0^2} = C_Y(-\bar{T}_{\parallel 0}\cos\theta_0 + \bar{T}_{\perp 0}\sin\theta_0). \tag{5.22b}$$

with $\mathbf{F}_0$ expressed using (5.16e), with boundary conditions

$$\theta_0 = 0, \text{ at } \bar{s}_0 = 0, \tag{5.22c}$$

$$\bar{\mathbf{T}}_0 = \mathbf{0}, \text{ at } \bar{s}_0 = \bar{h}, \tag{5.22d}$$

$$\frac{\partial\theta_0}{\partial\bar{s}_0} = 0, \text{ at } \bar{s}_0 = \bar{h}. \tag{5.22e}$$

We are now required to express $\bar{s}_0$ and τ_0 in (5.22) in terms of (x, z, t). Recall that from (5.14), a plant that is rooted at $\bar{x} = \bar{X}$ can be expressed as

$$\bar{\mathbf{r}} = \begin{pmatrix}\bar{X}\\ -\bar{H} + \bar{s}\end{pmatrix} + \alpha\bar{\bar{\gamma}}\begin{pmatrix}\tilde{x}\\ \tilde{z}\end{pmatrix}. \tag{5.23}$$

Thus,

$$\frac{\partial\bar{\mathbf{r}}}{\partial\bar{s}} = \begin{pmatrix}0\\ 1\end{pmatrix} + \alpha\bar{\bar{\gamma}}\begin{pmatrix}\partial\tilde{x}/\partial\bar{s}\\ \partial\tilde{z}/\partial\bar{s}\end{pmatrix} = \begin{pmatrix}\sin\theta\\ \cos\theta\end{pmatrix}. \tag{5.24}$$

To be consistent with the expansion in $\alpha \ll 1$, we have to apply the small deflection approximation $\theta \ll 1$ in (5.24). As a result, we have the arc length being

$$\bar{s}_0 = \bar{z} + \bar{H}. \tag{5.25}$$

This simple vertical shift in $\bar{H}$ implies the deformed height of the canopy is asymptotically equal to the original (undeformed) canopy height *i.e.* $h_{d0} = h$ or equivalently $\bar{h}_{d0} = \bar{h}$. Secondly, since every point on a plant that is parametrised by $\bar{s}_0$ can be asymptotically described by a fixed $\bar{z}$ via (5.25), we also result in that

$$\tau_0 = t. \tag{5.26}$$

Furthermore, we express θ_0 in terms of the leading-order horizontal displacement $\tilde{x}_0$ by considering

$$\sin\theta_0 = \theta_0 = \alpha\bar{\gamma}\frac{\partial\tilde{x}_0}{\partial\bar{z}} \quad \text{and} \quad \cos\theta_0 = 1. \tag{5.27}$$

With the expansions above, we can now rewrite the governing equations for the plant dynamics.

5.3.3 *Leading-order plant dynamics*

Summarising the derivations from the previous section, by rewriting the leading-order plant problem (5.22) with the transformations (5.25)–(5.27), we can solve for the plant dynamics via the horizontal displacement $\tilde{x}_0$, which satisfies

$$\tilde{x}_{0\bar{z}\bar{z}\bar{z}\bar{z}} = C_{\text{eff}}\left[\frac{1}{2}\left(u_0 - \tilde{x}_{0t}\right)\left|u_0 - \tilde{x}_{0t}\right| + \left(M_1 + M_2\right)\left(u_{0t} - \tilde{x}_{0tt}\right)\right], \tag{5.28a}$$

with u_0 given by (5.21b) and $\tilde{x}_0$ satisfying the boundary conditions

$$\tilde{x}_0 = 0,\ \frac{\partial\tilde{x}_0}{\partial\bar{z}} = 0, \qquad \text{at } \bar{z} = -\bar{H}, \tag{5.28b}$$

$$\frac{\partial^2\tilde{x}_0}{\partial\bar{z}^2} = 0,\ \frac{\partial^3\tilde{x}_0}{\partial\bar{z}^3} = 0, \qquad \text{at } \bar{z} = -\bar{H} + \bar{h}. \tag{5.28c}$$

Note that (5.28a) solves for the leading-order deflection, where we regard $\tilde{x}_0$ in functional form as

$$\tilde{x}_0 = \tilde{x}_0(\bar{z},\ t,\ u_0(\bar{z}, t; x, \bar{x})\,). \tag{5.29}$$

That is, to be consistent with the expansion in α, we evaluate u_0 given by (5.21b) at a specified macroscopic location, x, and with $\bar{x}$ equal to the root position, $\bar{X}$, which will be constant for all $\bar{z}$ and t.

The equation above for $\tilde{x}_0$ can be interpreted as a dynamic Euler-Bernoulli beam equation (Landau and Lifshitz, 1960), with the load being dependent on both the surrounding flow and plant dynamics itself. The dimensionless parameter

$$C_{\text{eff}} = \frac{C_Y}{\alpha\bar{\gamma}} = \frac{\rho b C_D A_0 \omega_0^2 (g/\omega_0^2)^4}{EI}, \tag{5.30}$$

describes the effective balance between load and deflection in the limit of small deflections. We will use this parameter for the rest of our analysis.

For large deflections, we note that it is more appropriate to characterise the balance with the original Cauchy number, C_Y, given in (5.17). However, we will only consider such regimes for the current-dominated problem in Chapter 6.

Thus far, the analysis above only addresses how to obtain the leading-order waveform (5.21), and how to solve for the dynamics of a beam due to a given wave. We now return to the multiple-scales analysis and use the results above to determine the evolution of the wave along the entire domain.

5.3.4 *Formulating the higher-order problem*

After evaluating the plant dynamics (5.28) numerically, let us abbreviate the evaluated Heaviside and delta-functions, $\mathrm{H}(\bar{h} - \bar{H} - \bar{z})$ with H, and $\delta(\bar{h} - \bar{H} - \bar{z})$ with δ. By considering the $O(\alpha)$-problem in the expansion for (5.18), p_1 satisfies

$$\bar{\nabla}^2 p_1 + \frac{\mathrm{d}k}{\mathrm{d}x} p_{0\bar{x}} + 2k p_{0\bar{x}x} + \bar{\lambda}(kF_{\parallel 0\bar{x}} + F_{\perp 0\bar{z}})\mathrm{H} + \bar{\gamma}\Gamma = \bar{\lambda} M_2 F_{\perp 0}\delta \tag{5.31}$$

with the function Γ and the boundary conditions defined in (2.29). Note that although the above equation for p_1 seems identical to the analogous version for the rigid-canopy problem in (2.29), in fact, the function $\mathbf{F}_0$ now includes additional components to account for flexibility. That is,

$$\mathbf{F}_0 = \begin{pmatrix} F_{\parallel 0} \\ F_{\perp 0} \end{pmatrix} = \begin{pmatrix} \frac{1}{2}(u_0 - \tilde{x}_{0t})\,|u_0 - \tilde{x}_{0t}| + M_1\,(u_{0t} - \tilde{x}_{0tt}) + M_2 u_{0t} \\ M_2 w_{0t} \end{pmatrix}. \tag{5.32}$$

We do not solve for the higher-order corrections of $\mathbf{F}$ since we are aware from both (5.31) and the rigid-canopy analysis in §2.5 that we only require the leading-order canopy configuration to obtain $A(x)$.

We are now ready to derive the solvability condition for $A(x)$.

5.3.5 *Deriving the solvability condition*

We follow the identical procedures given in §2.5.4 to derive an evolution equation for the amplitude $A(x)$ for flexible canopies.

In particular, we evaluate the identity [as given in (2.30)]

$$\int_{\bar{\Omega}} \begin{pmatrix} p_1 \\ -p_0^* \end{pmatrix} \cdot \begin{pmatrix} \bar{\nabla}^2 p_0^* \\ \bar{\nabla}^2 p_1 \end{pmatrix} \mathrm{d}V = \int_{\partial\bar{\Omega}} \left[p_1 \begin{pmatrix} k^2 p_{0\bar{x}}^* \\ p_{0\bar{z}}^* \end{pmatrix} - p_0^* \begin{pmatrix} k^2 p_{1\bar{x}} \\ p_{1\bar{z}} \end{pmatrix} \right] \cdot \mathrm{d}\mathbf{n}_{\bar{\Omega}}, \tag{5.33}$$

with $p_0^* \propto \sin(\bar{x} - t)$ being the leading-order adjoint solution given by (2.31) and the domain of integration $\bar{\Omega}$ specified in Figure 5.2. We also recall from (2.23a) that the Laplacian operator $\bar{\nabla}^2$ for $\bar{\nabla}^2 p$ denotes $(\Phi')^2 p_{\bar{x}\bar{x}} + p_{\bar{z}\bar{z}}$.

If we further integrate both sides of the identity (5.33) in time over one time period $t \in [0, 2\pi]$, with p_0^* and $\bar{\Omega}$ stated above, all of the contour integrals along $\partial\bar{\Omega}$ average to zero apart from the contributions from the

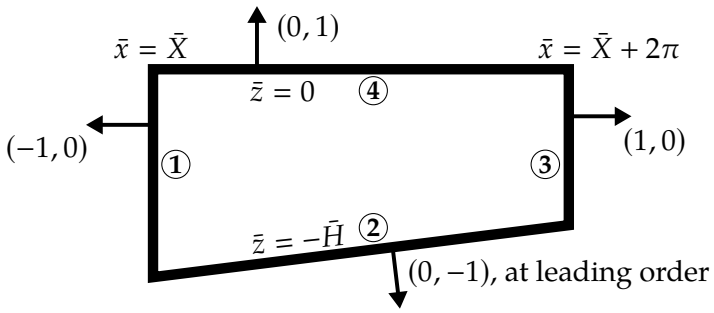

Figure 5.2: Schematic diagram for the periodic cell $\bar{\Omega} = [\bar{X}, \bar{X} + 2\pi] \times [-\bar{H}, 0]$ in the multiple-scales analysis. Notice that the definitions of $\bar{\Omega}$ between this figure and Figure 2.3 are identical—the figures are duplicated for the ease of reference.

slowly varying substrate $\bar{z} = -\bar{H}(x)$—the detailed derivation is given in §2.5. By also realising that $\bar{\nabla}^2 p_0^* = 0$ by construction (of an adjoint solution) and $\bar{\nabla}^2 p_1$ can be rewritten in terms of the leading-order solution via (5.31), we deduce from (5.33) the same solvability condition for the rigid-canopy problem (2.37), namely

$$\int_{t=0}^{2\pi} \int_{\bar{\Omega}} p_0^* \left[k' p_{0\bar{x}} + 2k p_{0\bar{x}x} + \bar{\lambda}(k F_{\parallel 0\bar{x}} + F_{\perp 0\bar{z}})\mathrm{H} - \bar{\lambda} F_{\perp 0} \delta \right] \mathrm{d}V \mathrm{d}t$$
$$= -\int_{t=0}^{2\pi} \int_{\bar{x}=\bar{X}}^{\bar{X}+2\pi} k\bar{H}' p_0^* p_{0\bar{x}}|_{\bar{z}=-\bar{H}} \, \mathrm{d}\bar{x} \, \mathrm{d}t. \qquad (5.34)$$

Note that the derivation of (5.33)–(5.34) is entirely identical between the rigid and the flexible case, with the only difference being the new expression of $\mathbf{F}_0$ given by (5.32) instead for flexible canopies.

In contrast to the rigid-canopy problem, we cannot deduce from the solvability condition (5.34) a differential equation for $A(x)$ in analytical form due to the canopy dynamics. However, we can evaluate some of the integrals above to further simplify the equation, with the strategy listed in §2.5.4. In particular, we can show that the integrals involving $\mathbf{F}_0$ with factors multiplying M_2 are zero. Then if we also integrate the $F_{\parallel 0\bar{x}}$-dependent integral by parts in the solvability condition (5.34), we deduce a differential equation for $A(x)$ in the form of (2.38), with

$$\frac{\pi^2 A}{\bar{\lambda} k \cosh^2 k\bar{H}} \left[2A(\bar{H} - 1) \frac{\mathrm{d}(k\bar{H})}{\mathrm{d}x} - (2k\bar{H} + \sinh 2k\bar{H}) \frac{\mathrm{d}A}{\mathrm{d}x} \right] = \mathcal{D}, \qquad (5.35)$$

with the new contribution $\mathcal{D} = \mathcal{D}(x)$ for flexible canopies being

$$\mathcal{D} = \int_{t=0}^{2\pi} \int_{\bar{\Omega}} p_{0\bar{x}}^* \left[\frac{1}{2} (u_0 - \tilde{x}_{0t}) |u_0 - \tilde{x}_{0t}| + M_1 (u_{0t} - \tilde{x}_{0tt}) \right] \mathrm{d}V \mathrm{d}t. \qquad (5.36)$$

In the rigid limit, M_1-dependent integral averages to zero and the expression for $\mathcal{D}$ above simplifies to the rigid-canopy contribution (2.39). However, we note that in both the rigid and the flexible problem, only the momentum exchange along the x-direction is responsible for the wave decay.

5.3.6 *Summary of the multiple-scales analysis*

In summary, we deduce from the multiple-scales analysis that the wave and the canopy are decoupled at leading order. Hence, the wave is sinusoidal

with depth variation at leading order, given by (5.21). Suppose the system is initialised with a known amplitude $A(x = 0)$ and wavenumber $k(x = 0)$. To solve for the evolution of the amplitude $\mathrm{d}A/\mathrm{d}x$ at $x = 0$, we first determine $\mathcal{D}$ (5.36), which depends on:

(i) The local amplitude $A(x = 0)$ and wavenumber $k(x = 0)$ via u_0 in (5.21b);

(ii) The time-harmonic solutions of both the horizontal velocity and acceleration, $\tilde{x}_{0t}$ and $\tilde{x}_{0tt}$, of every plant in $\bar{\Omega}$ (illustrated in Figure 5.2) due to this wave. The dynamics of individual plants can be determined from the beam equation (5.28). The details of the numerical solutions of the beam equation are given in §5.4.1.

Finally, the value of $\mathcal{D}$ can be substituted into the differential equation (5.35) to determine $\mathrm{d}A/\mathrm{d}x$ at $x = 0$. This can be used to predict A at the neighbouring spatial increment. The process can be recursed to obtain the profile $A(x)$. We now discuss the practicalities in solving for $A(x)$.

Although the new solvability condition (5.35)–(5.36) is a compact generalisation of the rigid-canopy problem, it appears at first sight that it is computationally costly to solve for $A(x)$ due to the canopy dynamics. In particular,

1. For any given $x = X$, we need to evaluate the wave-induced dynamics of every plant that is rooted between $\bar{x} \in [\bar{X}, \bar{X} + 2\pi]$.
2. We have to update $A(x)$ and $k(x)$, and repeat step 1 for every x along the domain since the wave continuously evolves along x.

In the next section, we will illustrate how we can simplify step 1 from solving for multiple plant configurations to the configuration of a single plant. After giving some numerical strategies and physical insights on the local canopy dynamics, in §5.6, we will also illustrate how we can simplify step 2 in different special cases.

5.4 NUMERICAL INSIGHTS ON THE CANOPY DYNAMICS

In the multiple-scales analysis in the previous section, we have derived that the plant dynamics are involved in determining the evolution of the wave along the domain. In this section, we explore the local canopy configuration by solving for time-harmonic solutions of (5.28). We will first outline the numerical strategies involved in solving for the canopy configuration before we present our results. Since we only solve for the leading-order dynamics, we drop the subscript ('0') for convenience. Furthermore, we also write $M = M_1 + M_2$.

5.4.1 Numerical strategy for solving individual plant configurations

For a given flow u (5.21b) and dimensionless parameters C_{eff} and M, we solve for periodic solutions of the plant configuration (5.28) numerically

in MATLAB. We first discretise time-derivatives in (5.28) explicitly using a second-order backward finite-difference method and solutions from the previous time steps. At each time step, we solve a boundary value problem for $\tilde{x}$ in $\bar{z}$ with the inbuilt solver `bvp4c`. We then iterate in time with time step $\Delta t = 2\pi/1000$ until every configuration that we have solved over a time period is 2π-periodic in time. In particular, we define that any two plant configurations $f(\bar{x}, \bar{z}, t)$ and $g(\bar{x}, \bar{z}, t) = f(\bar{x}, \bar{z}, t + 2\pi)$ are identical if

$$\frac{\|f - g\|}{\|f\|} = \frac{\sqrt{< f - g, f - g >}}{\sqrt{< f, f >}} = \sqrt{\frac{\int (f - g)^2 \, \mathrm{d}\bar{z}}{\int f^2 \, \mathrm{d}\bar{z}}} < 10^{-2}. \tag{5.37}$$

5.4.2 *Canopy dynamics over one wavelength*

Suppose we have solved the time-harmonic configurations of a single plant that is rooted at a given $\bar{x} = \bar{X}$ over a time period. To solve for the configuration of any neighbouring plants, the key concept here is to exploit the linearity of the wave. In particular, since the plants are assumed to be identical, the configuration of a given plant at a given time is identical to the original plant configuration with an appropriate temporal shift.

The details of this temporal shifting are as follows. Without loss of generality, suppose we have evaluated the original plant configuration at $\bar{X} = 0$ for $t \in [0, 2\pi]$. To evaluate the configuration of a new plant that is at $\bar{X} = n\Delta t \in [0, 2\pi]$ at time $t = m\Delta t \in [0, 2\pi]$, with $n, m \in \mathbb{N}$, we use the form of u from (5.21b) but now with the argument

$$\bar{X} - t = (n - m)\Delta t, \tag{5.38}$$

in the cosine function. Thus the desired wave is identical to a wave at $\bar{x} = 0$ but at time

$$t = -(n - m)\Delta t = \begin{cases} (m - n)\Delta t, & \text{if } m \geq n, \\ 2\pi - (n - m)\Delta t, & \text{otherwise.} \end{cases} \tag{5.39}$$

With this temporal shift (equivalent to a spatial shift along the domain), we can evaluate the configuration of any given plant that is rooted at $\bar{X} \in [0, 2\pi]$. The correspondence between space and time is illustrated in Figure 5.3 for the two cases of $M = 0$ (blue) and $M = 0.5$ (orange). Again, recall that we defined $M \equiv M_1 + M_2$.

In terms of the multiple-scales analysis, once we have determined $\tilde{x}_0$ by the above procedure, then we can then evaluate $\mathcal{D}$ in (5.36), which is subsequently used to solve for the evolution of the amplitude (5.35).

Based on the observations in Figure 5.3, we might ask the question of whether the fluid velocity in the wave and the beam velocity are in phase. More specifically, note that the fluid velocity at the tip is given by u_0 evaluated at $\bar{z} = \bar{h} - \bar{H}$, while the plant velocity is given by $\tilde{x}_t$ at the same height.

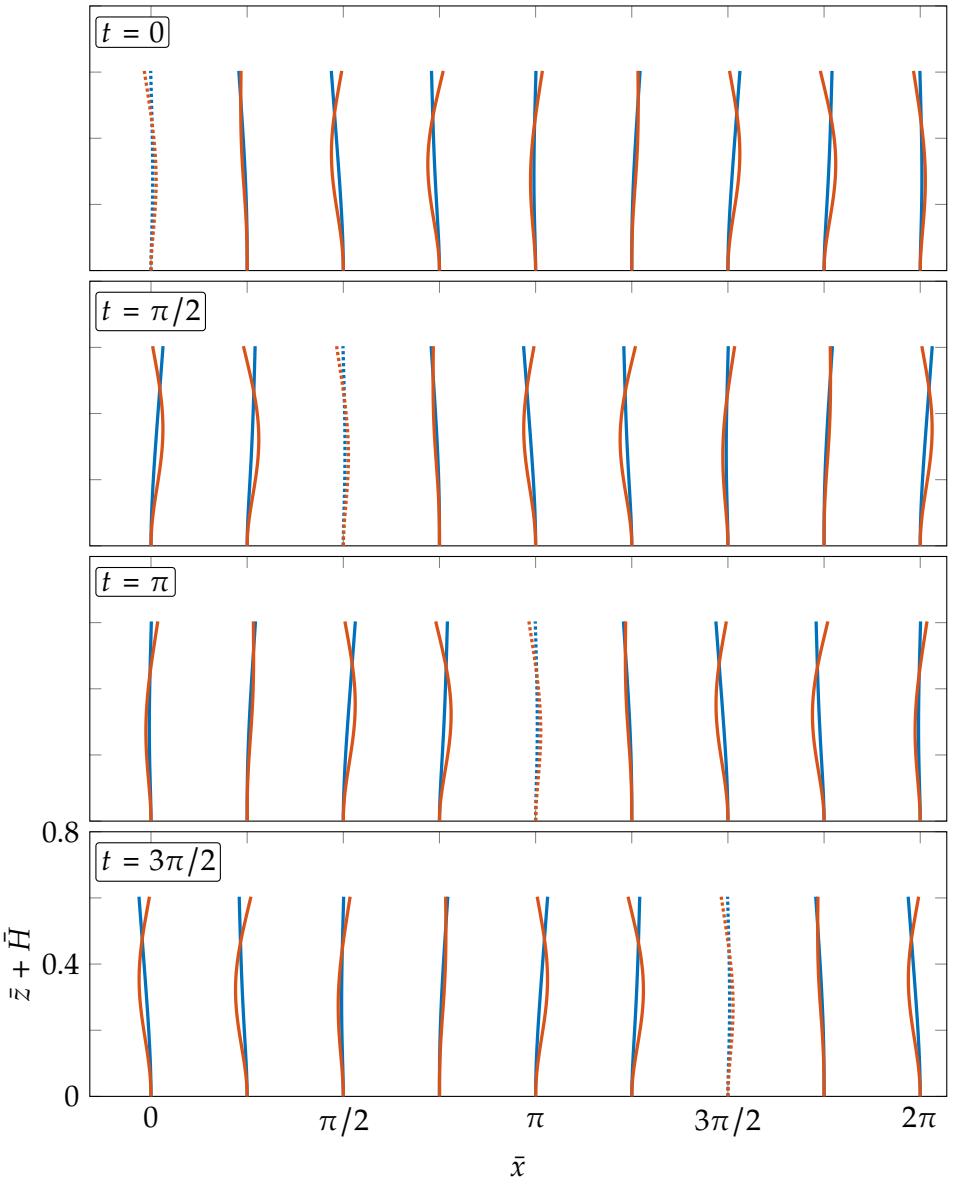

Figure 5.3: Periodic canopy configurations over one wavelength at different instances in time, solved using (5.28) and the procedures in §5.4.1. Blue and orange beams correspond to individual plants with inertia neglected ($M = 0$) and incorporated ($M = 0.5$) respectively. The dotted beam lines indicate plants that have the *same* configuration due to the linear theory stated in §5.4.2. Below this caption, we also plot the velocity of both the water wave u (5.21b) (black) and the plants $\tilde{x}_t$ from the main figure at $\bar{z} = \bar{h} - \bar{H}$. The parameters used to generate this figure coincide with the flume experiments by Luhar et al. (2017) (see §5.5 for further details). In particular, we have: $A = 1$, $k = 1.14$, $\bar{H} = 1.21$, $C_{\text{eff}} = 10^4$, $\alpha = 0.068$; $\bar{h} = 0.5\bar{H}$ and $\alpha\bar{\gamma} = 0.1$.

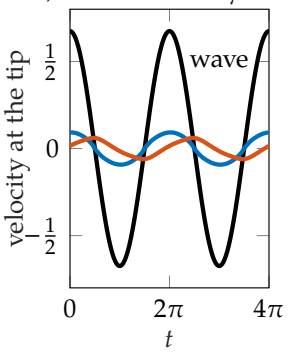

In Figure 5.3, we notice from the main figure that if inertial effects are insignificant compared to drag, the plant-deflections (blue) would monotonically increase with distance from the root. Furthermore, from the side-figure below the caption, we also find that the plant velocity (blue) is in phase with the fluid velocity (black). However, both observations are not universal – we demonstrate this with the example of $M = 0.5$ (orange) where drag and inertial effects are comparable. Here, the non-monotonicity in plant deflection is noted in the main figure, while the out-of-phase behaviour is noted in the side figure.

Several studies have also sought to understand wave-induced beam deflections as a function of wave frequency – depending on the regime, the phase difference between the wave and plant velocities may or may not increase with wave frequency. We refer the reader to the more detailed

discussion in Gijón Mancheño (2016) and the references therein.

For the remainder of this section, we will highlight some asymptotic insights which are particularly relevant to the experimental observations in §5.5, as well as for the calculation of A. This discussion parallels that found in the work of Leclercq and de Langre (2018).

5.4.3 *Resonance effects due to flexibility*

We observe that under certain conditions, a flexible plant may experience additional load effects compared to a rigid plant, even when they share the same (undeformed) geometry. This can be explained by the fundamental frequencies of a plant that is submerged in water. Specifically, let us consider a steady-state base flow, with $\mathbf{u}_t = \mathbf{0}$ in (5.28). In the limit of $M = M_1 + M_2 \gg 1$, we notice that the dynamics are essentially a force balance of the form

$$\tilde{x}_{\bar{z}\bar{z}\bar{z}\bar{z}} = -C_{\text{eff}} M \tilde{x}_{tt} \tag{5.40}$$

with the same boundary conditions as before. Since the problem is linear in $\bar{z}$ and t with constant coefficients, suppose we let $\tilde{x} = f(\bar{z})e^{i\Lambda t}$ (real part understood), the boundary value problem then reduces to the eigenvalue problem

$$f'''' = C_{\text{eff}} M \Lambda^2 f \tag{5.41}$$

for eigenvalue $C_{\text{eff}} M\Lambda^2$ with $f(-\bar{H}) = 0$, $f'(-\bar{H}) = 0$, $f''(-\bar{H} + \bar{h}) = 0$, $f'''(-\bar{H} + \bar{h}) = 0$. Since we have scaled time so that the wave has period 2π, we fix $\Lambda = 1$ and determine values of $C_{\text{eff}} M$ such that the system resonates (by solving for non-trivial solutions f). We will give numerical examples of such effects in §5.5.

5.4.4 *In the limit of very flexible plants*

We also recall from our beam equation (5.28) that the plant deflection is balanced by the load via the flexibility parameter C_{eff}. Hence, in the limit where $C_{\text{eff}} \to \infty$, which corresponds to the plant having negligible resistance to the fluid load, we expect the plant to be advected by the flow with matching velocities $\tilde{x}_t \to u$ given by (5.21b). This solution for $\tilde{x}$, however, does not satisfy the clamped boundary condition at the root. Hence, we can understand what happens in this very flexible limit by considering a singular perturbation analysis in the vicinity of the root.

We begin by rescaling $\bar{z} = -\bar{H} + \epsilon Z$ for some $\epsilon \ll 1$ and rewrite the displacement as

$$\tilde{x} = -A(x)\frac{\cosh[k(\bar{z} + \bar{H})]}{\sinh k\bar{H}} \sin(\bar{x} - t) + \tilde{\epsilon} f(Z, t), \tag{5.42}$$

so that $u_0 - \tilde{x}_t = -\tilde{\epsilon} f_t$ for some factor $\tilde{\epsilon}$ that will be determined later.

Substituting the expansions into the beam equation (5.28) give

$$\frac{1}{\epsilon^4 C_{\text{eff}}}\left[A\frac{\cosh(k\epsilon Z)}{\sinh k\bar{H}}\sin(\bar{x}-t)-\tilde{\epsilon}f\right]_{ZZZZ}=\frac{1}{2}\tilde{\epsilon}^2 f_t|f_t|+\tilde{\epsilon}Mf_{tt} \tag{5.43}$$

with the boundary conditions $\tilde{\epsilon}f(0)=A\sin(\bar{x}-t)/\sinh k\bar{H}$, $f_Z(0)=0$, $f\to 0$ as $Z\to\infty$. Since we want to choose $\tilde{\epsilon}$ so that the relatively displacement f near the root is $O(1)$, we take $\tilde{\epsilon}=1$. Hence,

$$\frac{1}{\epsilon^4 C_{\text{eff}}}\left[Ak^4\epsilon^4\frac{\cosh(k\epsilon Z)}{\sinh k\bar{H}}\sin(\bar{x}-t)-f_{ZZZZ}\right]=\frac{1}{2}f_t|f_t|+Mf_{tt}. \tag{5.44}$$

The appropriate balance of this equation is to have $\epsilon=C_{\text{eff}}^{-1/4}$. By expanding the dependent variables in powers of ϵ, the relative displacement f at leading order satisfies the equation

$$f_{ZZZZ}=-\left(\frac{1}{2}f_t|f_t|+Mf_{tt}\right), \tag{5.45}$$

with the boundary conditions $f(0)=A\sin(k\bar{x}-t)/\sinh k\bar{H}$, $f_Z(0)=0$, $f\to 0$ as $Z\to\infty$. We solve for the periodic solution of this boundary value problem numerically, using the same method as for solving the original beam equation (5.28) outlined in §5.4.1.

Physically, the derivation indicates that in this flexible limit, most of the plant is advected with the flow and is under negligible load. Most of the load is contributed by the boundary layer close to the root, where the plant is upright due to the clamping condition. The size of this boundary layer scales with $C_{\text{eff}}^{-1/4}$, as reported from previous studies (Mullarney and Henderson, 2010; Luhar and Nepf, 2016; Leclercq and de Langre, 2018). Finally, we also note that since the convergence is weak, it requires $C_{\text{eff}}\gg 1$ for the asymptotic approximation to be valid. For example, it requires C_{eff} to increase by a factor of 16 for the boundary layer to reduce its thickness by a factor of 2.

5.5 VERIFICATION OF THE PLANT MODEL

With the insights that we have on plant dynamics, we compare our dynamic beam model on a single plant (5.28) against experimental data. We will consider the recent experimental work from Luhar and Nepf (2016) and Lei and Nepf (2019) on individual blades in horizontal wave flumes. In particular, since we are primarily interested in the blade load, which affects the momentum loss in the wave, we will compare the predicted and measured values of load.

Although the expressions for individual components of the plant load (5.16e) are adapted from Luhar and Nepf (2016) and Leclercq and de Langre (2018), we emphasise that the comparison between the total load and experimental data, and the resulting insights are new. More importantly, the comparison will be useful when we extend the results to our main work on wave evolution in the presence of flexible canopies.

We emphasise that the process of comparing experimental results to the mathematical models we have developed formed a highly non-trivial part of this work. This was primarily due to two factors. The first is that different measures for the load ratio, $\mathcal{R}$, were used by Luhar and Nepf (2016) and Lei and Nepf (2019), and both quantities involve different normalisations. Secondly, extensive parameter sweeps of our computational model(s) are required to cover the requisite experimental range.

5.5.1 *Effective length and the flexibility parameter*

Suppose we have a submerged plant with a uniform cross-section that is loaded by a steady uniform flow. The *effective length* of this plant h_{eff} is first defined by Luhar and Nepf (2011) to be the dimensional length for which a rigid version of the plant would experience the same horizontal load. We thus have the load ratio

$$\mathcal{R} = \frac{h_{\text{eff}}}{h} = \frac{\int_{s=0}^{h} F_{\parallel,\text{flex}}\,\mathrm{d}s}{\int_{s=0}^{h} F_{\parallel,\text{rigid}}\,\mathrm{d}s}, \tag{5.46}$$

with $F_{\parallel}$ being the measured horizontal load per unit length. By construction, the load ratio $\mathcal{R}$ tends to unity in the rigid-plant limit. The definition of $\mathcal{R}$ has since been generalised to analyse oscillatory (unsteady) flows, where inertial effects are present in addition to drag. Since $\mathcal{R}$ is then time-dependent, there are multiple conventions that we can consider. To compare with the experimental data from previous work by Luhar and Nepf (2016) and Lei and Nepf (2019), we will consider both the maximum value over a period, T, and the root-mean-square value over a period, given by

$$\mathcal{R}_{\text{max}} = \frac{\max\limits_{t\in[0,T]}\left(\int_{s=0}^{h} F_{\parallel,\text{flex}}\,\mathrm{d}s\right)}{\max\limits_{t\in[0,T]}\left(\int_{s=0}^{h} F_{\parallel,\text{rigid}}\,\mathrm{d}s\right)} \quad \text{and} \quad \mathcal{R}_{\text{rms}} = \frac{\operatorname{rms}\limits_{t\in[0,T]}\left(\int_{s=0}^{h} F_{\parallel,\text{flex}}\,\mathrm{d}s\right)}{\operatorname{rms}\limits_{t\in[0,T]}\left(\int_{s=0}^{h} F_{\parallel,\text{rigid}}\,\mathrm{d}s\right)} \tag{5.47}$$

respectively. The expression for $\mathcal{R}_{\text{max}}$ can also be referred to as the *reconfiguration number* for terrestrial flows (de Langre, 2008). In both sets of experiments that we are considering, the loads on rigid plants *i.e.* the denominators of $\mathcal{R}_{\text{max}}$ and $\mathcal{R}_{\text{rms}}$ (5.47) are calculated via (5.32), while both of the numerators are measured. Hence, another verification on the load model (5.32) is to check whether $\mathcal{R} \to 1$ in the rigid-plant limit.

Finally, before we continue, measurements from both studies are presented as plots of $\mathcal{R}$ as a function of C—a rescaled version of the flexibility parameter C_{eff} in (5.30). The mapping between the two flexibility parameters is

$$C = \frac{\operatorname{csch}(k\bar{H})}{C_D}\left(\frac{h}{g/\omega_0^2}\right)^4 C_{\text{eff}}. \tag{5.48}$$

The additional hyperbolic function in the expression for C originates from selecting different fluid velocity scales compared to our nondimensionalisation. In our work, we have chosen to scale $\mathbf{u}$ with the dimensional quantity $A_0\omega_0$ in (2.15). Whilst, in both sets of experiments, the velocity scales were chosen to be the horizontal velocity along the bed; this velocity is $A_0\omega_0 \operatorname{csch} k\bar{H}$ by linear wave theory in (5.21b). Hence, the ratio between the two velocity scales gives $\operatorname{csch} k\bar{H}$.

	Luhar and Nepf (2016)	Lei and Nepf (2019)
Mean water depth H	30 cm	28 cm
Wave amplitude A_0	0.9–3.9 cm	0.8–5 cm
Time period $T = 2\pi/\omega_0$	1.1–2 s	2 s
Blade material	HPDE or foam	LPDE
Blade length h	5–20 cm	3–15 cm
Blade width b	2 cm	1 cm
Blade thickness W	0.19 cm	0.005–0.025 cm
Drag coefficient C_D	3.65–6.47	2.92–5.09

Table 5.1: Selected physical parameters of the experiments in Luhar and Nepf (2016) and Lei and Nepf (2019) on waves-induced dynamics of a single blade.

5.5.2 *Experimental setup*

In both sets of experiments, a flexible rectangular blade with uniform cross-section is placed in cross-flow with the incident monochromatic wave in a horizontal flume that has a fixed mean water depth *i.e.* $\mathrm{d}H/\mathrm{d}x = 0$. Measurements of different quantities are made once transients have decayed, and the system is periodic in time. We summarise the various experimental parameters in Table 5.1.

For the drag coefficient C_D that is presented in Table 5.1, we note that a range of values have been quoted, despite that the blade cross-sections are uniform. The quoted values from both studies originate from established experimental results on how C_D varies under a uniform oscillatory flow (Keulegan and Carpenter, 1958). Assuming that the relations hold under flexible conditions, the values are above $C_D = 1.95$, which is the coefficient for steady flows.

Since the full details of individual data points are not always available, we have chosen to predict using the mean between the minimum and the maximum value of C_D quoted in Table 5.1 in each study. We emphasise that there are no fitting parameters in this problem.

To measure the total load, we recall from Table 2.1 that $M_2 \ll M_1$ for blades. Hence, when we apply a local force balance on the blade in (5.16c), we can approximate $M_2 = 0$ so that

$$\frac{\partial \mathbf{T}}{\partial s} + \mathbf{F} = \mathbf{0}, \tag{5.49}$$

which can be integrated to get

$$\mathbf{T}(s = 0) = \int_{s=0}^{h} \mathbf{F}\, \mathrm{d}s. \tag{5.50}$$

Since the horizontal component of $\mathbf{T}(s = 0)$ coincides with the total horizontal load on the blade, the numerators of $\mathcal{R}_{\max}$ and $\mathcal{R}_{\mathrm{rms}}$ (5.47) are measured

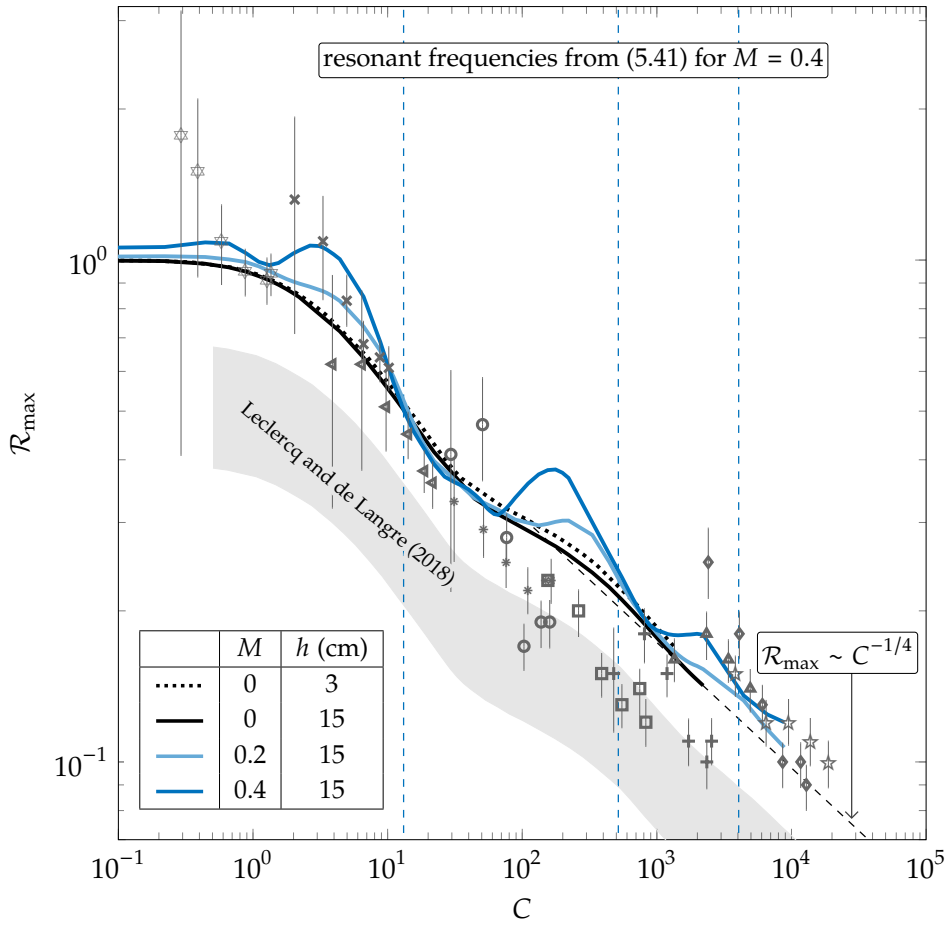

Figure 5.4: Predicting the load ratio $\mathcal{R}_{\max}$ (5.47) as a function of the flexibility parameter C (5.48) for wave-induced plant oscillations with a fixed wave frequency. The data points for $\mathcal{R}_{\max}(C)$ are extracted from Lei and Nepf (2019) with markers indicating different plant lengths and thicknesses (see values in their original article). Our numerical predictions from solving (5.28) with $C_D = 4.01$ (see §5.5.2) are shown via black and blue. For $M = 0$ (black), predictions for the shortest (dotted) and longest (solid) plants are shown; for the longest plants, the annotated dashed line gives the $\mathcal{R}_{\max} \sim C^{-1/4}$ approximation for $C \gg 1$ from solving (5.45). The shaded region indicates the small-deflection predictions from Leclercq and de Langre (2018, Figure 10b) using nonlinear beam theory for $M \ll 1$.

by Luhar and Nepf (2016) and Lei and Nepf (2019) at the clamping position of a blade using a force transducer.

We are now ready to compare loads predicted with (5.28) versus experimental data. We separate our analysis between the load radio $\mathcal{R}_{\max}$ from Lei and Nepf (2019) for waves with a fixed frequency and values of $\mathcal{R}_{\text{rms}}$ from Luhar and Nepf (2016) for waves with different frequencies.

5.5.3 *Analysis of the experimental results on $\mathcal{R}_{\max}$*

In Figure 5.4, we compare our theoretical predictions on plant loads under a single wave frequency against experimental data for different plant lengths and inertia.

If we neglect inertia (by taking $M = 0$), we capture most of the quantitative behaviour with a single theoretical curve, shown black, in Figure 5.4. This is highlighted by the collapse between simulations with the shortest blade and the longest blade (when we compare the black dotted line and the black solid line). The agreement remains good until $C \gtrapprox 10^2$ where we are, on average, over-predicting the load, despite having a similar decay rate. Finally, in the very flexible limit where $C \gg 1$, the data is more scattered, possibly due to the viscous effects from the substrate. However, we

capture the decay $\mathcal{R}_{\max} \sim C^{-1/4}$ reasonably well in this advective regime, as predicted by the solutions of (5.45) and shown dashed. Although we have mentioned in §5.4.4 that this scaling argument is presented in previous studies, in this work we have justified the scaling law using both formal asymptotic analysis and explicit calculation of the prefactor in $\mathcal{R}_{\max} \sim C^{-1/4}$.

When we account for inertial effects ($M > 0$), we can then capture the interesting behaviour of having more load compared to the rigid problem when C is $O(1)$. This is associated with light and dark blue curves in Figure 5.4. We also observe individual data points which are significantly above the $M = 0$ predictions for larger values of C. Recall the resonant predictions of §5.4.3 which are valid for $M \gg 1$. In the figure, we plot the predicted resonant values of C for the case of $M = 0.4$ – these vertical dashed lines can then compared to the peaks of the dark blue profile.

Although the number of resonant frequencies predicted by (5.41) for $M \gg 1$ matches the number of local peaks of $\mathcal{R}_{\max}$ when $M = 0.4$, their precise values do not. The presence of drag and damping effects due to fluid viscosity and the blade material itself appear to downshift the resonant frequencies. However, we expect the agreement to improve for larger values of M. Finally, we also expect the predictions to be more accurate for the fundamental mode since damping effects, which are typically negligible, can become more prominent with higher-order modes.

As an aside, we note that the study by Lei and Nepf (2019) assumed that the maximum load on a rigid plant is achieved when $u_0 = \max(u_0)$. At that instant, the flow is assumed to be steady. Hence, this is mathematically equivalent to evaluating the load on a rigid plant with $M = 0$ in (5.47). Although we found from the linear theory that this is only a reasonable approximation for flows with $M \ll 1$, we have used their convention for $\mathcal{R}_{\max}$ for a faithful comparison. This explains why the $M > 0$ theory curves tend to values above unity as $C \to 0$.

5.5.4 *Choosing the appropriate drag coefficient*

We now discuss the choice of the drag coefficient, C_D, on blades in our plant model, which primarily appears in the force expression (5.28), but then affects the values of $\mathcal{R}$ in (5.47). The key is that in rigid limit of $C \to 0$, if the chosen scaling on C_D is correct, then we expect $\mathcal{R}_{\max} \to 1$ as $M \to 0$. Indeed this seems to be the case by Figure 5.4 for the choice of $C_D = 4.01$.

What happens if C_D is chosen differently? Let us consider the choice of $C_D = 2$ studied in the work of Leclercq and de Langre (2018) – this choice corresponds to the steady flow drag coefficient $C_D = 1.95$ from Keulegan and Carpenter (1958). In their work, the authors produce a theoretical prediction of $\mathcal{R}_{\max}(C)$, which is computed by solving a nonlinear beam equation valid for $M \ll 1$ (Leclercq and de Langre, 2018, §4.1). To compare this with the measurements by Lei and Nepf (2019), we thus

rescale their predicted $\mathcal{R}_{\max}$ values by plotting $2\mathcal{R}_{\max}/C_D$ for $C_D = 2.92$–5.09 (following Table 5.1). This produces the light-grey band in Figure 5.4.

By comparing the envelope of the light-grey band with the black dotted line in Figure 5.4, we demonstrate that our short-blade predictions are in very good agreement with the prediction curve of Leclercq and de Langre (2018), up to a vertical shift due to the choice of C_D for normalisation. This indicates two things:

(i) We can consider the flow to be uniform in depths when the waves are sufficiently long or the blades are sufficiently short (the shallow-water limit).

(ii) Linear and nonlinear beam theory coincide in the experimental regimes considered. However, unlike the theoretical curve of Leclercq and de Langre (2018) which is based on setting the value of $C_D = 2$, we find that the experimental data of Lei and Nepf (2019) is better explained using an oscillatory drag coefficient shown in Figure 5.4. These two models coincide in the limit where the wave period is infinite [see the discussion on C_D in §2.10.1].

5.5.5 *Analysis of the experimental results on $\mathcal{R}_{\text{rms}}$*

We now turn our attention to the period-averaged load ratio $\mathcal{R}_{\text{rms}}$ (5.47). Compared to the analysis for $\mathcal{R}_{\max}$, this analysis is more important since values of $\mathcal{R}_{\text{rms}}$ ultimately determines the wave evolution (in the multiple-scales analysis). This discussion relates to Figure 5.5. In this figure, shaded regions bounded by solid and dotted lines correspond to fixing values of M (added mass) and T (period) and varying h.

We first note that the experimental data points $(C, \mathcal{R}_{\text{rms}})$ as determined in Luhar and Nepf (2016), correspond to different wave periods, T. In their study, the authors anticipate that the data points should collapse – hence, they are independent of wave period, T, and plant length. However, our theoretical analysis for $\mathcal{R}_{\max}$ indicates that this collapse is only true in the shallow-water limit—this can be seen via the orange theory curves in Figure 5.5 where the dashed and solid lines are nearly coincident. In other cases, such as for the black curves, predictions vary with plant length due to the increasing variation of u_0 in (5.21b) along z – this is seen via the gap in the shaded bands of Figure 5.5. Meanwhile, there is a tight collapse in the experimental data with $\mathcal{R}_{\text{rms}} \approx 1$ when C is small, again indicating that it is reasonable to predict load using the oscillatory drag coefficient.

If we neglect inertia (by taking $M = 0$), we predict a very similar decay trend between $\mathcal{R}_{\text{rms}}$ and $\mathcal{R}_{\max}$ as we increase C. Quantitatively, we are able to bound a majority of the data points for foam blades (shown using grey markers in Figure 5.5) and capture the $\mathcal{R}_{\text{rms}} \sim C^{-1/4}$ decay particularly well in the $C \gg 1$ limit (see §5.4.4). However, we are on average under-predicting the load for HPDE-blades (shown using black markers in Figure 5.5).

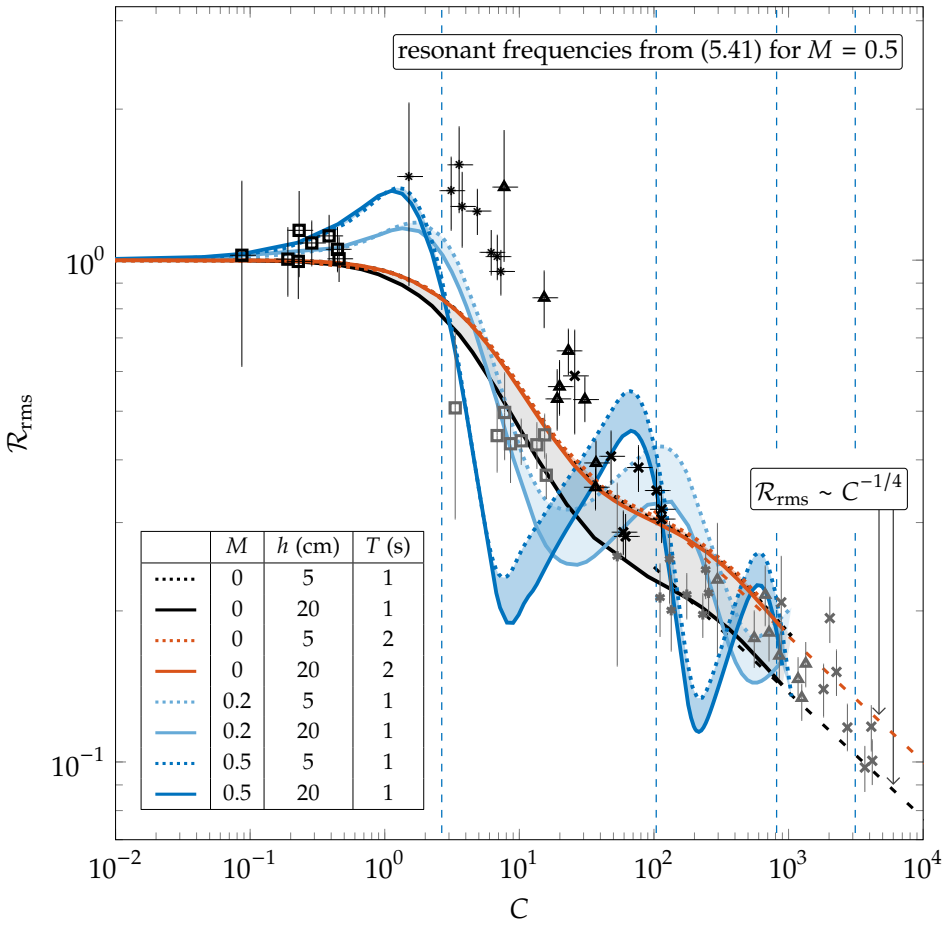

Figure 5.5: Predicting the load ratio $\mathcal{R}_{\text{rms}}$ (5.47) as a function of the flexibility parameter C (5.48) for wave-induced plant oscillations. The data points for $\mathcal{R}_{\text{rms}}(C)$ are extracted from Luhar and Nepf (2016) with markers indicating different plant lengths (the precise values can be found in the original article). The numerical predictions from solving (5.28) with $C_D = 5.06$ (see §5.5.2) are shown in curves. Predictions for the shortest and the longest plants are plotted with dotted and solid curves respectively with the region in-between shaded in for intermediate lengths. For the longest plants with $M = 0$, the annotated dashed lines give the $\mathcal{R}_{\text{rms}} \sim C^{-1/4}$ approximation for $C \gg 1$ from solving (5.45).

When we consider inertial effects, we note that unlike the predictions for $\mathcal{R}_{\text{max}}$, which have values that are close to the $M = 0$ case unless we have resonance, the predictions oscillate both above and below the $M = 0$ case. This is an observation that has not been discussed in previous studies. We appear to be able to capture the resonance effects that are observed in HPDE blades, albeit at smaller values of C – the theory curves reside on the left of the experimental data in Figure 5.5. We anticipate that this originates from the reported small curvature in the cross-section of the HPDE blades in Lei and Nepf (2019), which approximately doubled the flexural rigidity compared to its flat-blade value. We plotted the quoted variations as horizontal error bars in Figure 5.5. However, we expect this estimate to further vary due to the phase of the flow, and also the variations of the deformed cross-sections along the blade. Furthermore, a higher flexural rigidity would improve the data collapse between the two materials.

When $C \gg 1$, the $M = 0$ predictions seem to be more accurate and we do not observe any higher-order resonance effects in this set of data. We give two reasons for this. Firstly, it has been observed by Luhar and Nepf (2016) that for sufficiently long blades, the blades may twist due to infinitesimal asymmetries. This may significantly reduce the cross-sectional area for parts that are away from the root and hence, reducing added mass effects.

Secondly, it can be due to viscous damping and material damping that exists in reality.

As an aside, we note that the values of C which correspond to resonance (shown with blue vertical dashed lines) are independent of plant length. This is the result of nondimensionalising the arc length of the plant with the plant length, h, in Luhar and Nepf (2016) [and Lei and Nepf (2019)]. The corresponding eigenvalue problem to (5.41) is hence solved over a fixed (dimensionless) domain. Consequently, the eigenvalues are fixed.

5.5.6 *Summary on the validity of the plant model*

We have considered a plant model that is based on linear beam theory with the loading model by Luhar and Nepf (2016) and Leclercq and de Langre (2018) using an oscillatory drag coefficient. This model captures the majority of values of $\mathcal{R}_{\max}$ and $\mathcal{R}_{\mathrm{rms}}$ in Figures 5.4 and 5.5 even if we neglect inertia. A constant added mass model helps to capture the resonance effects at intermediate values of C due to the fundamental mode.

For all shallow-water waves, we can consider a single theory curve that is only C-dependent, which is a powerful tool in terms of applications. For sufficiently short waves or sufficiently long plants, however, we have to account for the variations of the flow field along the depth.

The experimental data also suggests that if we are to consider a refined load model, it should incorporate a variable added mass M, which varies with the cross-sectional change due to twisting. This would allow us to capture the fundamental mode while reducing to the $M = 0$ approximation when $C \gg 1$.

5.6 EVALUATING THE AMPLITUDE ALONG THE DOMAIN

After the discussion and insights on individual plants in §§5.4–5.5, we want to understand how the wave-induced plant dynamics ultimately affect the wave on the canopy-scale. In particular, we want to substitute the evaluated load into the multiple-scales analysis in §5.3 to determine the wave amplitude $A(x)$ via the solvability condition (5.35)–(5.36).

5.6.1 *The effects of inertia*

For rigid plants, we recall from the derivation of the solvability condition in §2.5 that the effects of inertia (both added mass and virtual buoyancy) average to zero over a time period of the wave. For flexible plants, however, the analysis on $\mathcal{R}_{\mathrm{rms}}$ (5.47) in §5.5 indicates that unlike the rigid-plant problem, inertial effects can still affect the time-averaged load (and hence, the momentum loss in the flow) by affecting the plant dynamics.

Although our modelling framework can be generalised to plants with all geometries, we have focused our analysis on the two main cases of blades

and cylindrical beams. From the beam equation (5.28), recall that we defined $M \equiv M_1 + M_2$. Moreover, for the case of blades, with $M = M_{\text{blade}}$, when we previously compared predictions between plant model and experimental data in §5.5, we applied the approximation $M_{\text{blade}} \sim M_1$ since $M_2 \ll M_1$. On the other hand, $M_1 = M_2$ for cylindrical beams (see Table 2.1), and thus their configurations are the same as for blades, with an inertial coefficient of

$$M_{\text{cylinder}} = 2M_{\text{blade}}. \tag{5.51}$$

Provided that the other dimensionless parameters are the same, we can thus solve for the dynamics of both blades and cylindrical beams simultaneously by mapping M accordingly.

5.6.2 *Extending from local canopy dynamics to wave evolution*

We also recall from the summary of the multiple-scales analysis in §5.3.6 that to solve for $A(x)$, we first (i) fix the x-value, and evaluate the canopy dynamics over a wavelength of the fast scale; we then (ii) repeat this procedure at every point along the domain. In §5.4, we stated how we could exploit the linearity of the wave to address step (i) *i.e.* evaluating the local canopy dynamics based on a single plant. Here, we address step (ii) in determining $A(x)$, which also has its own subtleties.

We recall that the solvability condition (5.35) is given by

$$\frac{\pi^2 A}{\bar{\lambda} k \cosh^2 k\bar{H}} \left[2A(\bar{H} - 1)\frac{\mathrm{d}(k\bar{H})}{\mathrm{d}x} - (2k\bar{H} + \sinh 2k\bar{H})\frac{\mathrm{d}A}{\mathrm{d}x} \right] = \mathcal{D}, \tag{5.52}$$

where the canopy contribution is specified by

$$\mathcal{D} = \mathcal{D}\left(A(x), C_{\text{eff}}, M, k(x), \bar{h}\right). \tag{5.53}$$

In the above functional form for $\mathcal{D}$, the dimensionless water depth $\bar{H}(x)$ is not an independent parameter since it is determined from $k(x)$ via the dispersion relation (2.28).

A natural numerical strategy for solving A in (5.52) along the entire domain is to first determine $A'(x)$ at $x = 0$, march forward in x, and recurse by determining $A'(x)$ at the next increment at runtime. However, we can also apply a parameter sweep on values of $\mathcal{D}$ in (5.36) *a priori* and solve for $A(x)$ by reading off such values. In particular, we want to take advantage of the numerical predictions in §5.5, which are evaluated for base waves of unit amplitude $A = 1$. For this, we outline the sampling strategy below.

For rigid plants, the integral expression for $\mathcal{D}$ in (2.39) can be evaluated explicitly. In this case, we find that

$$\mathcal{D}\left(A, 0, M, k, \bar{h}\right) = \frac{8\pi}{9}\frac{k}{\cosh^3 k\bar{H}}(3\sinh k\bar{h} + \sinh^3 k\bar{h})A^3. \tag{5.54}$$

For flexible plants, our aim here is to rewrite the solvability condition (5.35) in terms of $\mathcal{D}(A = 1)$, up to some mapping for the other dimensionless parameters.

From the nondimensionalisation of the original set of governing equations in (5.16), we recall from Table 2.1 and (5.30) that with A_0 being the dimensional amplitude scale,

$$C_{\text{eff}} \propto A_0, \quad M \propto \frac{1}{A_0}, \quad \left(\text{and} \quad A \propto \frac{1}{A_0}\right). \tag{5.55}$$

If we are to replace A_0 with $A_0 A$ in the nondimensionalisation, we can express the rescaled solvability condition (5.35) in terms of the same function $\mathcal{D}$, but with $\mathcal{D}(1, C_{\text{eff}}A, M/A, k, \bar{h})$ [see (5.53)]. Returning to the solvability condition, in terms of the original nondimensionalisation, we can hence show that

$$\frac{\pi^2 A}{\bar{\lambda} k \cosh^2 k\bar{H}} \left[2A(\bar{H} - 1)\frac{\mathrm{d}(k\bar{H})}{\mathrm{d}x} - (2k\bar{H} + \sinh 2k\bar{H})\frac{\mathrm{d}A}{\mathrm{d}x}\right] = A^3 \mathcal{D}\left(1, C_{\text{eff}}A, \frac{M}{A}, k, \bar{h}\right), \tag{5.56}$$

with

$$\mathcal{D}\left(1, 0, \frac{M}{A}, k, \bar{h}\right) = \frac{8\pi}{9}\frac{k}{\cosh^3 k\bar{H}}(3\sinh k\bar{h} + \sinh^3 k\bar{h}) \tag{5.57}$$

in the rigid-canopy limit $C_{\text{eff}} \to 0$ by (5.54). With $\mathcal{D}$ being in the new form in the solvability condition (5.56), we can then solve for $A = A(x)$ solely based on plants dynamics which are evaluated for base waves with $A = 1$. In particular, we can make use of the numerical predictions from §5.5.

We now present some numerical examples of $\mathcal{D}$.

5.6.3 *Numerical examples of $\mathcal{D}$ for waves with unit amplitude*

In Figure 5.6, we present some numerical examples of $\mathcal{D}$ as a function of C_{eff} for different values of M. In the limiting case where the substrate is horizontal (so that both k and $\bar{H}$ are constant), we can deduce from (5.56) that

$$\frac{\mathrm{d}A}{\mathrm{d}x} = -\bar{\lambda}A^2\left[\frac{k\cosh^2 k\bar{H}}{\pi^2(2k\bar{H} + \sinh 2k\bar{H})}\mathcal{D}\left(1, C_{\text{eff}}A, \frac{M}{A}, k, \bar{h}\right)\right]. \tag{5.58}$$

Hence, we plot $\mathcal{D}\left(1, C_{\text{eff}}A, M/A, k, \bar{h}\right)$ as a function of the scaled flexibility $C_{\text{eff}}A$ for different values of M/A in Figure 5.6. We can gain some physical intuitions from both the figure and the equation above as the amplitude A varies.

(i) Firstly, $\mathcal{D}$ in Figure 5.6 is always positive. By (5.58), this implies that the wave amplitude A alway decays.

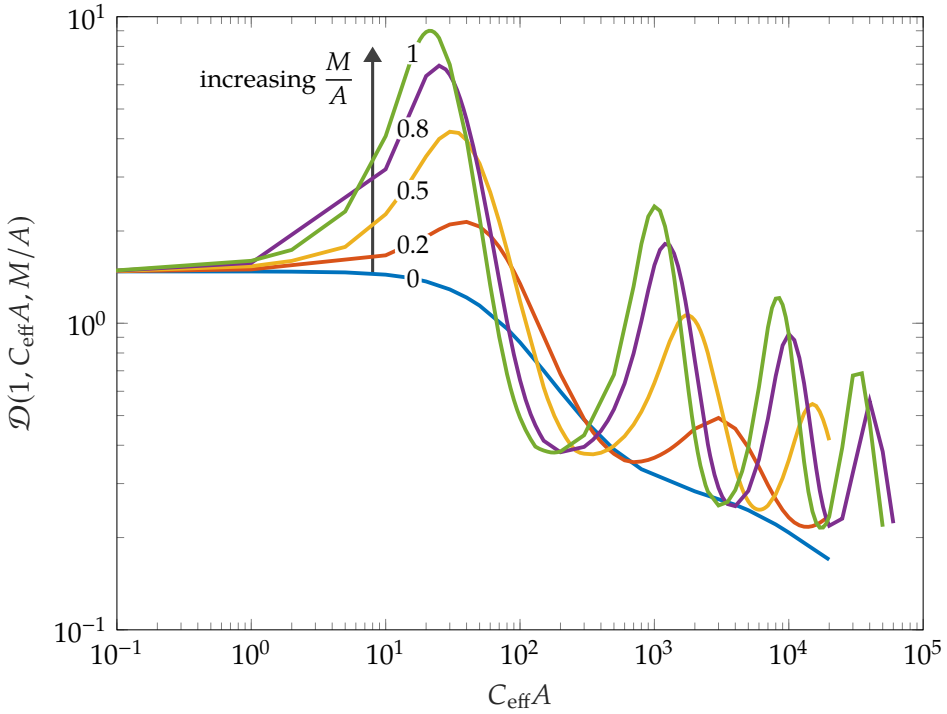

Figure 5.6: Canopy contribution $\mathcal{D}$ in the solvability condition (5.56) as a function of the scaled flexiblity parameter $C_{\text{eff}}A$ [see (5.30) for the definition of C_{eff}]. Colours indicate the effect of the scaled inertia M/A. The parameters are chosen to coincide with waves with time period $T = 1$ s and plants with length $h = 0.2$ m in Figure 5.5 for the experimental setup in Luhar and Nepf (2016). In the rigid-canopy limit $C_{\text{eff}} \to 0$, $\mathcal{D}$ is given by (5.54).

(ii) As A decreases, which corresponds to moving from right to left in Figure 5.6, plants become effectively stiffer. Mathematically, this is reflected in the A-scaling for the flexibility parameter C_{eff} in $\mathcal{D}$. Physically, as the wave decays, the plants undergo less deflection. Less deflection can also occur with stiffer plants. Hence, we have this interpretation of decreasing effective flexibility. Furthermore, as $C_{\text{eff}}A \to 0$, $\mathcal{D}$ tends to the constant value for rigid plants, given by (5.57).

(iii) For plants with $M > 0$, we know from the nondimensionalisation of the momentum sink $\mathbf{F}_0$ in (5.32) that drag scales quadratically with amplitude but inertial effects only scale linearly with amplitude. Hence, for smaller amplitude waves, the inertial effects become more prominent compared to drag. Mathematically, this is reflected in the $1/A$-scaling for the inertial parameter M in $\mathcal{D}$.

(iv) Unlike rigid plants, the variation of $\mathcal{D}$ in $C_{\text{eff}}A$ in Figure 5.6 implies that the local decay rate of A in (5.58) is not quadratic in A. In particular, when $M = 0$ (shown in blue), since $\mathcal{D}$ is always smaller than its rigid-canopy value (5.57) whenever $C_{\text{eff}}A > 0$, the amplitude decay for waves with flexible canopies are always weaker than the corresponding rigid-canopy problem.

We now use the results from this section on $\mathcal{D}$ in (5.56) to determine the wave amplitude $A(x)$.

From our analysis in §§5.3 and 5.6, we concluded that using our dynamic beam model (5.28) on flexible plants,

$$\frac{\mathrm{d}A}{\mathrm{d}x} \not\propto -\bar{\lambda}A^2 \tag{5.59}$$

in general by (5.58). For the constant depth problem, this is in contrast to the relation $\mathrm{d}A/\mathrm{d}x \propto -\bar{\lambda}A^2$ predicted by Lei and Nepf (2019). Although our predictions agree in the rigid-canopy limit with the expression of $A(x)$ given in (2.47)–(2.48) [up to a correction factor, which is considered by Lei and Nepf (2019) to account for the velocity reduction for flows within dense canopies], we now outline how the different modelling assumptions have resulted in the different predictions.

The modelling framework in Lei and Nepf (2019) considers that every flexible plant has an *effective length*, h_{eff} – we recall from §5.5 that this is the plant length which the rigid version of this plant would experience the same horizontal load. The plant length $\bar{h}$ in the rigid-canopy solvability condition (2.47) is then replaced by the effective length $\bar{h}_{\mathrm{eff}}$ so that for flexible plants

$$\frac{\mathrm{d}A}{\mathrm{d}x} = -\frac{8\bar{\lambda}}{9\pi}\frac{k^2}{\cosh k\bar{H}}\frac{3\sinh k\bar{h}_{\mathrm{eff}} + \sinh^3 k\bar{h}_{\mathrm{eff}}}{2k\bar{H} + \sinh 2k\bar{H}}A^2. \tag{5.60}$$

Firstly, since $\bar{h}_{\mathrm{eff}}$ is time-dependent, the authors have evaluated $\bar{h}_{\mathrm{eff}}$ based on the maximum load experienced over a period [see (5.47)]. Secondly, they have assumed that $\bar{h}_{\mathrm{eff}}$ is constant in the differential equation above (5.60). Based on our analysis on $\mathcal{D}$ in the solvability condition (5.58) in §5.6, this assumption is reasonable provided that A has small variations along the domain and that the plants are sufficiently stiff.

In this work, we attempt to give predictions which also accounts for both (i) the variation of plant load over a time period, and (ii) the new local canopy dynamics due to the variation of the amplitude along the domain.

We now present some numerical examples of $A(x)$ in Figure 5.7 for flows over horizontal substrates ($\mathrm{d}H/\mathrm{d}x = 0$). We divide our analysis into regimes where inertial effects are either negligible ($M = 0$) or comparable to drag ($M > 0$). We first consider the case where inertia is negligible ($M = 0$) *i.e.* momentum loss in the flow is solely due to drag [see (5.16e)]. In Figure 5.7, we observe that with increasing flexibility, the wave experiences a weaker decay. This is consistent with the analysis on $\mathcal{D}$ in §5.6 [see (iv) in §5.6.3]. Physically, increasing flexibility reduces a plant's resistance to fluid loading. This results in the plant advecting with the flow, which reduces relative velocity and subsequently drag.

For $M > 0$ however, we observe an interesting nonuniform variation in the profiles of $A(x)$ with increasing flexibility. First of all, we note that the rigid-canopy amplitude for $M > 0$ is identical to the $M = 0$ case for reasons explained in §2.5. For waves which are propagating through canopies

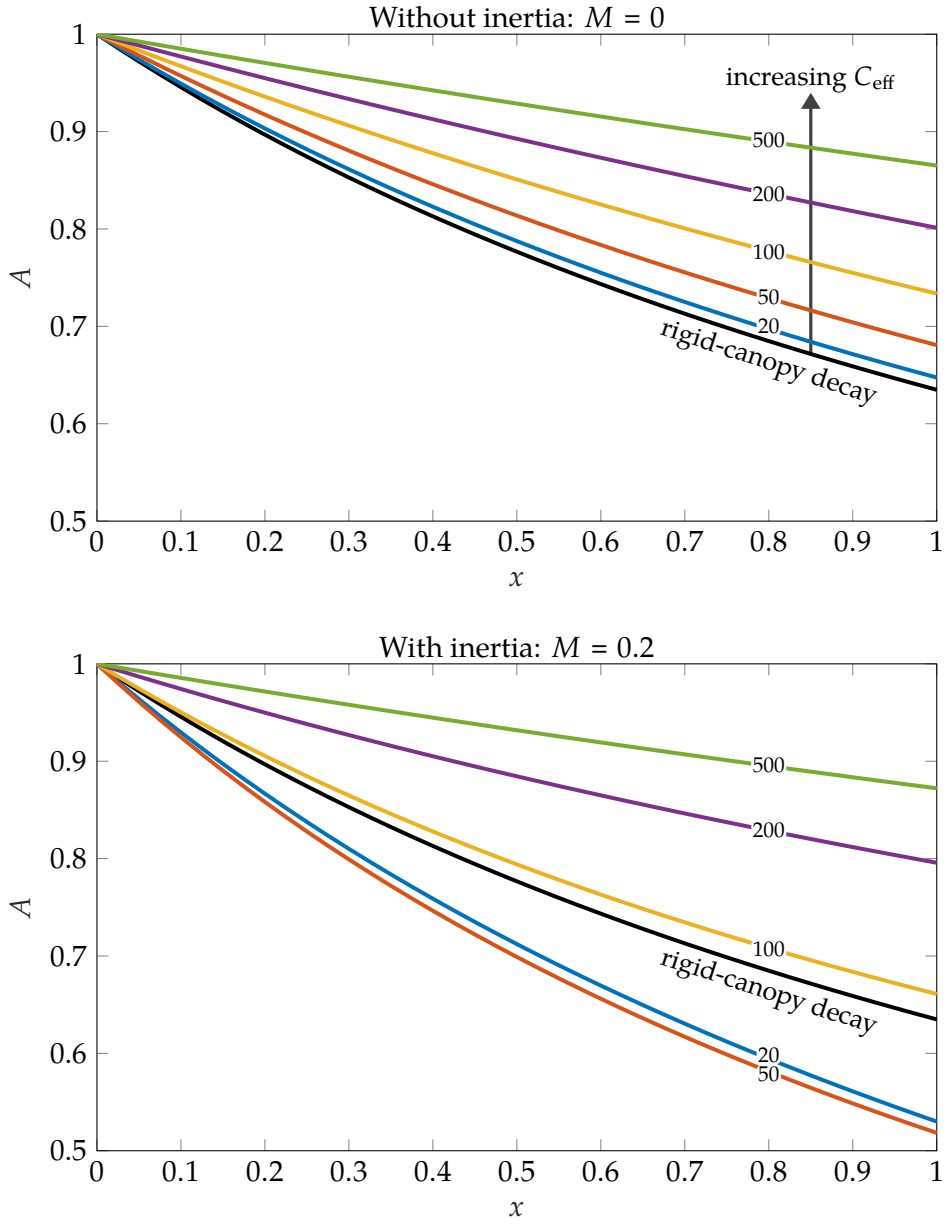

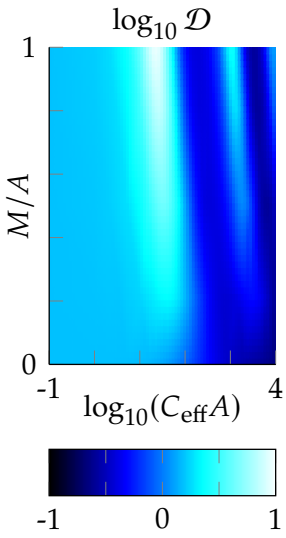

Figure 5.7: The effect of plant flexibility C_{eff} (5.30) on the evolution of the wave ampltiude A along a horizontal substrate. In both subfigures, x is the distance of propagation, normalised by the domain length $L = 100$ m. The rigid-canopy predictions (black) are given by (2.48). For $M = 0$, $\mathrm{d}A/\mathrm{d}x$ is determined from the blue curve for $\mathcal{D}$ in Figure 5.6. For $M > 0$, $\mathrm{d}A/\mathrm{d}x$ is evaluated by interpolating all of the plotted values in Figure 5.6. Below this caption, we plot this interpolated solution space for $\mathcal{D} = \mathcal{D}(C_{\text{eff}}A, M/A)$. In addition to the parameters used in Figure 5.6, we chose $\lambda = 0.02$ for the canopy density.

with $C_{\text{eff}} = 20$ and 50, the waves experience a stronger decay than in the rigid-canopy problem. This is explained by resonance effects near the fundamental frequency of the plants at the start of the domain (see values of $\mathcal{D}$ for the red curve in Figure 5.6). As we further increase C_{eff}, resonance effects diminish, and drag dominates the source of momentum loss. However, drag itself is also reduced with C_{eff} for the same physical reasons as in the $M = 0$ case above. Therefore, the waves experience a weaker decay.

In evaluating the numerical profiles of $A(x)$ in Figure 5.7 for $M > 0$, we interpolated the values of $\mathcal{D}$ which are plotted in Figure 5.6. An analogous interpolation on $\mathcal{D}$ can be done to account for flows with varying depth, with $k = k(x)$. This would require additional sampling of the plant dynamics in the high dimensional parameter space.

5.8 SUMMARY AND DISCUSSION

In this chapter, we considered the problem of small-amplitude waves propagating through flexible vegetation. This is an extension to the analysis in Chapter 2 on rigid vegetation, where the momentum loss in the flow is now additionally coupled to the plant dynamics, governed by the beam equations. The flexibility of the plants due to fluid loading is quantified by the dimensionless Cauchy number (5.17). By applying a multiple-scales analysis on this extended problem in §5.3, we derived a solvability condition for the wave amplitude A (5.35). To solve for A, we concluded that we have to evaluate the local plant dynamics at multiple positions in the flow, which requires additional computations. However, we emphasise that this is significantly more practical than solving the full system of equations in (5.16) numerically.

The most significant contribution of the work in this chapter is that it provides an important generalisation to the model and predictions by Lei and Nepf (2019). Our model, in contrast to theirs, includes the time variation of the canopy dynamics, and also provides a scheme that updates the downstream wave decay as a function of the local plant dynamics.

In addition to validating the numerical predictions from the beam model by comparing them with experimental data from Luhar and Nepf (2016) and Lei and Nepf (2019), the main conclusions are:

1. when inertial effects are negligible, waves experience less damping with increasing plant flexibility;
2. when inertial effects are comparable to drag, then resonance effects can cause significant damping to waves.

What if we have a combined current-wave flow? By following the multiple-scales analysis for the rigid-canopy problem in §3.4, we expect the wave decay to be affected by the velocity of the current, u_c, but not vice versa. Hence, for flexible canopies, the same mathematical deductions would give the same solvability condition for A as for the pure wave problem in this chapter *i.e.* in (5.35)–(5.36), but with u_0 in (5.21b) replaced by $u_c + u_0$. Since the base flow has changed, the resultant local plant dynamics also have to be re-evaluated. Although we can foresee that the plant configurations will have a mean bias downstream, we do not expect to gain much more physical insights after analysing these two extensions separately in this chapter and Chapter 3.

6 INSTABILITIES OF FLOWS THROUGH FLEXIBLE VEGETATION

In time and with water,
everything changes.

Leonardo da Vinci

SYNOPSIS

We consider the temporal instabilities of current-dominated flows through a submerged flexible canopy. We first predict the steady configuration of the plants in response to a unidirectional flow. The linear stability analysis on such steady configurations suggests new insights into the development of instabilities at the surface of the canopy. In particular, we show that shear at the top of the canopy is a dominant factor in determining the onset of instabilities known as *monami*. Based on numerical and asymptotic analysis of the quadratic eigenvalue problem, the system is shown to be stable if the canopy is sufficiently sparse. An article based on this work has been published in the *Journal of Fluid Mechanics* (Wong et al., 2020).

6.1 INTRODUCTION

Part of the emerging interest in instabilities of flow through a canopy is sparked by a phenomenon known as *monami* (see the schematic in Figure 6.1)—the progressive, synchronous oscillation of aquatic vegetation (Nepf, 2012). *Honami*, its counterpart in terrestrial flows is readily observable in daily life when the wind blows across a patch of grass or a crop field (de Langre, 2008) – this is further illustrated in Figure 1.3. Only relatively recently has the phenomenon of honami been explained by Raupach et al. (1996), pointing out that such instabilities arise due to a shearing mechanism that resembles the Kelvin-Helmholtz instability on free mixing layers at the top of the canopy. Once the shear exceeds a threshold, waves develop in the flow which roll into vortices over time (see top insets of Figure 6.1). The argument that such instabilities are distinct from boundary layer instabilities is supported by comparing statistics of turbulent kinetic energy in experiments (Finnigan, 2000; Poggi et al., 2004).

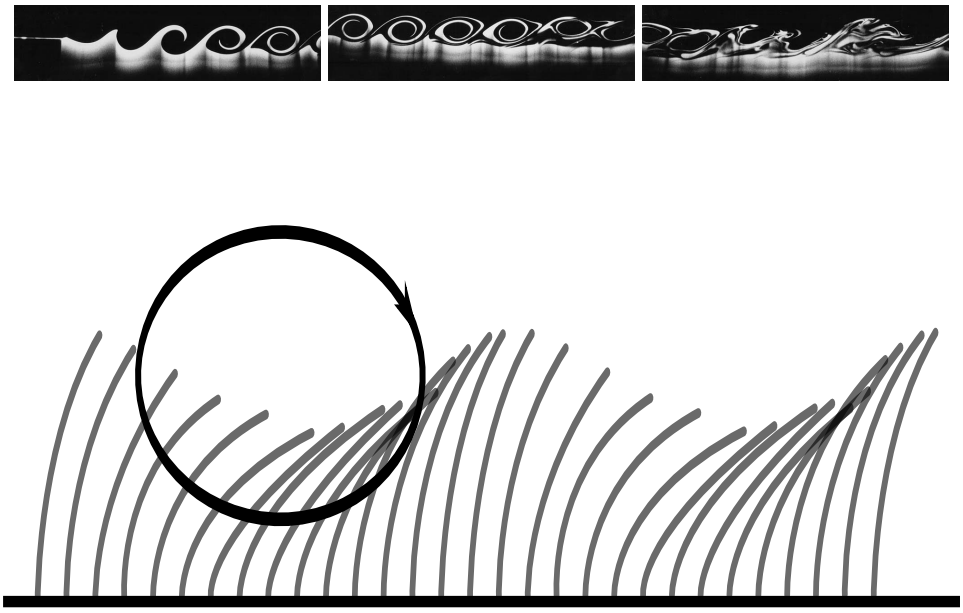

Figure 6.1: Schematic diagram of *monami*—the synchronous oscillation of aquatic plants. The grey curved obstacles indicate aquatic vegetation and the black arrow indicates a rolling vortex. The insets at the top are snapshots of Kelvin-Helmholtz instability developing along a channel [reprinted by permission from Springer Nature Customer Service Centre GmbH: Springer Environmental Fluid Mechanics Cushman-Roisin (2005), Copyright (2006)]. These show the result of two flows with different velocities meeting upstream (left) and mixing as they propagate downstream (right). Details on the laboratory experiment are given in Lawrence et al. (1991).

Many theoretical studies have applied similar explanations to the development of monami by analysing the stability of steady states in their respective model—a summary of previous work and their key features are presented in Table 6.1. The vast majority of previous work has fallen into two categories: either models of flow over a specified set of rigid obstacles; or models where plant deformation can occur, but only under a known imposed flow *e.g.* wave-induced plant oscillations in §5.4. There have been fewer models that emphasise the coupling between deformation and flow. We highlight, in particular, the pioneering work of Alben et al. (2002) on flow past a single elastic strip in 2D, Dupont et al. (2010) on flow past an array of rigid straight elements that are free to tilt, and Singh et al. (2016) on establishing the dependence between viscous effects and flow instabilities by analysing flows through an array of rigid beams.

The work in this chapter builds on previous work by Singh et al. (2016) and Sharma et al. (2017) in analysing the mechanical aspects of instabilities in flows through submerged vegetation. In particular, we are interested in addressing the unknown role of flexibility, the free surface, and inertial effects which have not been considered previously. For this, we adapt the mechanical model from Chapter 5 on waves through flexible vegetation to analyse current-dominated flows, in which the plants may experience large angles of deflection. By also incorporating viscous effects, we assess criteria and mechanisms for the onset of instability. Furthermore, we investigate under which regimes the governing equations for the flow and vegetation are approximately decoupled.

The structure of this chapter is as follows. In §6.2, we adapt the coupled flow-canopy model from Chapter 5 and highlight the key dimensionless

	FLOW	OBSTACLE	STABILITY ANALYSIS	COUPLING
Alben et al. (2002)	solved	elastic strip	no	
Ghisalberti and Nepf (2004)	solved	rigid cylinder	no	
Poggi et al. (2004)	solved	rigid cylinder	no	
Dupont et al. (2010)	solved	mechanical oscillator	yes	yes
Zeller et al. (2015)	solved	rigid strip	no	
Luminari et al. (2016)	solved	rigid cylinder	yes	no
Singh et al. (2016)	solved	rigid cylinder	yes	no
Zampogna et al. (2016)	solved	rigid cylinder	yes	no
	solved	rigid porous medium	yes	no
Sharma et al. (2017)	solved	dynamic cluster	yes	yes
	solved	rigid porous medium	yes	no
Leclercq and de Langre (2018)	imposed	elastic beam	yes	no
This work	solved	elastic beam	yes	yes

Table 6.1: Modelling approaches of a selection of previous work on current-dominated flows through a single or a collection of obstacles. The 'Coupling' category states whether the stability analysis takes into account for perturbations of both the flow and the obstacles.

parameters involved in such current-dominated regimes. Using this coupled model, we first analyse the steady unidirectional flows that develop along the domain in §6.3. In §§6.4–6.8, we assess the temporal stability of such steady configurations. The analysis attempts to predict the critical parameters for instabilities which resemble monami and highlight how these parameters differ when the plants are rigid and vertical. We summarise our findings in §6.9 and discuss limitations in §6.10.

6.2 MATHEMATICAL MODEL

To reduce complexity many previous models arbitrarily replace the free surface with a flat stress-free boundary (Singh et al., 2016). Here we wish to be more faithful to the physics and include the full free-surface conditions. However, with the analysis from Chapter 3 on combined current-wave flows, we can foresee that the water depth would vary along the domain to compensate vegetative drag (a more detailed discussion is given in §3.3.2). To compromise between having both full free-surface conditions and a simple unidirectional flow as our steady base flow, we consider a three-dimensional domain that is inclined at a constant angle of elevation β. By defining x as the downstream distance, and z as the perpendicular distance from the substrate, the fluid flows between $0 \leq z \leq H + \eta$, where H is the mean height, and $\eta = \eta(x, y, t)$ is free-surface displacement. The bottom substrate at $z = 0$ is covered by a fully-submerged vegetative canopy that consists of identical plants of length h, which shall later be specified as elastic beams. A schematic of the setup is given in Figure 6.2.

Our main objective in the forthcoming sections is to present a set of equations which further generalises the mathematical model (5.16) on waves through flexible vegetation in Chapter 5. The generalisation is to account for the additional physics considered, including viscosity (and its resultant

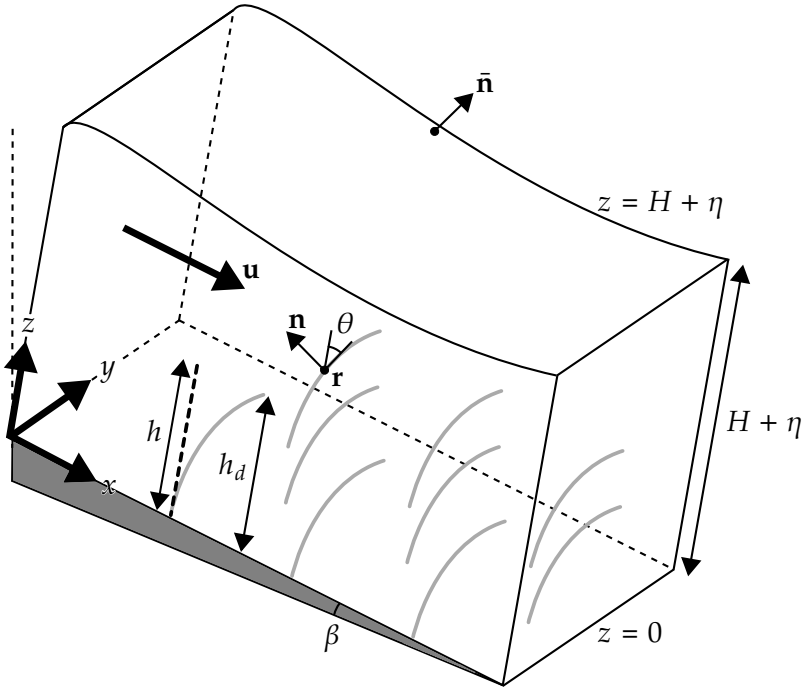

Figure 6.2: Schematic diagram of flow through a portion of the canopy. The fluid domain above has flow velocity $\mathbf{u}$, height $H+\eta$, and a free surface with outward normal $\bar{\mathbf{n}}$. The grey vegetative element with the centreline at $\mathbf{x} = (x, y, z) = \mathbf{r}$ denotes a plant that is rooted to the bottom substrate at $z = 0$, which has an angle of inclination, β. The plant configuration is parametrised by the arc length s and local angle of deflection θ. The vertical dashed line with length h denotes the configuration when it is load free and h_d is the height of the plant in the deformed configuration.

new boundary conditions), and currents which are gravity-driven. We thus consider an incompressible fluid with velocity $\mathbf{u} = (u, v, w)$ at time t satisfying the dimensional Navier-Stokes equations

$$\nabla \cdot \mathbf{u} = 0, \tag{6.1}$$

$$\rho\left(\frac{\partial \mathbf{u}}{\partial t} + \mathbf{u} \cdot \nabla \mathbf{u}\right) = -\nabla \bar{p} + \rho \mathbf{g} + \rho \nu^* \nabla^2 \mathbf{u} - \bar{\mathbf{F}}, \tag{6.2}$$

where ρ is the density of water, $\bar{p}$ is pressure (not the dynamic pressure), and $\mathbf{g} = g(\sin\beta, 0, -\cos\beta)$ is acceleration due to gravity. To account for the effect of viscosity on the onset of monami, we follow the approach by Singh et al. (2016) and assign a constant eddy viscosity ν^* in place of the kinematic viscosity of water. Finally, $\bar{\mathbf{F}}$ remains to be the homogenised sink (5.11), up to a positive shift H in z with the new coordinate system. For the remainder of this work, we confine our analysis to two-dimensional configurations (in xz) since the geometry and initial conditions are independent of y (the formal reduction from three-dimensional to two-dimensional flows is given in §2.3).

6.2.1 *Nondimensionalisation*

Since we are in the current-dominated regime, we nondimensionalise the mathematical model with distinct scales from the pure wave problem (5.15). Suppose we consider

$$[\mathbf{x}] = [s] = [\eta] = H, \quad [\mathbf{u}] = U, \quad [t] = \frac{H}{U}, \quad [\bar{p}] = \rho U^2, \quad [\mathbf{T}] = \rho b C_D H U^2. \tag{6.3}$$

	Symbol	Expression
Reynolds number	Re	$\dfrac{UH}{\nu^*}$
Froude number	Fr	$\dfrac{U}{\sqrt{gH}}$
Canopy density	λ	$C_D\bar{N}bH$
Cauchy number	C_Y	$\dfrac{\rho b C_D H^3 U^2}{EI}$
Added mass	M_1	$\dfrac{C_M m}{\rho b C_D H}$
Beam inertia (or virtual buoyancy)	M_2	$\dfrac{m}{\rho b C_D H}$

Table 6.2: A summary of the dimensionless parameters in the governing equations of current-dominated flows through a homogenised canopy (6.4). The definitions of the corresponding parameters in the pure wave problem are given in (5.17) for C_Y, and Table 2.1 for λ and $M_{1,2}$.

In particular, foreseeing the calculations ahead, we take U to be the streamwise velocity at the free surface for steady unidirectional flows: we will specify such flows in §6.3.

With all the variables being henceforth dimensionless, we have the following system of equations:

$$\nabla\cdot\mathbf{u}=0, \tag{6.4a}$$

$$\frac{\partial\mathbf{u}}{\partial t}+\mathbf{u}\cdot\nabla\mathbf{u}=-\nabla\bar{p}+\frac{1}{\mathrm{Fr}^2}\mathbf{g}+\frac{1}{\mathrm{Re}}\nabla^2\mathbf{u}-\lambda\sec\theta\mathrm{H}(h_d-z)\mathbf{F}, \tag{6.4b}$$

$$\frac{\partial\mathbf{T}}{\partial s}+\mathbf{F}=M_2\frac{\partial^2\mathbf{r}}{\partial\tau^2}, \tag{6.4c}$$

$$\frac{\partial^2\theta}{\partial s^2}=C_Y(-T_\parallel\cos\theta+T_\perp\sin\theta), \tag{6.4d}$$

with the homogenised sink $\mathbf{F}$ as defined in (5.16e). With $\boldsymbol{\sigma}$ as the fluid stress tensor, the corresponding boundary conditions in this problem are

$$\boxed{\text{substrate at } z=0}\quad w=0,\ \frac{\partial u}{\partial z}+\frac{\partial w}{\partial x}=0, \tag{6.4e}$$

$$\boxed{\text{free surface at } z=1+\eta}\quad \frac{\mathrm{D}}{\mathrm{D}t}(z-1-\eta)=0, \tag{6.4f}$$

$$\bar{\mathbf{n}}\cdot\boldsymbol{\sigma}\cdot\bar{\mathbf{n}}=0,\ \bar{\mathbf{n}}\times\boldsymbol{\sigma}\cdot\bar{\mathbf{n}}=\mathbf{0}, \tag{6.4g}$$

$$\boxed{\text{cantilever beam}}\quad \mathbf{T}|_{s=h}=\mathbf{0},\ \theta|_{s=0}=0,\ \left.\frac{\partial\theta}{\partial s}\right|_{s=h}=0, \tag{6.4h}$$

$$\boxed{\text{constraint on } h_d}\quad \int_0^{h_d}\sec\theta\,\mathrm{d}z=h. \tag{6.4i}$$

The dimensionless parameters Re, Fr, λ, M_1, M_2 and C_Y are defined in Table 6.2. In particular, we note that in apart from the Reynolds number and the Froude number, other parameters have been defined in the previous chapters on oscillatory flows. In this problem, however, we have rescaled length with the mean height H instead of the wave amplitude or the wavelength [see Table 2.1 and (5.17)]. Hence, for the remainder of this chapter,

we will consider the parameters defined in Table 6.2. We also note that since we are mostly considering the steady problem, we assume that the drag coefficient C_D (2.61) takes the steady value (see §2.10.1 for discussions on variations of the drag coefficient).

Along the bottom substrate, we impose a shear-free condition for the fluid based on the negligible size of the local boundary layer from experimental observations (Dunn et al., 1996; Ghisalberti and Nepf, 2002).

In contrast to the oscillatory flow problem in Chapter 5, the nature of the monami problem typically involves more significant canopy deformations. Hence, it is natural to write the Navier-Stokes equations with the Eulerian specification while keeping the beam equations in body-fitted coordinates (*i.e.* arc length s at time τ). At a given time, these systems are related via $\partial \mathbf{r}/\partial s = (\sin\theta, \cos\theta)$. We examine the translation between the two coordinate systems more fully in §6.4.1.

6.3 STEADY UNIDIRECTIONAL FLOW

In this section, we seek solutions of the governing system (6.4) where the flow is steady and unidirectional along the x–axis (the streamwise direction), with

$$\mathbf{u} = u(z)\hat{\mathbf{e}}_x. \tag{6.5}$$

The study of unidirectional flows provides not only significant mathematical reduction, but is also justified by many related experiments. For example, such flows emerge from current-dominated flows in experimental flumes with vegetation. As a result, field studies, controlled experiments, and more recently, numerical simulations typically consider such flows [see Nepf (2012) and references therein].

If the canopy is finite, we note that there exists a transition region for the incoming flow starting from the leading edge of the canopy (Chen et al., 2013). The mixed conclusions on how to systematically predict this development length have typically resulted in calibrations and verifications in individual experiments [see *e.g.* Dunn et al. (1996); Ghisalberti and Nepf (2004)]. The flow then settles beyond this region. Hence, when we consider steady unidirectional flows of the form stated above in (6.5), we are only considering the fully-developed regions downstream.

6.3.1 Theoretical formulation

Since the flow is both steady and unidirectional, we can deduce from the momentum equation of the fluid (6.2) that the free surface is flat at $z = 1$ and the flow is driven by a constant pressure gradient. It is particularly convenient to re-write the pressure, $\bar{p}$, in terms of the dynamic fluid pressure,

p, as we have done in the previous chapters, so that

$$p = \bar{p} - \frac{1}{\mathrm{Fr}^2}(x \sin\beta - z\cos\beta). \tag{6.6}$$

We consider our equations in terms of p for the remainder of this chapter. The governing equations (6.4) reduce to the following system of differential equations:

$$\frac{\mathrm{d}^2 u}{\mathrm{d}z^2} = -\mathrm{ReP} + \mathrm{H}(h_d - z)\frac{\mathrm{Re}\lambda}{2} u\cos\theta|u\cos\theta|, \tag{6.7a}$$

$$\frac{\mathrm{d}T_\parallel}{\mathrm{d}s} = -\frac{1}{2}u\cos^2\theta|u\cos\theta|, \tag{6.7b}$$

$$\frac{\mathrm{d}T_\perp}{\mathrm{d}s} = \frac{1}{2}u\sin\theta\cos\theta|u\cos\theta|, \tag{6.7c}$$

$$\frac{\mathrm{d}^2\theta}{\mathrm{d}s^2} = C_Y(-T_\parallel\cos\theta + T_\perp\sin\theta), \tag{6.7d}$$

where the pressure gradient $\mathrm{P} = \sin\beta/\mathrm{Fr}^2 > 0$ is imposed such that $u(1) = 1$ [*i.e.* the velocity scale U in Fr is chosen to make $u(1) = 1$]. To solve for the steady configuration, we rewrite the equations (6.7) as a system of ordinary differential equations in z and solve the equations numerically [with the corresponding boundary conditions in (6.4)] in MATLAB using the boundary value problem solver `bvp4c`. Once we obtain the solution, the centreline of the homogenised plant configuration, $\mathbf{r}$, can be determined in Cartesian coordinates from the relation

$$\frac{\mathrm{d}x}{\mathrm{d}z} = \tan\theta. \tag{6.8}$$

As an aside, we note that our model predicts a parabolic flow profile above the canopy rather than logarithmic as in classic boundary layer flows (Nikora, 2010). Since the canopy enhances flow mixing above the canopy, it has been experimentally shown that the logarithmic scaling is only recovered when $z \gtrapprox 2h$ [see Sharma and García-Mayoral (2018) and references therein]. Provided that $h = O(1)$, which is typical for aquatic vegetation (Nepf, 2012), we can assume that we are not in the logarithmic regime. For flows with $h \ll 1$, the transition zone where $h \leq z \lessapprox 2h$ is known as the roughness sublayer (Finnigan, 2000).

6.3.2 *Unidirectional flows through rigid canopies*

We first examine the case of flow through a rigid canopy ($C_Y = 0$), considering the limits of sparse and dense canopies.

Flow approximations for sparse canopies ($\lambda \ll 1$)

The velocity profiles at different values of the canopy density parameter λ are shown in Figure 6.3. In the limit the canopy density tends to zero,

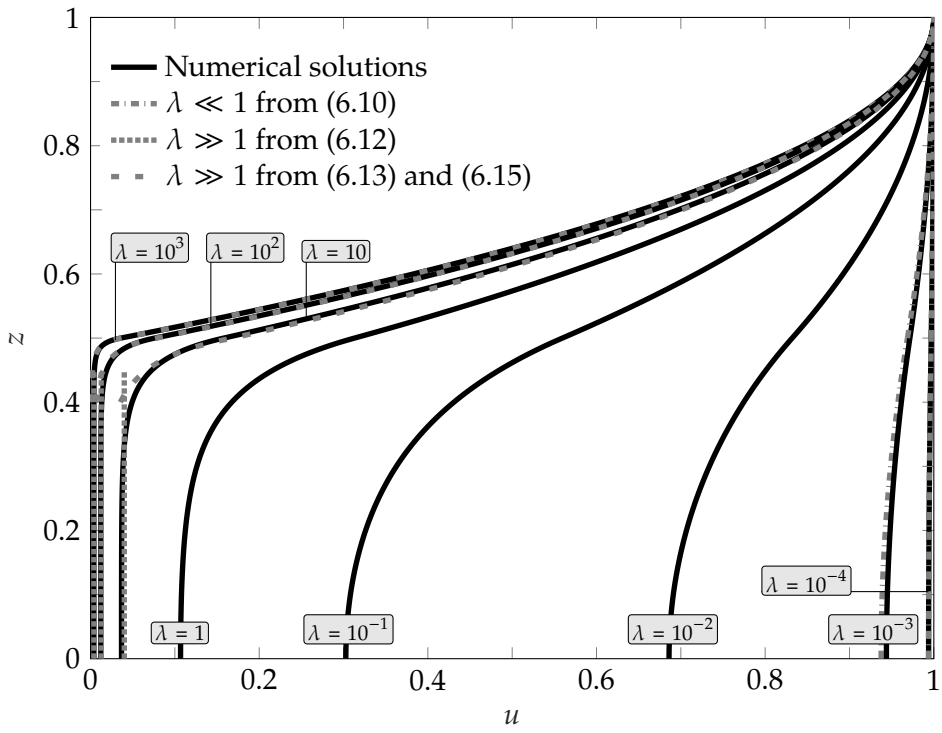

Figure 6.3: The effect of increasing canopy density to steady unidirectional flows through a rigid canopy when $\mathrm{Re} = 10^3$ and $h = 0.5$. Flow profiles are shown in black solid lines with grey lines indicating asymptotic approximations as described in §6.3.2.

the velocity profile approaches that corresponding to uniform unobstructed flow. Noting that a more convenient perturbation parameter is $\mathrm{Re}\lambda$, we let $u = 1 + \mathrm{Re}\lambda\tilde{u}$ and $\mathrm{P} = \lambda\tilde{\mathrm{P}}$. Then by (6.7a), we have

$$\frac{\mathrm{d}^2\tilde{u}}{\mathrm{d}z^2} \sim \begin{cases} -\tilde{\mathrm{P}} + \dfrac{1}{2}, & \text{if } z \le h, \\ -\tilde{\mathrm{P}}, & \text{if } z > h. \end{cases} \tag{6.9}$$

By solving for $\tilde{u}$ (and $\tilde{\mathrm{P}}$), we deduce that

$$u = 1 + \mathrm{Re}\lambda\tilde{u} \sim \begin{cases} 1 - \dfrac{\mathrm{Re}\lambda}{4}(1-h)(h-z^2), & \text{if } z \le h, \\ 1 - \dfrac{\mathrm{Re}\lambda}{4}h\,(z-1)^2\,, & \text{if } z > h, \end{cases} \tag{6.10}$$

confirming the behaviour illustrated in Figure 6.3. In particular, as the canopy density increases, the flow velocity reduces everywhere due to increased drag; however, as expected, the reduction is greatest within the canopy itself ($z \le h$).

Flow approximations for dense canopies ($\lambda \gg 1$)

We also observe from Figure 6.3 that in the dense-canopy limit the flow is apparently divided into two outer regions ($z < h$ and $z > h$), as well as a transition region near $z = h$. In the limit $\lambda \to \infty$, we observe that the flow becomes approximately uniform in the canopy, where $0 \le z \le h$ and $h - z = O(1)$. From (6.7a), we have that in this region,

$$\frac{\mathrm{d}^2u}{\mathrm{d}\hat{z}^2} = -\mathrm{ReP} + \frac{\mathrm{Re}\lambda}{2}u|u|, \tag{6.11}$$

and thus to leading order, the pressure gradient balances the drag, and the velocity below the canopy satisfies

$$u_{\text{below}}(z) \sim \left(\frac{2\mathrm{P}}{\lambda}\right)^{1/2} \quad \text{for } 0 \le z \le h \text{ and } h - z = O(1). \tag{6.12}$$

This matches the result of Poggi et al. (2004, §5) and Singh et al. (2016, §3). This approximation is plotted with dotted lines in Figure 6.3.

Before deriving the solution in the boundary layer at the top of the canopy, we note that the solution for $z \ge h$ can be found exactly: integrating (6.7a) and applying the surface boundary conditions, $u(1) = 1$ and $u'(1) = 0$, we find that for the solution above the canopy,

$$u_{\text{above}}(z) = \mathrm{ReP}\left(z - \frac{z^2}{2} - \frac{1}{2}\right) + 1 \quad \text{for } z \ge h. \tag{6.13}$$

Note that the constant quantity, P, itself must be expanded in λ and will be determined through boundary conditions. In the inner region, we substitute $z = h - \lambda^{-1/3}\xi$ and $u = \lambda^{-1/3}\tilde{u}$ into (6.7a) with $\xi \ge 0$. The inner solution satisfies

$$\left(\frac{\mathrm{d}\tilde{u}}{\mathrm{d}\xi}\right)^2 \sim \frac{\mathrm{Re}}{3}\tilde{u}^3 + C, \tag{6.14}$$

where the integration constant $C = 0$ to match (6.12) to this order of approximation. As a result, taking the relevant branch of (6.14) and requiring that the solution is continuous with (6.13), we have that for the solution within the boundary layer,

$$u_{\text{layer}}(z) \sim \left[\left(\frac{\mathrm{Re}\lambda}{12}\right)^{1/2}(h - z) + \left\{1 - \frac{\mathrm{ReP}}{2}(1-h)^2\right\}^{-1/2}\right]^{-2}, \tag{6.15}$$

which is valid for $z \le h$ and $h - z = O(\lambda^{-1/3})$. Finally, to determine the leading-order behaviour of the constant pressure gradient, P, we require that the gradient of (6.13) matches that given by the boundary layer of (6.14) at $z = h$. This yields

$$\mathrm{P} \sim \frac{2}{\mathrm{Re}(1-h)^2}\left(1 - \left[\frac{12}{\mathrm{Re}\lambda(1-h)^2}\right]^{1/3}\right). \tag{6.16}$$

Note that in the above expression, we have retained the first two orders in P so as to ensure higher accuracy in the above-canopy solution for a wider range of λ values. In Figure 6.3, we observe good agreement between the exact numerical flow profiles and the matched-asymptotic approximations given in (6.13) and (6.15).

6.3.3 *Unidirectional flows through flexible canopies*

Having gained some intuition on flows through rigid canopies, we now explore the differences in flows through flexible canopies ($C_Y > 0$)—the

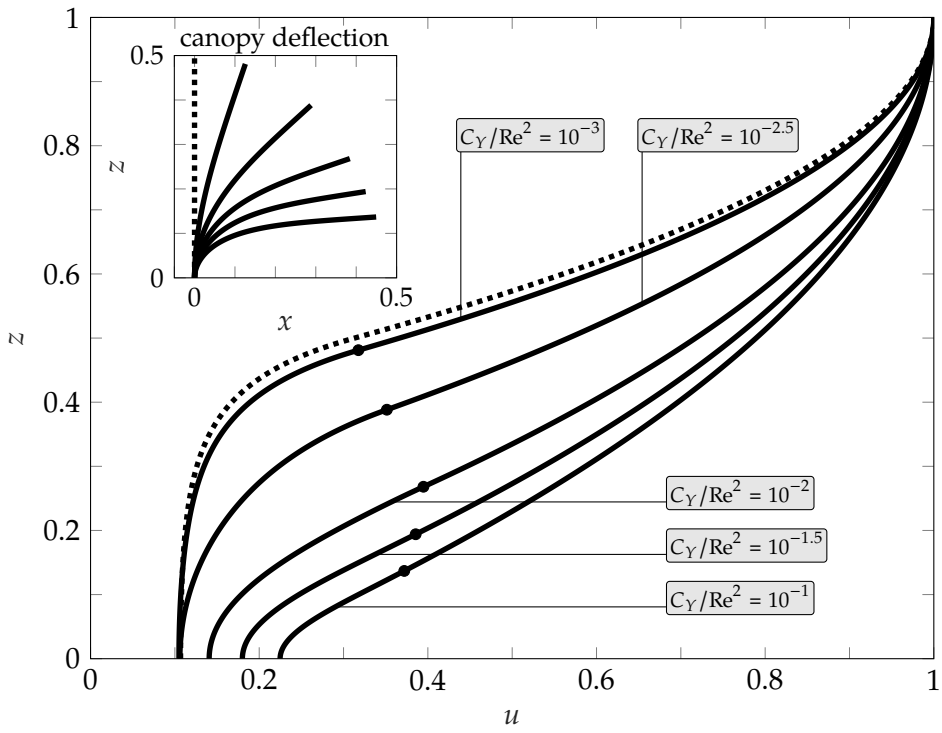

Figure 6.4: The effect of increasing the flexibility of vegetation to steady unidirectional flows when $\mathrm{Re} = 10^3$, $\lambda = 1$ and $h = 0.5$. Flow profiles are shown in solid lines for different values of C_Y/Re^2, with the corresponding homogenised beam configuration (to scale) in the inset. Dots in the main figure indicate the respective height of the canopy and dotted lines indicate the configuration in the rigid canopy limit $C_Y/\mathrm{Re}^2 = 0$.

main motivation of this work. Before we continue, we first define how we will vary the flexibility. We recall from §6.2 that the Cauchy number, C_Y, characterises the amount of deflection due to drag. Hence, it varies with the velocity scale (see Table 6.2). To vary flexibility independently of velocity, we vary the ratio

$$\frac{C_Y}{\mathrm{Re}^2} = \frac{\rho C_D b H v^{*2}}{EI} \tag{6.17}$$

in our analysis for the remainder of this work. Flow profiles for varying C_Y/Re^2 and fixed canopy density are shown in Figure 6.4.

As for flows through rigid canopies, every flow profile in Figure 6.4 increases monotonically, and inflects at the top of the canopy. As we increase the flexibility of the vegetation (by increasing C_Y/Re^2), less of the domain is obstructed, and we get faster flows at any given z. For applications such as flood control, if we use the (dimensional) maximum velocity as a simple measure for damage, the results suggest that upright obstacles attenuate a steady flow most effectively. We will revisit this conclusion in the next section when we consider the unsteady problem.

As an aside, we note that for regimes where the canopy is dense ($\lambda \gg 1$), we expect the approximations in §6.3.2 to hold for sufficiently stiff plants. In this limit, since $u = O(\lambda^{-1/3})$, the load and hence the deflection of each plant is negligible.

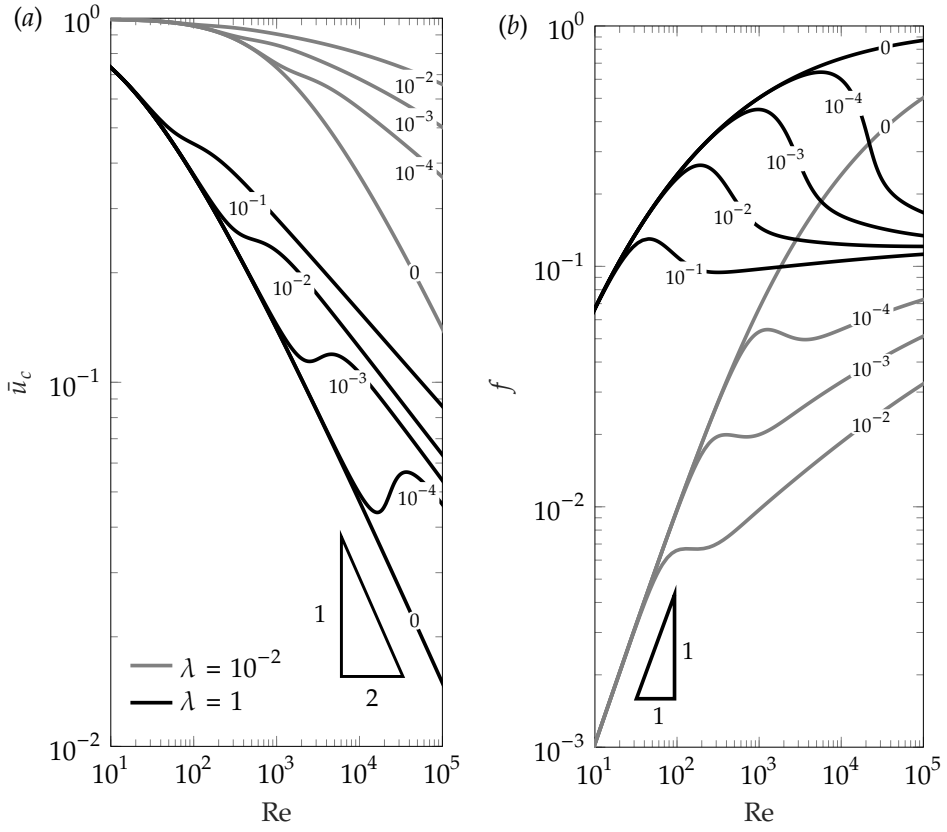

Figure 6.5: Height-averaged in-canopy velocity $\bar{u}_c$ in (*a*), and relative canopy drag f (6.18) in (*b*), versus Re for $h = 0.5$, with canopy density $\lambda = 1$ (shown black) and $\lambda = 10^{-2}$ (shown grey). Labels on the solid lines indicate plant flexibility, C_Y/Re^2.

Height-averaged in-canopy velocity

One quantity of practical interest is the in-canopy velocity, considered by many studies on canopy physics [see Nepf (2012) and references therein]. Note that our choice of nondimensionalisation makes it easy to compare between the in-canopy flow and the unobstructed flow. Since velocities are scaled with the free-surface velocity, the height-averaged dimensionless in-canopy velocity, $\bar{u}_c$ say, corresponds to the ratio between the canopy and free-surface velocities.

We observe from Figure 6.5a that when canopy effects are negligible, which corresponds to the canopy being sparse or the Reynolds number low, $\bar{u}_c \to 1$. As canopy effects become more prominent, we can infer from the analysis in §6.3.2 that, for rigid canopies, $\bar{u}_c = O((\mathrm{Re}\lambda)^{-1/2})$. For flexible canopies, however, $\bar{u}_c$ is not monotonic, as the plants transition from being upright to fully bent-over with increasing Reynolds number. The slower decay of $\bar{u}_c$ for fully bent-over plants can be explained by drag being negligible along most of the length of the plant, apart from a boundary layer near the root, where the plant is forced upright by the clamped condition.

Canopy drag, pressure gradient, and flux

Another quantity of practical interest is the canopy drag. Typically, drag is defined in terms of velocity. However, it is difficult to compare the

drag between two flows if the flux is not fixed. Consequently, to specify a nondimensional measure of the drag on the flow which is easier to interpret, we define

$$f = a\frac{\mathrm{ReP}}{Q}, \tag{6.18}$$

where Q is the dimensionless flux, and the scale factor a is chosen such that $f = 1$ when the canopy is infinitely dense, corresponding to (the lower-half of) a Poiseuille flow in $z \in [h, 1]$. Thus, for less dense canopies, f represents the relative pressure gradient required to generate the same flux as this Poiseuille flow. As a result, we can directly compare the drag between any two flows by comparing f, and this permits several interesting observations.

For rigid canopies, since the classic expression for drag scales with velocity-squared, f monotonically increases with the Reynolds number. For instance, we can deduce from the analysis in §6.3.2 that $f = O(\mathrm{Re}\lambda)$ when $\mathrm{Re}\lambda \ll 1$, whilst, for high Reynolds numbers, rigid-canopy flows become akin to the classic Poiseuille flow *i.e.* $f \to 1$. For flexible canopies, however, as with the in-canopy velocity, we observe in Figure 6.5b that there is non-monotonic behaviour as the plants transition from being upright to fully bent-over. In contrast to rigid canopy flows, there is an interesting competition between the effects of increasing the Reynolds number and canopy reconfiguration.

6.4 STABILITY ANALYSIS OF THE STEADY CONFIGURATION

Our main task in this section is to extend the stability analysis of Singh et al. (2016) for rigid canopies to flexible canopies with a free surface. By modelling the canopy as an array of elastic beams, we are interested in the temporal evolution of both the perturbed flow and the canopy configuration.

By considering the steady configurations of §6.3 as base states, we first derive the system of equations the perturbations satisfy at leading order. We then impose a spectral decomposition on the perturbations, and solve the corresponding quadratic eigenvalue problem numerically. In this work, we consider two-dimensional disturbances in the xz-plane, which is sufficient if we are primarily interested in the critical conditions for instability (Drazin and Reid, 1982).

6.4.1 Relating Eulerian and Lagrangian frames

Before we consider perturbations of the base flow, we again note that the spatial variables of the fluid are in the Eulerian frame, but the variables of the homogenised plant are parametrised by the arc length, s. Since it is natural for us to perform the stability analysis in Cartesian coordinates, we first express the variables in the system (6.4) in terms of $(\mathbf{x}, t)$.

Firstly, although the transformation between s and z still holds in the dynamic problem, namely

$$s = \int_0^z \sec\theta \, \mathrm{d}\bar{z}, \tag{6.19}$$

this transformation is perturbed when θ is perturbed and must be solved as part of the problem. Expanding all variables as

$$f = f^* + \epsilon \hat{f} + \ldots, \tag{6.20}$$

where f^* is the steady-state and $\epsilon \hat{f}$ is the perturbation, and linearising in $\epsilon \ll 1$, we find that

$$s^* = \int_0^z \sec\theta^* \, \mathrm{d}\bar{z} \quad \text{and} \quad \hat{s} = \int_0^z \sec\theta^* \tan\theta^* \hat{\theta} \, \mathrm{d}\bar{z}. \tag{6.21}$$

Secondly, the Lagrangian time derivative, $\partial/\partial\tau$, is distinct from the Eulerian time derivative, $\partial/\partial t$. As a result, by (6.19),

$$\frac{\partial}{\partial t} = \frac{\partial\tau}{\partial t}\frac{\partial}{\partial\tau} + \frac{\partial s}{\partial t}\frac{\partial}{\partial s} = \frac{\partial}{\partial\tau} + \left(\frac{\partial}{\partial t}\int_0^z \sec\theta \, \mathrm{d}\bar{z}\right)\left(\cos\theta\frac{\partial}{\partial z}\right). \tag{6.22}$$

With the transformations above, we can now rewrite every dependent variable with respect to $(\mathbf{x}, t)$. Before we write down the linearised equations, we need to determine the expansions of three key quantities: the velocity of the homogenised plant, $\partial\mathbf{r}/\partial\tau$, the acceleration of the homogenised plant, $\partial^2\mathbf{r}/\partial\tau^2$, and the height of the canopy, h_d.

Expression for the plant velocity and acceleration

We first express the velocity of a fixed point on the plant, $\partial\mathbf{r}/\partial\tau = (V_\parallel, V_\perp)$ say, in terms of $(\mathbf{x}, t)$. We have, for a given s,

$$\frac{\partial r_\parallel}{\partial\tau} = \frac{\partial}{\partial\tau}\int_0^s \sin\theta \, \mathrm{d}\bar{s} = \int_0^s \cos\theta\frac{\partial\theta}{\partial\tau} \, \mathrm{d}\bar{s} = \int_0^z \left[\frac{\partial\theta}{\partial t} - \cos\theta\frac{\partial\theta}{\partial z}\frac{\partial s}{\partial t}\right] \mathrm{d}\bar{z} \tag{6.23}$$

using (6.22). Similarly,

$$\frac{\partial r_\perp}{\partial\tau} = -\int_0^z \tan\theta\left[\frac{\partial\theta}{\partial t} - \cos\theta\frac{\partial\theta}{\partial z}\frac{\partial s}{\partial t}\right] \mathrm{d}\bar{z}. \tag{6.24}$$

Since for the base state $V_\parallel^* = V_\perp^* = 0$, we have

$$\hat{V}_\parallel = \int_0^z \left[\frac{\partial\hat{\theta}}{\partial t} - \cos\theta^*\frac{\mathrm{d}\theta^*}{\mathrm{d}z}\frac{\partial\hat{s}}{\partial t}\right] \mathrm{d}\bar{z}, \tag{6.25a}$$

$$\hat{V}_\perp = -\int_0^z \tan\theta^*\left[\frac{\partial\hat{\theta}}{\partial t} - \cos\theta^*\frac{\mathrm{d}\theta^*}{\mathrm{d}z}\frac{\partial\hat{s}}{\partial t}\right] \mathrm{d}\bar{z}. \tag{6.25b}$$

Similarly, writing $a_\parallel = \partial^2 r_\parallel/\partial\tau^2$ and $a_\perp = \partial^2 r_\perp/\partial\tau^2$ for the accelerations, we have $a^*_\parallel = a^*_\perp = 0$ and

$$\hat{a}_\parallel = \int_0^z \left[\frac{\partial^2\hat{\theta}}{\partial t^2} - \cos\theta^* \frac{\mathrm{d}\theta^*}{\mathrm{d}z}\frac{\partial^2\hat{s}}{\partial t^2}\right]\mathrm{d}\overline{z}, \tag{6.26a}$$

$$\hat{a}_\perp = -\int_0^z \tan\theta^* \left[\frac{\partial^2\hat{\theta}}{\partial t^2} - \cos\theta^* \frac{\mathrm{d}\theta^*}{\mathrm{d}z}\frac{\partial^2\hat{s}}{\partial t^2}\right]\mathrm{d}\overline{z}. \tag{6.26b}$$

Expression for the height of the canopy

The height of the canopy, h_d, also varies as we perturb the base state, which has to be taken into account because of the jump in drag there. Using the expansion of θ in the integral constraint on h_d (6.4i), gives

$$\hat{h}_d = -\cos\theta^*(h_d^*)\int_0^{h_d^*} \sec\theta^*\tan\theta^*\hat{\theta}\,\mathrm{d}z. \tag{6.27}$$

Having derived for expressions of $\hat{V}_{\parallel,\perp}$, $\hat{a}_{\parallel,\perp}$ and $\hat{h}_d$, we now proceed to derive the system of equations the perturbations satisfy.

6.4.2 *Linear stability analysis*

By substituting in the perturbed base state into the original system (6.4) and collecting the linear terms, we find that the perturbations satisfy

$$\frac{\partial\hat{u}}{\partial x} + \frac{\partial\hat{w}}{\partial z} = 0, \tag{6.28a}$$

$$\frac{\partial\hat{u}}{\partial t} + u^*\frac{\partial\hat{u}}{\partial x} = -\lambda\mathrm{H}(h_d^*-z)\left(\hat{\alpha}_D + M_1\hat{\alpha}_M + M_2\sec\theta^*\frac{\partial\hat{u}}{\partial t}\right) - \hat{w}\frac{\mathrm{d}u^*}{\mathrm{d}z} - \frac{\partial\hat{p}}{\partial x} + \frac{1}{\mathrm{Re}}\nabla^2\hat{u} - \frac{\lambda}{2}\delta(z-h_d^*)u^{*2}\cos^2\theta^*\hat{h}_d, \tag{6.28b}$$

$$\frac{\partial\hat{w}}{\partial t} + u^*\frac{\partial\hat{w}}{\partial x} = \lambda\mathrm{H}(h_d^*-z)\left[\frac{1}{2}u^{*2}\hat{\theta} + \tan\theta^*(\hat{\alpha}_D + M_1\hat{\alpha}_M) - M_2\sec\theta^*\frac{\partial\hat{w}}{\partial t}\right] - \frac{\partial\hat{p}}{\partial z} + \frac{1}{\mathrm{Re}}\nabla^2\hat{w} + \frac{\lambda}{2}\delta(z-h_d^*)u^{*2}\sin\theta^*\cos\theta^*\hat{h}_d, \tag{6.28c}$$

$$\frac{\partial\hat{T}_\parallel}{\partial z} = -(\hat{\alpha}_D + M_1\hat{\alpha}_M) - M_2\sec\theta^*\left(\frac{\partial\hat{u}}{\partial t} - \hat{a}_\parallel\right), \tag{6.28d}$$

$$\frac{\partial\hat{T}_\perp}{\partial z} - \frac{1}{2}u^{*2}\hat{\theta} = \tan\theta^*(\hat{\alpha}_D + M_1\hat{\alpha}_M) - M_2\sec\theta^*\left(\frac{\partial\hat{w}}{\partial t} - \hat{a}_\perp\right), \tag{6.28e}$$

$$\frac{\partial^2\hat{\theta}}{\partial z^2} = C_Y\sec\theta^*\left[\tan\theta^*\hat{T}_\perp + T^*_\perp(2\sec^2\theta^*-1)\hat{\theta} - \hat{T}_\parallel - T^*_\parallel\tan\theta^*\hat{\theta}\right] + 2\tan\theta^*\frac{\mathrm{d}\theta^*}{\mathrm{d}z}\frac{\partial\hat{\theta}}{\partial z} + \sec^2\theta^*\left(\frac{\mathrm{d}\theta^*}{\mathrm{d}z}\right)^2\hat{\theta} \tag{6.28f}$$

where

$$\hat{\alpha}_D = u^*\cos\theta^*\left[\cos\theta^*\left(\hat{u} - \hat{V}_\parallel\right) - \sin\theta^*\left(u^*\hat{\theta} + \hat{w} - \hat{V}_\perp\right)\right], \tag{6.28g}$$

$$\hat{\alpha}_M = \left(\frac{\partial\hat{u}}{\partial t} - \hat{a}_\parallel\right)\cos\theta^* - \left(\frac{\partial\hat{w}}{\partial t} - \hat{a}_\perp\right)\sin\theta^*. \tag{6.28h}$$

We will give the boundary conditions explicitly in the next section when we consider travelling-wave perturbations.

Travelling wave solutions of the perturbed problem

Anticipating the calculations ahead, it is convenient to first define the stream function of the flow, $\psi = \psi^* + \epsilon\hat{\psi} + \dots$, such that

$$u^* = \frac{\mathrm{d}\psi^*}{\mathrm{d}z} \qquad \text{and} \qquad \begin{pmatrix}\hat{u}\\ \hat{w}\end{pmatrix} = \begin{pmatrix}\partial\hat{\psi}/\partial z\\ -\partial\hat{\psi}/\partial x\end{pmatrix}. \tag{6.29}$$

By rewriting $\hat{u}$ and $\hat{w}$ in (6.28a)–(6.28c) as derivatives of $\hat{\psi}$, the incompressibility condition (6.28a) is then automatically satisfied. Furthermore, by equating the derivatives of $\hat{p}$, we can combine (6.28b)–(6.28c) into a single differential equation for $\hat{\psi}$. With $\hat{u}$, $\hat{w}$, and $\hat{p}$ being eliminated, we consider a Fourier decomposition in the streamwise direction by letting

$$(\hat{\psi}, \hat{\theta}, \hat{T}_{\parallel}, \hat{T}_{\perp}) = (\phi(z), \vartheta(z), \mathcal{T}_{\parallel}(z), \mathcal{T}_{\perp}(z))\mathrm{e}^{\mathrm{i}kx+\sigma t}, \tag{6.30}$$

real part understood, with k the wavenumber of the perturbation along the domain and σ the eigenvalue.

By substituting the ansatz (6.30) into (6.28) and using primes ($'$) to denote derivatives in z, we find that ϕ satisfies the modified Orr-Sommerfeld equation (Drazin and Reid, 1982)

$$\begin{aligned}\frac{\phi'''' - 2k^2\phi'' + k^4\phi}{\mathrm{Re}} - (\sigma + \mathrm{i}ku^*)(\phi'' - k^2\phi) + \mathrm{i}ku^{*\prime\prime}\phi \\ = \begin{cases}\lambda(\mathcal{S}_{\mathrm{c}}' + \mathrm{i}k\mathcal{S}_{\mathrm{s}}), & \text{if } z \le h_d^*,\\ 0, & \text{if } z > h_d^*.\end{cases}\end{aligned} \tag{6.31a}$$

Note that the expression for the momentum sinks $\mathcal{S}_{\mathrm{c}}'$ and $\mathcal{S}_{\mathrm{s}}$ are further coupled to the perturbed beam equations to account for canopy deformation, and thus involve additional components. Such effects are only active in the obstructed part of the domain ($z \le h_d^*$ after linearising). The perturbed beam equations are

$$\mathcal{T}_{\parallel}'(z) = -\mathcal{S}_c + M_2 \sec\theta^*\sigma^2\mathcal{A}, \tag{6.31b}$$

$$\mathcal{T}_{\perp}'(z) = -(\mathcal{S}_s + M_2 \sec\theta^*\sigma^2\mathcal{B}), \tag{6.31c}$$

$$\begin{aligned}\vartheta''(z) = C_Y \sec\theta^* \Big[\tan\theta^*\mathcal{T}_{\perp} + T_{\perp}^*(2\sec^2\theta^* - 1)\vartheta - \mathcal{T}_{\parallel} - T_{\parallel}^*\tan\theta^*\vartheta\Big] \\ + 2\tan\theta^*\theta^{*\prime}\vartheta' + \sec^2\theta^*\left(\theta^{*\prime}\right)^2\vartheta.\end{aligned} \tag{6.31d}$$

The expressions for $\mathcal{S}_c$, $\mathcal{S}_s$, $\mathcal{A}$ and $\mathcal{B}$ are functions of z, ϑ, and ϕ, given by

$$\begin{aligned}\mathcal{S}_c(z) = {} & u^* \cos\theta^* \left[\cos\theta^* \left(\phi' - \sigma\mathcal{A}\right) - \sin\theta^* \left(u^*\vartheta - \mathrm{i}k\phi + \sigma\mathcal{B}\right)\right] \\ & + M_1 \left[\left(\sigma\phi' - \sigma^2\mathcal{A}\right)\cos\theta^* + \left(\mathrm{i}k\sigma\phi - \sigma^2\mathcal{B}\right)\sin\theta^*\right] \\ & + M_2 \sec\theta^* \sigma\phi', \end{aligned} \tag{6.31e}$$

$$\begin{aligned}\mathcal{S}_s(z) = {} & u^* \sin\theta^* \left[\cos\theta^* \left(\phi' - \sigma\mathcal{A}\right) - \sin\theta^* \left(u^*\vartheta - \mathrm{i}k\phi + \sigma\mathcal{B}\right)\right] \\ & + M_1 \tan\theta^* \left[\left(\sigma\phi' - \sigma^2\mathcal{A}\right)\cos\theta^* + \left(\mathrm{i}k\sigma\phi - \sigma^2\mathcal{B}\right)\sin\theta^*\right] \\ & + M_2 \sec\theta^* \mathrm{i}k\sigma\phi + \frac{1}{2}u^{*2}\vartheta, \end{aligned} \tag{6.31f}$$

with

$$\mathcal{A}(z) = \int_0^z \vartheta - C\cos\theta^*\theta^{*\prime}\,\mathrm{d}\overline{z}, \tag{6.31g}$$

$$\mathcal{B}(z) = \int_0^z \tan\theta^* \left(\vartheta - C\cos\theta^*\theta^{*\prime}\right)\,\mathrm{d}\overline{z}, \tag{6.31h}$$

$$C(z) = \int_0^z \sec\theta^* \tan\theta^* \vartheta\,\mathrm{d}\overline{z}. \tag{6.31i}$$

Boundary conditions of the problem

The corresponding boundary conditions of this problem are

$$\boxed{z = 0}\ \phi = 0,\ \phi'' = 0, \tag{6.31j}$$

$$\boxed{z = 1}\ (\sigma + \mathrm{i}ku^*)(\phi'' + k^2\phi) = \mathrm{i}ku^{*\prime\prime}\phi, \tag{6.31k}$$

$$\frac{1}{u^{*\prime\prime}}\frac{\mathrm{Re}}{\mathrm{Fr}^2}\cos\alpha\mathrm{i}k(\phi'' + k^2\phi) + \phi'''' = [3k^2 + \mathrm{Re}(\sigma + \mathrm{i}ku^*)]\phi', \tag{6.31l}$$

for the fluid and

$$\boxed{z = 0}\quad \vartheta = 0, \tag{6.31m}$$

$$\boxed{z = h_d^*}\quad \vartheta' = 0,\ \mathcal{T}_\parallel = -\frac{u^{*2}}{2}C\cos^3\theta^*,\ \mathcal{T}_\perp = \frac{u^{*2}}{2}C\sin\theta^*\cos^2\theta^* \tag{6.31n}$$

for the plant. Finally, although ϕ and ϕ' are continuous at $z = h_d^*$, due to the discontinuous momentum sink in (6.4b) we have

$$\left[\phi''(z)\right]_{h_d^{*-}}^{h_d^{*+}} = -\mathrm{Re}\lambda\left[\frac{1}{2}u^{*2}C\cos^3\theta^*\right]_{z=h_d^*}, \tag{6.31o}$$

$$\left[\phi'''(z)\right]_{h_d^{*-}}^{h_d^{*+}} = -\mathrm{Re}\lambda\left[\mathcal{S}_c + \frac{\mathrm{i}k}{2}\left(u^{*2}C\sin\theta^*\cos^2\theta^*\right)\right]_{z=h_d^*}. \tag{6.31p}$$

For a given base state and a given k, we seek values of $\sigma(k)$ such that there are non-trivial eigenmodes of the system of integro-differential equations for ϕ, ϑ, $\mathcal{T}_\parallel$, and $\mathcal{T}_\perp$ (6.31). In particular, we are interested in the most unstable (or the least stable) mode. We solve this eigenvalue problem numerically.

6.5 METHOD FOR SOLVING THE EIGENVALUE PROBLEM

We briefly outline our numerical method for solving the eigenvalue problem. First the eigenvalue problem (6.31) is rewritten as a system of ordinary differential equations in z. In this setting, ϕ is defined in $[0, 1]$ while other variables are only defined in $[0, h_d^*]$. Furthermore, ϕ has discontinuous derivatives at $z = h_d^*$. Therefore, we partition the domain into $[0, h_d^*]$ and $[h_d^*, 1]$ and split ϕ into two separate functions, namely

$$\phi_{\text{bot}} = \phi(z \leq h_d^*) \qquad \text{and} \qquad \phi_{\text{top}} = \phi(z \geq h_d^*). \tag{6.32}$$

Following the practice of previous work in solving Orr-Sommerfeld problems, we solve this system of equations numerically using a spectral method with Chebyshev polynomials of the second kind (Orszag, 1971). To implement this method, in each interval, we discretise the dependent variables in (6.31) into their function values at N Chebyshev nodes. Note that $z = h_d^*$ is an edge node in each interval, which represents h_d^{*-} and h_d^{*+} when we impose the jump conditions (6.31o)–(6.31p). Once we have defined the nodes, we then construct the discrete version of the differential operators in (6.31) with *Chebfun* (Driscoll et al., 2014). Finally, we can rearrange the discrete equations so that σ satisfies a quadratic eigenvalue problem (QEP) of the form

$$\left(\mathbf{A} + \sigma\mathbf{B} + \sigma^2\mathbf{C}\right)\mathbf{X} = 0, \tag{6.33}$$

where $\mathbf{A}$, $\mathbf{B}$ and $\mathbf{C}$ are known matrices and $\mathbf{X}$ is the eigenvector of function values. We solve for all possible pairs of $\mathbf{X}$ and σ with `quadeig`, a QEP-solver in MATLAB developed by Hammarling et al. (2013) which we found outperforms `polyeig`, the inbuilt solver for polynomial eigenvalue problems, in terms of efficiency.

The classic Orr-Sommerfeld problem is known for its non-normality—its eigenvalues are highly sensitive to perturbations (Reddy et al., 1993). To ensure that the eigenvalues converge, we eliminate rows in the matrix problem (6.33) that are independent of σ (Weideman and Reddy, 2000)—this removes spurious modes which disrupt the convergence of the physical spectrum (Goussis and Pearlstein, 1989). Furthermore, we precondition the problem by rescaling each row with $\|\mathbf{a}_j\|_1$, where $\mathbf{a}_j$ is the j^{th} row of $\mathbf{A}$ (Wathen, 2015). We note that without pre-conditioning, the numerical solutions of the eigenvalue problem can exhibit convergence issues between consecutive values of N if N is sufficiently large.

We solve the eigenvalue problem with a starting value of $N = 80$ Chebyshev nodes. We increase the number of nodes in intervals of 20 and recalculate the spectrum until the most unstable eigenvalue is within 0.1% of the previous estimate in the L_2–norm.

6.6 SOLUTION SPACE

While we will vary the dimensionless parameters given in Table 6.2 as we explore the solution space, we will fix certain parameters which are representative of the full physical problem. For the inertia of the beams, we will fix $M_1 = M_2 = 0.2$ for cylindrical beams and $M_1 = 0.2$, $M_2 = 0$ for blades. Finally, as we vary the Reynolds number, we will keep its ratio with the Froude number

$$J = \frac{\mathrm{Fr}}{\mathrm{Re}} = \frac{\nu^*}{\sqrt{gH^3}} \tag{6.34}$$

fixed at 10^{-5}. We now elaborate on such choices.

6.6.1 *The choice of a representative inertia*

For cylindrical beams, the cross-sectional mass per unit length $m = \rho\pi b^2/4$. With the drag coefficient C_D being $O(1)$, $M_{1,2} = O(b/H) \ll 1$ *i.e.* the aspect ratio of the beam provided that h/H is $O(1)$. The same calculation for blades with thickness w gives $M_1 = O(b/H) \ll 1$, but $M_2 = O(w/H) \ll b/H \ll 1$. Although both M_1 and M_2 can be small in relation to drag, inertia can still play a role in beam dynamics for large values of C_Y (6.4d). In order to highlight the effects of different types of inertia in this problem, we consider non-negligible but representative values of M_1 and M_2 in §§6.7 and 6.8: $M_1 = M_2 = 0.2$ for cylindrical beams and $M_1 = 0.2$, $M_2 = 0$ for blades. The approximation for $M_2 = 0$ for blades follows from the analysis in Chapter 5.

6.6.2 *The choice of a representative Froude number*

As with the Cauchy number, the Froude number also scales with the velocity scale U (see Table 6.2). To vary the Reynolds number (by varying U) while keeping the geometry of the domain fixed, we compare flows that have the same ratio, J (6.34). Note that typically, $J \ll 1$. For reference, if we take $\nu^* = 10^{-4}$ m^{2}s^{-1} as a representative value for canopy flows (Singh et al., 2016), then J is at the order of 10^{-5} for a flow of depth $H = 1$ m.

Previous stability analysis on flows through vegetation have also considered imposing the shear-free condition for the flow at $z = 1$ (Dupont et al., 2010; Singh et al., 2016). Mathematically, this corresponds to considering the limit when $\mathrm{Fr} \to 0$ (*i.e.* $J \to 0$), in which the full free-surface conditions (6.31k)–(6.31l) reduce to $\phi(1) = \phi''(1) = 0$. Our investigation suggests that this is a reasonable simplification in this model: in Figure 6.6, we demonstrate that for $\mathrm{Re} = 10^3$, a typical Reynolds number in our model for the onset of instabilities (shown in §6.8), the change in the spectrum is negligible until J reaches values that are beyond our regime of interest. In such cases, the free surface appears to be suppressing instabilities by comparison

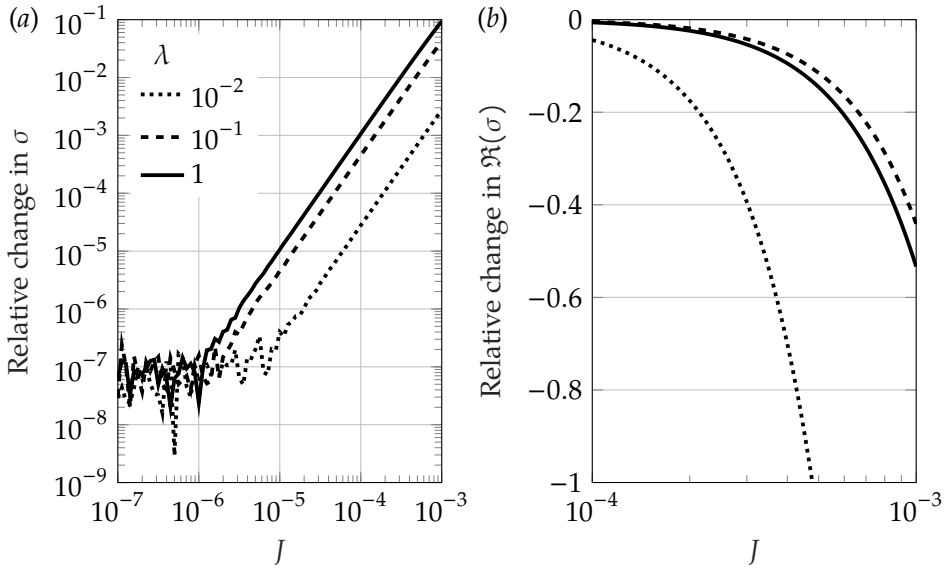

Figure 6.6: Comparing the most unstable eigenvalue of the problem against the same results calculated using the approximation $J = 0$. Shown is the case where $h = 0.5$, $\mathrm{Re} = 10^3$, $C_Y/\mathrm{Re}^2 = 10^{-4}$, $M_1 = M_2 = 0$ and $k = 1$. Line styles are used to indicate canopy densities, as stated in the legend of (*a*).

to a symmetry condition at $z = 1$. We note that we also get similar trends when we include inertia.

6.7 TYPICAL UNSTABLE MODES OF THE EIGENVALUE PROBLEM

In this section, we visualise some typical solutions for the unstable modes, and compare our numerically determined eigenvalues to those of simplified problems with the hope of gaining some physical insights.

6.7.1 Properties of the eigenfunctions

Typical results for ϕ and ϑ are shown in Figure 6.7, which correspond to flow perturbation and plant deflection respectively.

We first note from the behaviour of $|\phi|$ that in all cases, the energy of the flow perturbation is localised near the top of the canopy. For slower flows, $|\vartheta|$ increases monotonically in z so that the perturbations to the deflection angle are also largest at the top of the canopy. Moreover, for faster flows, the largest perturbation to the deflection may be in the middle of the canopy. The temporal evolution of such a mode is illustrated in Figure 6.8.

We can also visualise how the physical configuration evolves in time by perturbing the base flow with a single unstable mode. We plot the streamlines of the flow given by

$$\begin{pmatrix} u \\ w \end{pmatrix} = \begin{pmatrix} u^*(z) \\ 0 \end{pmatrix} + \gamma \mathrm{e}^{\Re(\sigma)t} \Re \left[\begin{pmatrix} \phi'(z) \mathrm{e}^{\mathrm{i}[kx + \Im(\sigma)t]} \\ -\mathrm{i}k\phi(z) \mathrm{e}^{\mathrm{i}[kx+\Im(\sigma)t]} \end{pmatrix} \right], \tag{6.35}$$

where γ is the (arbitrarily chosen) initial amplitude.

In Figure 6.8, we present the perturbed configuration at three different instances. The amplitude of the travelling wave grows in time as it convects downstream. If we plot the streamlines in Figure 6.8 without the base flow,

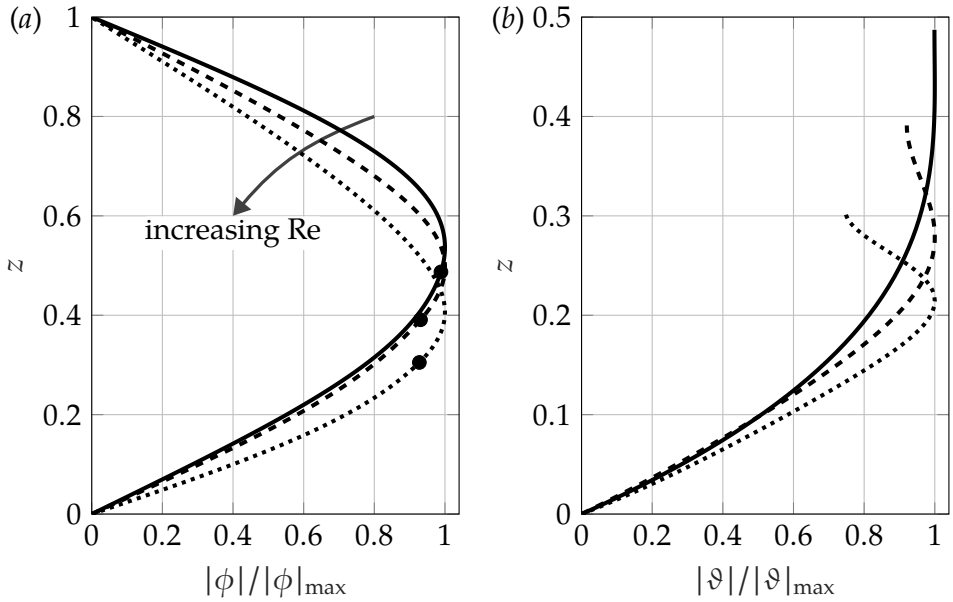

Figure 6.7: Magnitudes of unstable eigenmodes ϕ and ϑ as normalised functions of z when $h = 0.5$, $\lambda = 10^{-1.5}$, $C_Y/\mathrm{Re}^2 = 10^{-4}$, $M_1 = M_2 = 0.2$, $J = 10^{-5}$ and $k = 1$. Results are shown with $\mathrm{Re} = 859$ (solid), 2466 (dashed), and 4607 (dotted). The markers on the stream functions in (*a*) indicate their respective canopy height at steady state.

we will find closed contours along the top of the canopy corresponding to rolling vortices. Regarding the canopy configuration, plants oscillate synchronously, resembling monami. In particular, at later times, we see that when the deflection near the base of the canopy is increased, the canopy becomes more aligned with the flow. The drag higher up the canopy is then reduced. As a result, the deflection angle higher up the canopy is also reduced. We highlight that our flexible canopy model can capture the streamwise variation of the canopy height and the local angle of deflection for each plant.

6.7.2 *Stability of flows for sparse and dense canopies*

Analogous to the analysis on the base flow in §6.3.2, we can gain some insight on the stability of the system by considering the asymptotic limits of small and large canopy densities. In the dense-canopy limit, we expect the perturbations to be less sensitive to plant flexibility: there will be less flow in the canopy, which also leads to less deformation. In the opposite limit, we expect a sparse canopy to have limited influence on the macroscopic flow, irrespective of the physical properties of individual plants.

Stability of flows for sparse canopies

In the limit where the canopy is sparse, in the sense that $\mathrm{Re}\lambda$, $\mathrm{Re}^2\lambda \ll 1$, we know from §6.3.2 that $u_0 \sim 1$ and the momentum sink in (6.31a) becomes negligible. Since the perturbations of the beams are then decoupled from the fluid, we can approximate the eigenvalues of the full problem by only solving the Orr-Sommerfeld equation

$$\frac{1}{\mathrm{Re}}(\phi'''' - 2k^2\phi'' + k^4\phi) = (\sigma + \mathrm{i}k)(\phi'' - k^2\phi). \tag{6.36}$$

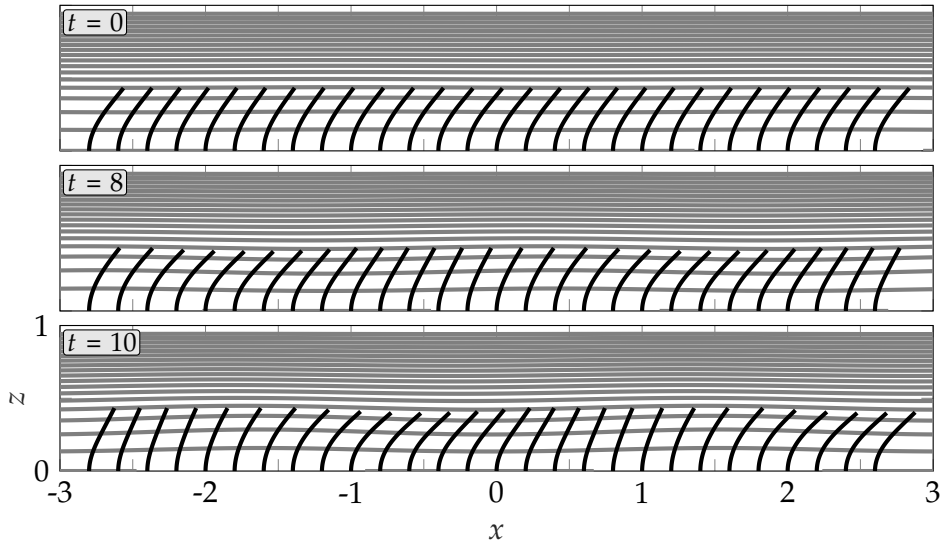

Figure 6.8: Temporal evolution of a steady unidirectional base flow in the domain due to the growth of a single unstable eigenmode. The configuration of individual plants in the canopy are represented by black solid lines (to scale) along the bottom of the domain with streamlines in grey. For the eigenmode, ϕ and ϑ are rescaled by $|\phi|_{\max}$ before we impose an initial amplitude of $\gamma = 10^{-3}$ in (6.35). Shown is the case where $h = 0.5$, $\mathrm{Re} = 2936$, $\lambda = 10^{-1}$, $C_Y/\mathrm{Re}^2 = 10^{-4}$, $M_1 = M_2 = 0.2$, $J = 10^{-5}$ and $k = 2$.

We can solve this equation analytically in the limit when $J = \mathrm{Fr}/\mathrm{Re} \to 0$, for which

$$\phi(0) = 0,\ \phi(1) = 0,\ \phi''(0) = 0,\ \phi''(1) = 0 \tag{6.37}$$

to give

$$\sigma(k) = -\frac{1}{\mathrm{Re}}(k^2 + n^2\pi^2) - k\mathrm{i}, \tag{6.38}$$

where $n \in \mathbb{N}$. Thus a uniform flow in this limit is globally stable. As a check on both our asymptotic and numerical results, we compare the leading eigenvalue with that of the full numerical solution in Figure 6.9a.

In the distinguished limit in which $\mathrm{Re}\lambda \ll 1$ with $\mathrm{Re}^2\lambda$ being $O(1)$, we can apply the approximations for the velocity profile in §6.3.2 for rigid canopies and rewrite the eigenvalue problem as a universal problem

$$\phi'''' - 2k^2\phi'' + k^4\phi = (\sigma_{\mathrm{new}} + \mathrm{i}k\mathrm{Re}^2\lambda\tilde{u})(\phi'' - k^2\phi) - \mathrm{i}k\mathrm{Re}^2\lambda\tilde{u}''\phi, \tag{6.39}$$

with $\tilde{u}$ given by (6.10) and $\sigma_{\mathrm{new}} = \mathrm{Re}(\sigma + k\mathrm{i})$, where ϕ satisfies the simplified boundary conditions (6.37) for small J. Furthermore, note from (6.39) that the eigenfunctions are determined via the single parameter, $\mathrm{Re}^2\lambda$. In fact, this determines the critical Reynolds number for instability when the canopy is sparse, as verified in §6.8.

Stability of flows for dense canopies

Recall from our dense-canopy analysis in §6.3.2 that in the limit $\lambda \to \infty$, the flow inside the canopy satisfies $u^* = O(\lambda^{-1/2})$ from (6.12). Moreover, the flow above the canopy is parabolic and given by (6.13) and (6.16). Thus in the limit where $J \to 0$, we should recover the eigenvalues of the classic Orr-Sommerfeld problem for a plane Poiseuille flow between $[h, 2-h]$ with $u_0 = 0$ at $z = h$ (the channel bottom) and $u_0 = 1$ at $z = 1$ (the flow centreline). Mathematically, this gives [compare with Drazin and Reid (1982)]

$$\frac{1}{\mathrm{Re}}(\phi'''' - 2k^2\phi'' + k^4\phi) = (\sigma + \mathrm{i}ku_0)(\phi'' - k^2\phi) - \mathrm{i}ku_0''\phi, \tag{6.40a}$$

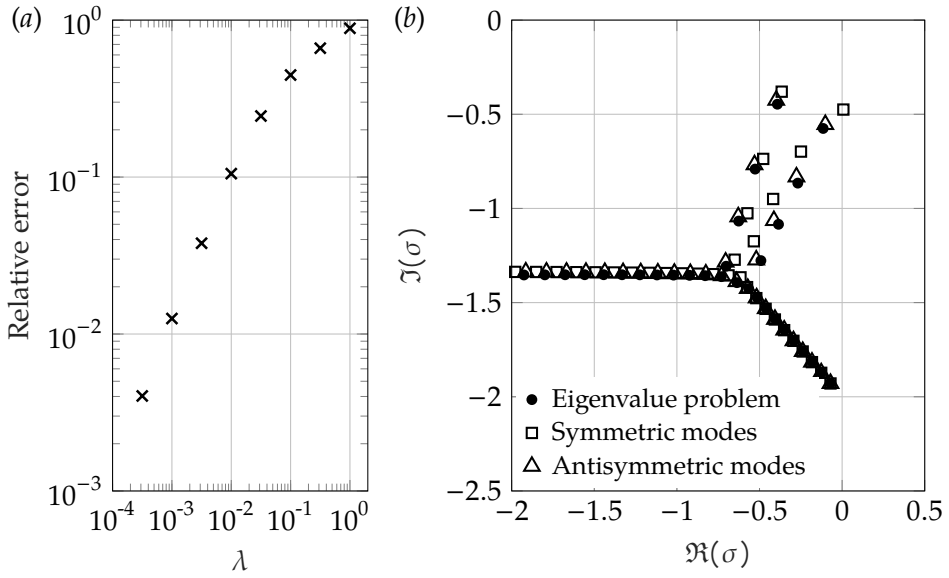

Figure 6.9: Comparison between the spectrum of the eigenvalue problem (6.31) and some reduced problems for $h = 0.5$, $C_Y/\mathrm{Re}^2 = 10^{-4}$, $M_1 = M_2 = 0$, $J = 10^{-5}$ and $k = 2$. (*a*) Relative error between the least stable eigenvalue of the eigenvalue problem and the sparse canopy approximation (6.38) for different values of λ when Re = 200. (*b*) Positions of the most unstable eigenvalues for the full problem and the corresponding symmetric and antisymmetric modes of the classic Orr-Sommerfeld problem (6.40) when $\mathrm{Re} = 2 \times 10^4$, $\lambda = 10^5$.

with

$$\phi(h) = 0,\ \phi'(h) = 0,\ \phi(2-h) = 0,\ \phi'(2-h) = 0. \tag{6.40b}$$

Note that the above problem has two types of modes: symmetric and antisymmetric modes (Chapman, 2002). Since we have imposed the simplified shear-free condition at $z = 1$, eigenmodes of our problem (6.31) in this limit will only correspond to the antisymmetric modes of the classic problem (6.40), as seen in Figure 6.9b. These modes are always stable (Orszag, 1971). Therefore, our problem is also linearly stable in the dense-canopy limit.

6.8 CRITICAL CONDITIONS FOR THE ONSET OF INSTABILITY

In the previous section, we have seen that the system is linearly stable when the canopy is infinitely sparse or dense. However, we found that unstable modes exist for intermediate canopy densities. Therefore, it is natural for us to investigate the critical conditions for the onset of instability. The purpose of this section is to describe the global stability structure of the perturbed system. This leads up to the main results of this work on the role of flexibility, inertia, and shear in flows through vegetation.

6.8.1 Evolution of the neutral curve

Our main objective is to observe the change in the neutral stability curves as four key parameters are changed: the flexibility C_Y/Re^2; canopy density λ; added mass M_1; and beam inertia and virtual buoyancy M_2. For each choice of these four parameters, our numerical scheme is used to generate heat maps of $\Re(\sigma)$ in the (Re, k)-plane. For example, values of $\Re(\sigma)$ at fixed values of $M_1 = 0.2$ and $M_2 = 0.2$ are represented by the greyscale colours of insets in Figure 6.10b–f. Then, the key contour is given by the neutral

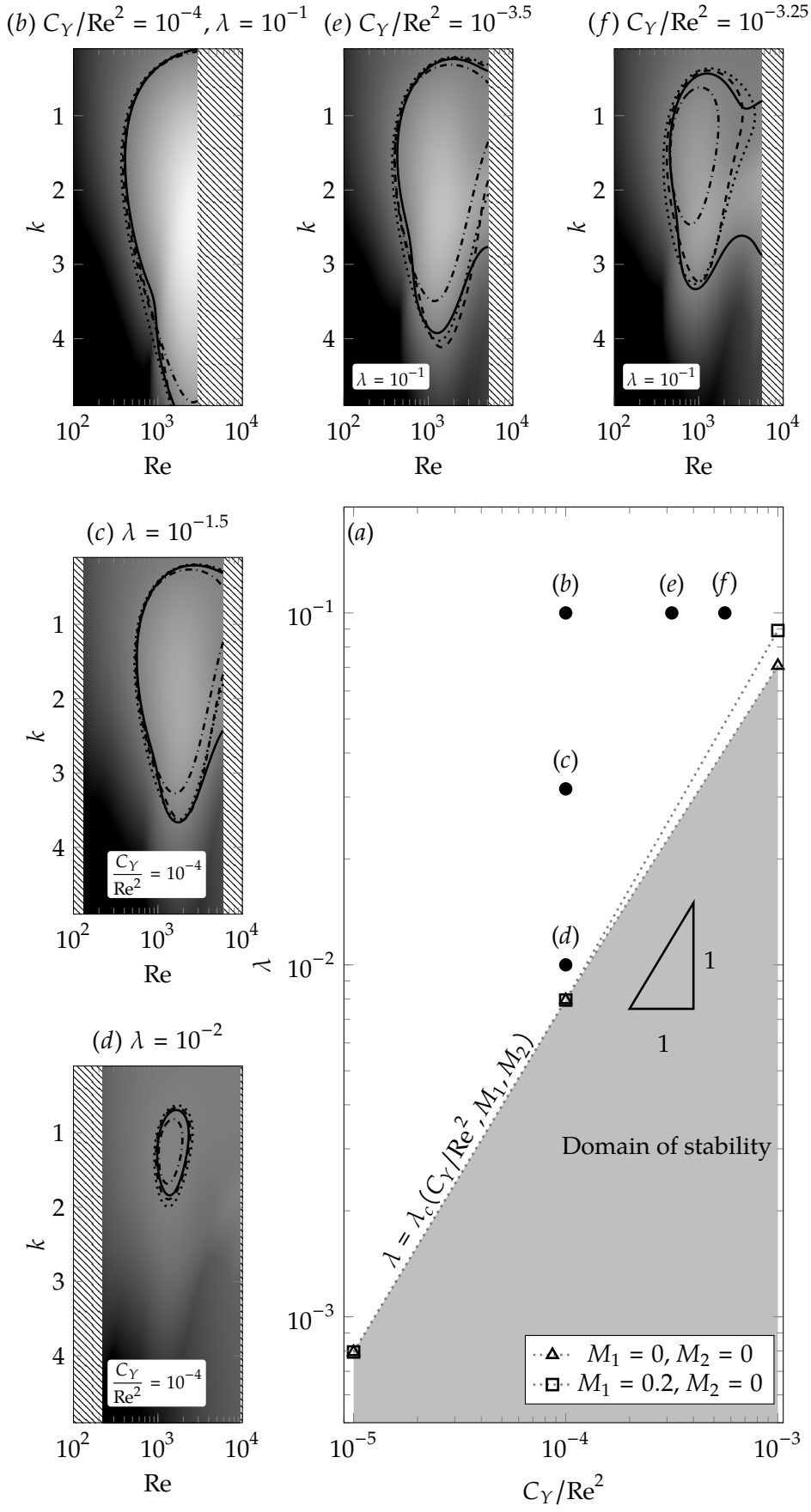

Figure 6.10: The main figure (*a*) shows the $(C_Y/\mathrm{Re}^2, \lambda)$-solution space for the eigenvalue problem (6.31) for $M_2 = 0$. The shaded region indicates where perturbations of the base state are stable, and lies below the critical curve for instability, $\lambda = \lambda_c$ (6.41). Hollow markers are numerically determined solutions with $M_1 = 0$ (triangles) and $M_1 = 0.2$ (squares). The five insets (*b*) through (*f*) show heat maps of $\mathfrak{R}(\sigma)$ in the (Re, k)-plane. In all heat maps, colours correspond to values of $\mathfrak{R}(\sigma)$ ranging from -0.2 (black) to 0.2 (white) specifically for $M_1 = M_2 = 0.2$; areas that have not been swept are hatched. The neutral stability curve, $\mathfrak{R}(\sigma) = 0$, for $M_1 = M_2 = 0.2$ is given by a solid line. Other line styles are used to indicate neutral curves with $M_1 = 0.2$, $M_2 = 0$ (dashed), $M_1 = M_2 = 0$ (dotted), and the decoupled model in §6.8.1 (dash-dotted).

stability curve, $\mathfrak{R}(\sigma) = 0$, and is shown solid in these insets. In addition, simulations are performed by varying M_1 and M_2; these give the shifted neutral stability curves and are plotted with other line styles. We shall discuss these elements in §6.8.1.

Once the heat maps are generated for a range of parameters, the results are visualised in the $(C_Y/\mathrm{Re}^2, \lambda)$-plane, as shown in Figure 6.10a. Here, solutions are either classified as stable or unstable (corresponding to a non-trivial neutral stability curve).

Before proceeding further, let us make two basic observations. Firstly, for a given choice of the four parameters, if instabilities exist, then the base state will initially become unstable at a critical wavenumber, k, that is $O(1)$. Secondly, although not shown in the figure, all of the unstable modes have $\mathfrak{I}(\sigma) < 0$, with $|\mathfrak{I}(\sigma)|$ increasing nonlinearly with k for any given Re. This corresponds to the instabilities being convective downstream and dispersive, and is in agreement with the predictions by Singh et al. (2016) and Luminari et al. (2016) on flows through rigid canopies.

Variations due to inertia

We now discuss how the neutral stability curves shown in Figure 6.10b–f vary as a function of the four parameters. We make the following observations:

(i) For fixed flexibility, C_Y/Re^2, added mass, M_1, beam inertia, M_2, and decreasing canopy density, λ, *i.e.* as we transition from (*b*) to (*c*) to (*d*) in Figure 6.10a, the topology of the neutral curves change: the area enclosed by the neutral curves shown in the insets tends to zero and the system becomes globally stable.

(ii) Thus for each M_1, M_2 there exists a critical curve

$$\lambda = \lambda_c\left(\frac{C_Y}{\mathrm{Re}^2}; M_1, M_2\right), \tag{6.41}$$

in the $(C_Y/\mathrm{Re}^2, \lambda)$-plane that separates the two possibilities—globally stable for all Re, or unstable for some Re. However, with the insight that we have from the dense-canopy asymptotic analysis in §6.7.2, we expect a stable region (that is off Figure 6.10a) for sufficiently large λ.

(iii) The critical curve, $\lambda = \lambda_c$, is shown in Figure 6.10a, with points on this critical curve for $(M_1, M_2) = (0, 0)$ and $(0.2, 0)$ are shown as triangles and squares respectively (and joined by dotted lines). Our numerical results suggest that the curve for $M_1 = 0$ lies below that for $M_1 = 0.2$ for $C_Y/\mathrm{Re}^2 = 10^{-3}$. We will return to such features in §6.8.4 where we interpret the existence of λ_c in terms of shear.

(iv) This trend of a shrinking domain of instability also occurs for fixed λ and for increasing C_Y/Re^2 *i.e.* as we transition from (*b*) to (*e*) to (*f*) in Figure 6.10a.

In the case of cylindrical beams, a non-zero but small beam inertia (or virtual buoyancy), M_2, has the effect of shifting the neutral stability curve slightly to the right. Furthermore, as we increase the beam flexibility, C_Y/Re^2, from (*b*) to (*e*) to (*f*) in Figure 6.10, it appears as though the neutral curve for $M_2 = 0.2$ may not close and vanish in the same way as the neutral curve for $M_2 = 0$, so that there may always be an unstable mode at that canopy density. To really check this would require moving to even higher flexibilities. However, because the beams are bent close to horizontal at such high flexibilities and speeds, the validity of the model in this regime is not clear, in addition to the numerical challenges it poses.

A decoupled model: Ignoring canopy perturbations

Despite the complexity of the solution space presented above, it appears that some qualitative behaviour of the neutral stability curves shown in Figure 6.10 can be understood through hydrodynamical effects. To this end, we investigate the effect of considering only perturbations in the flow, effectively treating the canopy as rigid and fixed in its deflected position due to the base flow. This is equivalent to setting the perturbations on the canopy, ϑ, and stresses, $\mathcal{T}_{1,3}$, to zero in (6.30) and solving the single equation (6.31a) for ϕ. Once this is done, the neutral stability curves for this decoupled problem are derived.

We return to the heat maps shown in the insets (*b*)–(*f*) of Figure 6.10, where the neutral stability curves of the decoupled system are shown dash-dotted, in contrast to those of the full problem shown solid. Note that consistent with the analysis in §6.3.3, when the canopy is dense or the plants are stiff, we would expect agreement between the two models. As either density, λ, decreases or plant flexibility, C_Y/Re^2 increases, the effects of the fluid-plant coupling can then be seen by noticing the growing separation between the curves.

6.8.2 *Behaviour of the critical Reynolds number*

We saw in Figure 6.10 that if there are any unstable modes in the parameter space, then for every neutral curve there exists a minimum value, $\mathrm{Re} = \mathrm{Re}_{\mathrm{crit}}$, such that flows will be first unstable if $\mathrm{Re} > \mathrm{Re}_{\mathrm{crit}}$. Therefore, it is natural for us to analyse the behaviour of $\mathrm{Re}_{\mathrm{crit}}$ as a function of the other parameters, *i.e.*

$$\mathrm{Re}_{\mathrm{crit}} = \mathrm{Re}_{\mathrm{crit}}(\lambda,\, C_Y,\, M_1,\, M_2). \tag{6.42}$$

For fixed flexibility C_Y/Re^2, we observe in Figure 6.11a there is a critical density λ at which $\mathrm{Re}_{\mathrm{crit}}$ is minimum. Higher or lower canopy densities are both more stable, in that they lead to a higher $\mathrm{Re}_{\mathrm{crit}}$. This non-monotonic behaviour can be understood through the asymptotic analysis of §6.7.2. In particular, as the canopy density decreases to zero or increases to infinity, the base flow is globally stable. For small λ the system is stable for $\lambda < \lambda_c$

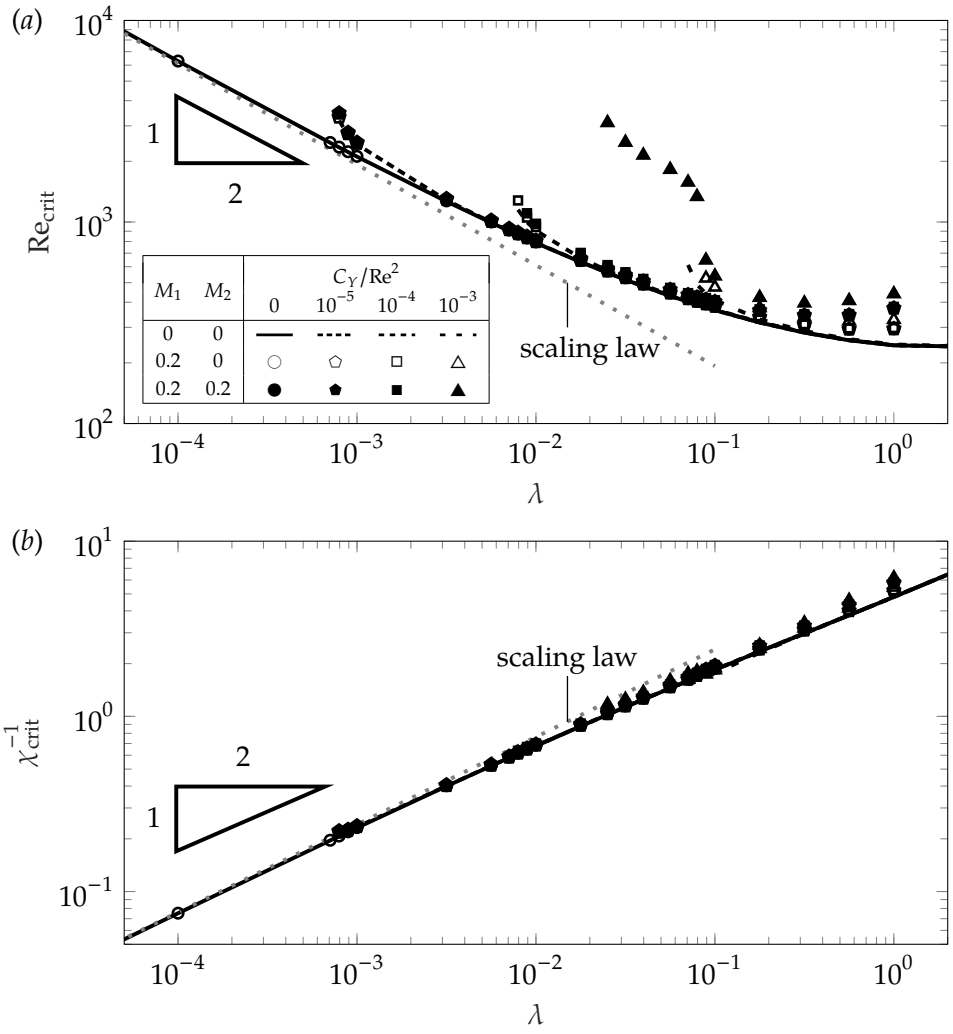

Figure 6.11: (*a*) Critical Reynolds number, $\mathrm{Re}_{\mathrm{crit}}$, and (*b*) the corresponding collapsed data for the critical shear at the top of the canopy, $\chi^{-1}_{\mathrm{crit}}$ in (6.43), for flows with different canopy densities. Shown is the case where $h = 0.5$ and $J = 10^{-5}$. Symbols and black lines are used to indicate plant flexibilities, C_Y/Re^2, and values of M_1 and M_2, as stated in the legend of (*a*). The grey dotted lines indicate the scaling predictions for sparse canopies [see discussion following equation (6.39)].

at which point $\mathrm{Re}_{\mathrm{crit}} \to \infty$. On the other hand, we also expect the system to be globally stable for sufficiently large λ (from the analysis in §6.7.2).

For all values of M_1, M_2 and λ the critical Reynolds number $\mathrm{Re}_{\mathrm{crit}}$ increases with flexibility, with the effect more pronounced for low canopy densities. Finally, it always requires a higher Reynolds number to destabilise flows through the same canopy when we account for inertia.

6.8.3 Behaviour of the critical shear

In the previous discussion, we have sought to understand the effects of plant flexibility, canopy density and inertia on the critical value of Re separating stable and unstable flows. However, there are interesting insights once this is viewed in terms of shear.

As mentioned in the introduction, it is known from turbulence statistics that canopy-scale instabilities are generated by shear of the flow along the top of the canopy (Raupach et al., 1996; Finnigan, 2000). However, previous stability analyses did not account for the free surface, canopy perturbations

or inertial effects such as added mass and virtual buoyancy. We would like to understand whether these additional physical effects affect the shearing mechanism.

A simple measurement for shear at a given depth is to consider its reciprocal—the (dimensionless) Navier slip length. In particular, suppose we let χ be this slip length at steady state at the top of the canopy $z = h_d^*$. We then define

$$\chi = \frac{u^*(h_d^*)}{u^{*\prime}(h_d^*)}. \tag{6.43}$$

For every flow that is marginally stable, we can quantify the critical shear with χ_{crit}^{-1}.

We observe from Figure 6.11b that for any given canopy density:

(i) The critical shear, χ_{crit}^{-1}, increases monotonically with λ;

(ii) The critical shear, χ_{crit}^{-1}, is nearly identical across different plant flexibilities when we neglect inertial effects – even when Re_{crit} and the configuration of the canopies (at their base states) are distinct;

(iii) Although there is a significant collapse in the data compared to the same plot for Re_{crit}, there is a spread for χ_{crit}^{-1} for different flexibilities. This spread increases with increasing M_1 and M_2 for any given λ.

The significant collapse in the data suggests that shear at the top of the canopy remains the relevant criterion in determining the stability of steady unidirectional flows. There is a slight spread when inertial effects are prominent, with the critical shear being larger for non-zero added mass and beam inertia. Nevertheless, the collapse of the data for different plant flexibilities means the simplified model where inertia is neglected, $M_1 = M_2 = 0$, can still provide a useful reference value for the critical shear.

Many features of Figure 6.11b in the limits of dense or spare canopies are explained by the asymptotic analysis of §6.7.2. For instance, in the case of sparse rigid canopies, we previously found that $\text{Re}_{\text{crit}} = O(\lambda^{-1/2})$ (see Figure 6.11a). Thus in combination with (6.43), $\chi_{\text{crit}} = O(\lambda^{-1/2})$ as $\lambda \to 0$; this is shown dotted in Figure 6.11b.

6.8.4 Summary of the physical mechanisms

In §6.8, we have sought to study the key conditions for the onset of instabilities. Our primary conclusion is that instabilities are induced by sufficient shear along the top of the canopy, and this is accompanied by non-monotonic behaviour of the critical Reynolds number, Re_{crit}, with canopy density, λ.

We have found that if $\lambda > \lambda_c$ as given in (6.41) the base flow can be unstable for sufficiently large Reynolds numbers. In such cases, let us write $\Lambda = \Lambda(C_Y/\text{Re}^2, M_1, M_2)$ for the canopy density corresponding to the minimum Re_{crit} (the turning point in Figure 6.11a). For canopies

with $\lambda > \Lambda$, the shear threshold is greater, and therefore, a faster flow is required for instability. On the other hand for $\lambda < \Lambda$, although the shear threshold is lower, a faster flow is required to generate this shear; this is due to the reduced momentum loss on account of reconfiguration, which can also be achieved by increasing flexibility, C_Y/Re^2. However, if $\lambda < \lambda_c$, this shear threshold will never be reached, irrespective of the flow speed. This differentiates flexible canopies from rigid canopies, where drag monotonically increases with flow speed (see Figure 6.5b) and hence, $\lambda_c = 0$. Finally, for both cylindrical beams and blades, added mass increases the shear threshold, which stabilises the flow.

6.9 SUMMARY

In this chapter, we considered free-surface flows through a flexible canopy, and attempted to analyse conditions for the onset of instabilities under strong currents. We studied the roles of various physical factors in triggering or suppressing a monami.

Our results allowed us to confirm that shear at the top of the canopy can be considered as a primary mechanism for instability, and this indeed agrees with previous analyses for the specific case of rigid vegetation. Our study, however, extends this conclusion by exploring vegetative flows with additional effects such as canopy flexibility and inertia.

Our results suggest that flexibility affects the flow stability in two distinct ways. Firstly, compared to rigid-canopy flows, flexible-canopy flows are more stable by having less drag due to plant reconfiguration in the underlying base state. In particular, if the canopy density is below a critical threshold, the flow will not be able to generate sufficient shear to trigger instabilities, irrespective of the Reynolds number. Secondly, by decoupling the fluid perturbations from the canopy perturbations, we found that for a given base flow, flexibility can encourage instability. Furthermore, by studying the growth of a single unstable eigenmode, our model can also capture the temporal evolution of monami.

6.10 DISCUSSION

One important conclusion from the present study is that the shear at the top of the canopy remains the dominant factor in determining the stability of a flow. Thus one interesting question that follows is whether there may be particular flow regimes where more involved models are required, and for which the central mechanism for instability may be different. As a particular example, we highlight the review by Nepf (2012), who notes that as the canopy becomes increasingly sparse, the flow transitions from a mixing-layer-like flow to a boundary-layer flow. In our current model, we have neglected the effects of bed shear, and this hints at the need for a

model for which the sparse-canopy limit can be more accurately captured.

Which length scales might be involved in a complete model? An important avenue for progress is the consideration of a complete turbulence model. Note that we analysed flow stability using a single mixing length at the top of the canopy (6.43) and our constant eddy viscosity closure model can be interpreted as effectively averaging the various length scales involved. However, in limits of small or large elasticity/density, it is unclear whether it may be necessary to consider a better closure model to capture disparate length scales in the flow.

Firstly, the bed can be rough in reality, and the boundary layer along it may contribute one length scale. Secondly, there is an element scale inside the canopy, which is determined by the wakes of individual plants. Thirdly, for deeply submerged canopies ($h \ll 1$), the turbulence that is generated far below is expected to be negligible far above. Thus, there is a length scale that is determined by the decay of the canopy-scale vortices. Finally, in a more general setting where the pressure gradient of the flow is not maintained, there will also be a decay length scale for the flow. A more detailed description of the different length scales can be found in Marion et al. (2014).

We envision that a more refined model will capture a number of these length scales. However, to implement such a scheme, we require a better understanding of the importance of these length scales. Moreover, we would hope to determine these scales as part of the model, rather than verified *a posteriori* from given parameters [see discussion in Poggi et al. (2004)].

7 SUMMARY & FINAL REMARKS

> Nature's imagination is so much greater than man's, she is never going to let us relax.
>
> *Richard Feynman*

The work in this thesis develops a theory that addresses the mechanical aspects of coastal flows through vegetation. In particular, we focused on understanding (i) how various waves evolve in multiple scenarios and (ii) the instabilities that emerge under the effects of a steady current. We divided our analysis between rigid and flexible vegetation. One central result has been the systematic development of a general framework for modelling and analysing flows through vegetation. Although we have typically considered systems with certain key physical effects (*e.g.* gravity, flexibility and inertia), additional fluid and canopy properties can be incorporated into the model in a straightforward manner.

Below, we provide a summary of the analysis in each chapter, highlighting how each corresponding sub-problem is related to the work as a whole. Key results are summarised in Table 7.1. These key results are presented in two parts. First, in Table 7.1a, we summarise the underlying *base flows* that are used in the different mathematical models of Chapters 2–6. Similarly, Table 7.1b summarises the key results in terms of the resultant *mathematical predictions*. For instance, from Chapters 2–5, these key results relate to our derivation of the governing differential equations for the wave evolution, while for Chapter 6, the results relate to instability modes and analysis.

7.1 RIGID VEGETATION (CHAPTERS 2–4)

We began by understanding the fundamental problem of small-amplitude waves through rigid vegetation in Chapter 2. This allowed us to set up the main mathematical model of this work on free-surface flows with an additional bulk momentum sink. The momentum sink homogenises the inertial and drag contributions of individual plants. On the assumption that the ratio between wavelength and domain length is small, we applied a multiple-scales analysis to show that the wave and the momentum sink are decoupled at leading-order. The analysis predicts that the wave is sinusoidal at leading-order, with its amplitude and wavelength slowly evolving in space due to the presence of vegetation and the variation in depth.

Table 7.1a: Summary of key modelling components from Chapters 2–6.

CHAPTER	BASE FLOW η is free-surface elevation, u is streamwise velocity bars denote scaled quantities	CANOPY MODEL h is plant length λ is density	DEPTH, H
2	SMALL-AMPLITUDE WAVE (2.27) $\eta = A(x)\cos(\bar{x} - t)$, $u = A(x)\dfrac{\cosh[k(x)(\bar{z} + \bar{H}(x))]}{\sinh k(x)\bar{H}(x)}\cos(\bar{x} - t)$, dispersion relation $k(x)\tanh[k(x)\bar{H}(x)] = 1$; fast scale $\bar{x} = \dfrac{\Phi(x)}{\alpha}$, $\alpha \ll 1$; $\dfrac{\mathrm{d}\Phi}{\mathrm{d}x} = k$, $z = \alpha\bar{z}$, $H = \alpha\bar{H}$	rigid beams	varying
3	STEADY CURRENT WITH SMALL-AMPLITUDE WAVE (3.17) $\eta = \eta_c(x) + A(x)\cos(\bar{x} - t)$, $u = u_c(x) + A(x)\dfrac{\cosh[k(x)(\bar{z} + \bar{H}(x))]}{\sinh k(x)\bar{H}(x)}\cos(\bar{x} - t)$, dispersion relation $k(x)\tanh[k(x)\bar{H}(x)] = 1$; fast scale $\bar{x} = \dfrac{\Phi(x)}{\alpha}$, $\alpha \ll 1$; $\dfrac{\mathrm{d}\Phi}{\mathrm{d}x} = k$, $z = \alpha\bar{z}$, $H = \alpha\bar{H}$	rigid beams	varying
4	INTERMEIATE-AMPLITUDE CNOIDAL WAVE (4.39) $\eta = u = A(\chi)\left(B(m(\chi)) + \mathrm{cn}^2\left[\dfrac{2K(m(\chi))}{T}(\bar{\chi} - t)\middle|m(\chi)\right]\right)$; wave height A (not amplitude), elliptic parameter m, scaled distance $\chi = \epsilon h\lambda x$, $\epsilon h\lambda \ll 1$, fast scale $\bar{\chi} = \dfrac{\Phi(\chi)}{\epsilon h\lambda}$, $\dfrac{\mathrm{d}\Phi}{\mathrm{d}\chi} = \left(1 + \dfrac{\epsilon A}{m}\left[1 - \dfrac{m}{2} - \dfrac{3}{2}\dfrac{E(m)}{K(m)}\right]\right)^{-1}$ trough elevation $B = \dfrac{1}{m}\left[1 - m - \dfrac{E(m)}{K(m)}\right]$, constant period $T = 4K(m)\sqrt{\dfrac{m}{3A}}\dfrac{\mathrm{d}\Phi}{\mathrm{d}x}$	rigid beams	fixed
5	SMALL-AMPLITUDE WAVE (5.21) $\eta = A(x)\cos(\bar{x} - t)$, $u = A(x)\dfrac{\cosh[k(x)(\bar{z} + \bar{H}(x))]}{\sinh k(x)\bar{H}(x)}\cos(\bar{x} - t)$, dispersion relation $k(x)\tanh[k(x)\bar{H}(x)] = 1$; fast scale $\bar{x} = \dfrac{\Phi(x)}{\alpha}$, $\alpha \ll 1$; $\dfrac{\mathrm{d}\Phi}{\mathrm{d}x} = k$, $z = \alpha\bar{z}$, $H = \alpha\bar{H}$	flexible beams (5.28) small deflections horizontal displacement, $\tilde{x}$	varying
6	STEADY UNIDIRECTIONAL FLOW (6.7) $\eta \equiv 0$, $\mathbf{u} = u(z)\hat{\mathbf{e}}_x$	flexible beams (6.4c)–(6.4d) large deflections angle of deflection, θ	fixed

Table 7.1b: Summary of key predictions from Chapters 2–6.

CHAPTER	MATHEMATICAL PREDICTIONS
2	*Description:* Predicting the time-averaged evolution of wave amplitude, A, in distance of propagation, x $\frac{\pi^2 A}{\bar{\lambda} k \cosh^2 k\bar{H}} \left[2A(\bar{H}-1)\frac{\mathrm{d}(k\bar{H})}{\mathrm{d}x} - (2k\bar{H} + \sinh 2k\bar{H})\frac{\mathrm{d}A}{\mathrm{d}x} \right] = \mathcal{D}$ canopy term $\mathcal{D} = \frac{A}{2}\int_{t=0}^{2\pi}\int_{\bar{z}=-\bar{H}}^{-\bar{H}+\bar{h}}\int_{\bar{x}=\bar{X}}^{\bar{X}+2\pi} \frac{\cosh[k(\bar{z}+\bar{H})]}{\cosh k\bar{H}} \cos(\bar{x}-t)\, u\,|u|\ \mathrm{d}\bar{x}\mathrm{d}\bar{z}\mathrm{d}t$
3	*Description:* Predicting evolution of current and mean surface elevation, u_c & η_c, in addition to amplitude, A $u_c = \frac{Q}{\bar{H}}$, constant mean flux Q; $\frac{\mathrm{d}\eta_c}{\mathrm{d}x} = -\frac{\bar{\lambda}}{4\pi\bar{H}}\int_{t=0}^{2\pi}\int_{\bar{z}=-\bar{H}}^{-\bar{H}+\bar{h}}\int_{\bar{x}=\bar{X}}^{\bar{X}+2\pi} u|u|\ \mathrm{d}\bar{x}\mathrm{d}\bar{z}\mathrm{d}t$ $\frac{\pi^2 A}{\bar{\lambda} k \cosh^2 k\bar{H}} \left[2A(\bar{H}-1)\frac{\mathrm{d}(k\bar{H})}{\mathrm{d}x} - (2k\bar{H} + \sinh 2k\bar{H})\frac{\mathrm{d}A}{\mathrm{d}x} \right] = \mathcal{D}$ canopy term $\mathcal{D} = \frac{A}{2}\int_{t=0}^{2\pi}\int_{\bar{z}=-\bar{H}}^{-\bar{H}+\bar{h}}\int_{\bar{x}=\bar{X}}^{\bar{X}+2\pi} \frac{\cosh[k(\bar{z}+\bar{H})]}{\cosh k\bar{H}} \cos(\bar{x}-t)\, u\,|u|\ \mathrm{d}\bar{x}\mathrm{d}\bar{z}\mathrm{d}t$
4	*Description:* Predicting evolution of wave height and elliptic parameter, A & m $\int_{t=0}^{T}\int_{\bar{\chi}=0}^{T} \left\{ \eta\eta_\chi + \frac{3\epsilon}{2}\eta^2\eta_\chi + \frac{\epsilon}{2}\left[\left(\frac{\mathrm{d}\Phi}{\mathrm{d}\chi}\right)^2 \eta\eta_{\bar{x}\bar{x}\chi} + \frac{\mathrm{d}\Phi}{\mathrm{d}\chi}\frac{\mathrm{d}^2\Phi}{\mathrm{d}\chi^2}\eta\eta_{\bar{x}\bar{x}} \right] \right\} \mathrm{d}\bar{\chi}\mathrm{d}t = -\frac{1}{4}\int_{t=0}^{T}\int_{\bar{\chi}=0}^{T} \eta^2|\eta|\ \mathrm{d}\bar{\chi}\mathrm{d}t$ By expressing m in terms of A (via T), the equation above can be written as $\frac{\mathrm{d}A}{\mathrm{d}\chi} = f(A,\epsilon,T)$, some f m can be deduced from the chain rule $\frac{\mathrm{d}m}{\mathrm{d}\chi} = \frac{\mathrm{d}m}{\mathrm{d}A}\frac{\mathrm{d}A}{\mathrm{d}\chi}$
5	*Description:* Predicting time-harmonic canopy dynamics and ultimately the evolution of wave amplitude, A $\frac{\pi^2 A}{\bar{\lambda} k \cosh^2 k\bar{H}} \left[2A(\bar{H}-1)\frac{\mathrm{d}(k\bar{H})}{\mathrm{d}x} - (2k\bar{H} + \sinh 2k\bar{H})\frac{\mathrm{d}A}{\mathrm{d}x} \right] = \mathcal{D}$ canopy term $\mathcal{D} = A\int_{t=0}^{2\pi}\int_{\bar{z}=-\bar{H}}^{-\bar{H}+\bar{h}}\int_{\bar{x}=\bar{X}}^{\bar{X}+2\pi} \frac{\cosh[k(\bar{z}+\bar{H})]}{\cosh k\bar{H}} \cos(\bar{x}-t)\left[\frac{1}{2}(u-\tilde{x}_t)\,|u-\tilde{x}_t| + M_1\,(u_t - \tilde{x}_{tt}) \right] \mathrm{d}\bar{x}\mathrm{d}\bar{z}\mathrm{d}t$ Individual plant displacement, $\tilde{x}$, satisfying (5.28), is evaluated at every $\bar{x}$ & x (microscale & macroscale)
6	*Description:* Predicting unstable steady configurations & critical conditions which trigger monami Fourier modes from the linear stability analysis satisfy the quadratic eigenvalue problem (6.31)

A particularly significant result is our generalisation of the predictions by Keller (1958), Dalrymple et al. (1984), and Mendez and Losada (2004); these previous works did not consider the simultaneous effects of bottom topography variation, presence of vegetation, and non-shallow-water effects. We also demonstrated good agreement between our asymptotic results and both numerical and experimental results that appeared in other studies. This model was then extended in subsequent chapters to analyse different types of flows.

The analysis in Chapter 3 on combined current-waves through rigid vegetation provides a natural extension of the work in Chapter 2. In particular, we considered the regime in which the steady current and the wave velocity are comparable in magnitude. An analogous multiple-scales analysis predicts that the superimposed wave decays differently from a pure wave with no current. However, the current velocity does not deviate from one in the waveless problem. Our analysis generalises the predictions by Hu et al. (2014) and Losada et al. (2016) on combined wave-current flows by accounting for both the variation of the mean free surface and water depth.

In Chapter 4, we advanced from the small-amplitude approximation and analysed shallow-water waves of intermediate amplitudes through rigid vegetation. We derived that the free surface is governed by a modified Korteweg-de Vries equation which has an additional canopy sink. Our results provide new predictions on how cnoidal waves – nonlinear periodic solutions of the leading-order (vegetation-free) problem – decay in both their wave height and elliptic parameter. The predictions are validated with numerical simulations. In the small-amplitude limit, we were able to recover the corresponding shallow-water approximations from the predictions in Chapter 2.

7.2 FLEXIBLE VEGETATION (CHAPTERS 5–6)

After gaining some intuition on how different waves evolve in the presence of rigid vegetation, we turned to the analysis of flexible vegetation.

In Chapter 5, we investigated how small-amplitude waves evolve in the presence of flexible vegetation. The analysis forms a natural extension to the work in Chapter 2, but now with the individual plants modelled as elastic cantilever beams. Hence, the underlying base flows in these classes of problems will serve to deform the canopy. At the same time, the resultant vegetation dynamics will affect the flow dynamics in return. The corresponding multiple-scale analysis showed that the base flow and the canopy dynamics are decoupled at leading-order. Since the base flow is identical to the one for rigid canopies *i.e.* a sinusoidal wave, we provided a systematic procedure on how to first solve for the canopy dynamics, before determining the evolution of the wave along the domain. We then made a detailed comparison between the full predictions on plant load and

experimental results from previous studies. Finally, we gave numerical examples to highlight how waves decay differently with increasing plant flexibility and inertia. This analysis thus generalises the predictions from Luhar et al. (2017) and Lei and Nepf (2019) by accounting for variations of plant dynamics along the domain.

Finally, in Chapter 6, we moved away from wave evolution and provided an in-depth investigation into the instabilities of flows through flexible vegetation. We explored the interesting phenomenon of monami – the synchronous oscillation of vegetation in current-dominated flows. In contrast to the pure wave problem in Chapter 5, plants can undergo large deformations. By performing a stability analysis on steady configurations of the problem, we found that shear along the top of the canopy is a dominant factor in triggering such instabilities. Although shear was also highlighted in previous studies such as Singh et al. (2016) and Sharma et al. (2017), our model has accounted for important effects including the presence of inertia, free surface and large canopy deformations. Furthermore, we deduced that monami could be suppressed for canopies that are sufficiently sparse or have high effective inertia.

7.3 OPEN PROBLEMS AND FUTURE WORK

Although we have made significant progress in developing mathematical theory for various sub-problems on flows through vegetation, many open problems remain—indeed, the rich interplay of flow and vegetative dynamics naturally creates many avenues for further research. Below, we highlight and discuss three significant open problems on wave-vegetation interaction; for each of these, we highlight some of the complications involved and conjecture possible strategies in overcoming them.

7.3.1 Predicting wave evolution in 3D: aspects on adiabatic invariance

Let us recall the setup for one-dimensional small-amplitude waves propagating in the positive x-direction over a substrate with $z = -H(x)$. In terms of the multiple-scales analysis, we consider x to be the slow scale and

$$\bar{x} = \frac{\Phi(x)}{\alpha} \tag{7.1}$$

to be the fast variable, for some small parameter $\alpha \ll 1$. The function Φ is chosen such that any dependent wave variable $f = f(\bar{x}, x, z = \alpha\bar{z})$ is periodic in $\bar{x}$ with a known constant period.

Suppose we expand f in powers of α *i.e.*

$$f = f_0 + \alpha f_1 + O(\alpha^2), \tag{7.2}$$

If the leading-order problem for f is linear with constant coefficients in $\bar{x}$,

satisfying for example

$$\left(\frac{\mathrm{d}\Phi}{\mathrm{d}x}\right)^2 f_{0\bar{x}\bar{x}} + f_{0\bar{z}\bar{z}} = 0, \tag{7.3}$$

we know that f_0 then has sinusoidal solutions in $\bar{x}$, with $\mathrm{d}\Phi/\mathrm{d}x$ satisfying an eikonal equation.

Suppose we generalise this framework to waves in a three-dimensional domain with general topographies $z = -H(x, y)$ or other inhomogeneities in the y-direction. Then there are two aspects that we need to address.

Firstly, suppose we consider a similar expansion to the one in (7.2). If the system of governing equations for f is linear, f can be expressed via a WKB ansatz (Ablowitz, 2011, §4.5), when the multiple-scales structure is restricted so that there is only a single fast scale dependent on multiple slow scales *i.e.*

$$\bar{x} = \frac{\Phi(x, y)}{\alpha}. \tag{7.4}$$

For this problem, Φ is now chosen such that f is periodic in $\bar{x}$ with a known constant period. Thus f exhibits a multiple-scales structure $f(\bar{x}, x, y)$. In particular, with the example in (7.3), the leading-order solution f_0 satisfies

$$\nabla^2\Phi f_{0\bar{x}\bar{x}} + f_{0\bar{z}\bar{z}} = 0, \tag{7.5}$$

with $\nabla^2\Phi = \Phi_{xx} + \Phi_{yy}$ satisfying an eikonal equation. However, since our problem is nonlinear due to the presence of drag, we have to apply a generalised multiple-scales analysis (Kuzmak, 1959). In particular, we need to consider additional properties f has in y.

Secondly, throughout the two-dimensional analysis of this thesis, we have exploited the linearity of the leading-order problem. In particular, we have simple sinusoidal solutions for both the base flow and the adjoint solution of the flow for deriving the solvability condition (see §2.5 and also Chapters 3 and 5). Although we can foresee that the leading-order problem will remain linear in 3D, the wave can slowly refract—a classic example is how wave crests become increasing parallel to the shoreline with decreasing water depth (Mei, 1992, §3.3). Thus, we have to account for this refraction in the momentum sink formulation. More importantly, the resultant solvability conditions will be in the form of ray tracing equations, which can be more challenging to both derive and solve.

7.3.2 Dynamic beam model for plants: twisting & variable inertia

We recall from the comparison between predicted and experimentally measured load in §5.5 that we are over-estimating load for plants with intermediate or high flexibilities. The dynamic model that is used to predict load is based on the assumption that inertial effects are independent of flexibility. Although we could consider beam theories that account for large deflections (see *e.g.* Chapter 6), the key complication in these situations

is that blade-like plants may twist due to small asymmetries in real-life scenarios (Luhar and Nepf, 2016); this twisting significantly reduces their cross-sectional width and hence, the associated load. Therefore, in such cases, the load on each plant is better approximated without inertia.

An approach that we have considered is to have the inertial parameter varying with flexibility. The simplest estimate would be to consider a linear relationship between the two parameters, with inertia varying between the rigid-blade value and zero for very flexible plants. More importantly, since our primary focus is on predicting wave attenuation, it is crucial to not over-predict the effects of a canopy in applications such as coastal protection. In addition, we have also predicted that inertial effects can also significantly enhance wave modulation—an attractive idea that might be exploited in industrial or environmental applications. Previous researchers have regarded seagrass canopies as low-pass filters for waves (Bradley and Houser, 2009; Zeller et al., 2014) – this is reflected in our multiple-scales analysis on systems with the wavelength-to-domain ratio, $\alpha \ll 1$. However, we may hope that under certain conditions, long waves of the coastal wave spectrum could also be dampened.

7.3.3 *Predicting the evolution of random waves in the presence of vegetation*

Finally, although we have made significant progress in predicting wave evolution under various settings, our analyses are confined to monochromatic waves. A realistic coastal flow will involve superposition of waves with multiple frequencies and amplitudes. For numerical simulations and experiments, the generalisation is more readily achievable by, for example, generating incident waves using a real spectrum [see *e.g.* Wu et al. (2012), Anderson and Smith (2014) and Mattis et al. (2019) on wave generation using the JONSWAP (Joint North Sea Wave Project) spectrum]. However, the analogous generalisation of analytical predictions under the multiple-scales framework is significantly more challenging – the current derivations involve exploiting periodicity (on the microscale).

There have been attempts in generalising the evolution equations for random waves. We highlight the work by Mendez and Losada (2004) on generalising the predictions by Dalrymple et al. (1984) on rigid vegetation *i.e.* (2.48) to narrowly-banded random sinusoidal waves. Their energy balance argument assumes that the wave heights follow a fixed Rayleigh distribution, which is supported by statistical theory (Dean and Dalrymple, 1991, §7.2). Mathematically, compared to

$$\frac{A}{A(x=0)} = \frac{1}{1+\Lambda x} \tag{7.6}$$

in (2.48) for the monochromatic prediction, they approximated that

$$\frac{A_{\text{rms}}}{A_{\text{rms}}(x=0)} = \frac{1}{1+\Lambda_{\text{rms}} x}, \tag{7.7}$$

with Λ_{rms} increased by approximately one-third compared to Λ. This formula has since been adopted by other researchers *e.g.* Möller et al. (2014).

In terms of our multiple-scales analysis framework, we suggest to first consider cases which allow the base flow to be a superposition of multiple waves. For instance, when the mean water depth is constant, we can consider such waves if individual waves have commensurate space and time periods – that is, the ratio between any two (space or time) periods is a rational number, so that they share a period such that they are both periodic. We give a brief mathematical explanation on why this is possible:

(i) Individual waves with commensurate time periods together share a constant time period. Thus, the superimposed wave is also time-periodic.

(ii) Since the depth is constant, the wavelengths of individual waves are also constant in space by their respective dispersion relations. With commensurate spatial periods (wavelengths), a fast variable in which the superimposed wave is always spatially-periodic can be well-defined.

The only remaining complication is that the individual waves are coupled to each other via drag. Hence, we have to solve for all of the amplitudes simultaneously. This is analogous to solving for both the wave and the current simultaneously for combined flows in Chapter 3 (and similarly for amplitude and elliptic parameter for nonlinear waves in Chapter 4).

The simplified case which we have shown above is particularly useful for waves which are Fourier decomposed. Another limiting case which can be explored is waves with contrasting time periods (with the extreme case being the combined current-wave problem in Chapter 3).

The open problems that we have discussed only showcase some of the many complexities involved in modelling flows through vegetation. Indeed, there are many more resultant applications that are worth studying; these include mass transport (erosion and deposition), carbon capture, and how an ecosystem might be affected, in general, by such vegetative flows. Throughout this thesis, we have gained a significant appreciation for the enormous challenges that accompany such systems. Both classical analysis of coastal flows, as well as analysis of elastic structures, has been well-developed over centuries, and yet scientists have only scratched the surface of systems that involve their combined effects. As a basic point to this effect, we note that the full 'zoo' of solutions (across all involved parameters introduced in our work) remains unknown—vegetative flows are yet to be fully classified. This is expected to challenge theoretical, computational, and experimental scientists for many years to come.

EXPERIMENTAL DATA IN FIGURE 2.9

A

In this appendix, we provide in Figure A.1 the experimental data that is used to generate Figure 2.9 on small-amplitude waves propagating through rigid vegetation. For each dataset, we plot the dimensionless time-averaged amplitude, A, as a function of the distance of propagation, x as individual subplots. We also plot the corresponding theoretical prediction curve

$$A(x) = \frac{1}{1 + \Lambda x} \tag{A.1}$$

with Λ in (2.47) specified using the reported experimental setups. We emphasise that there are no fitting parameters involved. Out of the 23 datasets from Wu et al. (2012), we discarded the dataset '200662401' when we generated Figure 2.9 – this dataset is also plotted below for completeness.

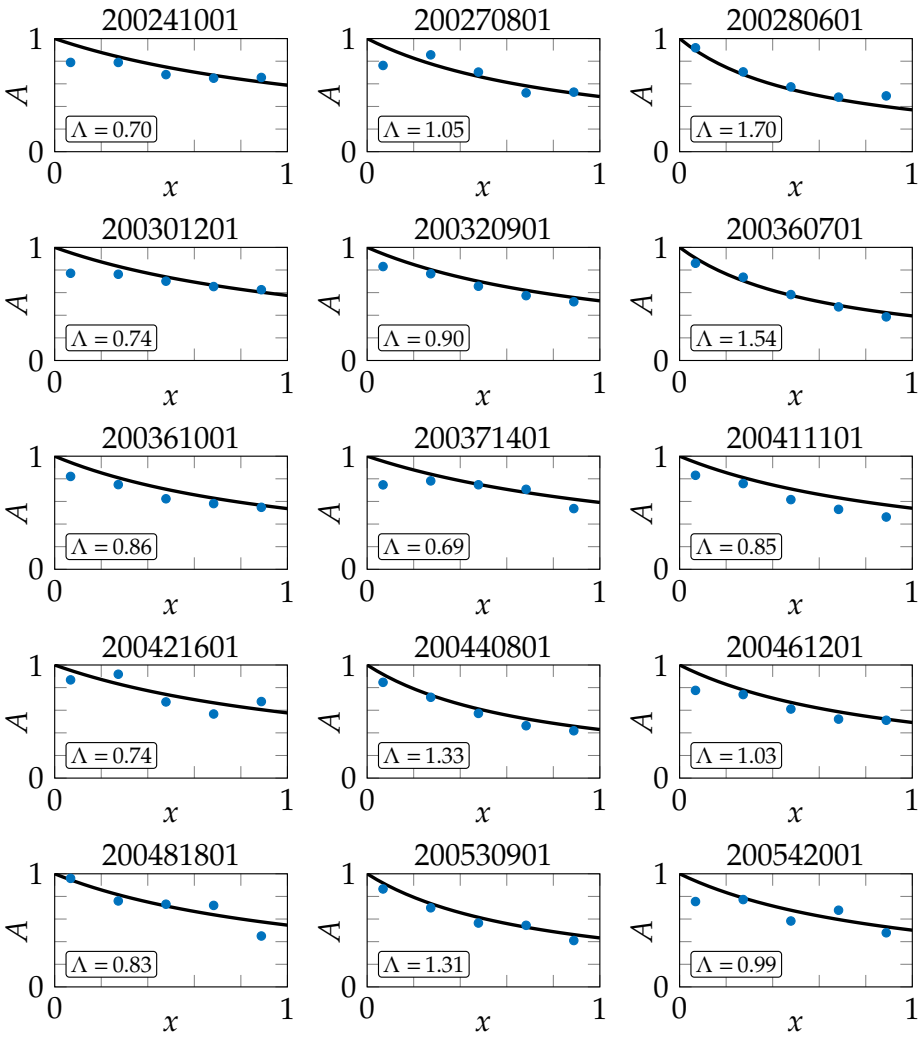

Figure A.1: Set of 29 plots for time-averaged amplitude, A, versus distance of propagation, x. In each plot, x is normalised by the length of the finite canopy and A is normalised by the amplitude at the start of the canopy ($x = 0$). Each subplot represents a different experiment, with experimental data shown in coloured dots and the corresponding prediction curve $A = (1 + \Lambda x)^{-1}$ from (A.1) shown in black. The title of each plot gives the name of the dataset or the source, with:

- Augustin et al. (2009)
- Wu et al. (2012)
- Ozeren et al. (2014)

In particular, for the data from Wu et al. (2012), we plotted the mean amplitude of multiple measurements that are made at every given x.

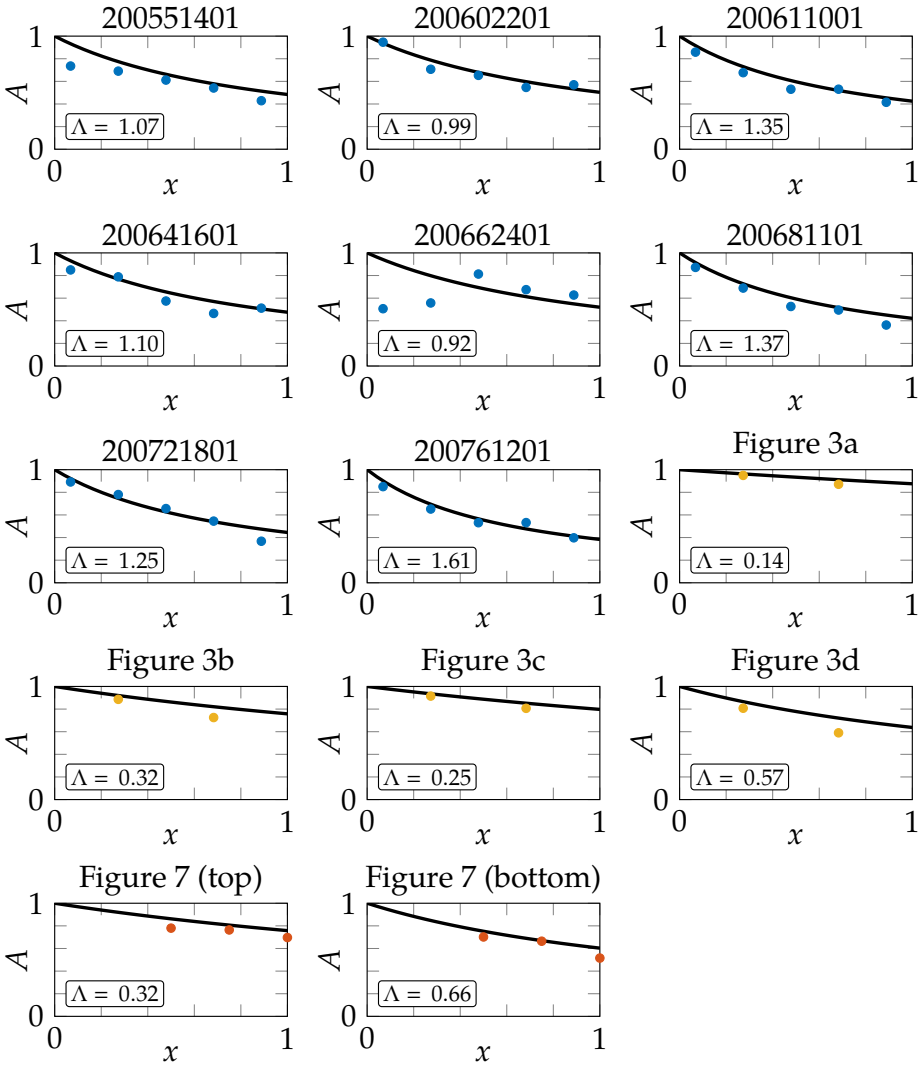

Here below, we also plot in Figure A.2 the corresponding predictions using $C_D \equiv 1.2$ in (A.1) (see Figure 2.9)—the R^2-value for this plot is 0.62.

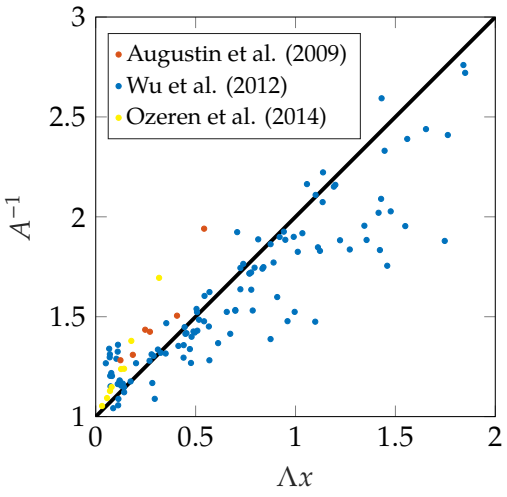

Figure A.2: Experimentally determined dimensionless decay for waves propagating through a rigid canopy. The black solid line indicates the theoretical prediction $A = (1 + \Lambda x)^{-1}$ (A.1) using $C_D \equiv 1.2$ and dots indicate the measurements for individual experiments.

B

FULL NUMERICAL SIMULATIONS WITH PROTEUS

In this appendix, we supplement the discussion in §2.9 by presenting additional numerical simulations with *Proteus* on small-amplitude waves through rigid vegetation. In particular, we highlight the effect of canopy height, h, in relation to the mean water depth, H. In contrast to the scenarios presented in Figure 2.8, here we consider $H \equiv 2$ m *i.e.* the canopy zone in Figure 2.6 has no elevation. Other specifications on the numerical wave flume can be found in §2.8.

For incident waves with the same initial amplitude and period, we compare in Figure B.1 the evolution of the wave amplitude due to different canopy heights. Although the numerical simulations (shown blue) are in good agreement with their respective analytical predictions (shown black), we found that damping is negligible when only half of the vertical domain is covered by vegetation ($h/H = 0.5$). On the other hand, when $h/H = 0.9$, damping is much more significant. This contrast highlights that for waves with intermediate wavelength [the dimensionless wavenumber k being $O(1)$ in the dispersion relation (2.28)], the momentum of the wave is confined near the free surface.

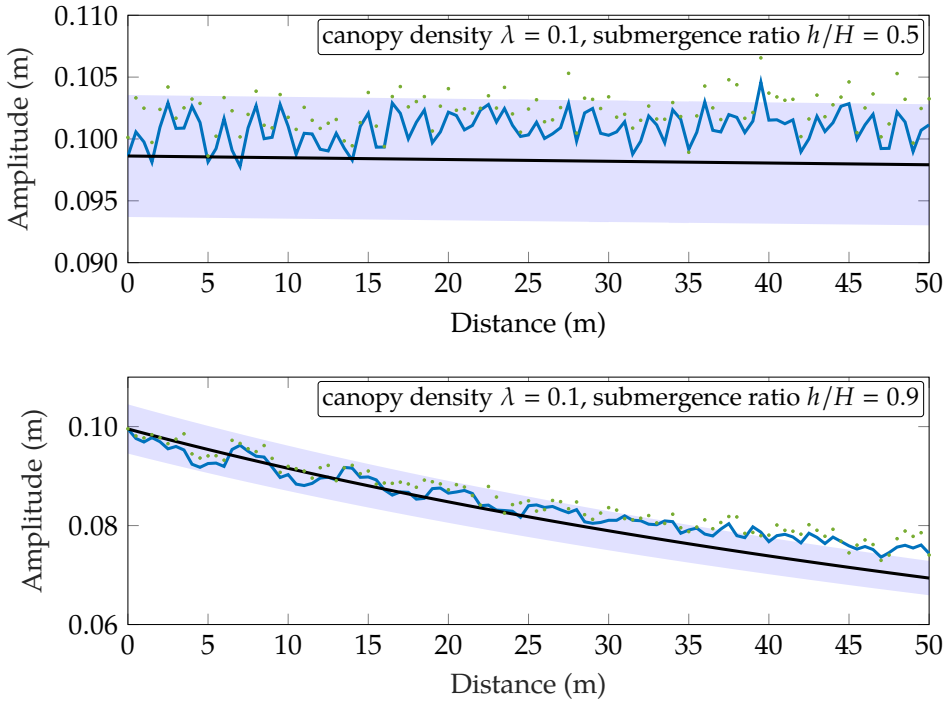

Figure B.1: Period-averaged amplitude for waves propagating through canopies with height h over a horizontal domain $H \equiv 2$ m. The green data points denote the amplitude of the numerical wave at each virtual gauge. The fundamental modes that are extracted at each gauge are connected by blue lines. The corresponding analytical predictions for the amplitude (2.40) are plotted in black, together with 5% error bands being shaded in as visual guides. The predictions are scaled so that the amplitudes match the fundamental mode at $x = 0$ m. We considered waves with amplitude 0.1 m and period 1.5 s.

C

SOLVING THE KDV EQUATION WITH FOURIER TRANSFORMS

In this appendix, we outline how we can solve the modified Korteweg-de Vries (KdV) equation (4.13) in Chapter 4 using discrete Fourier transforms and a split-step method. This numerical scheme is adapted from Taha and Ablowitz (1984) and implemented in MATLAB.

Suppose we denote

$$\hat{f}(k,t) = \int_{-\infty}^{\infty} f(x,t)\mathrm{e}^{-\mathrm{i}kx}\,\mathrm{d}x \tag{C.1}$$

to be the Fourier transform of the function $f(x,t)$ in space. The modified KdV equation (4.13) in the wavenumber space can be written as

$$\hat{\eta}_t = \underbrace{-\mathrm{i}k\hat{\eta} - \frac{\epsilon}{6}(\mathrm{i}k)^3\hat{\eta} + \frac{\epsilon h\lambda}{2}\mathrm{i}k\overline{M}\hat{\eta}}_{\mathcal{L}\hat{\eta},\,\text{linear}} \underbrace{-\frac{3\epsilon}{4}\mathrm{i}k\widehat{\eta^2} - \frac{\epsilon h\lambda}{4}\widehat{\eta|\eta|}}_{\mathcal{N}(\hat{\eta})\hat{\eta},\,\text{nonlinear}}. \tag{C.2}$$

A first-order approximation for $\hat{\eta}(k,t+\Delta t)$ is given by

$$\hat{\eta}(k,t+\Delta t) \approx \mathrm{e}^{\Delta t[\mathcal{L}+\mathcal{N}(\hat{\eta})]}\hat{\eta}(k,t) = \mathrm{e}^{\Delta t\mathcal{N}(\hat{\eta})}\underbrace{\mathrm{e}^{\Delta t\mathcal{L}}\hat{\eta}(k,t)}_{\hat{\eta}_\mathrm{I}}. \tag{C.3}$$

For a given $\hat{\eta}(k,t)$, the idea is to time-step to the intermediate solution $\hat{\eta}_I$ before we further time-step to approximate $\hat{\eta}(k,t+\Delta t)$. By doing so, this split-step method solves the linear and the nonlinear part of (C.2) separately. A discussion is given in Milewski and Tabak (1999) on how this procedure eliminates some of the stiffness that is associated with the original problem (4.13) when it is solved numerically.

In summary, we solve the pair of equations

$$\hat{\eta}_{\mathrm{I}t} = \left(-\mathrm{i}k - \frac{\epsilon}{6}\mathrm{i}k^3 + \frac{\epsilon h\lambda}{2}\mathrm{i}k\overline{M}\right)\hat{\eta} \tag{C.4}$$

$$\frac{\hat{\eta}(k,t+\Delta t) - \hat{\eta}_\mathrm{I}}{\Delta t} = -\frac{3\epsilon}{4}\mathrm{i}k\widehat{\eta_\mathrm{I}^2} - \frac{\epsilon h\lambda}{4}\widehat{\eta_\mathrm{I}|\eta_\mathrm{I}|} \tag{C.5}$$

in sequence, to approximate $\hat{\eta}(k,t+\Delta t)$. We note that for the nonlinear equation (C.5), we have chosen a simple Euler's method to approximate $\hat{\eta}(k,t+\Delta t)$. A higher-order method is given in Taha and Ablowitz (1984).

We first solve the linear equation (C.4) exactly and get

$$\hat{\eta}_\mathrm{I}(k,t+\Delta t) = \hat{\eta}\exp\left[\left(-\mathrm{i}k - \frac{\epsilon}{6}\mathrm{i}k^3 + \frac{\epsilon h\lambda}{2}\mathrm{i}k\overline{M}\right)\Delta t\right]. \tag{C.6}$$

If we also inverse Fourier transform the intermediate solution above, we can then substitute both $\hat{\eta}_{\mathrm{I}}$ and η_{I} into the nonlinear equation (C.5). We emphasise that although we have solved for both quantities at time $t + \Delta t$, this is the correct leading-order approximation for a Taylor expansion in $\Delta t \ll 1$. Finally, we can obtain $\eta(x, t + \Delta t)$ by inverse Fourier transforming $\hat{\eta}(k, t + \Delta t)$.

We found that this scheme may suffer from numerical instabilities at high spatial resolutions unless $\Delta t \ll 1$. In this case, the associated computational cost significantly increases due to the number of Fourier transforms involved at each time step.

BIBLIOGRAPHY

Ablowitz, M. J. (2011). *Nonlinear dispersive waves: asymptotic analysis and solitons*. Cambridge University Press, Cambridge.

Abramowitz, M. and Stegun, I. A. (1948). *Handbook of mathematical functions with formulas, graphs, and mathematical tables*. US Government printing office.

Alben, S., Shelley, M. J., and Zhang, J. (2002). Drag reduction through self-similar bending of a flexible body. *Nature*, 420(6915):479–481.

Anderson, M. E. and Smith, J. M. (2014). Wave attenuation by flexible, idealized salt marsh vegetation. *Coastal Engineering*, 83:82–92.

Augustin, L. N., Irish, J. L., and Lynett, P. (2009). Laboratory and numerical studies of wave damping by emergent and near-emergent wetland vegetation. *Coastal Engineering*, 56(3):332–340.

Baddour, R. E. and Song, S. (1990). On the interaction between waves and currents. *Ocean Engineering*, 17(1-2):1–21.

Balay, S., Abhyankar, S., Adams, M. F., Brown, J., Brune, P., Buschelman, K., Curfman McInnes, L., Dalcin, L. D., Dener, A., Eijkhout, V., Gropp, W. D., Karpeyev, D., Kaushik, D., Knepley, M. G., May, D. A., Mills, R. T., Munson, T., Rupp, K., Sanan, P., Smith, B., Zampini, S., and Zhang, H. (2019). PETSc users manual. Technical report, Argonne National Laboratory.

Balay, S., Curfman McInnes, L., Gropp, W. D., and Smith, B. F. (1997). Efficient management of parallelism in object-oriented numerical software libraries. In Arge, E., Bruaset, A. M., and Langtangen, H. P., editors, *Modern Software Tools for Scientific Computing*, pages 163–202. Birkhäuser Boston, Boston, MA.

Batchelor, G. K. (2000). *An introduction to fluid dynamics*. Cambridge University Press.

Benilov, E. S., Grimshaw, R., and Kuznetsova, E. P. (1993). The generation of radiating waves in a singularly-perturbed Korteweg-de Vries equation. *Physica D: Nonlinear Phenomena*, 69(3-4):270–278.

Bentley, A., Bootland, N., Wathen, A. J., and Kees, C. E. (2017). Implementation details of the level set two-phase Navier–Stokes equations in Proteus. Technical report, Department of Mathematical Sciences, Clemson University, Clemson, South Carolina, USA.

Boothroyd, R. J., Hardy, R. J., Warburton, J., and Marjoribanks, T. I. (2017). Modeling complex flow structures and drag around a submerged plant of varied posture. *Water Resources Research*, 53(4):2877–2901.

Borum, J., Duarte, C. M., Krause-Jensen, D., and Greve, T. M. (2004). *European seagrasses: an introduction to monitoring and management*. EU project Monitoring and Managing of European Seagrasses (M&MS) EVK3-CT-2000-00044.

Bradley, K. and Houser, C. (2009). Relative velocity of seagrass blades: Implications for wave attenuation in low-energy environments. *Journal of Geophysical Research: Earth Surface*, 114(1):1–13.

Brennen, C. E. (1982). A review of added mass and fluid inertial forces. Technical report, Naval Civil Engineering Laboratory, Sierra Madre (CA).

Chang, C. W. and Liu, P. L. F. (2019). Long waves dissipation and harmonic generation by coastal vegetation. *Applied Ocean Research*, 82(August 2018):210–224.

Chapman, S. J. (1995). A mean-field model of superconducting vortices in three dimensions. *SIAM Journal on Applied Mathematics*, 55(5):1259–1274.

Chapman, S. J. (2002). Subcritical transition in channel flows. *Journal of Fluid Mechanics*, 451:35–97.

Chapman, S. J. and Farrell, P. E. (2017). Analysis of Carrier's problem. *SIAM Journal on Applied Mathematics*, 77(3):924–950.

Chen, H., Ni, Y., Li, Y., Liu, F., Ou, S., Su, M., Peng, Y., Hu, Z., Uijttewaal, W. S., and Suzuki, T. (2018). Deriving vegetation drag coefficients in combined wave-current flows by calibration and direct measurement methods. *Advances in Water Resources*, 122(135):217–227.

Chen, Z., Jiang, C., and Nepf, H. M. (2013). Flow adjustment at the leading edge of a submerged aquatic canopy. *Water Resources Research*, 49(9):5537–5551.

Cushman-Roisin, B. (2005). Kelvin-Helmholtz instability as a boundary-value problem. *Environmental Fluid Mechanics*, 5(6):507–525.

Dalcin, L. D., Paz, R. R., Kler, P. A., and Cosimo, A. (2011). Parallel distributed computing using Python. *Advances in Water Resources*, 34(9):1124–1139.

Dalrymple, R. A., Kirby, J. T., and Hwang, P. A. (1984). Wave diffraction due to areas of energy dissipation. *Journal of Waterway, Port, Coastal, and Ocean Engineering*, 110(1):67–79.

de Langre, E. (2008). Effects of wind on plants. *Annual Review of Fluid Mechanics*, 40(1):141–168.

Dean, R. G. and Dalrymple, R. A. (1991). *Water wave mechanics for engineers and scientists*, volume 2 of *Advanced series on ocean engineering*. World Scientific.

Dimakopoulos, A. S., de Lataillade, T., and Kees, C. E. (2019). Fast random wave generation in numerical tanks. *Proceedings of the Institution of Civil Engineers - Engineering and Computational Mechanics*, 172(1):1–11.

Dingemans, M. W. (1997). *Water wave propagation over uneven bottoms*, volume 13 of *Advanced series on ocean engineering*. World Scientific.

Drazin, P. G. and Reid, W. H. (1982). *Hydrodynamic stability*. Cambridge University Press.

Driscoll, T. A., Hale, N., and Trefethen, L. N. (2014). *Chebfun guide*. Pafnuty Publications, Oxford, United Kingdom.

Dunn, C., Lopez, F., and García, M. H. (1996). Mean flow and turbulence in a laboratory channel with simulated vegetation. Technical Report 51, Department of Civil Engineering, University of Illinois at Urbana-Champaign, Urbana, Illinois, USA.

Dupont, S., Gosselin, F. P., Py, C., de Langre, E., Hemon, P., and Brunet, Y. (2010). Modelling waving crops using large-eddy simulation: Comparison with experiments and a linear stability analysis. *Journal of Fluid Mechanics*, 652:5–44.

El, G. A., Grimshaw, R. H., and Kamchatnov, A. M. (2007). Evolution of solitary waves and undular bores in shallow-water flows over a gradual slope with bottom friction. *Journal of Fluid Mechanics*, 585:213–244.

El, G. A. and Hoefer, M. A. (2016). Dispersive shock waves and modulation theory. *Physica D: Nonlinear Phenomena*, 333:11–65.

Fenton, J. D. (1988). The numerical solution of steady water wave problems. *Computers and Geosciences*, 14(3):357–368.

Finnigan, J. J. (2000). Turbulence in plant canopies. *Annual review of fluid mechanics*, 32(1):519–571.

Ghisalberti, M. and Nepf, H. M. (2002). Mixing layers and coherent structures in vegetated aquatic flows. *Journal of Geophysical Research*, 107(C2):3011.

Ghisalberti, M. and Nepf, H. M. (2004). The limited growth of vegetated shear layers. *Water Resources Research*, 40(7):1–12.

Gijón Mancheño, A. (2016). Interaction between wave hydrodynamics and flexible vegetation (MSc thesis). Technical report, Delft University of Technology.

Gosselin, F. P. (2019). Mechanics of a plant in fluid flow. *Journal of Experimental Botany*, 70(14):3533–3548.

Goussis, D. A. and Pearlstein, A. J. (1989). Removal of infinite eigenvalues in the generalized matrix eigenvalue problem. *Journal of Computational Physics*, 84(1):242–246.

Hamm, L., Madsen, P. A., and Peregrine, D. H. (1993). Wave transformation in the nearshore zone: A review. *Coastal Engineering*, 21(1-3):5–39.

Hammarling, S., Munro, C. J., and Tisseur, F. (2013). An algorithm for the complete solution of quadratic eigenvalue problems. *ACM Transactions on Mathematical Software*, 39(3):1–19.

Hu, Z., Suzuki, T., Zitman, T., Uittewaal, W., and Stive, M. (2014). Laboratory study on wave dissipation by vegetation in combined current-wave flow. *Coastal Engineering*, 88:131–142.

Huang, Z., Yao, Y., Sim, S. Y., and Yao, Y. (2011). Interaction of solitary waves with emergent, rigid vegetation. *Ocean Engineering*, 38(10):1080–1088.

Isobe, M. (1985). Calculation and application of first-order cnoidal wave theory. *Coastal Engineering*, 9(4):309–325.

Jackaman, J. and Pryer, T. (2019). Conservative Galerkin methods for dispersive Hamiltonian problems. arXiv:1811.09999v2.

Johnson, R. S. (1997). *A modern introduction to the mathematical theory of water waves*. Cambridge University Press.

Kaup, D. J. and Newell, A. C. (1978). Solitons as particles, oscillators, and in slowly changing media: a singular perturbation theory. *Proceedings of the Royal Society of London. A. Mathematical and Physical Sciences*, 361(1707):413–446.

Kees, C. E., Akkerman, I., Farthing, M. W., and Bazilevs, Y. (2011). A conservative level set method suitable for variable-order approximations and unstructured meshes. *Journal of Computational Physics*, 230(12):4536–4558.

Keller, J. B. (1958). Surface waves on water of non-uniform depth. *Journal of Fluid Mechanics*, 4(6):607–614.

Keulegan, G. H. and Carpenter, L. H. (1958). Forces on cylinders and spheres in a sinusoidally oscillating fluid. *Journal of Research of the National Bureau of Standards*, 60(5):423–440.

Kirby, J. T. (1984). A note on linear surface wave-current interaction over slowly varying topography. *Journal of Geophysical Research*, 89(C1):745.

Kobayashi, N., Raichle, A. W., and Asano, T. (1993). Wave attenuation by vegetation. *Journal of Waterway, Port, Coastal, and Ocean Engineering*, 119(1):30–48.

Koehl, M. A., Silk, W. K., Liang, H., and Mahadevan, L. (2008). How kelp produce blade shapes suited to different flow regimes: A new wrinkle. *Integrative and Comparative Biology*, 48(6):834–851.

Korteweg, D. J. and de Vries, G. (1895). XLI. On the change of form of long waves advancing in a rectangular canal, and on a new type of long stationary waves. *The London, Edinburgh, and Dublin Philosophical Magazine and Journal of Science*, 39(240):422–443.

Kuzmak, G. E. (1959). Asymptotic solutions of nonlinear second order differential equations with variable coefficients. *Journal of Applied Mathematics and Mechanics*, 23(3):730–744.

Lamb, H. (1932). *Hydrodynamics*. Dover Publications.

Landau, L. D. and Lifshitz, E. M. (1960). *Courses of theoretical physics - Volume 7. Theory of elasticity*. Pergamon Press, Oxford, United Kingdom, 2nd edition.

Landau, L. D. and Lifshitz, E. M. (1976). *Course of theoretical physics - Volume 1. Mechanics*. Pergamon Press, Oxford, United Kingdom, 3rd edition.

Lawrence, G. A., Browand, F. K., and Redekopp, L. G. (1991). The stability of a sheared density interface. *Physics of Fluids A*, 3(10):2360–2370.

Leclercq, T. and de Langre, E. (2018). Reconfiguration of elastic blades in oscillatory flow. *Journal of Fluid Mechanics*, 838:606–630.

Lei, J. and Nepf, H. M. (2019). Wave damping by flexible vegetation: Connecting individual blade dynamics to the meadow scale. *Coastal Engineering*, 147:138–148.

Losada, I. J., Maza, M., and Lara, J. L. (2016). A new formulation for vegetation-induced damping under combined waves and currents. *Coastal Engineering*, 107:1–13.

Lowe, R. J., Koseff, J. R., and Monismith, S. G. (2005). Oscillatory flow through submerged canopies: 1. Velocity structure. *Journal of Geophysical Research C: Oceans*, 110(10):1–17.

Luhar, M., Infantes, E., and Nepf, H. M. (2017). Seagrass blade motion under waves and its impact on wave decay. *Journal of Geophysical Research: Oceans*, 122(5):3736–3752.

Luhar, M. and Nepf, H. M. (2011). Flow-induced reconfiguration of buoyant and flexible aquatic vegetation. *Limnology and Oceanography*, 56(6):2003–2017.

Luhar, M. and Nepf, H. M. (2016). Wave-induced dynamics of flexible blades. *Journal of Fluids and Structures*, 61:20–41.

Luke, J. C. (1966). A perturbation method for nonlinear dispersive wave problems. *Proceedings of the Royal Society of London. Series A. Mathematical and Physical Sciences*, 292(1430):403–412.

Luminari, M. N., Airiau, C., and Bottaro, A. (2016). Drag-model sensitivity of Kelvin-Helmholtz waves in canopy flows. *Physics of Fluids*, 28(12):124103.

Marion, A., Nikora, V., Puijalon, S., Bouma, T. J., Koll, K., Ballio, F., Tait, S., Zaramella, M., Sukhodolov, A., O'Hare, M., Wharton, G., Aberle, J., Tregnaghi, M., Davies, P., Nepf, H. M., Parker, G., and Statzner, B. (2014). Aquatic interfaces: A hydrodynamic and ecological perspective. *Journal of Hydraulic Research*, 52(6):744–758.

Mattis, S. A., Kees, C. E., Wei, M. V., Dimakopoulos, A. S., and Dawson, C. N. (2019). Computational model for wave attenuation by flexible vegetation. *Journal of Waterway, Port, Coastal, and Ocean Engineering*, 145(1):04018033.

Maza, M., Lara, J. L., and Losada, I. J. (2015). Tsunami wave interaction with mangrove forests: A 3-D numerical approach. *Coastal Engineering*, 98:33–54.

Maza, M., Lara, J. L., and Losada, I. J. (2016). Solitary wave attenuation by vegetation patches. *Advances in Water Resources*, 98:159–172.

McMillen, T. and Goriely, A. (2003). Whip waves. *Physica D: Nonlinear Phenomena*, 184(1-4):192–225.

Mei, C. C. (1992). *The applied dynamics of ocean curface waves*, volume 1 of *Advanced Series on Ocean Engineering*. World Scientific.

Mei, C. C., Chan, I. C., and Liu, P. L. F. (2014). Waves of intermediate length through an array of vertical cylinders. *Environmental Fluid Mechanics*, 14(1):235–261.

Mei, C. C., Chan, I. C., Liu, P. L. F., Huang, Z., and Zhang, W. (2011). Long waves through emergent coastal vegetation. *Journal of Fluid Mechanics*, 687:461–491.

Mendez, F. J. and Losada, I. J. (2004). An empirical model to estimate the propagation of random breaking and nonbreaking waves over vegetation fields. *Coastal Engineering*, 51(2):103–118.

Meyer, R. (1979). Theory of water-wave refraction. In *Advances in Applied Mechanics*, pages 53–141. Academic Press.

Miles, J. W. (1980). Solitary waves. *Annual Review of Fluid Mechanics*, 12(1):11–43.

Miles, J. W. (1981). The Korteweg-de Vries equation: a historical essay. *Journal of Fluid Mechanics*, 106:131–147.

Miles, J. W. (1983a). Solitary Wave Evolution Over a Gradual Slope with Turbulent Friction. *Journal of Physical Oceanography*, 13(3):551–553.

Miles, J. W. (1983b). Wave evolution over a gradual slope with turbulent friction. *Journal of Fluid Mechanics*, 133:207–216.

Milewski, P. A. and Tabak, E. G. (1999). A PseudoSpectral Procedure for the Solution of Nonlinear Wave Equations with Examples from Free-Surface Flows. *SIAM Journal on Scientific Computing*, 21(3):1102–1114.

Möller, I., Kudella, M., Rupprecht, F., Spencer, T., Paul, M., van Wesenbeeck, B. K., Wolters, G., Jensen, K., Bouma, T. J., Miranda-Lange, M., and Schimmels, S. (2014). Wave attenuation over coastal salt marshes under storm surge conditions. *Nature Geoscience*, 7(10):727–731.

Montanelli, H. and Nakatsukasa, Y. (2018). Fourth-order time-stepping for stiff PDEs pn the sphere. *SIAM Journal on Scientific Computing*, 40(1):A421–A451.

Morris, R. L., Konlechner, T. M., Ghisalberti, M., and Swearer, S. E. (2018). From grey to green: Efficacy of eco-engineering solutions for nature-based coastal defence. *Global Change Biology*, 24(5):1827–1842.

Mullarney, J. C. and Henderson, S. M. (2010). Wave-forced motion of submerged single-stem vegetation. *Journal of Geophysical Research: Oceans*, 115(12):1–14.

Myint, S. and Grimshaw, R. (1995). The modulation of nonlinear periodic wavetrains by dissipative terms in the Korteweg-de Vries equation. *Wave Motion*, 22(2):215–238.

Nepf, H. M. (2012). Flow and transport in regions with aquatic vegetation. *Annual Review of Fluid Mechanics*, 44(1):123–142.

Newman, J. N. (1977). *Marine hydrodynamics*. MIT Press.

Nikora, V. (2010). Hydrodynamics of aquatic ecosystems: An interface between ecology, biomechanics and environmental fluid mechanics. *River Research and Applications*, 26(4):367–384.

Ockendon, H. and Tayler, A. B. (1983). *Inviscid fluid flows*, volume 43 of *Applied Mathematical Sciences*. Springer New York, New York, NY.

Okamoto, T. A. and Nezu, I. (2009). Turbulence structure and 'monami' phenomena in flexible vegetated open-channel flows. *Journal of Hydraulic Research*, 47(6):798–810.

Orszag, S. A. (1971). Accurate solution of the Orr-Sommerfeld stability equation. *Journal of Fluid Mechanics*, 50(4):689–703.

Ozeren, Y., Wren, D. G., and Wu, W. (2014). Experimental investigation of wave attenuation through model and live vegetation. *Journal of Waterway, Port, Coastal and Ocean Engineering*, 140(5):1–12.

Peregrine, D. H. (1976). Interaction of water waves and currents. *Advances in Applied Mechanics*, 16(C):9–117.

Poggi, D., Porporato, A., Ridolfi, L., Albertson, J. D., and Katul, G. G. (2004). The effect of vegetation density on canopy sub-layer turbulence. *Boundary-Layer Meteorology*, 111(3):565–587.

Ramberg, S. E. (1983). The effects of yaw and finite length upon the vortex wakes of stationary and vibrating circular cylinders. *Journal of Fluid Mechanics*, 128:81–107.

Rathgeber, F., Ham, D. A., Mitchell, L., Lange, M., Luporini, F., McRae, A. T., Bercea, G. T., Markall, G. R., and Kelly, P. H. (2016). Firedrake: Automating the finite element method by composing abstractions. *ACM Transactions on Mathematical Software*, 43(3).

Raupach, M. R., Finnigan, J. J., and Brunet, Y. (1996). Coherent eddies and turbulence in vegetation canopies: The mixing-layer analogy. *Boundary-Layer Meteorology*, 78(3-4):351–382.

Reddy, S. C., Schmid, P. J., and Henningson, D. S. (1993). Pseudospectra of the Orr-Sommerfeld operator. *SIAM Journal on Applied Mathematics*, 53(1):15–47.

Sharma, A. and García-Mayoral, R. (2018). Turbulent flows over sparse canopies. *Journal of Physics: Conference Series*, 1001(1):012012.

Sharma, A., Gomez de Segura, G., and García-Mayoral, R. (2017). Linear stability analysis of turbulent flows over dense filament canopies. In *10th International Symposium on Turbulence and Shear Flow Phenomena, TSFP 2017*.

Singh, R., Bandi, M. M., Mahadevan, A., and Mandre, S. (2016). Linear stability analysis for monami in a submerged seagrass bed. *Journal of Fluid Mechanics*, 786:R1–1–R1–12.

Stoker, J. J. (1947). Surface waves in water of variable depth. *Quarterly of Applied Mathematics*, 5(1):1–54.

Sumer, B. M. and Fredsøe, J. (2006). *Hydrodynamics around cylindrical structures*. World Scientific.

Suzuki, T., Zijlema, M., Burger, B., Meijer, M. C., and Narayan, S. (2012). Wave dissipation by vegetation with layer schematization in SWAN. *Coastal Engineering*, 59(1):64–71.

Svendsen, I. A. and Hansen, J. B. (1978). On the deformation of periodic long waves over a gently sloping bottom. *Journal of Fluid Mechanics*, 87(3):433–448.

Taha, T. R. and Ablowitz, M. J. (1984). Analytical and numerical aspects of certain nonlinear evolution equations. III. Numerical, Korteweg-de Vries equation. *Journal of Computational Physics*, 55(2):231–253.

Tang, J., Causon, D. M., Mingham, C. G., and Qian, L. (2013). Numerical study of vegetation damping effects on solitary wave run-up using the nonlinear shallow water equations. *Coastal Engineering*, 75:21–28.

Tang, J., Shen, Y., Causon, D. M., Qian, L., and Mingham, C. G. (2017). Numerical study of periodic long wave run-up on a rigid vegetation sloping beach. *Coastal Engineering*, 121(October 2016):158–166.

Tanino, Y. and Nepf, H. M. (2008). Laboratory investigation of mean drag in a random array of rigid, emergent cylinders. *Journal of Hydraulic Engineering*, 134(1):34–41.

Turpin, F. M., Benmoussa, C., and Mei, C. C. (1983). Effects of slowly varying depth and current on the evolution of a stokes wavepacket. *Journal of Fluid Mechanics*, 132(1978):1–23.

Vakil, A. and Green, S. I. (2009). Drag and lift coefficients of inclined finite circular cylinders at moderate Reynolds numbers. *Computers and Fluids*, 38(9):1771–1781.

Vogel, S. (1994). *Life in moving fluids: The physical biology of flow*. Princeton University Press.

Wathen, A. J. (2015). Preconditioning. *Acta Numerica*, 24:329–376.

Wazwaz, A.-M. (2010). *Partial differential equations and solitary waves theory*. Springer Science & Business Media.

Webster, P. J., Holland, G. J., Curry, J. A., and Chang, H.-R. (2005). Changes in tropical cyclone number, duration, and intensity in a warming environment. *Science*, 309(5742):1844–1846.

Weideman, J. A. C. and Reddy, S. C. (2000). A MATLAB differentiation matrix suite. *ACM Transactions on Mathematical Software*, 26(4):465–519.

Whitham, G. B. (1965a). A general approach to linear and non-linear dispersive waves using a Lagrangian. *Journal of Fluid Mechanics*, 22(2):273–283.

Whitham, G. B. (1965b). Non-linear dispersive waves. *Proceedings of the Royal Society of London. Series A. Mathematical and Physical Sciences*, 283(1393):238–261.

Whitham, G. B. (1974). *Linear and nonlinear waves*.

Wong, C. Y. H., Trinh, P. H., and Chapman, S. J. (2020). Shear-induced instabilities of flows through submerged vegetation. *Journal of Fluid Mechanics*, 891:A17.

Wu, W., Ozeren, Y., Wren, D., Chen, Q., Zhang, G., Holland, M., Marsooli, R., Lin, Q., Jadhav, R. S., Parker, K., and Pant, H. (2012). Investigation of Surge and Wave Reduction by Vegetation (Phase II) - Interaction of Hydrodynamics, Vegetation, and Soil. Technical Report 80037, University of Mississippi.

Zampogna, G. A., Pluvinage, F., Kourta, A., and Bottaro, A. (2016). Instability of canopy flows. *Water Resources Research*, 52(7):5421–5432.

Zeller, R. B., Weitzman, J. S., Abbett, M. E., Zarama, F. J., Fringer, O. B., and Koseff, J. R. (2014). Improved parameterization of seagrass blade dynamics and wave attenuation based on numerical and laboratory experiments. *Limnology and Oceanography*, 59(1):251–266.

Zeller, R. B., Zarama, F. J., Weitzman, J. S., and Koseff, J. R. (2015). A simple and practical model for combined wave-current canopy flows. *Journal of Fluid Mechanics*, 767:842–880.

Zhao, M., Cheng, L., and Zhou, T. (2009). Direct numerical simulation of three-dimensional flow past a yawed circular cylinder of infinite length. *Journal of Fluids and Structures*, 25(5):831–847.

Zhou, T., Wang, H., Razali, S. F. M., Zhou, Y., and Cheng, L. (2010). Three-dimensional vorticity measurements in the wake of a yawed circular cylinder. *Physics of Fluids*, 22(1):10–15.